Stanislav N. Gorb
Elena V. Gorb   *Editors*

Functional Surfaces in Biology III

Diversity of the Physical Phenomena

Springer

Biologically-Inspired Systems

Volume 10

Motto: Structure and function of biological systems as inspiration for technical developments

Throughout evolution, nature has constantly been called upon to act as an engineer in solving technical problems. Organisms have evolved an immense variety of shapes and structures from macro down to the nanoscale. Zoologists and botanists have collected a huge amount of information about the structure and functions of biological materials and systems. This information can be also utilized to mimic biological solutions in further technical developments. The most important feature of the evolution of biological systems is multiple origins of similar solutions in different lineages of living organisms. These examples should be the best candidates for biomimetics. This book series will deal with topics related to structure and function in biological systems and show how knowledge from biology can be used for technical developments in engineering and materials science. It is intended to accelerate interdisciplinary research on biological functional systems and to promote technical developments. Documenting of the advances in the field will be important for fellow scientists, students, public officials, and for the public in general. Each of the books in this series is expected to provide a comprehensive, authoritative synthesis of the topic.

Stanislav N. Gorb • Elena V. Gorb
Editors

Functional Surfaces in Biology III

Diversity of the Physical Phenomena

 Springer

Editors
Stanislav N. Gorb
Department of Functional Morphology
and Biomechanics, Zoological Institute
Kiel University
Kiel, Germany

Elena V. Gorb
Department of Functional Morphology
and Biomechanics, Zoological Institute
Kiel University
Kiel, Germany

Printed on acid-free paper

Preface: Diversity of the Physical Phenomena in Biological Surfaces

In 2009, in two volumes of "Functional Surfaces in Biology I and II", we quite naively tried to cover the diversity of the physical phenomena in biological surfaces (Gorb 2009a, b). However, it turned out that the field of functional biological surfaces is a very rapidly growing one with an increasing number of subfields, which are difficult to comprise even within several issues. The "Functional Surfaces in Biology III" continues the idea of the two previous issues and presents a new collection of chapters written in form either of topical reviews or original papers and devoted to structure-property relationships of biological surfaces.

Meanwhile it is well known that this kind of studies can inspire further technological developments (Heepe et al. 2017); however, the present book is primarily concentrated on interesting aspects of biological systems rather than on the development of technical systems inspired by mechanisms observed in biological systems. In other words, this issue aimed at revealing novel functional aspects of biological surfaces rather than implementing this knowledge in biomimetics.

The "Functional Surfaces in Biology III" shows a broad variety of facets of structural and experimental research on various biological surfaces in general. It covers a wide range of biological systems (from infrared receptors, photonic systems, moisture harvesting microstructures, water/oil absorbing surfaces, gas exchanging interfaces to adhesion enhancing and friction reducing systems) and their structure-function relationships and can be therefore interesting for biologists, physicists, chemists as well as materials scientists and engineers fascinated by the idea of biomimetics.

The first chapter by Anke Schmitz and Helmut Schmitz is devoted to the role of the cuticular surfaces in infrared reception of pyrophilous ('fire-loving') insects that rely on forest fires for their reproduction. In these insects, both the navigation towards a fire and short-range orientation on a freshly burnt material depend on a variety of specialized infrared sensors located on the thorax and abdomen. The chapter reviews the studied insect infrared receptors with an emphasis on the cuticle role in infrared perception. The authors distinguish three designs of receptors based on two different functional principles, which in turn rely on specialized types of cuticle serving as an interface between incoming radiation and sensory cells.

The Chap. 2 by Mikhail Kryuchkov, Artem Blagodatski, Vsevolod Cherepanov, and Vladimir L. Katanaev opens biophotonic section of the book. It provides an overview of the diversity of arthropod corneal nanostructures, which can be of nipple-, ridge-, maze-, or dimple-type with various transitions among them. With a diameter being thinner than the wavelength of the visible light, these structures provide a variety of functions ranging from reflection reduction to the enhancement of water-repellence. Interestingly, the entire diversity of these structures can be described by simple reaction-diffusion models that can explain formation of arthropod corneal nanostructures during eye development. The authors' vision is that real molecular identities, responsible for these reactions, can be revealed in model insect organisms and potentially used in bioengineering of novel nanocoatings.

In the Chap. 3, Villads Egede Johansen, Olimpia Domitilla Onelli, Lisa Maria Steiner, and Silvia Vignolini discuss biological structural colours caused by pigments organized in specific nano-scale architectures. Interestingly, these architectures in biological systems are very often not perfectly ordered, and such a disorder provides a broad range of functional optical effects. The authors discuss the influence of disorders on the photonic effects of biological surfaces by taking an example of the blue-winged *Morpho* butterfly. The role of hierarchical organization and pixelated surfaces is also demonstrated in the context of their role in tuning optical appearances of biological surfaces. Finally, this chapter provides mathematical tools for disorder analysis and using them describes examples of completely disordered structures having white appearance, such as in the dorsal surface of *Cyphochilus* beetle.

The Chap. 4 by Anna-Christin Joel, Gerda Buchberger, and Philipp Comanns opens section on the surface wettability by the review of structure-function relationships in moisture-harvesting reptiles that live in arid environments. The authors reveal special microstructural adaptations of the reptile integument enabling additional moisture-harvesting from various sources. Interestingly, this ability is often accompanied by a specific animal behavior. Most of these reptiles possess highly-specialized skin structures in form of microscopical capillary channels facilitating water flow in the anterior direction of the body. The authors discuss biomimetic potential (especially in the field of microfluidics) of these structural and experimental studies on reptiles.

The Chap. 5 by Anita Roth-Nebelsick, Frank Hauber, and Wilfried Konrad on porous structures for water absorption and gas exchange in orchids continues the wettability section. It is known that epiphytic orchids possess aerial roots with a special outer tissue layer, so called the velamen radicum, aiding in water condensation from the air and its absorption. The velamen radicum presumably played a very important role in successful radiation of epiphytic orchids. The authors show here that this tissue consists of dead cells building up a porous material with highly adapted surface and underlying tissues with interesting water draining behavior strongly depending on the thickness and structure of the tissue. They also provide comparison of velamen radicum in various orchid taxa and discuss structure-function relationships of this system.

The Chap. 6 by Elena V. Gorb, Philipp Hofmann, Alexander E. Filippov, and Stanislav N. Gorb deals with the adsorption ability of epicuticular wax coverages in plants that have been often shown to be impeding locomotion and reducing attachment of insects. One of mechanisms responsible for these effects, a possible adsorption of insect adhesive fluid by highly porous wax coverage, has been previously proposed. This chapter reports on experimental tests proving the adsorption ability of different fluids by plant wax blooms. Using a cryo scanning electron microscopy approach, high-speed video recordings of fluid drops behavior and numerical analysis of experimental data, the authors show that the wax coverage in the waxy zone of *Nepenthes alata*pitcher can strongly adsorb oil, but not water, which is a strong evidence that three-dimensional plant wax coverages will be anti-adhesive for insects relying on wet adhesion by oily substances.

The Chap. 7 by Janek von Byern, Carsten Müller, Karin Voigtländer, Victoria Dorrer, Martina Marchetti-Deschmann, Patrick Flammang, and Georg Mayer provides an overview of biological adhesives utilized by more than 100 marine and terrestrial organisms for defence and predation. These functions require specific combination of particular behaviours and properties of the adhesive, such as fast curing process, squirting over distance, bonding to various substrates, but organisms' protection against own glue. These organisms have a very wide environmental and phylogenetic diversity: hagfish, comb jellies, centipedes, salamanders, spiders, glowworms, velvet worms, etc. The review collects scattered published information about the composition, production, secretion mechanisms and mechanical properties of these glues, however, it concludes that only little is known about their functional principles. We are very much convinced that this chapter will facilitate new experimental studies on biological adhesives.

A case study from bioadhesion research is provided in the Chap. 8 by Lars Heepe, Constanze Grohmann, and Stanislav N. Gorb. This chapter deals with the visualization of tarsal adhesive setae in contact during normal and ceiling walk in the ladybird beetle. These setae form an intimate contact with the substrate and generate adhesion supporting insect walk on vertical walls or even on the ceiling. Previous adhesive force measurements at the level of individual setae provided estimation of the maximum adhesive capability of animals by assuming all setae being in contact. However, these values do not coincide with the results of adhesion measurements performed at the level of the whole animal. This discrepancy is due to the fact that not all setae are simultaneously applied during locomotion and this chapter deals with quantification of the beetle adhesive setae used during locomotion. It turned out that beetles use considerably more setae in contact during ceiling walk than during normal walk. The authors conclude that in order to control adhesion, animals are capable of controlling not only the amount of tarsal setae in contact, but also the type of setae depending on the type of substrate.

Another example of an effective high-speed biological adhesion is an adhesive tongue of frogs, which is an efficient tool capable of capturing fast moving prey. It is obvious that the interaction between the tongue surface and an adhesive mucus coating is crucial for generating strong pull-off forces with the prey surface. The Chap. 9 by Thomas Kleinteich and Stanislav N. Gorb is a comparative study of

tongue surfaces in nine frog species bearing microscopical papillae of different size and shape. The specific microstructure presumably contributes to the particular adhesive performance of different frog species and may correlate with the prey spectra between the taxa studied. This study also opens an interesting possibility of combining surface microstructure with adhesive fluids to enhance dynamical performance of the next generation of adhesives.

In fish, the combination of the scale surface structure with mucus leads to the friction reduction and generation of slippery surfaces. Dylan K. Wainwright and George V. Lauder discuss this system in detail in the Chap. 10 called "Mucus matters". The authors describe different categories of scales (cycloid, crenate, spinoid, ctenoid) and discuss structure-function relationships of sub-scale features, such as spines, ctenii, radii, and circuli. The authors suggest that three-dimensionality of these features is crucial for their hydrodynamic and protective functions. Additionally, fishskin is covered by mucus which was often ignored in previous studies. This chapter presents three-dimensional analyses of intact fish skin surfaces from seven species and compares them to the skin with the removed epidermis and mucus. This approach allowed demonstrating how mucus and epidermis interact with the scale surface and result in the functional surface texture, which remains a largely unexplored area. A very important feature of this chapter is the discussion on techniques for investigation and imaging the structure of fish surface, such as for example gel-based surface profilometry.

Another friction-related study is the book final Chap. 11 by Yoko Matsumura, Alexander E. Kovalev, Alexander E. Filippov, and Stanislav N. Gorb. It is devoted to the friction reduction mechanism during the super-long penis propulsion in beetles. There is no doubt that surface interactions of the male and female genitalia during copulation play a key role in evolution, but the morpho/physical diversity of interacting surfaces and their biomechanics in sexual intercourse of the vast majority of animals are not well studied. The authors take male and female genitalia in cassidinebeetles as a model system and using microscopical analysis of material composition reveal stiffness gradient in male penis. Furthermore, they numerically model its propulsion into the female duct. This simulation demonstrates that the type of the stiffness gradients observed in the real male (softer at the tip and stiffer at the base) aids in the faster propulsion than other types. This chapter indicates that previously ignored physical properties of genital surfaces may aid in understanding physical interactions of sexes and shed light on the evolution of genitalia.

In general, this book discusses numerous experimental methods for the characterization of the mechanical and optical properties of biological surfaces at the micro- and nanoscale. It combines approaches from biology, physics, chemistry, materials science, and engineering and therefore represents a good example of modern interdisciplinary science. Due to this latter reason, we hope that the contributions from this book will be of interest to both engineers and physicists, who use inspirations from biology to design technical surfaces and systems, as well as to biologists, who apply physical and engineering approaches to understand how biological systems function.

The editors would like to thank all the authors for contributing their first-class work to this book. We are also grateful to all referees Harvey B. Lillywhite (University of Florida, USA), Wolfgang Böhme (Zoologisches Forschungsmuseum Alexander Koenig, Bonn, Germany), Uwe Erb (University of Toronto, Canada), Dennis LaJeuness (The University of North Carolina at Greensboro, USA), Bodo Wilts (Adolphe Merkle Institute, Fribourg, Switzerland), Vladimir V. Tsukruk (Georgia Institute of Technology, Atlanta, USA), Akira Saito (Osaka University, Japan), Shinya Yoshioka (Tokyo University of Science, Japan), Douglas S. Fudge (Chapman University, Orange, USA), Mason Dean (Max Planck Institute of Colloids and Interfaces, Potsdam, Germany), Doekele G. Stavenga (University of Groningen, The Netherlands), Victor Benno Meyer-Rochow (Research Institute of Luminous Organisms, Tokyo, Japan), Lloyd Graham (CSIRO, North Epping, Australia), and Robert B. Suter (Vassar College, USA) for their constructive reports, which facilitated the high quality of the manuscripts and also allowed us to publish in a timely manner. Finally, we thank the Editorial Team at Springer-Nature for their continuous great support of biology- and biomimetics-related topics within BISY book series.

Kiel, Germany   Stanislav N. Gorb
December 2017   Elena V. Gorb

References

Gorb, S. N. (Ed.). (2009a). *Functional surfaces in biology: Little structures with big effects – Volume 1*. Dordrecht: Springer.

Gorb, S. N., (Ed.). (2009b). *Functional surfaces in biology: Adhesion related phenomena – Volume 2*. Dordrecht: Springer.

Heepe, L., Xue, L. & Gorb, S. N., (Eds.). (2017). *Bio-inspired structured adhesives: Biological prototypes, fabrication, tribological properties, contact mechanics, and novel concepts*. Dordrecht: Springer.

Contents

Contributors

Artem Blagodatski School of Biomedicine, Far Eastern Federal University, Vladivostok, Russian Federation

Department of Pharmacology and Toxicology, University of Lausanne, Lausanne, Switzerland

Gerda Buchberger Institute of Biomedical Mechatronics, JKU Linz, Linz, Austria

Vsevolod Cherepanov School of Biomedicine, Far Eastern Federal University, Vladivostok, Russian Federation

Philipp Comanns Institute of Zoology, RWTH Aachen University, Aachen, Germany

Victoria Dorrer Technische Universität Wien, Vienna, Austria

Alexander E. Filippov Department of Functional Morphology and Biomechanics, Zoological Institute, Kiel University, Kiel, Germany

Department N5, Donetsk Institute for Physics and Engineering, Donetsk, Ukraine

Patrick Flammang Université de Mons, Mons, Belgium

Elena V. Gorb Department of Functional Morphology and Biomechanics, Zoological Institute, Kiel University, Kiel, Germany

Stanislav N. Gorb Department of Functional Morphology and Biomechanics, Zoological Institute, Kiel University, Kiel, Germany

Constanze Grohmann Department of Functional Morphology and Biomechanics, Zoological Institute, Kiel University, Kiel, Germany

Frank Hauber Department of Geosciences, University of Tübingen, Tübingen, Germany

Lars Heepe Department of Functional Morphology and Biomechanics, Zoological Institute, Kiel University, Kiel, Germany

Philipp Hofmann Department of Functional Morphology and Biomechanics, Zoological Institute, Kiel University, Kiel, Germany

Anna-Christin Joel Institute of Zoology, RWTH Aachen University, Aachen, Germany

Westphalian Institute of Biomimetics, Westphalian University of Applied Science, Bocholt, Germany

Villads Egede Johansen Department of Chemistry, University of Cambridge, Cambridge, UK

Vladimir L. Katanaev Department of Pharmacology and Toxicology, University of Lausanne, Lausanne, Switzerland

School of Biomedicine, Far Eastern Federal University, Vladivostok, Russian Federation

Thomas Kleinteich Department of Functional Morphology and Biomechanics, Zoological Institute, Kiel University, Kiel, Germany

Wilfried Konrad Department of Geosciences, University of Tübingen, Tübingen, Germany

Alexander E. Kovalev Department of Functional Morphology and Biomechanics, Zoological Institute, Kiel University, Kiel, Germany

Mikhail Kryuchkov Department of Pharmacology and Toxicology, University of Lausanne, Lausanne, Switzerland

George V. Lauder Department of Organismic and Evolutionary Biology, Harvard University, Cambridge, MA, USA

Martina Marchetti-Deschmann Technische Universität Wien, Vienna, Austria

Yoko Matsumura Department of Functional Morphology and Biomechanics, Zoological Institute, Kiel University, Kiel, Germany

Department of Biology, Keio University, Yokohama, Japan

Georg Mayer University of Kassel, Kassel, Germany

Carsten Müller University of Greifswald, Greifswald, Germany

Olimpia Domitilla Onelli Department of Chemistry, University of Cambridge, Cambridge, UK

Anita Roth-Nebelsick State Museum of Natural History, Stuttgart, Germany

Anke Schmitz Institut für Zoologie, Universität Bonn, Bonn, Germany

Helmut Schmitz Institut für Zoologie, Universität Bonn, Bonn, Germany

Lisa Maria Steiner Department of Chemistry, University of Cambridge, Cambridge, UK

Silvia Vignolini Department of Chemistry, University of Cambridge, Cambridge, UK

Karin Voigtländer Senckenberg Museum für Naturkunde Görlitz, Görlitz, Germany

Janek von Byern Ludwig Boltzmann Institute for Experimental and Clinical Traumatology, Vienna, Austria

Dylan K. Wainwright Department of Organismic and Evolutionary Biology, Harvard University, Cambridge, MA, USA

Part I
Receptors

Chapter 1
Cuticle as Functional Interface in Insect Infrared Receptors

Anke Schmitz and Helmut Schmitz

Abstract Pyrophilous ('fire-loving') insects depend on forest fires for their reproduction. Therefore, such insects approach ongoing fires and invade the freshly burnt area immediately. In beetles members of two genera of jewel beetles (Buprestidae) and one species of the genus *Acanthocnemus* (Acanthocnemidae) show a highly pyrophilous behaviour. Additionally, pyrophilous behaviour has also been described for four species of the large flat bug genus *Aradus* (Aradidae). For the long-range navigation towards a fire as well as for the short-range orientation on a freshly burnt area these insects have developed special sensors for the smell of burning and for infrared (IR) radiation. Whereas the olfactory receptors for smoke are located on the antennae, the IR receptors are housed in extraantennal sensory organs. Although the community of pyrophilous insects is rather small, no 'standard' IR receptors exist. Receptors are located on the thorax or on the abdomen and show a stunning diversity with respect to structure and function. Two functional principles and three fundamentally different designs have been described. Nevertheless, in all receptors the cuticle plays an important role as interface between incoming radiation and the associated sensory cells. The cuticular apparatus of an IR receptor, therefore, has to manage effective absorption and subsequent fast transformation of photon energy into a state variable which can be perceived by the sensory cells. The chapter provides an overview about the known insect IR receptors with a focus on the impact of the cuticle in IR perception.

1.1 Introduction

About 25 insect species are attracted by forest fires and can be found on freshly burnt areas after fires. In three genera of pyrophilous beetles and one genus of pyrophilous bugs infrared (IR) receptors have been discovered. Although the number of IR sensitive insects is extremely small, no standard insect IR receptor exists. At least in three of the four IR sensitive genera receptors look totally different and

A. Schmitz · H. Schmitz (✉)
Institut für Zoologie, Universität Bonn, Bonn, Germany
e-mail: h.schmitz@uni-bonn.de

are located on different parts of the body. As a result, at least two different functional principles can be distinguished: bolometer like receptors and so-called photomechanic receptors. Consequently, insect IR receptors can be innervated by thermo- or mechanosensitive cells. However, in all insect IR receptors the IR absorbing cuticle is the very important interface ensuring effective absorption of IR photons and subsequent conversion of the photon energy into a stimulus detectable by the corresponding sensory cell. Insect cuticle can be regarded as a composite material consisting of biopolymers that show strong IR absorption bands in the mid infrared radiation region (MWIR). During the independent evolution of insect IR receptors in the four genera the cuticular components of the receptors have undergone profound structural and functional modifications to be able to fulfill their respective sensory tasks.

In this chapter the infrared organs of pyrophilous insects are outlined. Especially the IR absorbing cuticular apparatus of the different IR receptors and how absorbed IR quantum energy is transformed into a signal perceivable for the inherent sensory cells is in the focus of interest. After a short introduction in the nature of infrared radiation the pyrophilous behavior and the bolometer like IR receptors of the Australian Little Ash Beetle *Acanthocnemus nigricans* and the Australian Firebeetle *Merimna atrata* are described. Then the behavior and the so-called photomechanic IR receptor of buprestid beetles of the genus *Melanophila* and flat bugs of the genus *Aradus* are introduced. In the discussion the cuticle as effective IR absorber is dealt with and finally the different routes of converting IR quantum energy into bioelectric signals are highlighted.

1.2 Physical Properties of Infrared Radiation

Every body with a temperature above 0 K (-273.15 °C) emits IR radiation. This is caused by molecular movements starting at temperatures slightly above 0 K. In nature and engineering IR radiation can be used for the detection of objects with a temperature higher or lower than the ambient temperature. This is especially useful in complete darkness. Detection of IR radiation requires special detectors. Two classes of IR detectors are currently used: uncooled bolometer sensors and much more sensitive cooled quantum detectors. In a bolometer the temperature of an IR absorbing surface is measured with a temperature sensor; in a quantum detector the energy of an absorbed IR photon induces an electrical effect in a semiconductor material which can be read out with an integrated circuit. To suppress the thermal noise in the semiconductor, sensors routinely are cryogenically cooled. In this chapter electromagnetic radiation significant for living organisms is considered. Here the upper limit is represented by the surface temperature of sun at 5800 K; the lower limit by objects at ambient temperature. In their natural environment organisms are primarily subjected to a radiation spectrum ranging from high-level ultraviolet (UV) down to low-energy infrared (IR) radiation (Fig. 1.1). The spectral distribution of the radiation emitted e.g. by a high intensity forest fire with a temperature of 1300 K

can be calculated according to Planck's radiation law. At a given temperature the wavelength at which most of the radiant energy is emitted (λ_{max}) can be calculated by the law of Wien:

$$\lambda \max = \frac{2,897.8 [\mu m * K]}{T[K]}, \text{where T is the absolute temperature given in}$$

Kelvin [K].

For the perception of radiation in the mentioned wavelength range the photon energy is of special importance. When trying to detect an object by electromagnetic radiation (either emitted or reflected by the object) an ideal sensor should have its highest sensitivity at λ_{max} of the radiation source. This is realized in e.g. in photoreceptors of most diurnal animals, where the rhodopsin of the light-sensitive rods enabling scotopic vision exhibits its λ_{max} at about 0.5 μm (Schoenlein et al. 1991; Bowmaker and Hunt 2006), perfectly matching the emission maximum of the sun. In general, the spectral sensitivity of photo pigments is determined by the interaction of retinal with specific amino acids lining the ligand-binding pocket within the opsin (Bowmaker and Hunt 2006). Thus, the ability to see in the IR requires pigments showing sufficient absorption (i) in the *near infrared* (NIR, 0.75–1.4 μm (D'Amico et al. 2009)), (ii) in the *mid wavelength infrared* (MWIR, 3–8 μm) or (iii) even in the *long wavelength infrared* (LWIR, 8–12 μm; Fig. 1.1). The corresponding frequency *f* of an IR photon of a given wavelength λ can be calculated according to $f = c/\lambda$ with c = speed of light. Although some animals, e.g. some fish living in turbid waters, are obviously able to see in the NIR (Meuthen et al. 2012; Shcherbakov et al. 2013) by *"long-wavelengths"* (LWS) photoreceptors. However, LWS receptors with absorbance spectra beyond 800 nm are unknown (Douglas et al. 1998). The first essential step in vision always is the cis-trans torsional isomerization of the
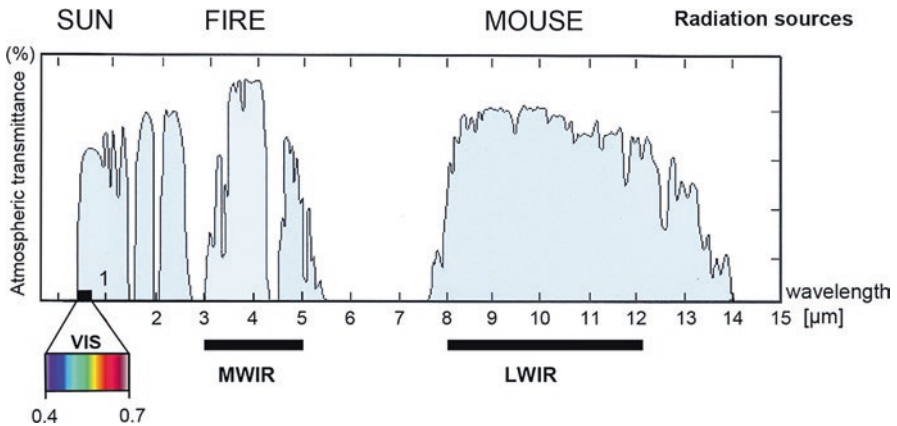

Fig. 1.1 Atmospheric transmittance of electromagnetic radiation emitted from objects with biological relevance. Atmospheric windows (indicated in blue) exist for visible light (VIS) radiated from the sun, MWIR radiated from high temperature sources like forest fires, and LWIR radiated from low temperature sources like warm-blooded creatures

rhodopsin chromophore (Schoenlein et al. 1991). This conformational switch requires a photon energy of more than 1.24 eV (the energy content of a 1 μm photon). However, IR photons emitted by a fire or a warm-blooded creature do not carry enough energy to initiate the isomerization of a visual pigment.

Consequently, in technical and biological IR receptors other mechanisms for converting the energy of an absorbed IR photon into an appropriate signal have to be realized. After absorption at the surface of a biological IR receptor thermal and/or mechanical effects initiated in the absorber material could be measured by underlying sensory cells. Thus it is proposed that the absorbing surfaces as well as the structuring of the absorber material have been improved by evolution to maximize these processes.
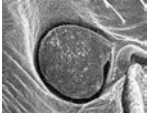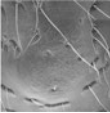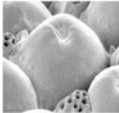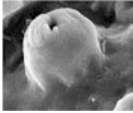
1.3   IR Receptors in Pyrophilous Insects

A fire not only devastates a forest but also creates a very interesting ecological niche within minutes: the burnt area (Bond and Keeley 2005). On a freshly burnt area, most biotic as well as many abiotic factors have changed dramatically. For insect species which feed on dead wood or fungi, such a place is of great interest (Saint-Germain et al. 2008). However, the area has to be approached quickly before more and more competitors arrive. In this regard it is of interest that ecological investigations have shown that a small community of insects can be found more frequently on burnt than on unburnt areas. This particular group of so-called pyrophilous insects consists of about 40 species out of the orders of Coleoptera, Hemiptera, Diptera, and Lepidoptera (Wikars 1997). It can be proposed that pyrophilous insects have developed sensory and behavioral adaptations to detect and approach fires and burnt areas. This is especially true for species which can be found on freshly burnt areas immediately after a fire.

In contrast to an approach by olfactory cues which can be considerably impeded by the wind, especially over longer distances, an orientation by electromagnetic radiation in the visible and in the infrared (IR) spectrum allows a straight approach to the source. This is also promoted by an atmospherical window transparent for MWIR (mid wavelength IR) radiation between 3 and 5 μm (Fig. 1.1). So it is evident that pyrophilous insects appear to be predestined to have evolved IR receptors.

At present 17 insect species out of four pyrophilous genera are known to possess IR sensory organs (Table 1.1). Compared to the amount of known insect species (roughly one million) this is a negligible number. Even though IR receptors are very rare in insects, no "standard" IR receptor seems to exist. At least three fundamentally different types of receptors could be identified: a pair of prothoracic discs covered with numerous tiny sensilla in *Acanthocnemus nigricans*, pairs of roundish abdominal IR organs in *Merimna atrata*, and the so-called photomechanic IR sensilla in *Melanophila* beetles and in a few species of pyrophilous *Aradus* bugs. With regard to the functional principles, two categories exist: bolometer-like receptors in *Acanthocnemus* and *Merimna* and photomechanic sensilla in *Melanophila* and

Table 1.1 Infrared receptors in pyrophilous insects

	'Little Ash Beetle' *Acanthocnemus nigricans* Only species in the genus	'Australian Fire Beetle' *Merimna atrata* Only species in the genus	'Black Fire Beetles' *Melanophila spec.* 11 species with IR receptors	'Pyrophilous Flat Bugs' *Aradus spec.* 4 species with IR receptors
Systematic position	**Beetle** (family: Acanthocnemidae)	Jewel **beetles** (family: Buprestidae)		Flat **bugs** (family: Aradidae)
Ventral habitus				
IR organs/ receptors indicated in yellow				
Legs omittedL: body length	L: 4 mm	L: 20 mm	L: 10 mm	L: 4 mm
Position of IR receptor	Prothorax	Abdomen	Metathorax	Pro−/mesothorax
Picture of IR organ or single sensillum	Left IR organ (diameter 150 μm)	Left anterior IR organ (trough-shaped cuticular depression, diameter 500 μm)	Single IR sensillum (about 70 sensilla in a sensory pit, diameter 20 μm)	Single IR sensillum (sensilla located between hair mechanoreceptors, diameter 20 μm)
Mode of operation	Bolometer (in *Merimna* with additional photomechanic unit)		Photomechanic receptors	

Aradus (cf. Table 1.1). The different configuration as well as the location at different spots on the thorax or the abdomen already provides strong evidence that IR receptors in the four genera have evolved independently from each other.

In all insect IR receptors, the cuticle of the exoskeleton constitutes the IR receiving interface interconnected between the environment and the interior sensory cells. Cuticle can be regarded as a biopolymer and, therefore, is a highly effective IR absorber. As already delineated in a previous publication (Schmitz and Bleckmann 1998a), chitin and protein molecules contain many C-H, N-H, and O-H groups swinging with frequencies in the range of 100 THz. As a result, cuticle shows distinctive stretch resonances in the range of 3 μm which corresponds to the emission maximum of a forest fire. The existence of stretch resonances is an ideal prerequisite for maximal absorption of photons in an absorber material inevitably causing a rise in temperature. Therefore, the cuticle plays a very important role in the different insect IR organs.

1.4   Bolometer Like IR Receptors in *Acanthocnemus* and *Merimna*

1.4.1   The 'little ash beetle' Acanthocnemus nigricans

1.4.1.1   Pyrophilous Behavior

Originally, the "little ash beetle" *A. nigricans* (family Acanthocnemidae, Table 1.1) was endemic to Australia (Champion 1922) and represents the only species within its family. In the last decades this beetle has been exported out of Australia and nowadays can also be found in several countries of the Palearctic ecozone (Alonso-Zarazaga et al. 2003; Mayor 2007; Liberti 2009; Valcárcel and Piloña 2009; Kovalenko 2011). The inconspicuous beetle is only 3–5 mm long and is strongly attracted by forest fires (own observations during the last decade). Immediately after a fire, *A. nigricans* can be found on freshly burnt areas, preferably close to fields of hot ashes. However, its biology is largely unknown. It has been speculated that the sexes meet around hot spots for mating. Observations of the behavior are very difficult because after landing on the ash and a short period of hectically running around the beetles dive into the ash and become invisible. So the substrate to which the eggs may be deposited is unknown. Nevertheless, there is strong evidence that *Acanthocnemus* depends on fires for its reproduction. As special adaptation to its pyrophilous way of life the beetle is equipped with a pair of complex IR receptors located on the first segment of the thorax (Kreiss et al. 2005).

1.4.1.2   The Prothoracic IR Organs

The IR organs of *A. nigricans* are unique in insects. As depicted in Table 1.1 and Fig. 1.2a one pair of IR organs is located on the prothorax (Schmitz et al. 2002; Kreiss et al. 2005). The main component of each organ is a little cuticular disc which is situated over a cavity (Fig. 1.2b). The air within the cavity beneath the disc communicates with the ambient air by a small gap around the disc. By this construction the thermal mass of the disc is considerably reduced and the underlying air layer thermally insulates the disc from the thorax. On the anterior surface of the disc about 90 tiny cuticular sensilla are situated. This is the part of the disc with the lowest thermal mass. A single disc sensillum consists of a small cuticular peg (diameter about 1.5 μm, length about 2 μm) which is connected to an unusual electron dense rod (Figs. 1.2c, d). The rod most probably represents the extremely hypertrophied dendritic sheath normally ensheathing the outer dendritic segment (DOS) in other mechanosensory sensilla (Kreiss et al. 2005). In the *A. nigricans* IR sensillum the outer peg effectively is connected to the inner dendritic segment (DIS) of the sensory cell, which is situated under the cuticle (Fig. 1.2d). However, the function of the rod remains enigmatic. Recently computer simulations have shown that rods may serve as heat conducting structures channeling heat to the underlying sensory
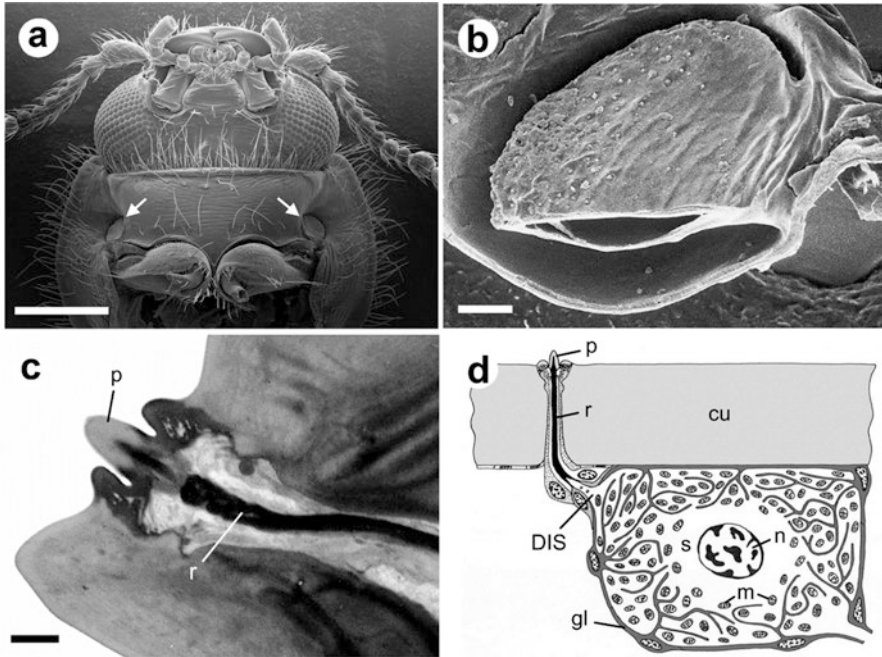
Fig. 1.2 (**a**) Head and prothorax of *Acanthocnemus nigricans*. The prothoracic IR organs are discernible as little cuticular discs (diameter 150 μm) located directly in front of the coxa of the forelegs. Bar: 500 μm. (**b**) Cut through the ventral part of the disc and the underlying cavity shows the composition of the organ. The disc is held above the cavity by a small posterior stalk. Bar: 20 μm. (**c**) Section through a single sensillum at the anterior rim of the disc. An electron dense rod (r) is connected to the outer peg (p) and continues through the dendritic canal down to the soma of a sensory cell located below the cuticle. Bar: 1 μm. (**d**) Schematic drawing of a disc sensillum. Note that numerous mitochondria (m) are housed inside the soma. DIS: short dendritic inner segment gl: glial cells, n: nucleus, p: peg, r: rod, s: soma. (**d**) Modified after Kreiss et al. (2005)

cells (Zhou et al. 2016). The soma of the sensory cell as well as the DIS is characterized by many deep invaginations of the cell membrane. The narrow extracellular spaces enclosed by the invaginated membranes are filled by darker glial cells. Especially the peripheral intracellular compartments inside the soma are densely filled with mitochondria (Fig. 1.2d).

Electrophysiological recordings from single disc sensilla have shown that sensilla responded with a phasic-tonic increase of neuronal activity to increasing temperature (Kreiss et al. 2007). In principle this corresponds to the typical response pattern of a thermoreceptive warm cell (Gingl and Tichy 2001). Threshold sensitivity has been determined to be between 11 and 25 mW/cm^2 tested with a red helium-neon laser (Kreiss et al. 2007).

Due to its morphology and response behavior the IR organs of *Acanthocnemus* can be classified as microbolometer-like IR sensors (cf. Table 1.1). In a bolometer, absorbed IR radiation heats up a thin absorber that corresponds to the outer surface

of the disc containing the cuticular parts of the sensilla. The resulting increase in temperature is measured by the sensory cells inside the disc. Commonly the absorbers of a technical microbolometer are coated with e.g. vanadium oxide whose electrical resistance strongly changes with temperature. This can be easily measured by an appropriate readout circuit (Rogalski 2002). Compared to microbolometer sensors used nowadays e.g. for thermal imaging, the sensivity of the *Acanthocnemus* IR receptors is rather low. Current technical microbolometers have sensitivities of a few μW/cm^2 (Budzier and Gerlach 2011) and, therefore, it is unlikely that *Acanthocnemus* uses its IR organs for fire detection from larger distances. Theoretical calculations suggest that *Acanthocnemus* might be able to detect a large fire of e.g. 10 ha from distances of a few kilometers. However, this still has to be shown experimentally. More likely beetles use their thoracic IR organs for the navigation on freshly burnt areas still showing many hot spots. *Acanthocnemus* is active during the day and most hot spots cannot be seen with their complex eyes by daylight. Because it has been frequently observed by the authors that beetles seem to aggregate very close to smaller hot spots (e.g. patches of hot ashes around a burnt stump) it can be concluded that the beetles are able to detect those hot spots from distances of some meters by IR reception. Furthermore, IR receptors could serve as early warning systems to avoid a landing on a hot spot.

1.4.2   IR receptors in **Merimna atrata**

1.4.2.1   **Pyrophilous Behavior**

The buprestid beetle *M. atrata* is the only species within the genus *Merimna* and is distributed all over Australia (Hawkeswood 2007). *Merimna* exclusively breeds in different species of fire-killed eucalyptus trees (Myrtaceae (Hawkeswood and Peterson 1982; Kitchin 2009)). Immediately after a fire, first *Merimna* beetles arrive at the border of the freshly burnt area where they can be observed resting or running around on the vegetation. However, to the earliest time when a human is able to enter the burnt area the beetles also start to invade the scorched terrain (Schmitz et al. 2015). Beetles rapidly spread over the burnt area and can be observed flying around relatively low or running over burnt ground, trees and shrubs (Poulton 1915; Schmitz and Schmitz 2002). Males primarily are in search for females. After copulation the females start to deposit their eggs under the bark of fire-scorched eucalyptus trees by inserting their ovipositor in small crevices. After hatching, the larvae start to feed inside the wood of the fire-killed trees; the new generation of beetles will emerge 1 or 2 years later (Kitchin 2009).

Additionally, *Merimna* also perceives the opportunity to forage on the burnt area. All material potentially edible is investigated and, if consumable, eaten up. Also carcases of small fire-killed vertebrates are devoured (Schmitz et al. 2015).

1.4.2.2 The Abdominal IR Organs

In *M. atrata* one pair of IR organs is located ventrolaterally on the second, third and sometimes also on the fourth abdominal sternite each (cf. Table 1.1) (Mainz et al. 2004). The IR organs consist of an external cuticular part – the radiation absorbing area – and an internal sensory complex innervating this area (Fig. 1.3a, c) (Schmitz et al. 2001).

The absorbing area is a roundish and shallow indentation of the cuticle. Depending on the size of the beetle, the average diameter is about 500 μm and the depth is about 150 μm (Fig. 1.3a, c, e) (Schneider and Schmitz 2013). An absorbing area is characterized by the following special features: (i) a lack of dark pigments within the exocuticle resulting in a yellowish color of the IR organ in contrast to the glossy dark brown color of 'normal' cuticle surrounding the absorbing area (Fig. 1.3c) (Schmitz et al. 2001); (ii) a honeycomb-like microstructure in the central region of the absorbing area (Fig. 1.3a, b) (Schmitz et al. 2000); (iii) and a reduced thickness of the cuticle in the center (Fig. 1.3e) (Schneider and Schmitz 2013, 2014)) under which the sensory complex is situated. It can be proposed that the lack of dark pigments in the cuticle of the absorbing area significantly reduces the absorption of visible light and subsequent heating, because dark pigments like melanins have their absorption maxima within the range of visible light (Stark et al. 2005). The reduction in thickness decreases the thermal mass of the cuticle which most probably allows faster heating and cooling of the cuticle above the sensory complex.

The sensory complex comprises a large multipolar Type1 neuron with a specialized dendritic region called terminal dendritic mass (TDM, Fig. 1.3d) and in close proximity to that a smaller chordotonal organ (CO), represented by two scolopidia (Schneider and Schmitz 2013). The thermoreceptive function of the multipolar neuron has been confirmed by electrophysiological recordings (Schmitz and Trenner 2003). Like the disc-sensilla in *Acanthocnemus*, the neuron responds in a phasic-tonic way with an increase of its spike frequency to increasing temperatures. Thus the thermoreceptive modality of the multipolar neuron also allows a classification of the *Merimna* IR organ as a bolometer. However, because of the rather low threshold sensitivity of 40 mW/cm^2, determined in the electrophysiological experiments conducted so far (Schmitz and Trenner 2003), it has been concluded that the *Merimna* IR organ is not suitable for remote sensing of forest fires but rather serves for short-distance sensing, e.g. to prevent the beetle from landing on hot surfaces (Schmitz and Trenner 2003). More recent investigations have concentrated on the CO as a second, putative receptor system involved in IR perception, which may increase the sensitivity of the IR organs (Schneider and Schmitz 2013). The CO represents a mechanosensory unit, consisting of two mononematic scolopidia, located in direct proximity to the multipolar neuron in the center of the absorbing area (Fig. 1.3c) (Schneider and Schmitz 2013)). Just like other scolopidia of this type, they are supposed to respond to axial stress or bending (Field and Matheson 1998). In general scolopidia function as proprioceptors or specialized mechanoreceptor organs, capable of detecting mechanical displacements over several orders of magnitude (Field and Matheson 1998) down to 0.6 nm (Michelsen and Larsen 1985). Therefore, it has
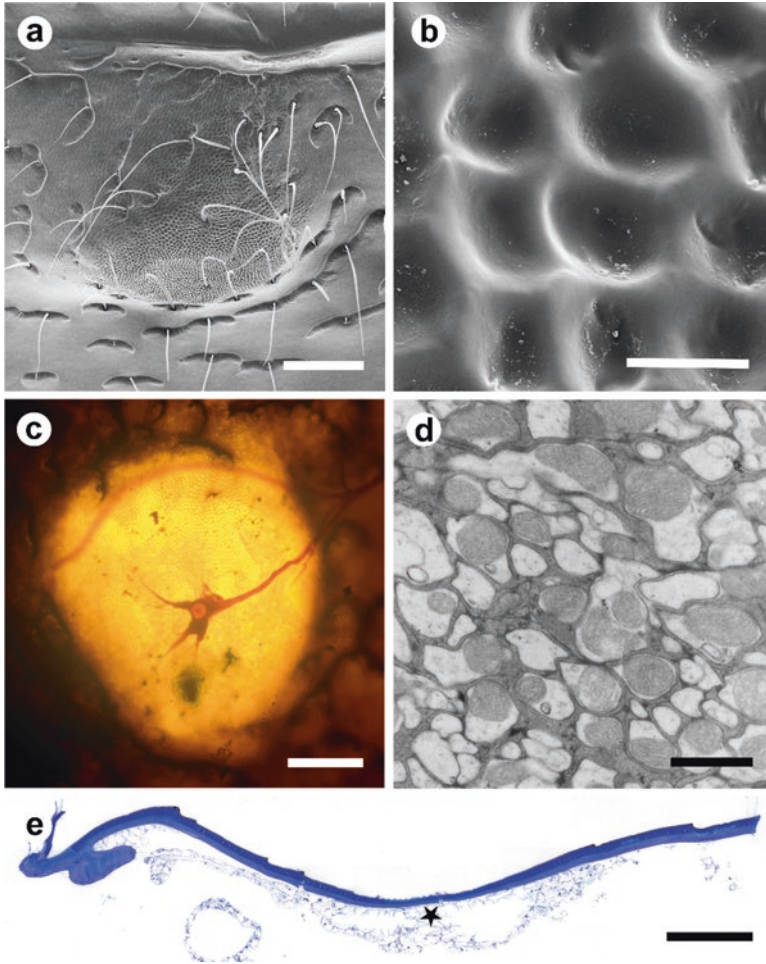
Fig. 1.3 IR-organ of *Merimna atrata*. (**a**) SEM-image of the absorbing area showing its three-dimensional shape and honeycomb-like surface structure. Bar: 200 μm. (**b**) Detail of the surface of the IR absorbing area showing a somewhat irregularly honeycomb microstructure. Bar: 10 μm. (**c**) LM-micrograph of the sensory complex stained with cobalt/nickel innervating the yellowish absorbing area. Bar: 200 μm. (**d**) TEM-micrograph of the terminal dendritic mass (TDM) of the thermosensitive multipolar neuron. Dendrites are densely filled with mitochondria. Bar: 1 μm. (**e**) Longitudinal section through the center of the absorbing area stained with toluidine-blue/borax (LM-image). Asterisk indicates position of the sensory complex. Orientation: top = exterior, bottom = interior. Bar: 100 μm. (**c**) and (**e**) Modified after Schneider and Schmitz (2013)

been proposed that the absorption of IR radiation could also lead to minute deformations of the absorbing area with its highest extend in the central region, corresponding to the attachment site of the CO (see asterisk in Fig. 1.3e). The CO could perceive these mechanical events and thus probably extend the measuring range, thereby increasing the sensitivity of the IR organ (Mainz et al. 2004; Schneider and

Schmitz 2013). Investigations of the mechanical properties of the IR absorbing area have revealed that – despite of the reduced thickness – the cuticle in the center of the absorbing areas is significantly stiffer and harder than the surrounding normal cuticle (Schneider and Schmitz 2014). This may result in a thermal deformation behavior specially adapted for the perception by mechanosensory units. Other probable advantages provided by the COs could include e.g. faster response times, a larger dynamic range, higher reliability or improved filter properties. However, unambiguous electrophysiological recordings from the CO are missing so far.

1.5 Photomechanic IR Receptors in *Melanophila* Beetles and Pyrophilous Flat Bugs of the Genus *Aradus*

There is considerable evidence that the so-called photomechanic IR receptors have developed from common mechanosensitive bristles. A possible evolutionary scenario can be outlined as follows: in insects, which already had started to develop a pyrophilous way of life, heat from hot surfaces on a burnt area may have stimulated external mechanoreceptors (see Discussion). This can be exemplified by looking at the photomechanic sensilla in *Melanophila* beetles and *Aradus* bugs. As discussed by Schmitz et al. (2007, 2010), there is strong evidence that in both pyrophilous species the IR sensilla have evolved directly from hair mechanoreceptors (sensilla trichodea). However, because photomechanic IR sensilla so far have only been found in recent species of the genus *Melanophila* within the beetles and in very few pyrophilous species of the genus *Aradus* within the bugs, sensilla must have developed independently in both genera. It is imaginable that e.g. the dome-shaped area provides a good surface to volume ratio allowing enhanced absorption of IR photons; the diameter of the sphere could reflect the penetration depth of IR photons into the cuticle of 3–4 μm (Schmitz et al. 2010).

1.5.1 IR Pit Organs in Melanophila *Beetles*

1.5.1.1 Pyrophilous Behaviour

Buprestid beetles of the genus *Melanophila* inhabit nearly all continents except Australia and Antarctica, and use fire killed trees as food for their larvae (Ricksecker 1885; Manee 1913; Sharp 1918; Van Dyke 1926; Linsley 1933; Sloop 1937; Linsley 1943; Evans 1964, 1966b; Wikars 1997; Bellamy 2008). As far as it is known, all recent species show the same pyrophilous biology and behavior as reported above for *Merimna* in Australia. Of course both genera use different tree species. Whereas *Merimna* breeds in scorched eucalyptus trees, *Melanophila* species breed in a variety of burnt conifers as well as in several species of scorched deciduous trees (Horion 1955; Apel 1991). Thus, it can be concluded that the two

buprestid genera have occupied the same ecological niche and have developed a nearly identical pyrophilous way of life on different continents. Surprisingly, their IR receptors are totally different.

A possible reason for the different type of construction of the *Melanophila* IR organ could be that the *Melanophila* IR receptors are more sensitive than the *Merimna* IR organs. It has been reported that untold numbers of *Melanophila consputa* were attracted to a burning 750,000-barrel oil storage tank near Coalinga in California in 1924 (Van Dyke 1926). A recent modeling of this historic oil tank fire suggested a remarkably high sensitivity of the IR receptors (Schmitz and Bousack 2012). The analysis of the geographical conditions around the tank fire yielded the result that most beetles must have become aware of this fire from a distance of 130 km. If IR radiation really was an important cue used by the beetles to detect the fire, this would result in a sensitivity of the IR pit organs of 4-13nW/cm^2 (Schmitz and Bousack 2012).

1.5.1.2 The Metathoracic IR Organs

The IR receptors are situated in two pit organs which are located on the metathorax (cf. Table 1.1). Each IR organ houses about 70 IR sensilla which are closely packed together at the bottom of the pit (Fig. 1.4a, (Evans 1966a; Vondran et al. 1995)). From the outside, a single sensillum can be recognized by a hemispherical dome with a diameter of about 15–20 μm. The dome is built by a thin cuticle which represents the outer boundary of a spherical internal cavity. The cavity is almost completely filled out by a tiny cuticular sphere with a diameter of about 12 μm (Fig. 1.4b, c). Based on transmission electron microscopic (TEM) observations, Vondran et al. (1995) described that the sphere consists of three different zones: (i) an outer lamellated mantle, also confirmed by scanning probe microscopy (Hazel et al. 2001), (ii) an intermediate layer of unstructured cuticle revealing many irregularly arranged microcavities (mc in Fig. 1.4c), and (iii) an innermost central zone where the cuticle appears uniform except for some spots of higher electron density. The sphere is connected to the vertex of the outer cuticular dome by a small cuticular stalk (Fig. 1.4b, c). The narrow gap surrounding the sphere is filled out by leaf-like extensions of at least two enveloping cells (not visible in the dried cuticular specimen shown in Fig. 1.4c). From below, the sphere is innervated by a single sensory cell (Fig. 1.6a). As a prominent feature it has been found that the outermost tip of the dendrite is located inside an inner pressure chamber in the sphere (ipc in Fig. 1.4c). All morphological as well as all physiological data available so far have demonstrated that this cell is a ciliary mechanoreceptor (Vondran et al. 1995; Schmitz et al. 1997; Schmitz and Bleckmann 1998b).

According to the current conception of how IR radiation may be converted into a mechanical event perceivable by the mechanoreceptive cell, absorbed IR radiation heats the sphere and causes an increase in pressure in the fluid filled system of communicating microcavities inside the sphere. Because the outer lamellated mantle consists of hard exocuticle reinforced by layers of chitin fibers (Schmitz et al. 2007),
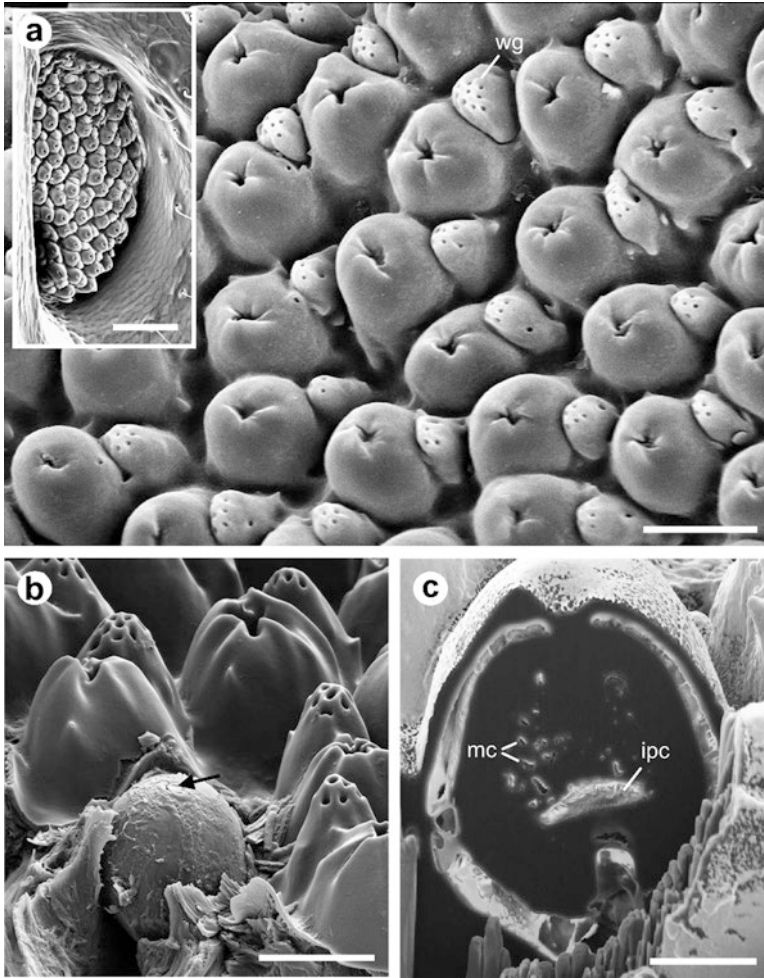
Fig. 1.4 Morphology of the IR organ of *Melanophila acuminata*. (**a**) Dome-shaped IR sensilla at the bottom of a pit organ (shown in the inset). Each sensillum is accompanied by a smaller wax gland (wg) characterized by tiny pores. SEM micrographs, bar: 15 μm (in inset 100 μm). (**b**) Group of IR sensilla at the bottom of the pit. The outermost dome of the front sensillum has been removed to show the internal sphere. At the top of the sphere the round insertion of the broken stalk is visible (arrow). Bar: 10 μm. (**c**) Single IR sensillum centrally opened by focused ion beam (FIB) in a SEM. Specimen was air-dried; therefore, only the cuticle is preserved. Microcavities (mc) of the intermediate layer and the inner pressure chamber (ipc) can be discerned inside the sphere. Bar: 5 μm

the only compliant structure in the sphere is the olive-shaped tip of the dendrite housed in the inner pressure chamber which becomes slightly squeezed by the increasing pressure. This lateral compression of the dendritic tip is the adequate stimulus for the mechanoreceptor (Thurm et al. 1983; French 1992).

Up to now the crucial question from which distances *Melanophila* beetles can detect a fire by IR reception cannot be answered satisfactorily. Extracellular electro-physiological recordings obtained by inserting a metal electrode between the IR sensilla have revealed a fast and strictly phasic response to heating (Schmitz et al. 1997) and a threshold sensitivity of 500 µW/cm^2 has been estimated (Schmitz and Bleckmann 1998b). It has been calculated that this sensitivity would enable a beetle to detect a larger forest fire of 10 ha with a temperature of 700 °C from a distance of about 10 km (Schmitz and Bleckmann 1998b). However, because the metal elec-trode may have sucked considerable amounts of heat energy away from the sensilla, this threshold most probably is underestimated.

In case that the above mentioned high sensitivity of only 4 nW/cm^2 derived from the modelling of the oil-tank fire should be true, the IR receptors of *Melanophila* beetles theoretically could compete with technical high sensitivity quantum IR sen-sors that have to be cooled, e.g. with liquid nitrogen, to suppress the thermal noise. However, in the uncooled biological *Melanophila* IR sensilla additional mecha-nisms like active amplification, which e.g. already has been described for auditory hearing organs in insects (Göpfert and Robert 2001, 2003; Mhatre and Robert 2013), and effective noise suppression have to be postulated. Recently some impor-tant morphological prerequisites for a hypothetical active amplification mechanism have been found (Schneider et al. 2015). In brief, a flying *Melanophila* beetle could make use of mechanical energy coupled out of its flight motor to induce minute vibrations of the stalked spheres. By using a sensory feedback loop a flying beetle could control the vibration amplitudes to allow mechanical prestimulation of the sensilla in the pit organs. In this operating condition only minimal additional amounts of quantum energy provided by IR photons are necessary to generate action potentials in a sensillum. By the proposed mechanism the sensitivity of the IR sensilla could be boosted to an extremely high level (Schneider et al. 2015).

1.5.2   IR Receptors in Pyrophilous *Aradus* Bugs

The family of Aradidae (flat bugs) comprises about 200 species (Heiss and Pericart 2007). Within this large family only eight species have been described to be associ-ated with forest fires because these species were found on burnt areas relatively soon after a fire (Wikars 1997; Lappalainen and Simola 1998; Wyniger et al. 2002; Schmitz et al. 2008, 2010; Johansson et al. 2010; Baena and Torres 2013). Also in *A. gracilicornis* and *A. gracilis* a pyrophilous behavior has been described (Deyrup and Mosley 2004). However, both species were found more than 1 year after the fire. Within the small group of pyrophilous flat bugs, IR receptors so far were only

found in 4 species: namely in *A. albicornis*, *A. flavicornis*, *A. fuscicornis* and *A. lugubris* (cf. Table 1.1) (Schmitz et al. 2010).

1.5.2.1 Pyrophilous Behavior

There is strong evidence that pyrophilous *Aradus* bugs are lured to burnt trees by fire specific cues like smoke, heat, and - after the fire has ceased - persisting smell of burning. Attracted by these cues those fire-adapted species arrive early on a burnt area. The behavior of *Aradus* species in general is hard to observe because the tiny flat bugs conceal themselves under the bark of the burnt trees. According to the current state of knowledge the adult bugs and their larvae feed on the mycelia of fast growing post-fire fungi, which start to grow on burnt wood immediately after a fire (Froeschner 1988; Wikars 1992). Sporadic own observations on *A. albicornis* on burnt sites in Western Australia revealed that bugs arrive on freshly burnt areas already a few hours after the fire. Apparently bugs prefer to colonize weak moisture-loving eucalyptus trees growing near creeks or lakes like *Eucalyptus rudis*. After copulation the females deposit their eggs at the base of the stem often already hidden a few centimeters in the soil. In this so-called collar region lignotuber bulges were frequently observed. These are specialized woody storage organs with an active cambium layer and a high moisture content. The lignotuber bulges are capable of resprouting after a fire even if the above-ground part of the tree is destroyed by the fire. However, if the lignotuber is also degraded by the fire, fungi find good conditions and start to grow immediately. If the collar region is carefully excavated about a week after the fire, groups of adults and first larvae can be found between the roots sucking on the mycelia. There is evidence that the pyrophilous *Aradus* species continue to reproduce at these favorable spots as long as the fungi stay alive.

1.5.2.2 The Thoracic IR Organs

Photomechanic IR receptors are mainly located on the propleurae of the prothorax (Table 1.1). The propleurae extend behind the bulges of the prothoracic leg bases and are developed as thin wing-like duplications of the body wall. Accordingly, the thermal mass is rather low. Very few IR sensilla were also found directly posterior to the bases of the mesothoracic legs (cf. Table 1.1) (Schmitz et al. 2010). At a first glance a single IR sensillum is very similar to an IR sensillum located in the pit organs of *Melanophila* (cf. Table 1.1, Figs. 1.4a, 1.5a and 1.6). However, numbers of sensilla are much lower in *Aradus* (one or two dozen on each propleura) and the sensilla are not confined to a pit but loosely interspersed between bollard-like hair mechanoreceptors (Fig. 1.5a). Furthermore, TEM micrographs show two additional differences to the *Melanophila* sensilla: a distinct cleft around the sphere is missing in the *Aradus* sensillum (Figs. 1.5b and 1.6) and the outermost tip of the mechano-sensitive dendrite anchored in the cuticle of the sphere remains only about 500 nm below the bottom of the indentation (Fig. 1.5b, c). On the other hand, the same basic
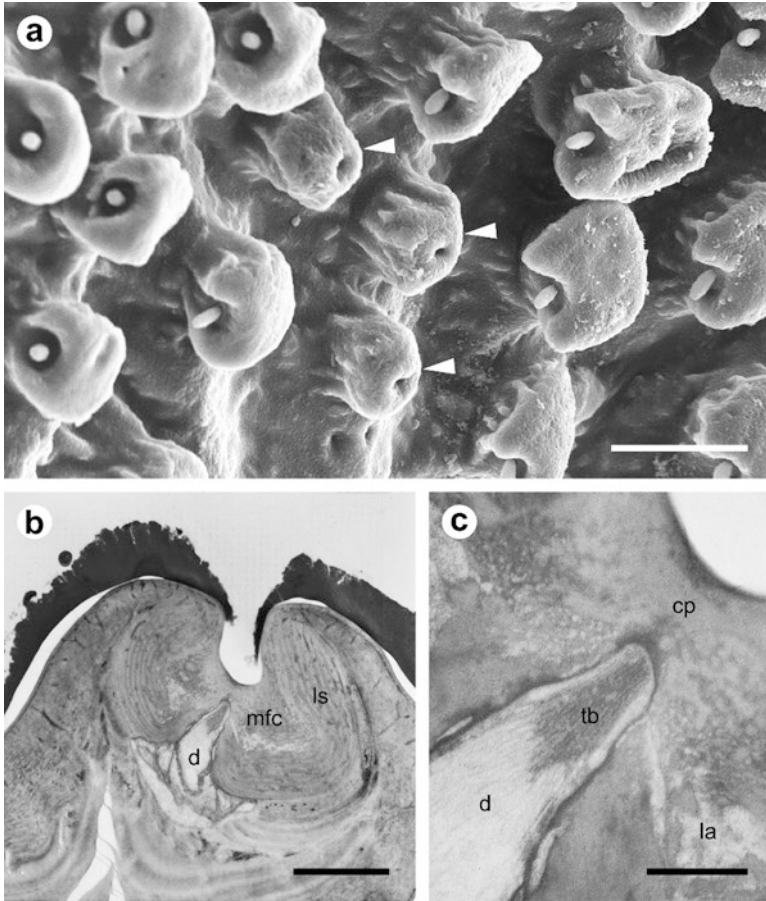
Fig. 1.5 (**a**) Detail of the right propleura of *Aradus albicornis*. Between several bollard-like hair mechanoreceptors with short bristles three IR sensilla are interspersed (white arrowheads). IR sensilla are characterized by a central dent. SEM micrograph. Bar: 20 μm. (**b**) Section through the center of an IR sensillum at the position of the dent. The sensillum is covered by an electron dense superficial layer. The internal sphere with a diameter of 10 μm shows a lamellated shell (ls) with an inner microfluidic core (mfc). In the center of the core the dendritic tip (**d**) of the mechanosensory neuron is situated. TEM micrograph. Bar: 3 μm. (**c**) Detail of the insertion site of the dendrite. The dendrite contains a well developed tubular body (tb), very characteristic for insect mechanoreceptors, and ends in a cuticular plug (cp) about 500 nm below the bottom of dent. la: lacuna of the fluidic core. TEM micrograph. Bar: 0.5 μm

components of a photomechanic IR sensillum described in *Melanophila* beetles are present: an outer lamellated shell enclosing a microfluidic core which is innervated by one ciliary mechanosensory cell. At its outermost tip, the dendrite of the mechanoreceptor is in direct contact to the fluid inside the sphere (Figs. 1.5b, c). Thus, the IR sensilla of pyrophilous *Aradus* bugs also can be classified as photomechanic IR

Fig. 1.6 Schematic drawings of photomechanic IR sensilla in (**a**) *Melanophila* beetles and (**b**) pyrophilous *Aradus* bugs. In both receptors the expansion of the fluid encapsulated inside an inner microfluidic center is measured by a ciliary mechanosensitive cell. d: dendrite, Exo: exocuticle; Meso: mesocuticle. (**a**) Adapted from Schmitz et al. (2007). (**b**) Adapted from Schmitz et al. (2008).
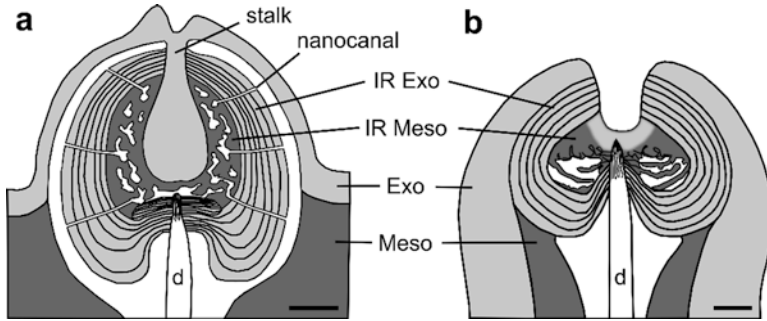
receptors and, therefore, most probably function according to the mechanism described above for the *Melanophila* receptors.

First electrophysiological recordings revealed that the sensillum responds to heating in a phasic-tonic way. At high stimulation intensities first spike latencies were only 3–7 ms like in the *Melanophila* sensilla. However, the sensitivity seems to be considerably lower. So far a threshold sensitivity of 11 mW/cm^2 has been determined by extracellular recordings (Schmitz et al. 2008). As in the beetle *Acanthocnemus* it cannot be completely ruled out that the bugs may use their IR receptors for the detection of fires from distances of some kilometers. Because the pyrophilous *Aradus* species are also very small and appear to be weak flyers it seems unlikely that they use their IR receptor for fire detection from larger distances. Most probably bugs also use the IR sensilla for the localization of hot spots prior to landing.

1.6 Discussion

1.6.1 The Cuticle As an Effective IR Absorber

A freshly burnt area is a valuable ecological niche for specialists like pyrophilous insects. Large quantities of food such as the wood of fire-killed tress and fast grow-ing post-fire fungi sprouting on burnt wood and soil are suddenly available. Furthermore, in the first days after the fire, food competition by other insects is negligible. However, all pyrophilous insects have a fundamental problem because the outbreak of a forest fire is unpredictable. So even extended search flights would not increase the chance to detect a fire. Pyrophilous insects, therefore, should be able to detect fires from distances as large as possible. It is reasonable to suppose that the sensory organs, which are used for fire detection, have been subjected to a

strong evolutionary pressure with regard to sensitivity. This is especially true for the IR receptors.

To build a good absorber, the IR photons must be absorbed efficiently to cause measurable effects in the absorber material. Absorption will be maximal if the frequency of vibration of a chemical bond between two atoms of the absorber and the frequency of an incoming photon match (so-called resonance condition). Most organic molecules show vibrational absorption bands in the MWIR region (Barth 2007). The insect cuticle consists of protein and chitin (N-acetylglucosamines) showing many C-H, N-H, and O-H groups (Neville 1975; Chapman 1998). Molecules with these groups oscillate with frequencies of about 100 THz and, therefore, show stretch or vibrational resonances around 3 μm (Herzberg and Huber 1950). In general, most organic molecules strongly absorb in the MWIR and LWIR region of the electromagnetic spectrum (Hesse et al. 1995). In case of absorption of an IR photon the vibrational energy is converted within fractions of a millisecond into translational energy, i. e. heat, by non-radiative de-excitation processes. Thus, as already pointed out in some previous publications (Vondran et al. 1995; Schmitz and Bleckmann 1997; Schmitz et al. 2007), insect cuticle *per se* can be regarded as a composite material that shows strong IR absorption bands in the MWIR and, therefore, is an excellent natural IR absorber. This may have been a very important prerequisite for the evolution of all insect IR receptors from initial non-IR sensilla.

1.6.2   Different Routes of Converting IR Quantum Energy into Bioelectrical Signals

Any heating inevitably causes thermal deformation. The absorber of a thermal IR detector, therefore, could be monitored by a temperature and/or a mechanical displacement sensor. Both measuring methods are realized in insect IR receptors (cf. Table 1.1) and, consequently, no uniform IR receptor exists in insects.

The driving forces fostering the development of IR receptors can be summarized as follows: in insects, which already had started to develop a pyrophilous way of life, heat from hot surfaces on a burnt area may have unspecifically stimulated certain peripheral receptors. Subcuticular proprioceptors as well as external mechanoreceptors could have been affected by incident IR radiation. As pointed out, absorption caused heating and thermal expansion of nearby cuticle or water in the receptor lymph cavities of the receptors. By this, an evolutionary pressure came into play and — as a first important step — the IR absorbing outer cuticular apparatus of the evolving IR sensillum had to be optimized.

In the two species of IR sensitive beetles which have developed bolometer like IR receptors (i.e. *Acanthocnemus* and *Merimna*) this process can be easily comprehended. In *Acanthocnemus* a small carrier plate, the sensory disc, separated from the cuticle of the thorax. This non-sensory auxiliary structure acts as IR absorber of low thermal mass: the temperature of the disc can quickly follow any changes in IR

radiation. Consequently, the about 90 tiny thermoreceptive sensilla are located on the surface of the anterior half of the disc exhibiting the lowest thermal mass. Currently the origin of the disc sensilla is enigmatic. It can be speculated that the disc sensilla have developed from cuticular hair mechanoreceptor (sensilla trichodea) which have undergone a profound change in structure and function. The tiny sensilla are embedded in the cuticle of the outer surface of the disc and, therefore, could act as discrete temperature measurement points (Zhou et al. 2016).

In *Merimna* the bolometer principle is realized in a different way. In the *Merimna* receptor the cuticular part of the IR organ consists of a specialized area which is slightly sunken in the surrounding cuticle. In contrast to the sensory disc of *Acanthocnemus* the sensory cells are attached to the bottom of the cuticle and thermal insulation of the absorbing area of the receptor is accomplished by a system of larger airsacs shielding the sensory complex against the haemocoel. Another step to decrease the thermal mass of the absorbing surface is a significant decrease in thickness (Schneider and Schmitz 2014). The function of the honeycomb like microstructure of the surface is still unclear. An optical function could be proposed namely an enhanced reflection of unwanted visible radiation. However, this has to be tested experimentally. According to electrophysiological recordings the sensory cells in the IR organs of *Merimna* an *Acanthocnemus* function as thermoreceptors. Singe unit recordings from both organs have revealed that the disc sensilla of *Acanthocnemus* seem to be two- to fourfold more sensitive than the multipolar thermoreceptor in the *Merimna* IR organ. However, the reason for the difference in sensitivity is unknown because the molecular mechanism of thermoreception is unknown in both types of sensory cells.

The *Merimna* receptor leads over to the so called photomechanic IR receptors. A small chordotonal organ has been found in the sensory complex in the center of the absorbing area. Although electrophysiological evidence is missing so far it has been proposed that the mechanosensory unit measured thermal deformation of the absorbing area caused by IR irradiation (Schneider and Schmitz 2013).

In the photomechanic IR receptor of *Melanophila* beetles and *Aradus* bugs the thermal expansion of a tiny cuticular sphere is measured by a mechanoreceptive cell. As already discussed by Schmitz et al. (2007, 2010), there is strong evidence that in both pyrophilous species the IR sensilla have evolved directly from hair mechanoreceptors (sensilla trichodea). However, because photomechanic IR sensilla so far have only been found in recent species of the genus *Melanophila* within the beetles and in very few pyrophilous species of the genus *Aradus* within the bugs, sensilla must have developed independently in both genera. It is imaginable that e.g. the dome-shaped surface provides a good surface to volume ratio allowing enhanced absorption of IR photons; the diameter of the sphere could reflect the penetration depth of IR photons into the cuticle of 3–4 μm (Schmitz et al. 2010). Due to the mechanosensory innervation one advantage of a photomechanic IR sensillum is its fast response time of only a few milliseconds (Schmitz and Bleckmann 1998c). This could result in a high spatio-temporal resolution of the IR sensory system providing the flying insect with constantly updated information about its current position relative to an IR source.

References

Alonso-Zarazaga, M., Sánchez-Ruiz, M., & Sánchez-Ruiz, A. (2003). Una nueva familia de Coleoptera para España: Acanthocnemidae. *Boletín de la Sociedad Entomológica Aragonesa, 32*, 179–180.

Apel, K.-H. (1991). *Die Kiefernprachtkäfer*. Eberswalde: Forschungsanstalt für Forst- und Holzwirtschaft.

Baena, M., & Torres, J. L. (2013). Notes on the biology and Iberian distribution of *Aradus flavicornis* (Dalmann, 1823) (Hemiptera, Heteroptera, Aradidae). *Boletin de la Asociacion Espanola de Entomologia, 37*, 277–284.

Barth, A. (2007). Infrared spectroscopy of proteins. *Biochimica et Biophysica Acta, 1767*, 1073–1101.

Bellamy, C. L. (2008). *A world catalogue and bibliography of the jewel beetles (Coleoptera: Buprestoidea). Volume 3. Buprestinae: Pterobothrini through Agrilinae: Rhaeboscelina*. Sofia/ Moscow: Pensoft.

Bond, W. J., & Keeley, J. E. (2005). Fire as a global 'herbivore': The ecology and evolution of flammable ecosystems. *Trends in Ecology & Evolution, 20*, 387–394.

Bowmaker, J., & Hunt, D. (2006). Evolution of vertebrate visual pigments. *Current Biology, 16*, R484–R487.

Budzier, H., & Gerlach, G. (2011). *Thermal infrared sensors*. Chichester: Wiley.

Champion, G. C. (1922). The geographical distribution and synonomy of the dasytid-beetle *Acanthocnemus nigricans* hope (= *ciliatus* Perris). *Entomologist's Monthly Magazine, 58*, 77–79.

Chapman, R. F. (1998). *The insects: Structure and function*. Cambridge: Cambridge University Press.

D'Amico, A., Di Natale, C., Castro, F. L., Iarossi, S., Catini, A., & Martinelli, E. (2009). Volatile compounds detection by IR acousto-optic detectors. In J. Byrnes (Ed.), *Unexploded ordnance detection and mitigation* (pp. 21–59). Dordrecht: Springer.

Deyrup, M., & Mosley, J. G. (2004). Natural history of the flat bug *Aradus glacilicornis* in fire-killed pines (Heteroptera: Aradidae). *Florida Entomologist, 87*, 79–81.

Douglas, R. H., Partridge, J. C., Dulai, K., Hunt, D., Mullineaux, C. W., Tauber, A. Y., & Hynninen, P. H. (1998). Dragon fish see using chlorophyll. *Nature, 393*, 423–424.

Evans, W. G. (1964). Infra-red receptors in *Melanophila acuminata* DeGeer. *Nature, 202*, 211–211.

Evans, W. G. (1966a). Morphology of the infrared sense organ of *Melanophila acuminata* (Buprestidae: Coleoptera). *Annals of the Entomological Society of America, 59*, 873–877.

Evans, W. G. (1966b). Perception of infrared radiation from forest fires by *Melanophila acuminata* de Geer (Buprestidae, Coleoptera). *Ecology, 47*, 1061–1065.

Field, L. H., & Matheson, T. (1998). Chordotonal organs of insects. In P. D. Evans (Ed.), *Advances in insect physiology* (pp. 1–228). San Diego: Academic Press.

French, A. S. (1992). Mechanotransduction. *Annual Review of Physiology, 54*, 135–152.

Froeschner, R. C. (1988). Family Aradidae Spinola 1837 (=Dysodiidae Reuter, 1912; Meziridae Oshanin, 1908), the flat bugs. In T. J. Henry & R. C. Froeschner (Eds.), *Catalog of the Heteroptera, or true bugs, of Canada and the United States* (pp. 29–46). New York: E. J. Brill Co..

Gingl, E., & Tichy, H. (2001). Infrared sensitivity of thermoreceptors. *Journal of Comparative Physiology. A, 187*, 467–475.

Göpfert, M. C., & Robert, D. (2001). Active auditory mechanics in mosquitoes. *Proceedings of the Royal Society of London B, 268*, 333–339.

Göpfert, M. C., & Robert, D. (2003). Motion generation by *Drosophila* mechanosensory neurons. *Proceedings of the National Academy of Sciences of the United States of America, 100*, 5514–5519.

Hawkeswood, T. J. (2007). Review of the biology of the genus *Merimna* Saunders, 1868 (Coleoptera: Buprestidae). *Calodema, 9*, 12–13.

Hawkeswood, T. J., & Peterson, M. (1982). A review of the larval host records for Australian jewel beetles (Coleoptera: Buprestidae). *The Victorian Naturalist (Blackburn), 99*, 240–251.

Hazel, J., Fuchigami, N., Gorbunov, V., Schmitz, H., Stone, M., & Tsukruk, V. V. (2001). Ultramicrostructure and microthermomechanics of biological IR detectors: Materials properties from a biomimetic perspective. *Biomacromolecules, 2*, 304–312.

Heiss, E., & Pericart, J. (2007). *Hemiptères Aradidae Piesmatidae et Dipsocoromorphes Euromediterranéens*. Paris: Fédération Francaise des Sociétés de Sciences Naturelles.

Herzberg, H., & Huber, K.-P. (1950). *Molecular spectra and molecular structure. I. Spectra of diatomic molecules*. New York: Van Nostrand and Reinhold.

Hesse, M., Meier, H., & Zeeh, B. (1995). *Spektroskopische Methoden in der organischen Chemie*. Stuttgart/New York: Georg Thieme Verlag.

Horion, A. (1955). Faunistik der mitteleuropäischen Käfer. 4, Sternoxia (Buprestidæ)*, Fossipedes, Macrodactylia, Brachymera*. München.

Johansson, T., Hjältén, J., Stenbacka, F., & Dynesius, M. (2010). Responses of eight boreal flat bug (Heteroptera: Aradidae) species to clear-cutting and forest fire. *Journal of Insect Conservation, 14*, 3–9.

Kitchin, D. R. (2009). Notes on the biology of *Merimna atrata* (Gory & Laporte) (Coleoptera: Buprestidae). *Australian Entomologist, 36*, 1–2.

Kovalenko, Y. N. (2011). Acanthocnemidae (Coleoptera), a family of beetles new to Russia. *Zoosystematica Rossica, 20*, 71–73.

Kreiss, E.-J., Schmitz, A., & Schmitz, H. (2005). Morphology of the prothoracic discs and associated sensilla of *Acanthocnemus nigricans* (Coleoptera, Acanthocnemidae). *Arthropod Structure & Development, 34*, 419–428.

Kreiss, E.-J., Schmitz, H., & Gebhardt, M. (2007). Electrophysiological characterisation of the infrared organ of the Australian "Little Ash Beetle" *Acanthocnemus nigricans* (Coleoptera, Acanthocnemidae). *Journal of Comparative Physiology. A, 193*, 729–739.

Lappalainen, H., & Simola, H. (1998). The fire-adapted flatbug *Aradus laeviusculus* Reuter (Heteroptera, Aradidae) rediscovered in Finland (North Karelia, Koli National Park). *Entomologica Fennica, 9*, 3–4.

Liberti, G. (2009). The Dasytidae (Coleoptera) of Sardinia. *Zootaxa, 2318*, 339–385.

Linsley, E. G. (1933). Some observations on the swarming of *Melanophila*. *Pan-Pacific Entomologist, 9*, 138.

Linsley, E. G. (1943). Attraction of *Melanophila* beetles by fire and smoke. *Journal of Economic Entomology, 36*, 341–342.

Mainz, T., Schmitz, A., & Schmitz, H. (2004). Variation in number and differentiation of the abdominal infrared receptors in the Australian 'fire-beetle' Merimna atrata (Coleoptera, Buprestidae). *Arthropod Structure & Development, 33*, 419–430.

Manee, A. H. (1913). Observations on Buprestidae at Southern Pines, North Carolina. *Entomological News, 24*, 167–171.

Mayor, A. (2007). Acanthocnemidae; Prionoceridae; Melyridae; Dasytidae. In I. Löbl & A. Smetana (Eds.), *Catalogue of Palaearctic Coleoptera, Vol. 4. Elateroidea - Derodontoidea - Bostrichoidea - Lymexyloidea - Cleroidea - Cucujoidea* (pp. 384–415). Stenstrup: Apollo Books.

Meuthen, D., Rick, I. P., Thünken, T., & Baldauf, S. A. (2012). Visual prey detection by near-infrared cues in a fish. *Naturwissenschaften, 99*, 1063–1066.

Mhatre, N., & Robert, D. (2013). A tympanal insect ear exploits a critical oscillator for active amplification and tuning. *Current Biology, 23*, 1–6.

Michelsen, A., & Larsen, O. N. (1985). Hearing and sound. In G. A. Kerkut & L. I. Gilbert (Eds.), *Comprehensive insect physiology, biochemistry, and pharmacology* (pp. 495–556). New York: Pergamon Press.

Neville, A. C. (1975). *Biology of the arthropod cuticle*. Berlin/Heidelberg/New York: Springer Verlag.

Poulton, E. B. (1915). The habits of the Australian buprestid "fire-beetle" *Merimna atrata*, (Laporte and Gory). *Transactions of the Entomological Society of London, Part 1*, iii–iiv.

Ricksecker, L. E. (1885). Habits of some California beetles. *Entomological America, 1*, 96–98.

Rogalski, A. (2002). Infrared detectors: An overview. *Infrared Physics & Technology, 43*, 187–210.

Saint-Germain, M., Drapeau, P., & Buddle, C. M. (2008). Persistence of pyrophilous insects in fire-driven boreal forests: Population dynamics in burned and unburned habitats. *Diversity and Distributions, 14*, 713–720.

Schmitz, H., & Bleckmann, H. (1997). Fine structure and physiology of the infrared receptor of beetles of the genus *Melanophila* (Coleoptera: Buprestidae). *International Journal of Insect Morphology and Embryology, 26*, 205–215.

Schmitz, H., & Bleckmann, H. (1998a). The photomechanic infrared receptor for the detection of forest fires in the beetle Melanophila acuminata (Coleoptera : Buprestidae). *Journal of Comparative Physiology. A, 182*, 647–657.

Schmitz, H., & Bleckmann, H. (1998b). The photomechanic infrared receptor for the detection of forest fires in the beetle *Melanophila acuminata* (Coleoptera: Buprestidae). *Journal of Comparative Physiology. A, 182*, 647–657.

Schmitz, H., & Bleckmann, H. (1998c). The photomechanic infrared receptor for the detection of forest fires in the buprestid beetle Melanophila acuminata. *Journal of Comparative Physiology. A, 182*, 647–657.

Schmitz, H., & Bousack, H. (2012). Modelling a historic oil-tank fire allows an estimation of the sensitivity of the infrared receptors in pyrophilous *Melanophila* beetles. *PLoS One, 7*, e37627.

Schmitz, H., & Schmitz, A. (2002). Australian fire-beetles. *Landscope, 18*, 36–41.

Schmitz, H., & Trenner, S. (2003). Electrophysiological characterization of the multipolar thermoreceptors in the "fire-beetle" *Merimna atrata* and comparison with the infrared sensilla of *Melanophila acuminata* (both Coleoptera, Buprestidae). *Journal of Comparative Physiology. A, 189*, 715–722.

Schmitz, H., Bleckmann, H., & Murtz, M. (1997). Infrared detection in a beetle. *Nature, 386*, 773–774.

Schmitz, H., Schmitz, A., & Bleckmann, H. (2000). A new type of infrared organ in the Australian "fire-beetle" *Merimna atrata* (Coleoptera: Buprestidae). *Naturwissenschaften, 87*, 542–545.

Schmitz, H., Schmitz, A., & Bleckmann, H. (2001). Morphology of a thermosensitive multipolar neuron in the infrared organ of Merimna atrata (Coleoptera, Buprestidae). *Arthropod Structure & Development, 30*, 99–111.

Schmitz, H., Schmitz, A., Trenner, S., & Bleckmann, H. (2002). A new type of insect infrared organ of low thermal mass. *Naturwissenschaften, 89*, 226–229.

Schmitz, A., Sehrbrock, A., & Schmitz, H. (2007). The analysis of the mechanosensory origin of the infrared sensilla in *Melanophila acuminata* (Coeloptera; Buprestidae) adduces new insight into the transduction mechanism. *Arthropod Structure & Development, 36*, 291–303.

Schmitz, A., Gebhardt, M., & Schmitz, H. (2008). Microfluidic photomechanic infrared receptors in a pyrophilous flat bug. *Naturwissenschaften, 95*, 455–460.

Schmitz, A., Schatzel, H., & Schmitz, H. (2010). Distribution and functional morphology of photomechanic infrared sensilla in flat bugs of the genus Aradus (Heteroptera, Aradidae). *Arthropod Structure & Development, 39*, 17–25.

Schmitz, A., Schneider, E. S., & Schmitz, H. (2015). Behaviour of the Australian 'fire-beetle' *Merimna atrata* (Coleoptera: Buprestidae) on burnt areas after bushfires. *Records of the Western Australian Museum, 30*, 1–11.

Schneider, E. S., & Schmitz, H. (2013). Bimodal innervation of the infrared organ of *Merimna atrata* (Coleoptera, Buprestidae) by thermo- and mechanosensory units. *Arthropod Structure & Development, 42*, 135–142.

Schneider, E. S., & Schmitz, H. (2014). Thermomechanical properties of the stimulus transducing cuticle in the infrared organ of *Merimna atrata* (Coleoptera, Buprestidae). *Journal of Morphology, 275*, 991–1003.

Schneider, E. S., Schmitz, A., & Schmitz, H. (2015). Concept of an active amplification mechanism in the infrared organ of pyrophilous *Melanophila* beetles. *Frontiers in Physiology, 6*, Article 391.

Schoenlein, R., Peteanu, L., Mathies, R., & Shank, C. (1991). The first step in vision: Femtosecond isomerization of rhodopsin. *Science, 254*, 412–415.

Sharp, W. E. (1918). *Melanophila acuminata* in Berkshire. *Entomologist's Monthly Magazine, 54*, 244–245.

Shcherbakov, D., Knörzer, A., Espenhahn, S., Hilbig, R., Haas, U., & Blum, M. (2013). Sensitivity differences in fish offer near-infrared vision as an adaptable evolutionary trait. *PLoS One, 8*, e64429.

Sloop, K. D. (1937). *A revision of the North American buprestid beetles belonging to the genus Melanophila (Coleoptera, Buprestidae)*. Berkeley: University of California Publications in Entomology.

Stark, K. B., Gallas, J. M., Zajac, G. W., Golab, J. T., Gidanian, S., McIntire, T., & Farmer, P. J. (2005). Effect of stacking and redox state on optical absorption spectra of melanins − Comparison of theoretical and experimental results. *The Journal of Physical Chemistry. B, 109*, 1970–1977.

Thurm, U., Erler, G., Gödde, J., Kastrup, H., Keil, T., Völker, W., & Vohwinkel, B. (1983). Cilia specialized for mechanoreception. *Journal of Submicroscopic Cytology and Pathology, 15*, 151–155.

Valcárcel, J. P., & Piloña, F. P. (2009). NOTA BREVE/SHORT NOTE Nota adicional sobre la presencia de Acanthocnemus nigricans (Hope, 1843) en la Península Ibérica. *Arquivos Entomoloxicos, 2*, 21.

Van Dyke, E. C. (1926). Buprestid swarming. *Pan-Pacific Entomologist, 3*, 41.

Vondran, T., Apel, K.-H., & Schmitz, H. (1995). The infrared receptor of *Melanophila acuminata* De Geer (Coleoptera: Buprestidae): Ultrastructural study of a unique insect thermoreceptor and its possible descent from a hair mechanoreceptor. *Tissue & Cell, 27*, 645–658.

Wikars, L.-O. (1992). Skogsbränder och insekter. *Entomologisk Tidskrift, 113*, 1–12.

Wikars, L.-O. (1997). *Effects of forest fire and the ecology of fire-adapted insects*. Uppsala: Doctor Uppsala University.

Wyniger, D., Moretti, M., & Duelli, P. (2002). *Aradus lugubris* fallen, 1807 (Hemiptera, Heteroptera, Aradidae) in a chestnut forest of Southern Switzerland after a fire experiment. *Mitt Schweizerische Entomologische Gesellschaft, 75*, 61–64.

Zhou, Z., Gong, Y., Yang, D., Schmitz, A., & Schmitz, H. (2016). Function modeling of the infrared organ of "little ash beetle" *Acanthocnemus nigricans* (Coleoptera, Acanthocnemidae). *Journal of Bionic Engineering, 13*, 650–658.

Part II
Photonics

Chapter 2
Arthropod Corneal Nanocoatings: Diversity, Mechanisms, and Functions

Mikhail Kryuchkov, Artem Blagodatski, Vsevolod Cherepanov, and Vladimir L. Katanaev

Abstract Corneal surfaces of terrestrial insects and other arthropods are covered with elaborate nanocoatings. Initially described as moth-eye nanostructures – paraboloid nipple-like evaginations regularly assembled on the lenses of some Lepidopterans – they were in recent years discovered to be omnipresent across insect lineages. In addition to the nipple-type morphology, corneal nanocoatings can be built as ridge-, maze-, or dimple-type nanopatterns, with various transitions among these morphologies seen in different species or even within the same specimen. Varying in the height of dozens to hundreds nanometers, and in the diameter being thinner than the wavelength of the visible light, these nanostructures provide the antireflective function to the surfaces they coat. Additional functionalities, such as water-repelling, antifouling, or antibacterial, could also be attributed to them. Turing reaction-diffusion and the block copolymerization mechanisms of molecular self-assembly have been proposed to guide the formation of corneal nanostructures during insect eye development. Both mechanisms envision interactions of two types of molecular agents with different diffusion and/or hydrophobicity properties as the underlying principle of building of the nanostructures. Using model insect organisms, the molecular identities of these agents can be revealed. These studies will

M. Kryuchkov
Department of Pharmacology and Toxicology, University of Lausanne,
Lausanne, Switzerland

A. Blagodatski
School of Biomedicine, Far Eastern Federal University, Vladivostok, Russian Federation

Department of Pharmacology and Toxicology, University of Lausanne,
Lausanne, Switzerland

V. Cherepanov
School of Biomedicine, Far Eastern Federal University, Vladivostok, Russian Federation

V. L. Katanaev (✉)
Department of Pharmacology and Toxicology, University of Lausanne,
Lausanne, Switzerland

School of Biomedicine, Far Eastern Federal University, Vladivostok, Russian Federation
e-mail: vladimir.katanaev@unil.ch

elucidate the mechanism of formation and diversity of the corneal nanostructures in arthropods. Further, they will lay the ground for bioengineering, *in vivo* and *in vitro*, of novel nanocoatings with desired properties.

2.1   Introduction

In order to interact with the environment, animals use a variety of complex micro- or nano-scale interfaces. Well-studied examples of such interfaces are footpads of geckos covered by microscopic hairs providing adhesive force (Autumn et al. 2000) or cicada wings covered with micro-protuberances, which bring about the water-bane effect (Daly 1970; Watson et al. 2017). Arthropods possess such a general multifunctional environment-interacting integument as the chitin-made shell or cuticle, which can additionally contain proteins, lipids, waxes and cement and is secreted through the apical membrane of the underlying cells (Daly 1970).

In addition to the protective function, the cuticle also procures the properties of antireflection, color, mechano- and chemo-sensitivity, anti- or super adhesiveness, and others. To achieve these functions, the cuticle is covered with functionally active bristles, folds and protrusions of micro- and nano-size (Watson et al. 2017). A particular and very interesting case of arthropod functional coverings can be found on the eye lenses, which are most extensively studied in compound eyes of insects. The compound eye consists of tens to hundreds of individual facets or ommatidia, and every ommatidium is formed by pigment, photoreceptor and cone cells, the latter producing the crystalline cone covered by a corneal lens (Katanaev and Kryuchkov 2011). The lens material is secreted by the cone cells, and the surface of the corneae in many insect lineages is covered by nanostructures. They were first discovered by means of scanning electron microscopy (SEM) in 1962 (Bernhard and Miller 1962) in compound eyes of some moths. These nanostructures were described as arrays of nipples varying in height (generally not exceeding 150 nm) and width (of the range of 100–300 nm). While the regularly packed nipple arrays were the main focus of the earlier studies, less ordered protrusions were also seen (Bernhard et al. 1970; Mishra and Meyer-Rochow 2006; Kryuchkov et al. 2011; Blagodatski et al. 2015). The structural-functional relationships of the nipple arrays have been extensively analyzed, and the main function attributed to them was the antireflection (Liu et al. 2010; Gorb and Speck 2017); their other possible roles relate to the anti-wetting and anti-adhesion effects (Liu et al. 2010; Martins et al. 2013).

Initially, the studies of insect corneal nanostructures were mostly limited to Lepidopterans. With the advance of SEM and atomic force microscopy (AFM), insects of different groups were discovered to harbor other types of corneal nano-coatings, such as parallel ridges (found also in spiders), twisted maze-like structures varying in width and height, and the dimpled nano-pattern seen in various insect orders and also in millipedes (Fig. 2.1) (Aghaeipour et al. 2014; Blagodatski et al. 2015; Watson et al. 2017). These diverse arthropod corneal nanostructures represent
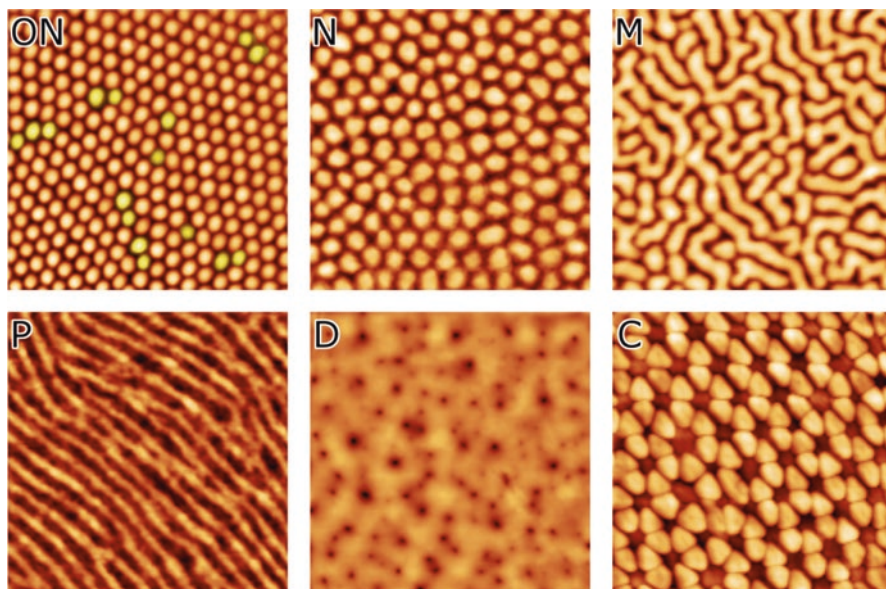
Fig. 2.1 The main types of arthropod corneal nanocoatings. ON – ordered nipples, typical for moths and butterflies. Yellow-labelled nipples indicate coordination defects in the crystal lattice, which form boundaries of highly-ordered domains. N – a non-ordered nipple array. M – a maze-like structure. P – parallel strands. D – a dimpled pattern. C – a special mushroom-shaped hexagonal pattern found on the eyes of *Collembola*. Each square is 3 × 3 μm

a fascinating object for structural and functional research on organisms' integuments. They are easily accessible for microscopy analysis and can be artificially modified in the genetic model insect *Drosophila melanogaster* (Kryuchkov et al. 2011).

Artificial biomimetic micro- and nano-structured surfaces represent a rapidly developing domain of modern technology (Liu et al. 2010; Gorb and Speck 2017). According to rough estimates, the profit in the global market of materials with nanostructured surfaces will reach approximately 14.2 billion USD by 2022 (Wood 2017). Therefore, the necessity for cheap and simple methods for their production increases yearly. Most methods for creation of nanostructures involve usage of ultraclean rooms, high temperatures, X-ray treatment, and aggressive chemical treatment (Martins et al. 2013; Aghaeipour et al. 2014; Schuster et al. 2015). At the same time, the biological nanostructures of the insects' eyes are formed under mild conditions in the absence of exposure to corrosive chemical compounds. Understanding of the exact features that set the functional properties of the nanostructured eye surfaces of arthropods and of the mechanisms underlying their formation will bring us closer to the possibility of low-cost engineering of artificial nanostructured biomimetic surfaces with desired traits. One famous example is the inspiration of antireflective nanocoatings of photoactive materials in high performance solar cells from the nano-nipple moth-eye nanostructures (Brongersma

et al. 2014). Another – the development of self-cleaning and anti-fouling surfaces for medical applications following natural micro-structured designs (Bixler et al. 2014).

2.2 Functions of Corneal Nanostructures

2.2.1 Optical Properties of the Arthropod Eye Nanocoatings

Arthropod integuments in general and the corneal nanocoatings in particular contain chitin, proteins, and lipids (Anderson and Gaimari 2003; Nickerl et al. 2014). These materials are dielectric, meaning that they can be polarized by an applied electric field, cannot conduct electricity, and (importantly for their optic properties) have very low conductivity and polarization losses at optical frequencies – meaning that they are, by default, transparent. Therefore, the following discussion will touch upon the optical properties of dielectric nanostructured materials, while the conductive features of biomimetic nanocoatings will not be covered.

Historically, the first described property of the arthropod corneal nanocoating was the anti-reflectivity (Bernhard et al. 1965; Miller 1979; Blagodatski et al. 2014) increasing the quantity of light transmitted into the eyes and eradicating (to less than 1%) the amount of reflected light – the latter also contributing to the decreased visibility of nocturnal insects to predators (Miller 1979; Stavenga et al. 2006).

Due to a large difference between the refractive index of air and that of the lens of the eye – 1 *vs*. 1.5–1.8 (Varela and Wiitanen 1970; Meyer-Rochow 1978; Toh and Okamura 2007) – part of the incoming light does not reach the photoreceptor cells and is instead reflected from the lens. The reflected part can be calculated according to the Fresnel equation and equals 4–8% of the incident light. This problem can be compensated at the level of the size of individual ommatidia or the compound eye as a whole. The former solution relates to enlargement of the lens area or thickness. The latter – to the overall increase in the eye size through multiplying the number of ommatidia. Both solutions are limited by the maximal possible size of an ommatidium and of the insect itself.

As a direct approach to the problem, the amount of light transmitted into the eye can be increased through minimizing the amount of the reflected light, by means of the following alternative mechanisms. The first relies on a film positioned between the lens and the air, with the refractive index intermediate of the two media. If the film thickness is an odd multiple of $\lambda/4$, where λ is the light wavelength, then the beam reflected from the second interface (film and lens), will be out of phase with beam reflected from the first interface (air and film). These two beams will interfere and cancel each other, thereby decreasing the energy of the reflected light (Fig. 2.2A). Although used in many technological applications, this approach is limited to a particular angle and wavelength of the incoming light (Raut et al. 2011), which becomes problematic for eyes of the superposition type (Stavenga 2006) or with small, strongly convex ommatidia (Meyer-Rochow and Stringer 1993). The second
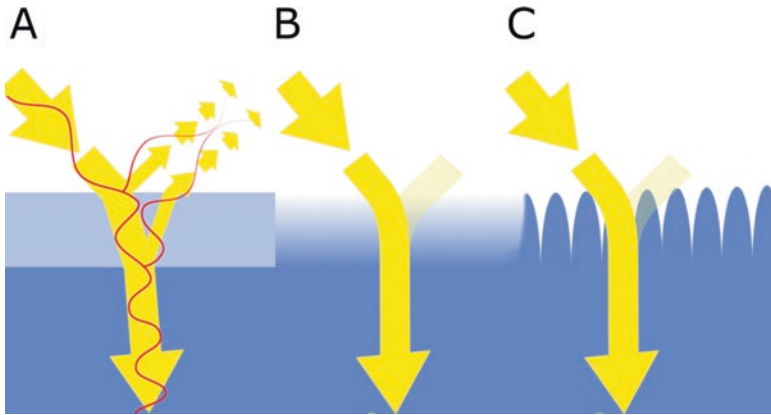
Fig. 2.2 Different designs of antireflective coatings. For a single-layer film (**A**), the two reflected waves may interfere cancelling each other. This coating functions for selected wavelengths and incident angles. An ideal antireflective coating (**B**) gradually approximates the refractive index of the incoming medium to that of the receiving medium. If the surface is coated with structures with dimensions smaller than the light wavelength (**C**), light interacts with the surface as if it has such a gradient of refractive indices

approach is an approximation to the ideal Rayleigh's film and relies on the fact that the sum of reflections from two interfaces is less than reflection from one interface, provided that the refractive index of the film is intermediate between those of the surrounding media. With this approach, multiple film layers gradually decreasing refractive indices from that of air to that of the lens should be coated (Fig. 2.2B) (Raut et al. 2011).

The third alternative produces largely an angle-independent effect and relies on the coating with structures, which cannot be resolved by the incident light, i.e. whose diameter is smaller than the wavelength of incoming light for perpendicular incidence and smaller than half-wavelength for oblique incidence. Under these conditions, the effective refractive index at any given depth of the coating is the sum of refractive indices of the coating materials multiplied by their proportions at that depth. That is, if at a given depth of the coating, half of the cross-section is filled with the lens material and the other half – with air (Fig. 2.2C), the effective refractive index at this level will be exactly between that of the air and that of the lens material. Quanta of light go through such nanostructured coating like through the medium with a smooth gradient of refractive index (Wilson and Hutley 1982; Deinega et al. 2011; Raut et al. 2011) (Fig. 2.2C). The antireflective function depends on the shape and location of nanostructures, and can be accurately determined by numerical solution of Maxwell's equations. One of the commonly used methods to obtain an approximate solution to these equations is FDTD (finite-difference time domain) (Deinega et al. 2011). Simulations based on these approximations correlate well with the experimental data (Daglar et al. 2013; Aghaeipour et al. 2014; Yu et al. 2015; Xin et al. 2016).

An increase in the diameter of nanostructures (Aghaeipour et al. 2014; Yu et al. 2015) or of the distance among them (Son et al. 2011) increases the wavelength of light with the maximal reduction in reflectance. This feature provides a way to fine-tune light transmission to the wavelengths needed for a particular insect's life style. Accordingly, different insects possess corneal nanostructures with different widths. For example, maze-like structures on the surface of ladybirds' eyes are 100–200 nm broad (sometimes going down to 50 nm), while similar structures in a Staphylinidae beetle have an atypical width of 400–500 nm (Blagodatski et al. 2015).

Another important dimensional characteristic of the nanostructures is their height. Several theoretical and experimental studies on ordered structures have demonstrated that the higher the structures are, the less light they reflect (Stavenga et al. 2006; Deinega et al. 2011; Raut et al. 2011). Using the predatory Neuropteran *Libelloides macaronius* with the eyes split into dorso-frontal and ventro-lateral halves, we have directly shown that a mere increase in the nanostructures' height from 8 to 32 nm decreases by 20–40% (depending on the wavelength) the amount of reflected light in the dorso-frontal half relative to the ventro-lateral one (Kryuchkov et al. 2017b). The trade-off here is that higher nanostructures are more susceptible to injury with subsequent loss of functionality. The evolutionary pressure in this case provides conflicting demands: to maximize the efficiency of the nanostructures on one hand, and to minimize the risk of losing them by harsh interactions with the environment, on the other. This conflict is illustrated by the fact that flying insects such as butterflies can afford higher nanopillars than the crawlers who are confronted with a bigger risk of collision with the substrate and resulting damage to the eye surfaces. The highest known protrusions are the highly-ordered nipples from *Euxanthe wakefieldii* butterflies of the Nymphalidae family with a height of 230 nm (Stavenga et al. 2006). At the same time, the minimum height of nanostructures is around 10 nm (10 nm for Lepismatidae, 5–15 nm for Platycnemedidae, 8–15 nm for Scutelleridae) (Blagodatski et al. 2015).

The shape of corneal nanostructures is another characteristic important for their function. It can be convex or concave, cylindrical or conical, and each may have its own advantages depending on other conditions (height, density, and ordering). Theoretical considerations indicate that the refractive index gradient is the smoothest for linear cones, although these calculations are valid only for the structures taller than 250 nm (Ji et al. 2012; Han and Zhao 2014; Siddique et al. 2015). Cone-shaped nanostructures have been found as the most effective anti-reflectors also in the case of the low angle of the incident light (Stavenga et al. 2006; Ji et al. 2012; Leem et al. 2012).

Insects' corneal protrusions do not exceed 250 nm due to mechanical instability of higher structures. As opposed to the cone shapes, nanostructures of the convex form were shown to be effective at the height < 100 nm for the visible and UV light (Stavenga et al. 2006; Ji et al. 2012; Leem et al. 2012; Daglar et al. 2013). Among different possible convex structures, bullet-like bi-paraboloid shapes have been described to grant maximal antireflection efficiency at the wavelengths of 300–800 nm (Leem et al. 2012). According to the existing data, most insects indeed possess nanostructures of the convex shape, with a slight bullet-shape outline (Stavenga et al. 2006).
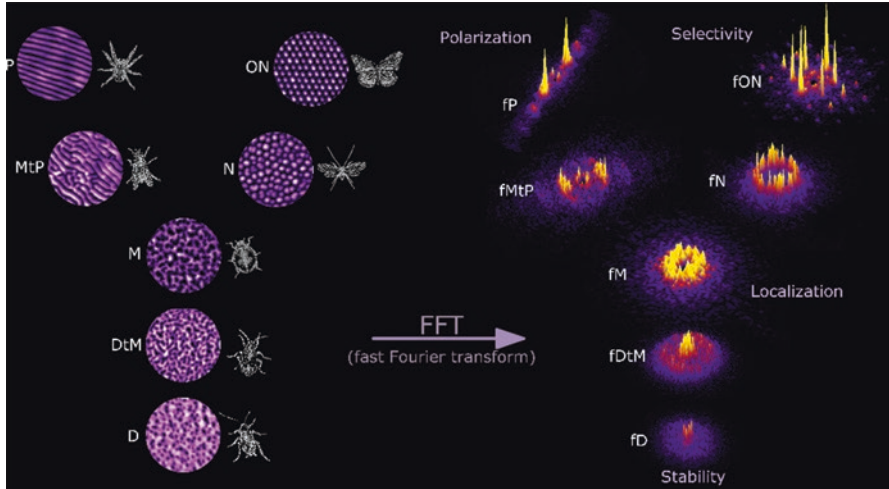
Fig. 2.3 Fourier analysis of different corneal nanostructures in relation to their possible properties. D: dimpled pattern from Blattidea, DtM: dimple-to-maze transition from Hemiptera, M: maze-type from Coleoptera, N: nipple-like structures from Psocoptera, ON: highly ordered nipples from Lepidoptera, MtP: maze to parallel strands transition from Diptera, P: parallel strands from a true spider. The prefix "f" denotes 2D Fourier transform of the corresponding structure. In the order from bottom to top, physical stability decreases, while selectivity for the light wavelengths increases. Non-ordered structures can localize the beam of light. Parallel strands can polarize the incident light and transfer it in the unidimensional manner with a minimal loss of energy

Another characteristic affecting the anti-reflectivity of nanostructured surfaces is the degree of order in the packing of the nanostructures, which is linked to the uniformity of their shape and dimensions, as well as with the packing density. A common way to analyze the degree of order and the packing density is FFT (fast Fourier transform, referred to as 'Fourier transform' throughout the text) (Wiersma 2013). Existence, position, and sharpness of reflexes in Fourier transforms speak about the degree of crystallinity in the packing. For example, clear reflexes in the corners of the hexagon show that the structures are hexagonally packed, representing high order (ON and fON structures of Fig. 2.3). In contrast, fusing of reflexes into concentric circles indicates lack of order in the packing yet uniformity of the dimensions of the densely packed individual nanostructures (N and fN structures of Fig. 2.3) (Kryuchkov et al. 2011; Wiersma 2013). The level of disorder is reflected in the Fourier transforms by the form and size of the area with prominent peaks (Martins et al. 2013). Correspondingly, fusion of protrusions into mazes (M, fM on Fig. 2.3) and the further merge of maze-like forms into dimpled patterns (DtM and D, fDtM and fD on Fig. 2.3) are reflected in the Fourier transforms by merging of the concentric circles into a solid disk with subsequent reduction of its size. It is thus evident that the packing order in insect nanocoatings decreases in the direction from highly ordered nipple arrays to the non-ordered ones, then to maze-like structures

and further to dimpled patterns (Martins et al. 2013; van Lare and Polman 2015) (Fig. 2.3).

Regarding the highly ordered *vs.* disordered nipple arrays, numerous studies have shown that higher degrees of order increase the amount of reflected light in comparison to non-ordered protrusions, but enhance the wavelength's selectivity (Fig. 2.3) of the allowed transmitted light. In contrast, disordered nanostructures allow the transmission of light of a broader wavelength range, leading to a bigger quantity of the total transmitted light (Du et al. 2011; Oskooi et al. 2012; Zhou et al. 2015).

Further, higher order increases the haze intensity, whereas disordered or quasi-random structures result in reduced light scattering (Zhou et al. 2015). Another potential problem associated with the highly ordered arrays of nanostructures is the strong intensity of the -1 diffraction order appearing at high angles of incidence. In other words, the highly ordered arrays, while providing a general anti-reflectivity, suffer from the intense glare emanating from the surface if viewed at a particular high angle – which would be problematic in terms of the attempts of the insect to camouflage itself from prey or predators. In contrast, if the surface is covered by 2D–crystalline patches of different orientations, the glare is dramatically reduced (Stavroulakis et al. 2013). It is thus not surprising that in the insect corneal nano-coatings built by highly ordered nipple arrays, the high degree of order exists within clusters separated by more disordered borders (Fig. 2.1 ON). In addition to the potential need for such organization for the antiglare function, this effect is also an unavoidable consequence of the curvature of the lens, as in any convex polyhedron decorated with hexagons, there have to be pentagons as defects, like in a soccer ball (Sergeev et al. 2015; Lee et al. 2016).

The maze-type nanocoating produce the blurred circle-like form of the peaks of reflexes in the Fourier transform (Fig. 2.3) This type is intermediate between fully disordered and (quasi-)ordered structures and has been called a quasi-random type of organization; it may be effective as a broad-band antireflective surface (Martins et al. 2013).

The most disorganized (but still not fully random) yet mechanically stable structures are the dimpled patterns or nano-holes (Fig. 2.3). The dimple parameters (diameter and depth) influence the light transmission (Son et al. 2011), but other factors are also important. Indeed, corneae of the domesticated silkmoth reflect up to 40% more light than the corneae of its wild ancestor *Bombyx mandarina*, yet the average dimensions of nanostructures in these species remain approximately the same. It is the type of nanostructures which changes from fully random sponge-like coating in *Bombyx mori* to the quasi-random nano-holes of *Bombyx mandarina* (Kryuchkov et al. 2017a), agreeing with some experimental findings in artificial surfaces (Son et al. 2011; Lin et al. 2013; Pratesi et al. 2013).

Upon increasing in the ordering of maze-type structures, another type of highly packed structures emerges: parallel rows (Fig. 2.1 P, MtP and P on Fig. 2.3). The parallel strands, unlike nipples, can maintain their crystallinity throughout the entire surface of the lens and thus achieve a higher degree of order. These structures may mediate some unique optical functions. Subwavelength rows are anisotropic formations, which could produce different phase shifts for the transverse electric and

transverse magnetic polarized incident light, allowing functioning of these formations as polarizers (Fig. 2.3). A similar function was previously attributed to parallel strands, formed by filaments covering bracts of edelweiss flowers (Vigneron et al. 2005). Such all-dielectric nanostructures would function in the way different from the metal polarizers and described by the elementary diffraction potential theory and approximations of the effective-medium theory (Lin et al. 2014; Yoon et al. 2015).

Corneal parallel strands can be organized in two different ways (Blagodatski et al. 2015). The first patterns the entire corneal surface by parallel rows and can be found in some spiders and may function as a polarizer of the incident light. The second employs radiation of the strands from the center of an ommatidium to its periphery; the center in this case is often covered by nipple-like nanostructures (Meyer-Rochow and Stringer 1993; Blagodatski et al. 2015). This way of patterning can be found in many Dipterans (Blagodatski et al. 2015), including an extinct dolichopodid fly from Eocene amber (Tanaka et al. 2009). Such organization may also result in light polarization. It could also be beneficial to boost the antireflection functionality for insects with small ommatidia with the resulting strongly convex surface, such as those of *Leucoptera coffeela* (Meyer-Rochow and Stringer 1993). In such ommatidial shapes, the vertical incident beam is perpendicular to the surface only in the center of the lens – which is covered with nano-nipples. Towards the edges of the lens, nippled structures will reduce their functionality, as they light beam entering a nipple will transverse it and enter the air-filled concentric inter-nipple space, before entering another nipple and finally the lens. Substitution of the nipples with radial parallel ridges with similar widths and heights brings back the functionality.

2.2.2 Anti-Wetting, Self-Cleaning and Antimicrobial Properties of Arthropod Corneal Nanocoatings

Another important feature of the nanocoatings is that they may change the wettability of the material of which they are built. There are no less than six different theoretical models describing interactions among rough materials, gases, and liquids; the two extremes among these models are the Wenzel and the Cassie-Baxter models. The Wenzel model presumes complete wetting of the entire surface of the material, whereas the Cassie-Baxter model suggests that gas is trapped in all the cavities formed by the roughness of the solid material. Experimental data show that the real solid-liquid-gas interactions represent different intermediates between these two models and depend on the morphology of the structures (Sun et al. 2005).

There are two well-known natural examples of the interactions of structured surfaces and liquids. These are the "Petal effect" and the "Lotus effect". The red rose petals are coated by micropapillae harboring nanoprotrusions. However, between the papillae the surface is smooth, which increases the adhesion of the liquid. This structuring leads to a decrease in the spreading of the droplet over the surface (a super-hydrophobic surface with contact angle >150°), but at the same time it keeps the

drop from rolling-off. The lotus leaf coating layer has a rough surface and a low contact angle hysteresis, which means the water droplet is not able to wet the micro-structure as in the Cassie-Baxter model and the liquid can roll-off easily (a super-repelling surface with the contact angle >150° and roll-off angle <10°). This effect allows not only avoiding retention of liquids on the surface, but also makes it easy to clean the surface with water (Sun et al. 2005, 2012; Feng et al. 2008; Liu and Kim 2014).

In the work on mutant *Drosophila*, it has been proposed that the change in adhesion force and hence the surface energy depends on the chemical nature of the nanocoating (Lavanya Devi et al. 2016). However, as the exact composition of corneal nanostructures remains unknown, we will focus only on the adhesion properties resulting from the morphology of the eye surface.

Super-hydrophobicity of an insect's eye has been directly proven in experiments with eyes of mosquitoes, monitoring failure of nucleation of tiny fog drops on their surface (Gao et al. 2007). In our previous work, we have illustrated that the maze-type nanocoating of the corneal lens of Gyrinidae whirligig beetles does not provide any additional hydrophobicity in comparison with a smooth surface. Analysis of the contact angles of the droplets of water placed on these surfaces produced almost identical results, less than 90° (Blagodatski et al. 2014) (Fig. 2.4). In (Peisker and Gorb 2010) it was shown that hydrophobic properties of corneal nanostructures could be calculated by using the JKR (Johnson-Kendall-Roberts) model, and these data fit very well with experimental results demonstrating that hydrophobicity is positively correlated with the height and density of the convex-formed protrusions (Sun et al. 2012) (Fig. 2.4).

Cuticle of small Collembola hexapods, including their corneae, is covered with unique mushroom-shaped nanostructures (Figs. 2.1C and 2.4) (Nickerl et al. 2014). Curiously, size of these nanostructures varies widely on the body surface, but is minimal on the eye surfaces, likely accommodating the antireflective function as the

Fig. 2.4 Anti-wetting properties of different types of insect corneal nanocoatings. First column – 3D images of corneal nanostructures (each square is 2 × 2 μm). Second column – schematic interactions of 1 μm cross-sections of the nanocoatings with water (blue). Air bubbles (white) are trapped in the 'pockets' of the nanostructures of *Clossiana* and Collembola, mediating the effect of super-hydrophobicity
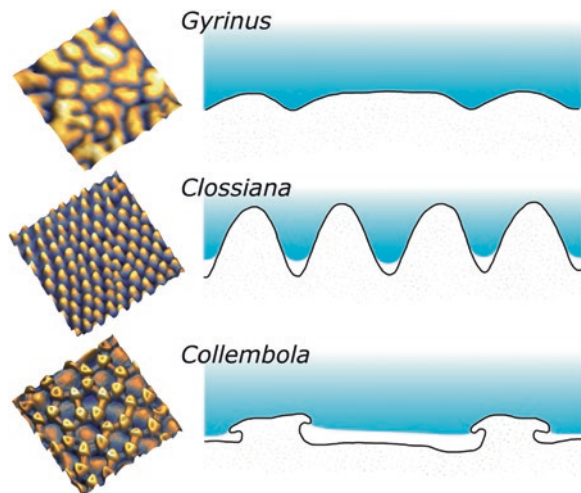
other types of corneal nanocoatings described above. However, the main function of these Collembola nanostructures is hydrophobicity: trapping air bubbles in the 'pockets' at their basis, they prevent effective liquid-surface interactions (Helbig et al. 2011; Hensel et al. 2016) (Fig. 2.4). In fact, these structures are not only super-hydrophobic, but display omniphobicity, as the body of Collembola cannot become wet neither in water nor in oil or alcohol (Helbig et al. 2011; Hensel et al. 2016). Curiously, these mushroom shaped structures are remarkably similar to synthetic structures fabricated in SiO_2 by Liu and Kim (2014) that super-repel all liquids, including perfluorohexane, which has never been observed to form the spherical drop, and *a fortiori* to roll off from any surface.

In continuation of this topic, it could be argued that adhesiveness to nanostructured surfaces is reduced not only for liquids but also for biological objects like bacteria. Indeed, such surfaces play a strong antibacterial and antifungal role, and allow microbes neither to attach to nor to grow on them (Helbig et al. 2011). Such observations have been made e.g. with the cicada wing nanocoatings and with artificial materials bioinspired by the cicada wings (Green et al. 2012). Moreover, when exposed to water vapor, cicada wing surfaces can display self-cleaning from contaminating particles through the self-propelled jumping mechanism of the liquid condensate (Wisdom et al. 2013). The same effect can be expected (but has not yet been experimentally observed) for the very similar eye nanocoatings, such as the butterflies' highly-ordered corneal protrusions (e.g. *Clossiana* genus, Fig. 2.4).

The antibacterial function can be fulfilled not only due to the anti-adhesive properties, but also through the small curvature radius of the nanostructures' peaks. This feature causes stretching of the bacterial cell wall on the nanostructures and results in mechanical laceration of bacteria and cell death (Ivanova et al. 2012; Pogodin et al. 2013; Xue et al. 2015).

In addition to the effects of the lotus leaf and rose petal, there also exists the so-called rice leaf effect (also known as the butterfly wing effect). Both surfaces are special by the anisotropy of the coating structures, i.e. the presence of parallel formation differently affecting the tendency of fluids to flow in transverse *vs*. longitudinal directions (Sun et al. 2005; Hancock et al. 2012; Bixler and Bhushan 2014). The resembling corneal nanocoatings, such as the radiating ridges in some Dipterans (Fig. 2.1 P and P on Fig. 2.3), could also be expected to direct the removal of contaminants towards the edges of the ommatidium.

2.3 Hypotheses of Formation of Corneal Nanostructures

2.3.1 Physical, Chemical and Biological Mechanisms of Formation of Corneal Nanostructures

Initially, as the corneal nanostructures had been known only in the form of ordered Lepidopteran nipple arrays, with other types understudied or regarded as insignificant irregularities (Bernhard et al. 1970), it was postulated that the nipple-like

protrusions are formed in the developing eye by secretion from the regularly spaced microvilli of the cone cells (Gemne 1966, 1971; Bernhard et al. 1970; Fröhlich 2001). Later studies revealing existence of alternative nanostructural patterns have set this hypothesis under question. Indeed, the microvillied cell surface somewhat resembles the nippled corneal pattern but, given the current diversity of the arthropod eye nanostructures and a variety of transitions among them, sometimes even within the same lens (Blagodatski et al. 2015), this hypothesis is not satisfactory any more. Instead, several other concepts, partly complementing each other, have been proposed, suggesting that specific mechanisms of patterning at the nanoscale are involved. These mechanisms assume formation of nanopatterns through a series of physical and chemical interactions and are discussed in the following subsections.

2.3.1.1 The Reaction-Diffusion Model

It has been noticed that the diversity of corneal nanostructures in arthropods is remarkably similar to the set of the patterns described by Alan Turing in his famous reaction-diffusion system (Turing 1952; Blagodatski et al. 2015). This system of differential equations shows how two reacting morphogens – a slowly diffusing activator and a fast diffusing inhibitor – can provide a broad variety of biological, chemical, and physical patterns, previously demonstrated to work at the macro- and micro-scale (Sick et al. 2006; Nakamasu et al. 2009; Raspopovic et al. 2014). The arthropod corneal nanopatterns are different from these prior examples in the sense that they represent not just one of the many possible forms described by the reaction-diffusion model, but a complete set of all possible variants including the intermediate forms. Such complete coverage of the modelled patterns with those found in nature provides a strong argument in favor of the hypothesis that the corneal nanopatterns are indeed a product of the Turing reaction-diffusion mechanism. The reaction-diffusion model allows producing patterns only in a certain range of parameters (activation, inhibition and diffusion constants); outside of the permitted parameter space, no stable patterns can appear. Mathematical Turing modeling of corneal nanopattern formation has shown that the nanoscale patterns are expected to form under conditions where diffusion properties are reduced (in comparison to the liquid phase), corresponding to the reaction-diffusion system acting in colloidal or liquid crystal-type environment, similar to that of the developing eye lens. Importantly, a set of patterns has been modeled with dimensions identical to those of the experimentally described insect corneal nanocoatings, and all the modeling parameters thereof were found inhabiting the parameter space predefined for the Turing patterns, thus also speaking in favor of the hypothesis (Blagodatski et al. 2015). Remarkably, while different combinations of the reaction-diffusion parameters can produce different nanopatterns in the model, simulations reveal that three of the four main corneal pattern types found in arthropods belong to defined regions within the parameter space and transform one to another in the following way: dimples ↔ mazes ↔ nipples. The dimpled pattern appears to be the most primitive in this system, since it requires minimal values of the diffusion parameters. It might

have emerged first during arthropod evolution when these parameters just exceeded the threshold values, allowing the generation of the Turing-type structures (Miura and Maini 2004; Kondo and Miura 2010; Blagodatski et al. 2015). The primordiality of the dimpled pattern is also indirectly suggested by the fact that it is typical for centipedes (Blagodatski et al. 2015), which are presumably the closest taxon to the ancestral primitive arthropods (Chipman et al. 2014). The structures with the highest degree of order, such as the hexagonally packed nipple arrays or parallel strands, evolve in this model from their predecessors (irregular nipples and maze-like structures, respectively, Fig. 2.3) when the diffusion coefficient of the activator reaches its maximally allowed levels within the parameter space. On the other hand, the maximal possible values of the inhibitor diffusion coefficient bring the system to increase in the width of the nanostructures (nipples or ridges, respectively) (Blagodatski et al. 2015).

2.3.1.2 Formation of Order in the Nipple Arrays

Among the variety of corneal nanostructures, the "classical" hexagonally packed nipple arrays have received the most interest so far. They have been analyzed from various points of view, including regarding them as crystal lattices and studying them by AFM, SEM and mathematical modeling. These nanopatterns have also been the focus of analysis addressing the origin of order in nanostructures. Thus, nippled nanocoatings of representatives of six different insect orders (Diptera, Lepidoptera, Psocoptera, Hemiptera, Trichoptera and Thysanura) were studied with a special algorithm, permitting simultaneous assessment of geometric characteristics of the nanostructures (such as height, width, inter-nipple distance) in relation to the regularity of the nipple packing (Sergeev et al. 2015). The regularity was determined by mutual orientation of the neighboring nipples and, by analogy with condensed matter science, nipples that did not possess exactly six neighbors were characterized as defects, which are made either by vacancies in the densely packed arrays or/and by non-equal sizes and shapes of nipples. Defects of the nipple "crystal lattice" were predominantly detected between hexagonally-packed ordered domains, which varied in diameter from 2 to 12 μm in different insects (Sergeev et al. 2015). These defects effectively form the domain boundaries (Fig. 2.1 ON). Degree of order in the nipple arrays was characterized by the hexagonal packing coefficient (HPC) – the relative number of grains with a coordination number (the number of nearest neighbors) equal to 6: the greater the HPC, the higher is the packing order. The HPC values revealed a positive correlation with the nipple packing density and the nipple height, negative correlation with the nipple diameter and the inter-nipple distance, and no correlation of HPC with the lens size or the nipple volume. This led to conclude that patterning mechanisms such as described by Turing probably coexist with the packing density forcing appearance of order in the biological nanostructures. Dense packing leads to formation of more ordered arrays of taller and thinner nipples with smaller inter-nipple distances. External patterning mechanisms may be at play to provide the initial positioning of the nanostructures and/or to elicit the

interactions among the building blocks, thus opening a possibility for the dense packing to serve as the driving force responsible for the order formation. Analysis of the degree of order and of the order generation mechanisms in other types of nanopatterns such as mazes or parallel ridges is subject of further investigation.

As an extension and complementation to the reaction-diffusion mechanism, a nucleation and growth mechanism similar to that acting during formation of crystals has been proposed (Lee et al. 2016). Similarly to the previous study (Sergeev et al. 2015), corneal nipple arrays of the butterfly *Nymphalis antiopa* were regarded as a crystal lattice and analyzed by SEM at the nanoscale to study the crystal and defect structures, and at the mesoscale to estimate the crystal domain sizes as well as the orientations between the domains over the entire ommatidium. The results obtained were in general consistent with the previous study. At the nanoscale, vacancies and fusion defects were found at a low frequency. The 5–7 coordination defect predominated and was found almost exclusively at boundaries between adjacent domains with the perfect hexagonal structure, in a manner similar to grain boundaries in 2D hexagonal structures (Lee and Erb 2013, 2015). At the mesoscale, rows of 5–7 coordination defects were found to form an interconnected network of domain boundaries, subdividing the entire ommatidium into numerous domains (about 120 per facet), each containing nipples in the perfect hexagonal arrangement (Lee et al. 2016). Very little order was found at the ommatidial boundaries and triple junctions; no indications of crystals or crystal orientations extending from one ommatidium to a neighboring one were seen. Generation of multiple domains within a single ommatidium can be explained by the Turing model, when a cascade of independent pattern formations is initiated by local fluctuations of the activator/inhibitor concentrations, each formation responsible for a discrete domain. Mathematical simulations of the nipple "nucleations", which could potentially be triggered in numerous locations, filling the lens surface with multiple sets of ordered hexagonal arrays, have been performed. It was found that the Turing modeling allows covering areas large enough to fill the entire ommatidium, without requiring existence of pre-patterning cone cell microvilli (Lee et al. 2016). However, microvilli might still contribute to the pattern formation e.g. as initiators of nipple "nucleation" or by providing means to control the activator/inhibitor concentrations during eye development.

2.3.1.3   The Block Copolymer Model of Nanostructure Formation

Being an impressive explanation of the general principle of nanopattern formation, the reaction-diffusion model currently lacks the specifics on the exact chemical identities of the molecules interacting during developing of the nanostructures. A potent example of *in vitro* self-assembly of nanoscale patterns resembling that of arthropod corneae (Figs. 2.1 and 2.5), which may give a clue to a possible chemical nature of their mechanism of formation, is provided by the block copolymer (BCP) systems. Block copolymers are made of blocks of different polymerized monomers (styrene and methylmethacrylate being classical examples). Due to different hydrophilicity/hydrophobicity of the blocks, block copolymers are capable of microphase
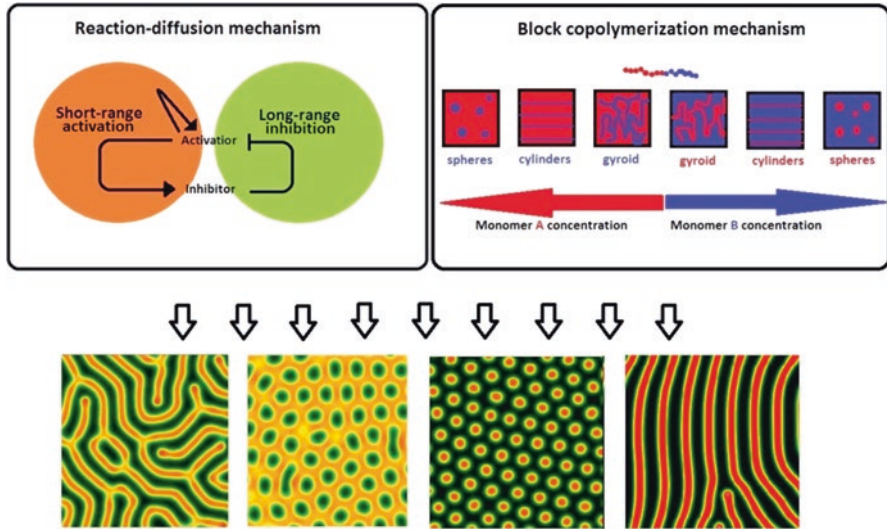
Fig. 2.5 The reaction-diffusion mechanisms (above left) driven by short-ranged and long-ranged interactions of a slowly diffusing activator and a fast diffusing inhibitor, as well as block copolymerization (above right) driven by physico-chemical interactions and concentration ratios of two polymerizing monomers with different physical properties, give rise to similar patterns defined as spheres, cylinders and gyroids (above right) in case of block copolymerization or as mazes, dimples, nipples, or ridges in case of arthropod corneal nanostructures (below)

separation – a process similar to phase separation of oil and water. Because the blocks are covalently bound to each other, they cannot demix macroscopically as two liquids would, separating in microscale and forming nanometer-sized structures instead (Hamley 1998; Hamley et al. 2004). Self-assembly in BCP systems is driven via a thermodynamic process where chemical dis-affinity between the blocks separating them is balanced by a restorative force derived from the chemical bonds between the blocks (Farrell et al. 2009). Block copolymerization can serve as a tool to engineer nanostructured thin films, where patterns similar to nipples, dimples, ridges and mazes can be found, albeit markedly smaller in dimensions than those found on arthropod eyes: their usual thickness is about 5–50 nm (Wu et al. 2005). Interestingly, artificial design of nanopatterns from block copolymers often requires a careful chemical and topographical pre-patterning of the surface upon which they are formed (Farrell et al. 2009). In the case of chemical pre-patterning, the substrate surface is treated with a compound that selectively chemically interacts with one block of the copolymer, so that the micro-phase separated structure tends to align to the pre-pattern (Chen and Chakrabarti 1998). Surface topography plays a role in formation of the nanostructures along with chemical properties of the substrate. The graphoepitaxy (topographical alignment), first described in Fasolka et al. (1997), is an example of topographical pre-patterning, where a single relatively large substrate feature such as a channel can be used to direct the BCP nanopattern with precise alignment into almost single crystal-like periodicity within such a channel (Farrell

et al. 2009). Graphoepitaxical photolitography-based pre-patterning has been used to influence the form of nanopatterns created by block copolymerisation, resulting in formation of parallel nano-strands on a pre-patterned surface by a polystyrene-block-polymethylmethacrylate copolymer, which otherwise formed maze-like structures on untreated or undertreated surfaces (Kim et al. 2003). In another example, pre-patterned grooves were used to create cylinder arrays resembling those of regular nipples using the same copolymer (Xiao et al. 2005). Thus, not only the chemical nature of molecules forming the nanopatterns, but also physical or chemical pretreatment of the environment where they are formed affects the nanostructural features. This can bring to a reconsideration of the potential role of the cone cell microvilli in development of the corneal nanostructures. Indeed, the microvilli might not be directly used for secretion of nipple arrays or other nanostructures but may instead serve, either through forming the basement for the nanostructures or through production of some metabolites, as a chemical or topographical pre-patterning tool for the nanopatterns. Another hint can be that the form of the ommatidia itself serves as a kind of a template directing the nanostructural development. The two mechanisms – the Turing reaction-diffusion system and the BCP system – can generate very similar patterns (Fig. 2.5) and involve interactions of at least two chemical entities with different properties. Identification of these entities and recapitulation of the patterns through their admixtures in controlled experiments are required in order to identify the exact mechanism behind the corneal nanostructures.

2.3.1.4 The Genetics of the Nanostructure Formation

In this regard, molecules regulating genesis of the biological nanostructures are of a special interest and remain largely unrevealed. A study on *Drosophila melanogaster* corneal nipples has been performed, not only describing their physical parameters and regularity, but also addressing the question of signaling pathways potentially involved in the development of the nipple arrays (Kryuchkov et al. 2011). Being a thoroughly studied model animal, *Drosophila* allows numerous genetic manipulations with subsequent investigation of the resultant mutant phenotypes (Katanaev and Kryuchkov 2011). We tested the potential role of one of the most important developmental signaling pathways, namely the Wg-Frizzled pathway, in formation of the corneal nanostructures. One of the very first mutants discovered by the 'father' of *Drosophila* genetics Thomas Morgan had been named *Glazed* due to the glossy eye appearance and was decades later revealed to be caused by overexpression of the Wg morphogen, overactivating the Wg-Frizzled signaling pathway (Bhanot et al. 1996). AFM analysis of the nipple arrays of a Wg-overexpressing *Drosophila* line with the glazed eye phenotype demonstrated a drastic loss of nipples, while the remaining degenerated nanostructures were randomly spaced in ommatidia with large gap areas (Kryuchkov et al. 2011). Thus, the glossy appearance of *Drosophila* eyes correlates with the loss of corneal nanostructures. These findings further suggest that development of the corneal nanostructures is influenced (directly or indirectly) by the Wg signaling.

Another application of *Drosophila* as a model organism to study formation of the nanostructures involved an RNAi screen, where a series of genes responsible for cuticle formation and cell polarity were systematically knocked down by RNAi expression or analyzed using the existing mutant collections, in a search for genes affecting the phenotype of corneal nanostructures (Minami et al. 2016). Interestingly, some of the identified glossy eye mutants demonstrate a nipple-to-maze transition (*gl* mutant) and even a maze-like phenotype (*spa* mutant), while other mutations have shown a complete vanishing and degradation of nipples (mutants *lz* and *Glazed*, again). RNAi silencing of some genes also led to partial nipple-to-maze merging (*Cpr49Ah*, *Act5C*) and partial nipple enlargement (*Cpr23B*, *Syx1A*, *Sec61ß*). This study is a proof-of-concept of the possibility to alter the nanostructure type in a model animal using genetic manipulations. However, it would be premature to suspect that the genes identified are the ones directly responsible for e.g. the nipple-maze transition, as these mutant flies demonstrated not merely alterations at the level of the nanostructures but also a drastic disorder at the macro- and micro-levels ("rough eye" phenotypes, merging and degradation of ommatidia, eye size decrease, *etc*.). Thus, the observed nanostructural defects are likely due to indirect effects caused by general disturbances of the eye development which occur frequently during genetic studies on *Drosophila* eye (Katanaev and Kryuchkov 2011).

2.3.2 Ontogenesis of the Corneal Nanostructures

Most EM and AFM studies of corneal nanostructures have been performed on corneal samples of adult insects or other arthropods. Presently, surprisingly little is known about larval or pupal formation of the eye nanostructures, although their generation takes place at these earlier development stages.

Early data on pupal development of corneal nanostructures were produced from EM-derived pictures of 1960s–1970s, when the theory of nanostructure formation via microvilli secretion dominated (Gemne 1966, 1971). Extensive EM analysis of the nipple development over an 8-day pupation period of the moth *Manduca sexta* concluded that the nipple arrays are an integral part of the lens surface (Gemne 1971). According to this study, nipple formation begins about 5 days after pupation with the development of initial patches on the epicorneal lamina on top of underlying microvilli. This is followed by formation of the nipple anlage, first as low cupoles, then as higher cupoles after 6.5–7 days. After 7.5–8 days, the high cupoles become filled with the corneal substance through the microvilli and consolidate, forming the final nipple structure. The arrangement of microvilli tips in the cone cells was believed to be organized in the hexagonal packing manner, explaining the observed arrangement of the nipples in hexagonal domains. Defects in the nipple arrangement showing deviation from the perfect hexagonal packing were explained by the convex shape of the lens. Currently, we know that these defects are distributed in a specific manner, lying predominantly on the nipple domain boundaries, as discussed above (Sergeev et al. 2015; Lee et al. 2016). Interestingly, the detailed EM study revealed

that corneal nipples emerge in the very beginning of the lens formation, and the chitinous layer seems to be secreted later, underlying the nanostructures. Thus the chitin itself is unlikely to take part in the assembly of the nanocoatings but merely serves as one of the building materials for the lens itself (Gemne 1971).

The main challenge for the microvilli model is that it lacks explanation for formation of the patterns other than the nipple arrays. In the 1970s, the non-nippled nanostructures were regarded rather as degenerate or underdeveloped structures, whose appearance was linked with defects in the microvilli-lamina evagination bridges on the epicorneal lamina (Bernhard et al. 1970; Gemne 1971). Even if we apply the microvilli theory exclusively to the nipple arrays, it is still hard to explain by its means the formation of boundaries of hexagonally-packed ordered domains with very specific configurations – formed by rows of coordination defects as described in (Sergeev et al. 2015; Lee et al. 2016). The model requires that the initial arrangement of microvilli serves as an exact template for the specific nipple arrangements before the nipples are actually formed. However, this is not the case, since the one-to-one correspondence between the positions of microvilli and the initial patch locations or the final nipple positions is not apparent from the presented electron micrographs (Gemne 1971).

A detailed SEM study was performed on the pupal eye of a developing *Drosophila* (Fröhlich 2001), with a description of corneal nipple formation in parallel with secretion of the lens cuticle at later stages of pupation (42–46 h). Interestingly, the author found that the nipple arrays arise almost immediately after the cuticle begins to appear. These observations matched well with the earlier studies (Gemne 1971), suggesting that formation of the nanostructures takes place during the pupal phase as an early and fast event preceding formation of major parts of the lens. It can be hypothesized that self-organization of the nanostructures takes place while secretions of the cone cells form the eye cuticle. As a result, near-complete nanocoatings already exist upon the lens while it is still growing (Fig. 2.6).

Summarizing the data known up to date, we can conclude that formation of the corneal nanostructures in arthropods is a complex process, which is under regulation by a series of factors. While the Turing reaction-diffusion patterning and the block copolymerisation are the two main candidates to be the underlying mechanism, we still do not possess exact information on the identity of the compounds taking part in the generation of the nanostructures, nor on the chemical nature of their interactions. On the other hand, these processes can be influenced by auxiliary mechanisms, such as dense packing bringing more order into the structures, chemical pre-patterning or topographical pre-patterning (graphoepitaxy). If it comes to the pre-patterning mechanisms, the role of the cone cell microvilli can be reconsidered, not as being an exact template upon which the nipple arrays are built, but rather as a more sophisticated tool affecting the patterning mechanisms either by chemical secretion of morphogenetically active compounds or by forming the underlying surface structure. Certain compounds secreted by the microvilli may play a role of initiating factors for nucleation of the Turing-like processes. The mesoscale structural parameters such as the lens size and shape are likely to further influence formation of the nanostructures as well. It is known that biological pat-
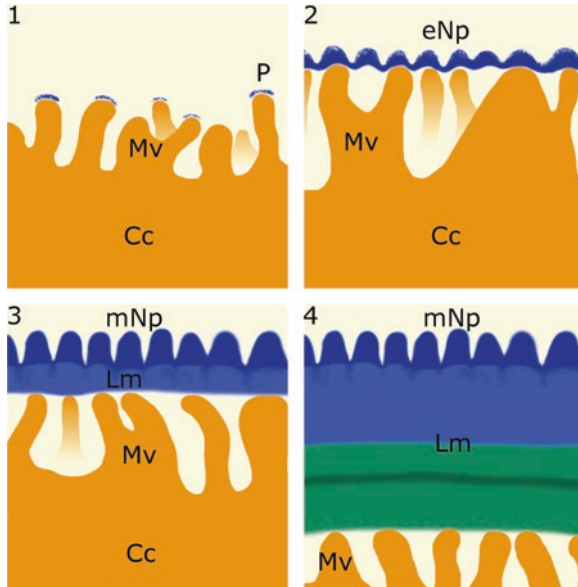
Fig. 2.6 Schematic representation of ontogenesis of the corneal nanostructures using formation of nipple arrays on the surface of a single ommatidium as an example. 1 – Secretion of the corneal material by the cone cells (Cc) with nucleation of initial patches (P) on tips of microvilli (Mv). 2 – Self-assembly of the corneal nanostructures, in this case early nipples (eNp) upon the secreting corneal material, with tips of microvilli (Mv) still attached to the inner surface of the cornea. 3 – After nanostructures are formed as mature nipples (mNp), cone cells continue to secrete the bulk lens lamina material (light blue, Lm) containing chitin and other biopolymers forming the entire lens. 4 – The lens is completely formed; lamina (light blue and green) separates the outer layer with the nanostructures from microvilli of the cone cells

terns are generated by Turing mechanism at the macro- and mesoscale (Nakamasu et al. 2009) and that artificial block copolymerization yields nanostructures with proportions an order of magnitude smaller (usually 5–10 nm in width and height) than the corneal nanocoatings of the arthropods. Thus, the arthropod corneal nanocoatings, in the matter of their size, are positioned between the traditional "zones of responsibility" of the block copolymerization and reaction-diffusion mechanisms. Although the exact chemical nature of the compounds responsible for the processes of nanopattern organization is unknown, it may be assumed that one of them could be hydrophobic – probably a wax or a lipid, while the other is of hydrophilic nature (a protein or a glycoprotein). Such a system would remind the block copolymerization outline, but also be similar to the Turing mechanism in that the hydrophobic wax or lipid would block the action of the hydrophilic protein. Investigation of the composition of the nanocoatings and of the biochemical interactions governing their formation thus remains a task of high priority in this scientific field. Actually, these questions expand the discipline of insect corneal nanostructures and touch upon the general mechanisms of biological pattern formation on the

100 nm scale. Thus, the corneal nanocoatings emerge as a remarkable model to tackle issues of general importance for biology and physics.

Finally, identification of the molecular mechanisms governing formation of the corneal nanopatterns may have technological importance. Unraveling of these mechanisms will make it possible to (bio)engineer biological or biomimetic nanostructured surfaces with desired features and parameters. Their applications for the optical, anti-wetting and self-cleaning functions discussed in this chapter may be complemented with other uses, such as the selective molecular separations, selective adsorption, or the high activity catalysis attributed to the pattern with regular sized pores resembling the dimpled pattern of the arthropod corneae (Farrell et al. 2009). Through the genetic tools provided by the model insect *Drosophila melanogaster* suitable for the study of biological nanostructures (Kryuchkov et al. 2011; Minami et al. 2016), this fruit fly can serve as a powerful instrument to further investigate the exact mechanisms of the bionanopattern formation processes, to identify the molecular interactions taking part in the generation of corneal nanocoatings, and to produce artificially designed nanopatterns with novel physical properties by means of bioengineering and synthetic biology.

References

Aghaeipour, M., Anttu, N., Nylund, G., Samuelson, L., Lehmann, S., & Pistol, M.-E. (2014). Tunable absorption resonances in the ultraviolet for InP nanowire arrays. *Optics Express, 22*(23), 29204–29212.

Anderson, M. S., & Gaimari, S. D. (2003). Raman-atomic force microscopy of the ommatidial surfaces of dipteran compound eyes. *Journal of Structural Biology, 142*(3), 364–368.

Autumn, K., Liang, Y. A., Hsieh, S. T., Zesch, W., Chan, W. P., Kenny, T. W., Fearing, R., & Full, R. J. (2000). Adhesive force of a single gecko foot-hair. *Nature, 405*(6787), 681–685.

Bernhard, C. G., & Miller, W. H. (1962). A corneal nipple pattern in insect compound eyes. *Acta Physiologica Scandinavica, 56*(3–4), 385–386.

Bernhard, C.G., Miller, W.H., & Møller, A.R. (1965). The insect corneal nipple array: A biological, broad-band impedance transformer that acts as an antireflection coating. *Zeitschrift für vergleichende Physiologie, 67*(1), 1–25.

Bhanot, P., Brink, M., Samos, C.H., Hsieh, J.C., Wang, Y., Macke, J.P., Andrew. D., Nathans, J., & Nusse, R. (1996). A new member of the frizzled family from Drosophila functions as a Wingless receptor. *Nature, 382*(6588), 225–230.

Bernhard, C. G., Gemne, G., & Sällström, J. (1970). Comparative ultrastructure of corneal surface topography in insects with aspects on phylogenesis and function. *Journal of Comparative Physiology. A, 67*(1), 1–25.

Bixler, G. D., & Bhushan, B. (2014). Rice- and butterfly-wing effect inspired self-cleaning and low drag micro/nanopatterned surfaces in water, oil, and air flow. *Nanoscale, 6*(1), 76–96.

Bixler, G. D., Theiss, A., Bhushan, B., & Lee, S. C. (2014). Anti-fouling properties of microstructured surfaces bio-inspired by rice leaves and butterfly wings. *Journal of Colloid and Interface Science, 419*, 114–133.

Blagodatski, A., Kryuchkov, M., Sergeev, A., Klimov, A. A., Shcherbakov, M. R., Enin, G. A., & Katanaev, V. L. (2014). Under- and over-water halves of Gyrinidae beetle eyes harbor different corneal nanocoatings providing adaptation to the water and air environments. *Scientific Reports, 4*, 6004.

Blagodatski, A., Sergeev, A., Kryuchkov, M., Lopatina, Y., & Katanaev, V. L. (2015). Diverse set of Turing nanopatterns coat corneae across insect lineages. *Proceedings of the National Academy of Sciences of the United States of America, 112*(34), 10750–10755.

Brongersma, M. L., Cui, Y., & Fan, S. H. (2014). Light management for photovoltaics using high-index nanostructures. *Nature Materials, 13*(5), 451–460.

Chen, H., & Chakrabarti, A. (1998). Morphology of thin block copolymer films on chemically patterned substrates. *The Journal of Chemical Physics, 108*(16), 6897–6905.

Chipman, A. D., Ferrier, D. E., Brena, C., Qu, J., Hughes, D. S., Schroder, R., Torres-Oliva, M., Znassi, N., Jiang, H., Almeida, F. C., et al. (2014). The first myriapod genome sequence reveals conservative arthropod gene content and genome organisation in the centipede *Strigamia maritima*. *PLoS Biology, 12*(11), e1002005.

Daglar, B., Khudiyev, T., Demirel, G. B., Buyukserin, F., & Bayindir, M. (2013). Soft biomimetic tapered nanostructures for large-area antireflective surfaces and SERS sensing. *Journal of Materials Chemistry C, 1*(47), 7842–7848.

Daly, H.V. (1970). The insects. Structure and function. R. F. Chapman. Elsevier, New York, 1969. *Science* 168(3935), 1082.

Deinega, A., Valuev, I., Potapkin, B., & Lozovik, Y. (2011). Minimizing light reflection from dielectric textured surfaces. *Journal of the Optical Society of America. A, 28*(5), 770–777.

Du, Q. G., Kam, C. H., Demir, H. V., Yu, H. Y., & Sun, X. W. (2011). Broadband absorption enhancement in randomly positioned silicon nanowire arrays for solar cell applications. *Optics Letters, 36*(10), 1884–1886.

Farrell, A. R., Fitzgerald, G. T., Borah, D., Holmes, D. J., & Morris, A. M. (2009). Chemical interactions and their role in the microphase separation of block copolymer thin films. *International Journal of Molecular Sciences, 10*(9), 3671–3712.

Fasolka, M. J., Harris, D. J., Mayes, A. M., Yoon, M., & Mochrie, S. G. J. (1997). Observed substrate topography-mediated lateral patterning of diblock copolymer films. *Physical Review Letters, 79*(16), 3018–3021.

Feng, L., Zhang, Y., Xi, J., Zhu, Y., Wang, N., Xia, F., & Jiang, L. (2008). Petal effect: A superhydrophobic state with high adhesive force. *Langmuir, 24*(8), 4114–4119.

Fröhlich, A. (2001). A scanning electron-microscopic study of apical contacts in the eye during postembryonic development of *Drosophila melanogaster*. *Cell and Tissue Research, 303*(1), 117–128.

Gao, X., Yan, X., Yao, X., Xu, L., Zhang, K., Zhang, J., Yang, B., & Jiang, L. (2007). The dry-style antifogging properties of mosquito compound eyes and artificial analogues prepared by soft lithography. *Advanced Materials, 19*(17), 2213–2217.

Gemne, G. (1966). Ultrastructural ontogenesis of cornea and corneal nipples in compound eye of insects. *Acta Physiologica Scandinavica, 66*(4), 511–512.

Gemne, G. (1971). Ontogenesis of corneal surface ultrastructure in nocturnal Lepidoptera. *Philosophical Transactions of the Royal Society B, 262*(843), 343–363.

Gorb, S., & Speck, T. (2017). Biological and biomimetic materials and surfaces. *Beilstein Journal of Nanotechnology, 8*, 403–407.

Green, D. W., Watson, G. S., Watson, J., & Abraham, S. J. K. (2012). New biomimetic directions in regenerative ophthalmology. *Advance Healthcare Maternité, 1*(2), 140–148.

Hamley, I. W. (1998). *The physics of block copolymers*. Oxford: Oxford University Press.

Hamley, I. W., Connell, S. D., Collins, S., Fundin, J., & Yang, Z. (2004). In situ AFM imaging of block copolymer micelles adsorbed on a solid substrate. *Abstracts of Papers of the American Chemical Society, 227*, 551–551.

Han, L., & Zhao, H. P. (2014). Surface antireflection properties of GaN nanostructures with various effective refractive index profiles. *Optics Express, 22*(26), 31907–31916.

Hancock, M. J., Sekeroglu, K., & Demirel, M. C. (2012). Bioinspired directional surfaces for adhesion, wetting, and transport. *Advanced Functional Materials, 22*(11), 2223–2234.

Helbig, R., Nickerl, J., Neinhuis, C., & Werner, C. (2011). Smart skin patterns protect springtails. *PLoS One, 6*(9), e25105.

Hensel, R., Neinhuis, C., & Werner, C. (2016). The springtail cuticle as a blueprint for omniphobic surfaces. *Chemical Society Reviews, 45*(2), 323–341.

Ivanova, E. P., Hasan, J., Webb, H. K., Truong, V. K., Watson, G. S., Watson, J. A., Baulin, V. A., Pogodin, S., Wang, J. Y., Tobin, M. J., et al. (2012). Natural bactericidal surfaces: Mechanical rupture of *Pseudomonas aeruginosa* cells by cicada wings. *Small, 8*(16), 2489–2494.

Ji, S., Park, J., & Lim, H. (2012). Improved antireflection properties of moth eye mimicking nanopillars on transparent glass: Flat antireflection and color tuning. *Nanoscale, 4*(15), 4603–4610.

Katanaev, V. L., & Kryuchkov, M. V. (2011). The eye of *Drosophil*a as a model system for studying intracellular signaling in ontogenesis and pathogenesis. *Biochemistry (Moscow), 76*(13), 1556–1581.

Kim, S. O., Solak, H. H., Stoykovich, M. P., Ferrier, N. J., de Pablo, J. J., & Nealey, P. F. (2003). Epitaxial self-assembly of block copolymers on lithographically defined nanopatterned substrates. *Nature, 424*(6947), 411–414.

Kondo, S., & Miura, T. (2010). Reaction-diffusion model as a framework for understanding biological pattern formation. *Science, 329*(5999), 1616–1620.

Kryuchkov, M., Katanaev, V. L., Enin, G. A., Sergeev, A., Timchenko, A. A., & Serdyuk, I. N. (2011). Analysis of micro- and nano-structures of the corneal surface of *Drosophila* and its mutants by atomic force microscopy and optical diffraction. *PLoS One, 6*(7), e22237.

Kryuchkov, M., Lehmann, J., Schaab, J., Cherepanov, V., Blagodatski, A., Fiebig, M., & Katanaev, V. L. (2017a). Alternative moth-eye nanostructures: Antireflective properties and composition of dimpled corneal nanocoatings in silk-moth ancestors. *J. NanoBiotechnology, 15*(1), 61.

Kryuchkov, M., Lehmann, J., Schaab, J., Fiebig, M., & Katanaev, V. L. (2017b). Antireflective nanocoatings for UV-sensation: The case of predatory owlfly insects. *Journal of Nanobiotechnology, 15*(1), 52.

Lavanya Devi, A. L., Nongthomba, U., & Bobji, M. S. (2016). Quantitative characterization of adhesion and stiffness of corneal lens of *Drosophila melanogaster* using atomic force microscopy. *Journal of the Mechanical Behavior of Biomedical Materials, 53*, 161–173.

Lee, K. C., & Erb, U. (2013). Grain boundaries and coincidence site lattices in the corneal nanonipple structure of the mourning cloak butterfly. *Beilstein Journal of Nanotechnology, 4*, 292–299.

Lee, K. C., & Erb, U. (2015). Remarkable crystal and defect structures in butterfly eye nano-nipple arrays. *Arthropod Structure & Development, 44*(6), 587–594.

Lee, K. C., Yu, Q., & Erb, U. (2016). Mesostructure of ordered corneal nano-nipple arrays: The role of 5–7 coordination defects. *Scientific Reports, 6*, 28342.

Leem, J. W., Yeh, Y., & Yu, J. S. (2012). Enhanced transmittance and hydrophilicity of nanostructured glass substrates with antireflective properties using disordered gold nanopatterns. *Optics Express, 20*(4), 4056–4066.

Lin, C., Martínez, L. J., & Povinelli, M. L. (2013). Experimental broadband absorption enhancement in silicon nanohole structures with optimized complex unit cells. *Optics Express, 21*(S5), A872–A882.

Lin, D., Fan, P., Hasman, E., & Brongersma, M. L. (2014). Dielectric gradient metasurface optical elements. *Science, 345*(6194), 298.

Liu, T. L., & Kim, C. J. (2014). Repellent surfaces. Turning a surface superrepellent even to completely wetting liquids. *Science, 346*(6213), 1096–1100.

Liu, H., Xu, J., Li, Y., & Li, Y. (2010). Aggregate nanostructures of organic molecular materials. *Accounts of Chemical Research, 43*(12), 1496–1508.

Martins, E. R., Li, J., Liu, Y., Depauw, V., Chen, Z., Zhou, J., & Krauss, T. F. (2013). Deterministic quasi-random nanostructures for photon control. *Nature Communications, 4*, 2665.

Meyer-Rochow, V. B. (1978). Retina and dioptric apparatus of the dung beetle *Euoniticellus africanus*. *Journal of Insect Physiology, 24*(2), 165–179.

Meyer-Rochow, V. B., & Stringer, I. A. N. (1993). A system of regular ridges instead of nipples on a compound eye that has to operate near the diffraction limit. *Vision Research, 33*(18), 2645–2647.

Miller, W. H. (1979). Ocular optical filtering. In H. Autrum (Ed.), *Handbook of sensory physiology* (Vol. VII/6A, pp. 69–143). Berlin/Heidelberg/New York: Springer.

Minami, R., Sato, C., Yamahama, Y., Kubo, H., Hariyama, T., & Kimura, K.-i. (2016). An RNAi screen for genes involved in nanoscale protrusion formation on corneal lens in *Drosophila melanogaster*. *Zoological Science, 33*(6), 583–591.

Mishra, M., & Meyer-Rochow, V. B. (2006). Eye ultrastructure in the pollen-feeding beetle, *Xanthochroa luteipennis* (Coleoptera: Cucujiformia: Oedemeridae). *Journal of Electron Microscopy, 55*(6), 289–300.

Miura, T., & Maini, P. K. (2004). Periodic pattern formation in reaction–diffusion systems: An introduction for numerical simulation. *Anatomical Science International, 79*(3), 112–123.

Nakamasu, A., Takahashi, G., Kanbe, A., & Kondo, S. (2009). Interactions between zebrafish pigment cells responsible for the generation of Turing patterns. *Proceedings of the National Academy of Sciences of the United States of America, 106*(21), 8429–8434.

Nickerl, J., Tsurkan, M., Hensel, R., Neinhuis, C., & Werner, C. (2014). The multi-layered protective cuticle of Collembola: A chemical analysis. *Journal of The Royal Society Interface, 11*(99), 20140619.

Oskooi, A., Favuzzi, P. A., Tanaka, Y., Shigeta, H., Kawakami, Y., & Noda, S. (2012). Partially disordered photonic-crystal thin films for enhanced and robust photovoltaics. *Applied Physics Letters, 100*(18), 181110.

Peisker, H., & Gorb, S. N. (2010). Always on the bright side of life: Anti-adhesive properties of insect ommatidia grating. *The Journal of Experimental Biology, 213*(20), 3457–3462.

Pogodin, S., Hasan, J., Baulin, V. A., Webb, H. K., Truong, V. K., Phong Nguyen, T. H., Boshkovikj, V., Fluke, C. J., Watson, G. S., Watson, J. A., et al. (2013). Biophysical model of bacterial cell interactions with nanopatterned cicada wing surfaces. *Biophysical Journal, 104*(4), 835–840.

Pratesi, F., Burresi, M., Riboli, F., Vynck, K., & Wiersma, D. S. (2013). Disordered photonic structures for light harvesting in solar cells. *Optics Express, 21*(S3), A460–A468.

Raspopovic, J., Marcon, L., Russo, L., & Sharpe, J. (2014). Digit patterning is controlled by a bmp-Sox9-Wnt Turing network modulated by morphogen gradients. *Science, 345*(6196), 566–570.

Raut, H. K., Ganesh, V. A., Nair, A. S., & Ramakrishna, S. (2011). Anti-reflective coatings: A critical, in-depth review. *Energy Environmental Sciences, 4*(10), 3779–3804.

Schuster, C. S., Morawiec, S., Mendes, M. J., Patrini, M., Martins, E. R., Lewis, L., Crupi, I., & Krauss, T. F. (2015). Plasmonic and diffractive nanostructures for light trapping–an experimental comparison. *Optica, 2*(3), 194–200.

Sergeev, A., Timchenko, A. A., Kryuchkov, M., Blagodatski, A., Enin, G. A., & Katanaev, V. L. (2015). Origin of order in bionanostructures. *RSC Advances, 5*(78), 63521–63527.

Sick, S., Reinker, S., Timmer, J., & Schlake, T. (2006). WNT and DKK determine hair follicle spacing through a reaction-diffusion mechanism. *Science, 314*(5804), 1447–1450.

Siddique, R. H., Gomard, G., & Holscher, H. (2015). The role of random nanostructures for the omnidirectional anti-reflection properties of the glasswing butterfly. *Nature Communications, 6*, 6909.

Son, J., Verma, L. K., Danner, A. J., Bhatia, C. S., & Yang, H. (2011). Enhancement of optical transmission with random nanohole structures. *Optics Express, 19*(S1), A35–A40.

Stavenga, D. G. (2006). Invertebrate superposition eyes-structures that behave like metamaterial with negative refractive index. *Journal of the European Optical Society-Rapid Publications, 1*, 06010.

Stavenga, D. G., Foletti, S., Palasantzas, G., & Arikawa, K. (2006). Light on the moth-eye corneal nipple array of butterflies. *Proceedings of the Royal Society B, 273*(1587), 661–667.

Stavroulakis, P. I., Boden, S. A., Johnson, T., & Bagnall, D. M. (2013). Suppression of backscattered diffraction from sub-wavelength 'moth-eye' arrays. *Optics Express, 21*(1), 1–11.

Sun, T. L., Feng, L., Gao, X. F., & Jiang, L. (2005). Bioinspired surfaces with special wettability. *Accounts of Chemical Research, 38*(8), 644–652.

Sun, M., Liang, A., Watson, G. S., Watson, J. A., Zheng, Y., Ju, J., & Jiang, L. (2012). Influence of cuticle nanostructuring on the wetting behaviour/states on cicada wings. *PLoS One, 7*(4), e35056.

Tanaka, G., Parker, A. R., Siveter, D. J., Maeda, H., & Furutani, M. (2009). An exceptionally well-preserved Eocene dolichopodid fly eye: Function and evolutionary significance. *Proceedings of the Royal Society B, 276*(1659), 1015–1019.

Toh, Y., & Okamura, J.-y. (2007). Morphological and optical properties of the corneal lens and retinal structure in the posterior large stemma of the tiger beetle larva. *Vision Research, 47*(13), 1756–1768.

Turing, A. M. (1952). The chemical basis of morphogenesis. *Philosophical Transactions of the Royal Society B, 237*(641), 37–72.

van Lare, M. C., & Polman, A. (2015). Optimized scattering power spectral density of photovoltaic light-trapping patterns. *ACS Photonics, 2*(7), 822–831.

Varela, F. G., & Wiitanen, W. (1970). The optics of the compound eye of the honeybee (*Apis mellifera*). *The Journal of General Physiology, 55*(3), 336–358.

Vigneron, J. P., Rassart, M., Vertesy, Z., Kertesz, K., Sarrazin, M. L., Biro, L. P., Ertz, D., & Lousse, V. (2005). Optical structure and function of the white filamentary hair covering the edelweiss bracts. *Physical Review E, 71*(1), 011906.

Watson, G. S., Watson, J. A., & Cribb, B. W. (2017). Diversity of cuticular micro- and nano-structures on insects: Properties, functions, and potential applications. *Annual Review of Entomology, 62*(1), 185–205.

Wiersma, D. S. (2013). Disordered photonics. *Nature Photonics, 7*(3), 188–196.

Wilson, S. J., & Hutley, M. C. (1982). The optical properties of 'moth eye' antireflection surfaces. *Optica Acta, 29*(7), 993–1009.

Wisdom, K. M., Watson, J. A., Qu, X., Liu, F., Watson, G. S., & Chen, C.-H. (2013). Self-cleaning of superhydrophobic surfaces by self-propelled jumping condensate. *Proceedings of the National Academy of Sciences of the United States of America, 110*(20), 7992–7997.

Wood, L. (2017). *Global nano coating market (2016–2022): Increasing technological advancement is a key driver ─ research and markets*. http://www.researchandmarkets.com/research/sqcx6v/global_nano

Wu, W., Huang, J. Y., Jia, S. J., Kowalewski, T., Matyjaszewski, K., Pakula, T., Gitsas, A., & Floudas, G. (2005). Self-assembly of pODMA-b-ptBA-b-pODMA triblock copolymers in bulk and on surfaces. A quantitative SAXS/AFM comparison. *Langmuir, 21*(21), 9721–9727.

Xiao, S. G., Yang, X. M., Edwards, E. W., La, Y. H., & Nealey, P. F. (2005). Graphoepitaxy of cylinder-forming block copolymers for use as templates to pattern magnetic metal dot arrays. *Nanotechnology, 16*(7), 324–329.

Xin, Y., Jin, H., Feng, G., Hongjie, L., Laixi, S., Lianghong, Y., Xiaodong, J., Weidong, W., & Wanguo, Z. (2016). High power laser antireflection subwavelength grating on fused silica by colloidal lithography. *Journal of Physics D: Applied Physics, 49*(26), 265104.

Xue, F., Liu, J., Guo, L., Zhang, L., & Li, Q. (2015). Theoretical study on the bactericidal nature of nanopatterned surfaces. *Journal of Theoretical Biology, 385*, 1–7.

Yoon, J. W., Lee, K. J., & Magnusson, R. (2015). Ultra-sparse dielectric nanowire grids as wide-band reflectors and polarizers. *Optics Express, 23*(22), 28849–28856.

Yu, Y. F., Zhu, A. Y., Paniagua-Domínguez, R., Fu, Y. H., Luk'yanchuk, B., & Kuznetsov, A. I. (2015). High-transmission dielectric metasurface with 2p phase control at visible wavelengths. *Laser & Photonics Reviews, 9*(4), 412–418.

Zhou, L., Dong, X., Zhou, Y., Su, W., Chen, X., Zhu, Y., & Shen, S. (2015). Multiscale micro–nano nested structures: Engineered surface morphology for efficient light escaping in organic light-emitting diodes. *ACS Applied Materials & Interfaces, 7*(48), 26989–26998.

Chapter 3
Photonics in Nature: From Order to Disorder

Villads Egede Johansen, Olimpia Domitilla Onelli, Lisa Maria Steiner, and Silvia Vignolini

Abstract The most vibrant and striking colours in living organisms are often caused by a combination of pigments and nano-scale transparent architectures, which interact with light to produce so-called structural colours. These colours are the result of light interfering with the nano-scale structures that are present in the materials. Such colour-producing structures are not perfect, and irregularities in the arrangements (disorder) are present in many organisms. However, disorder in natural structures is not detrimental but functional, as it allows a broader range of optical effects. This chapter reviews and attempts to classify structurally coloured organisms, highlighting the influence that disorder has on their visual appearance. It also showcases how photonic systems, such as the blue *Morpho* butterfly and the white *Cyphochilus* beetle, are capable of obtaining optical properties (long-distance visibility and whiteness, respectively) where disorder seems to be highly optimized, indicating that disorder is important for obtaining complex visual effects in natural systems.

The chapter first introduces the mathematical concepts required for analysing disordered systems, such as the Fourier transform and the structure factor. Ordered and disordered natural photonic systems are then reviewed. This is followed by examples of completely disordered structures responsible for white appearances. Finally, we review the possibilities of hierarchical organisation and pixelated surfaces to widen the range of optical appearances.

3.1 Introduction

Structural colours are widespread in nature, where a large variety of nanoscale structures give rise to a myriad of fascinating optical responses. These are often a combination of complex nanostructuring and hierarchical organisation. During the last few decades, the understanding of these photonic nanostructures and their response has improved greatly, mainly due to the development of imaging

V. E. Johansen · O. D. Onelli · L. M. Steiner · S. Vignolini (✉)
Department of Chemistry, University of Cambridge, Cambridge, UK
e-mail: sv319@cam.ac.uk

techniques and numerical tools to model light interaction (Vukusic and Stavenga 2009; Vignolini et al. 2013).

So far, reviews about structural colours in nature have mainly focused on optical effects caused by interference of light from approximately periodic structures (Vukusic and Sambles 2003; Kinoshita et al. 2008; Seago et al. 2009), even though biological organisms are often inherently structurally disordered (Kinoshita and Yoshioka 2005). In fact, disorder can be a desired feature: specific optical appearances, such as angular independent colour response, silver or bright white diffuse appearances, rely on partially disordered or fully random structures, respectively (Prum and Torres 2003b; Vukusic et al. 2007; Mäthger et al. 2009).

The investigation of these photonic nanostructures can help to address many questions in biological research, both in terms of their function and taxonomy (Bálint et al. 2012). It can, for example, contribute to investigations in evolutionary biology, or assessing the health of populations (Parker 2000; Doucet and Meadows 2009).

Moreover, structural colouration can have different functions, such as a cue to pollinators or for seed dispersal in some plants (Whitney et al. 2009; Vignolini et al. 2012). In some cases, it might be for camouflage, while in others it might be used for attracting mates (Seago et al. 2009; Wilts et al. 2014a). The repertoire is manifold and many more studies are necessary to elucidate this interplay between structural colouration, function, and behaviour.

Even though the field of structural colouration has progressed enormously over the last two decades, quantitatively assessing the role of order and disorder in photonic structures is still challenging. In Sect. 3.2, we introduce common approaches to detect periodicity and discuss light coherence. Then, we consider ordered and quasi-ordered photonic structures, proceeding from 1D, via 2D to 3D in Sect. 3.3. We describe a few random natural photonic structures in Sect. 3.4. Finally, the complex interplay of order and disorder and colour mixing is described for hierarchical structures that are found at the surface of various organisms in Sect. 3.5.

3.2 Theoretical Background

Light interference is the phenomenon at the basis of structural colouration in nature. When dielectric materials are organised periodically in space at a distance comparable to the wavelength of visible light, constructive and destructive interference occurs, providing intense metallic colourations with a strong angle-dependent behaviour (iridescence). By scrambling the periodic organisation, it is possible to drastically change the optical response, ranging from weak iridescence to matt colouration with no angular dependence to bright whiteness. It is therefore important to introduce methods to quantify periodicity in natural photonic structures, as we will return to these key concepts multiple times throughout the chapter.

Light coherence is also discussed, since the coherence properties of sunlight influence the overall appearance of ordered and disordered nanostructures.

3.2.1 The Fourier Transform

Spatial periodicity can be quantified using the Fourier transform, which decomposes a function (most often a 1D profile or a 2D image) into its periodic components. The Fourier transform G of a function g in one dimension is given as

$$G(f) = \int_{\infty}^{-\infty} g(x) e^{-2\pi i x f} dx,$$

where f is the spatial frequency, x is the spatial dimension, and i is the imaginary unit (Lathi 1998). For processing datasets (e.g. images) on a computer, a discretised version of the Fourier transform is required, for which the most common approach is the Fast Fourier Transform (FFT). The FFT is available in most math-oriented modern computer languages, such as Matlab, Python (numpy), and R. As an example, Fig. 3.1 shows the FFT analysis of the refractive index profile of an ideal artificial multilayer structure and an experimental dataset. In both cases, the periodicity can be extracted by reading out peak positions. The clear differences between peak values and backgrounds for the two examples indicate ordered structures. No peaks would be observable for completely disordered structures.
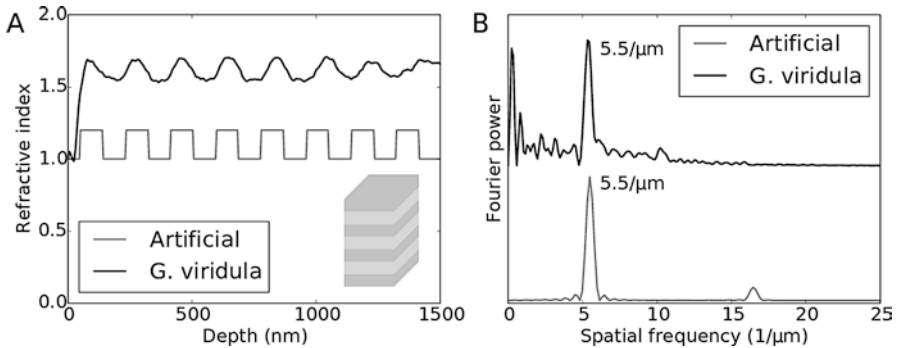
Fig. 3.1 (**a**) Refractive index profiles of an artificial ideal multilayer structure (see inset) and from the cuticle of a beetle (*Gastrophysa viridula*) extracted from Onelli et al. (2017). (**b**) Zero-padded FFT of the two profiles normalised to the peak intensity. The inverse values of the peak spatial frequencies reveal a periodicity of roughly 180 nm. Periodicities that are a multiple of the main frequency (so-called harmonics) will normally also be present, thus explaining the extra peaks observed in both spectra. The distinction between peak and background signal is weaker for *G. viridula* than for the artificial example, but still very clear. In general, a larger difference between peak and background indicates a more ordered structure

3.2.2 Structure Factor and Crystallography

Several other methods exist to detect periodicity. The mathematics behind the methods is generally similar to the Fourier transform in the sense that they also include integration or summation of complex exponentials.

In particular, the *structure factor* is useful to determine periodicity and correlations in two- and three-dimensional systems. For the structure factor, light is assumed incident from a specific direction on an ensemble of scattering elements that do not couple or shadow each other. In this configuration, the angularly resolved reflection or transmission of light is calculated based on information about the scattering elements and their positioning. The intensity of the structure factor I can be defined as

$$I\left(k_{\mathbf{i}}, k_{\mathbf{o}}\right) = \left| \sum_{j} f_{j}\left(k_{\mathbf{i}}, k_{\mathbf{o}}\right) e^{-i\left(k_{\mathbf{i}} - k_{\mathbf{o}}\right) \cdot r_{j}} \right|^{2},$$

where k_i, k_o are the vector incident and observation directions, respectively, scaled such that $|k_i| = |k_o| = 2\pi/\lambda$ where λ is the wavelength; r_j is the vector coordinate of the center of the j'th scatterer; i is the imaginary unit; and f_j describes the scattering intensity for the j'th scatterer.

If there is a periodic correlation of the distribution of scattering elements, this will show as strong reflection peaks at specific angles. A comparison between the structure factor for a periodic system and one with random perturbations is given in Fig. 3.2. A decrease in peak intensity is associated with a decrease in order, and the angular position can be calculated from the periodicity d through the grating equation (Johansen 2014)

$$d \sin \theta_{m} = m\lambda,$$

where λ is the wavelength of incident light, θ_m is the m'th reflection angle, and m is an integer known as the grating order and is calculated as the number of peaks from the specular reflection. For the example in Fig. 3.2, where $d = 2.5\lambda$, the peak locations for $m = 1, 2$ are $23.6°$ and $53.1°$ respectively. The methodology can be applied in several ways for assessing disorder.

Small/Wide-angle X-ray scattering (SAXS and WAXS) is used to investigate order-disorder properties experimentally (Noh et al. 2010). In this technique, the sample is illuminated by X-rays with a wavelength in the 0.1 nm range and transmission at different angles is recorded. As in Fig. 3.2, the peaks in the angle-resolved transmission spectrum can be associated with spatial correlation. The underlying theory is again very similar to that of the Fourier transform (Sellers et al. 2017).

Reflection from disordered surfaces can be predicted using the structure factor. More details on the theoretical background are given in Johansen (2014), and experimental validation and assessment of the quality of prediction are given in Johansen et al. (2015).
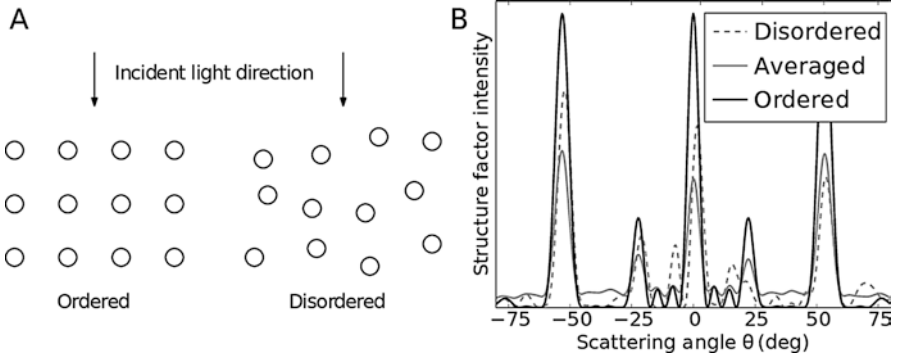
Fig. 3.2 (**a**) A strictly ordered system of 12 scatterers with $f_j = 1$ and a disordered system where the scatterers have been randomly displaced from their ordered lattice position. The lattice constant (separation) is 2.5λ. (**b**) Intensity of the structure factor with respect to angle calculated for the systems in (**a**). It is observed that for complete order (unbroken black), the response is confined to a few angles with very strong intensity. For the disordered realisation (dashed), the same peaks are present but with lower intensity, and a range of other peaks are seen. If such disordered samples are averaged over many random realisations taken from the same random distribution (unbroken grey), the effect is that the strong reflection angles are still present but less intense, with the remaining intensity almost evenly distributed in between

Structural analysis of scatterers can also be performed using the structure factor even if the scatterers couple and shadow each other, as long as the positions of the scatterers are known. In this case, the structure factor does not necessarily predict the optical response, but it works as a quantitative description of even advanced types of order/disorder relation such as hyperuniformity (Froufe-Pérez et al. 2016).

3.2.3 Light Coherence

Interference is caused by multiple reflections of light waves at interfaces between materials. The reflections can interfere constructively or destructively to promote an overall increase or decrease in reflection at specific wavelengths. For this effect to occur, it is essential that reflected waves are coherent.

Mathematically, light waves are considered perfectly coherent if they are perfectly sinusoidal. In reality, this is not the case, as every light source is only coherent over a certain distance. Sunlight, for example, can be considered the sum of (randomly occurring) spontaneous emissions from the surface of the sun. This means that the wave profile from the sun deviates from a perfect sinusoidal shape and can therefore be described as partially coherent or incoherent. The degree of temporal coherence is most commonly described by coherence time τ_c or coherence length l_c, which are related parameters. These parameters indicate the length (in time or space) that the sinusoidal wave shape is correlated above a certain degree. The coherence area A_c similarly describes the area where correlation is observed for an

illuminated surface (Wolf 2007; Hecht 2017). A small degree of correlation means that less intense interference effects can be observed for a given structure. For sunlight illumination, the coherence length is of the order of micrometers (Donges 1998) and the coherence area of the order of ∼4·10³ µm² (Wolf 2007; Divitt and Novotny 2015). The parameters vary depending on the environment (atmosphere, clouds, under water, etc.).

The degree of light coherence is rarely considered when analysing photonic structures. This is a valid approach if the photonic structures are small compared to the coherence parameters, since in this case light can be assumed coherent across the structures.

For larger structures, light cannot be considered coherent across the structure, but little is known about how this affects natural photonic structures and colouration. Bell et al. (2014) suggested that a locally ordered multilayer in a globally disordered arrangement makes the structural colour of the pyjama squid (*Sepioloidea lineolate*) unaffected by changes in light coherence properties, thus producing a consistent appearance in a changing underwater light environment. Dellieu et al. (2017) show how a structural colour system desaturates at short coherence lengths. The coherence area is also important for correctly predicting angle-resolved spectra from simulations, which would otherwise be dominated by strong, randomly located intensity fluctuations called speckle patterns. Saito and collaborators investigated this effect for a 2D natural photonic system, however the work has not been expanded since (Saito et al. 2011). It is therefore an area that deserves more attention as it may be an important factor for determining reflection and correlation properties in disordered natural photonic structures.

3.3 Ordered and Quasi-Ordered Photonic Structures

Most natural photonic structures are constituted by periodic arrangement of various materials on the nano- and micro-scale. We will start our discussion with one-dimensional structures and progress towards two- and three-dimensional ones.

3.3.1 One-Dimensional Photonic Structures

The simplest example of a one-dimensional (1D) photonic structure is a thin film of dielectric material in air. When light impinges on the film, the rays reflected at the two surfaces interfere with each other. Whether this results in a constructive or destructive interference depends on the wavelength and incident angle of the light, the thickness of the film, and the refractive index of the dielectric medium (Kinoshita et al. 2008).

By stacking multiple layers with different refractive indices, it is possible to obtain multiple reflections when light impinges on the various interfaces. This can
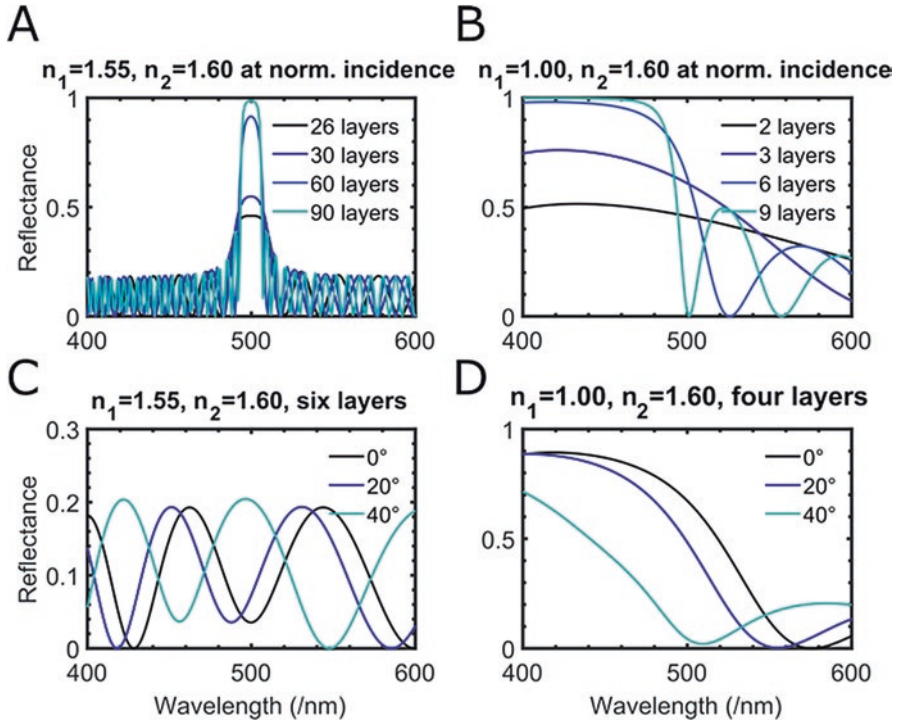
Fig. 3.3 Modelling of periodic multilayers in air based on Kinoshita (2008) and carried out using open source code (Byrnes 2016). (**a**) Increasing the number of layers (indicated in the legend) increases the reflectance. (**b**) The refractive index contrast between the layers is greater and therefore fewer layers are required to achieve a reflectance close to unity. The peak is now wider than in (**a**). (**c**) and (**d**) illustrate the phenomenon of iridescence (i.e. the peak wavelength depends on the angle of incidence of the incoming light). The thickness of layer 1 is 81 nm; the thickness of layer 2 is 78 nm. The spectra are normalised with respect to an ideal mirror of unit reflectivity. The two TE and TM polarisations are calculated separately and averaged to simulate unpolarised light.

enhance the reflection in a specific spectral region (Fig. 3.3). These structures are generally referred to as "Bragg stacks" or "Bragg reflectors". In particular, it can be shown that the condition for constructive interference in a two-material repetitive structure for incident light of wavelength λ is

$$2\left(n_A d_A \cos\theta_A + n_B d_B \cos\theta_B\right) = m\lambda,$$

where n_A and n_B are the refractive indices of the two layers of thicknesses d_A and d_B, respectively; θ_A and θ_B represent the refraction angles for each of those and m is an integer (Kinoshita et al. 2008). Figure 3.3 shows how the intensity of the reflected signal increases with the number of layers and how the response varies with the angle of incidence.

The most common multilayers in living organisms are made of pigments, usually melanin, arranged in layers alternating periodically (Land 1972; Noyes et al. 2007).

Natural systems are generally regarded as perfectly periodic; however, it should be pointed out that these systems always have a certain degree of disorder. For example, in Fig. 3.1 the multilayer of the *G. viridula* beetle shows an imperfect layer periodicity. Furthermore, the refractive index changes gradually between the layers rather than in abrupt steps, as it is often modelled. This and other imperfections can lead to a significant mismatch between experimental data and theoretical calculations.

3.3.1.1   Periodic Multilayers in Nature

Periodic multilayers have been reported in a number of species (Hunt et al. 2007; Del Río et al. 2016). They are extremely frequent in beetles (Coleoptera), in which this effect has long been known (see reviews by Land (1972) and Parker (1998)). Researchers have recently investigated this phenomenon numerically (Noyes et al. 2007; Stavenga et al. 2011b) and also in relation to external inputs, such as for example an increase in water content (Mouchet et al. 2016). *In vivo* imaging of the development of the layered cuticle was conducted too (Onelli et al. 2017). The study showed how the deposition of the layers takes place before the polymerisation of the melanin.

Reports of keratin-based multilayer reflectors in avian feathers are also numerous (Prum 2006; Nakamura et al. 2008; Stavenga et al. 2011a; Wilts et al. 2014a). Interestingly, in these systems, the structural colouration is particularly conspicuous (Fig. 3.4) and serves mating purposes as opposed to most arthropod reflectors, which are considered to have camouflaging purposes (Seago et al. 2009). Bragg reflectors in the underwater world have been comprehensively reviewed (Denton 1970). In the context of marine creatures, the refractive index contrast is provided by having anhydrous guanine crystals separated by cytoplasm, as shown in Fig. 3.4e–g (Gur et al. 2015). Guanine is highly birefringent, meaning that the refractive index of the crystals is different along the different axes. By arranging such crystals in different orientation, *Clupea harengus* (Atlantic herring) and *Sardina pilchardus* (European sardine) can reduce the polarising effect typical of multilayers to obtain a better camouflage whilst being able to reflect a large band of wavelengths (Jordan et al. 2012). Denton and Land (1971) also noted how the thickness of the layers was not perfectly periodic in the fish and cephalopods they investigated, which led to a lower peak intensity than in the ideal case. However, this also means that the reflectors appear silvery even for oblique incidence angles, which is the case for a fish illuminated by sunlight.

In the plant kingdom, many examples of multilayers can be found. Among land plants, the first multilayer example reported is the lycophyte *Selaginella willldeno-vii*. The optical response was first studied by Lowry and Lee (1975) and electron microscopy was later carried out by Hébant and Lee (1984) to confirm the existence of at least two layers atop the epidermal cells. Finally, the optical response was
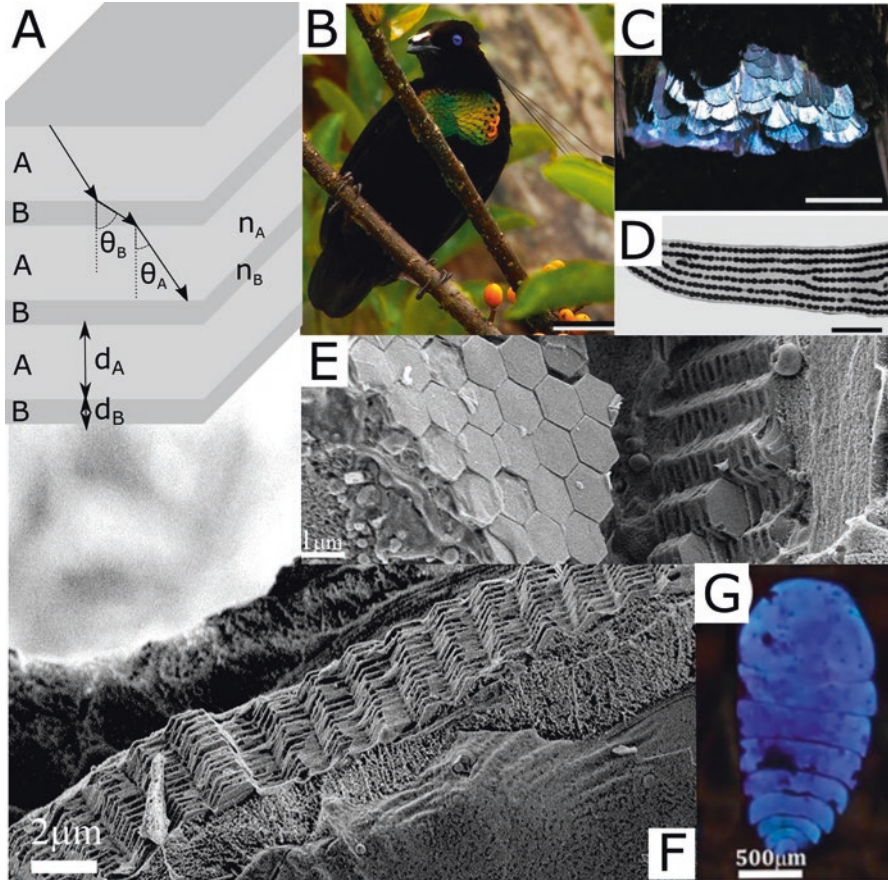
Fig. 3.4 (**a**) Scheme of a typical multilayer composed of two materials of refractive index n_A and n_B, respectively. (**b**, **c**, **d**) The bird of paradise *P. lawesii* (**b**; scale bar: 5 cm) and its mirror-like occipital feathers (**c**; scale bar: 1 cm) imaged with TEM (**d**; scale bar: 2 μm). Reproduced with permission from Wilts et al. (2014a). (**e**, **f**, **g**) Guanine multilayer giving rise to the blue colouration in *Sapphirina metallina* (Adapted with permission from Gur et al. (2015), copyright (2015) American Chemical Society)

thoroughly analysed by Thomas et al. (2010) who proved that the iridescent colouration is indeed caused by a multilayer in the cuticle. More examples of multilayers in plants leading to an iridescent appearance can be found, including *Trichomanes elegans*, *Phyllagathis rotundifolia*, *Begonia pavonina*, *Elaeocarpus angustifolius* and *Delarbrea michiana* (Glover and Whitney 2010).

More recently, Jacobs et al. (2016) found that thylakoid membranes in grana in iridoplasts in *Begonia pavonina* are arranged in multilayers, thus acting as photonic crystals, which enhance photosynthetic efficiency. This enhancement might be crucial in the extreme low-light conditions in the tropical forest understorey, and similar chloroplast structures have already been described in a phylogenetically diverse range of extreme shade dwelling plants.

In addition to those in the land plants, Bragg stacks are also found in some Rhodophyta (red algae). These algae display extracellular photonic nanostructures and have been recently analysed and reviewed (Chandler et al. 2017). For example, in the red alga *Chondrus crispus* the structural colouration is strongest at the tips of the frond, which constitute the youngest tissues (Chandler et al. 2015). The authors speculate that the loss of structural colour is due to the heterogeneity in the number and uniformity of the layers in the older parts of the alga. This is most probably due to the progressive deterioration and shedding of layers that are not regenerated, thus introducing disorder that suppresses the structural colouration.

3.3.1.2 Zig-Zag, Chirped, and Fractal Multilayers

Periodic structures typically reflect a narrow range of wavelengths. To achieve broadband reflectivity, it is necessary to vary the thickness (and/or the periodicity) of the layers in the stack so that a larger spectral range can be reflected efficiently. In the case of the beetles *Chrysina chrysagyrea* and *Anoplognathus parvulus*, the silvery colour originates from a chirped layering where the thickness of each layer decreases in the direction of light propagation (Parker 2005, Seago et al. 2009). A similar structure has been observed in the golden chrysalis of the butterfly *Euploea core* (Steinbrecht et al. 1985).

Another approach for obtaining a broadband silver reflection is the use of wavy multilayer reflectors as opposed to flat ones. This arrangement has been observed in the tissue surrounding the eyes of the squid *Loligo pealeii* (Mäthger et al. 2009).

In the blue-rayed limpet *Patella pellucida* co-oriented layers of calcite give rise to an intense blue reflection that is remarkably angle-independent (Li et al. 2015). The strong optical response is the result of the introduction of complexity in the system: the multilayer is folded into a zig-zag pattern and the growth of the calcite is anisotropic, leading to the formation of domains that have a different tilt with respect to the surrounding area. In addition, a completely disordered array of light-absorbing particles underneath the reflector attenuates the transmitted light, providing contrast to the reflected blue colour, even underwater, a strategy which is also known to occur in avian multilayers (Mason 1923).

Completely disordered (or chaotic) reflectors have been reported (Parker 2005), however more recent studies have found them to follow a fractal geometry (Bossard et al. 2016).

3.3.1.3 Helicoids

So far, we have mostly considered photonic stacks where the refractive index contrast between the layers is given by varying pigment content in alternating layers. Another strategy to produce bright colouration is to make helicoidal structures consisting of fibres arranged in birefringent layers (Middleton et al. 2017). In such structures, fibres lie parallel to each other in the plane, forming layers that are

stacked on top of the previous one with a small rotation angle, thus forming a helicoidal architecture. This rotating arrangement gives rise to constructive interference when

$$\lambda = 2np,$$

where λ is the wavelength of the reflected light, n is the average refractive index of the material, and p is the pitch of the stack. The pitch p is defined as the distance between fibrils that have the same orientation, i.e. after the stack has completed a 180° rotation. The refractive index of living tissues typically lies between 1.0 and 2.0, so the response from the layers will be in the visible range only if the pitch is comparable to the wavelength of visible light, as predicted by the equation above.

In nature, various organisms show such structures: in plants, helicoids are made of cellulose fibres in their cell wall (Fig. 3.5a), whilst beetles (Coleoptera) display helicoids of chitin fibres in their cuticle. It is worth noting that helicoids can be right- or left-handed, thus only reflecting right- or left-handed circularly polarised light. Figure 3.5b, c shows such a helicoidal stack, the height of the pitch p, and how circularly polarised light is transmitted or reflected, depending on the handedness.

In the plant kingdom, helicoidal arrangements are very common. However, in most cases the dimensions of the structure (the pitch p) are too large for interaction with visible light, thus producing no optical response.

Various plants from the ferns, monocots and dicots exhibit structural colouration caused by cellulose-based helicoidal structures. Among the ferns, the helicoidal cellulose arrangement of the fibres was first observed in the neotropical fern *Danaea nodosa*, via TEM (Graham et al. 1993). Interestingly, only juvenile leaves show the iridescent blue appearance. Adult leaves are green, and they exhibit considerably fewer and much less regular layers of helicoidal cellulose layers.

The same type of structure was observed in the Malaysian rainforest understorey plants *Lindsaea lucida* and *Diplazium tomentosum*, and characterised by spectroscopy and electron microscopy (Gould and Lee 1996). The helicoidal arrangement of fibres is responsible for the blue, left-handed circularly polarised reflection.
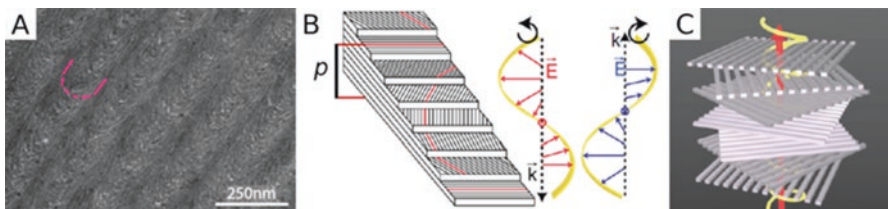
Fig. 3.5 (**a**) TEM of the helicoidal cellulose structure in the epicarp cell wall of *Pollia condensata*. The red lines correspond to the twisting direction of the cellulose fibres. (**b**) Scheme showing a wedge of a left-handed helicoid with the arched pattern exposed on the oblique face, showing the height of pitch p (left). Beams of circularly polarised light (right). (**c**) Scheme of a cellulose helicoid and a beam of transmitted circularly polarised light ((**a**) and (**c**) reproduced with permission from Vignolini et al. (2012). (**b**) adapted with permission from Wilts et al. (2014b))
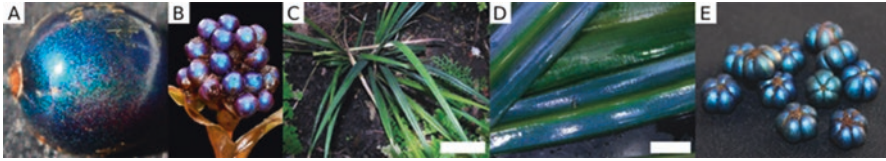
Fig. 3.6 (**a**, **b**) *Pollia condensata:* single dried fruit (**a**) and infructescence (cluster of fruits) from alcohol-preserved specimen (**b**); the diameter of each single fruit is about 5 mm. (**c**, **d**) *Mapania caudata*: young plants growing in shade (**c**; scale bar: 5 cm) and edge of leaf to midrib (**d**; scale bar: 1 cm). (E) Fresh fruits of *Margaritaria nobilis*. Diameter of each fruit is about 1 cm ((**a**, **b**) reproduced with permission from Vignolini et al. (2012). (**c**, **d**) reproduced with permission from Strout et al. (2013). (**e**) reproduced from Vignolini et al. (2016) licensed under CC-BY version 4.0))

Among the monocots, the fruit of the pantropical and warm-temperate perennial *Pollia condensata* (Fig. 3.6a, b), in contrast to the previous examples, shows both left-handed and right-handed circular polarised reflection. It is the only example of tissue in nature where helicoids of both handedntesses are found (Vignolini et al. 2012). The epicarp contains three to four layers of cells with very thick cell walls that exhibit the helicoidal arrangement of cellulose fibres (Fig. 3.5a).

Another monocot reported in the literature is the tropical rainforest understorey sedge *Mapania caudata*, which only shows reflection of left-handed polarised light. It exhibits blue structural colour (Fig. 3.6c, d) caused not only by the helicoidal cellulose arrangement in the adaxial epidermal cell wall, but also by the inclusion of silica granules into the cellulose layering (Strout et al. 2013).

In the class of dicots, the earliest report of helicoidal structures in plants is the work of Lee (1991) on the fruit of the rainforest tree *Elaeocarpus angustifolius*. However, these findings are not confirmed, since the reported electron micrographs showing the layering cannot resolve the cellulose fibres.

Finally, beautiful blue structural colour was also observed in the fruit of the dicot *Margaritaria nobilis* (Fig. 3.6e) (Vignolini et al. 2016). Interestingly, the hydrated fruits exhibit metallic blue appearance but, upon drying, they turn pearlescent white. This effect is reversible and can be understood by changes in the ultrastructure that facilitates light absorption when hydrated.

In summary, there are still many plants with helicoidal cellulose fibre arrangements in their cell walls that have not yet been characterised. To our knowledge, researchers have not tried to assess the degree of disorder in these structures.

Helicoidal chitin-based photonic structures have been observed in a number of beetle species (Coleoptera). Generally, such helicoids are responsible for the left-handed circularly polarised coloration of the beetles (Sharma et al. 2009). However, a few notable exceptions have been reported in which the cuticle can reflect both right- and left-handed light, such as *Chrisina resplendens* and *Chrisina boucardi* (Jewell et al. 2007) (note that both species used to belong to the genus *Plusiotis*, which has been placed into synonymy under the older name, *Chrysina*, in 2001 (Arwin et al. 2012)). The physical explanation underpinning this phenomenon created disagreement for half a century (Michelson 1911; Rayleigh 1919; Neville
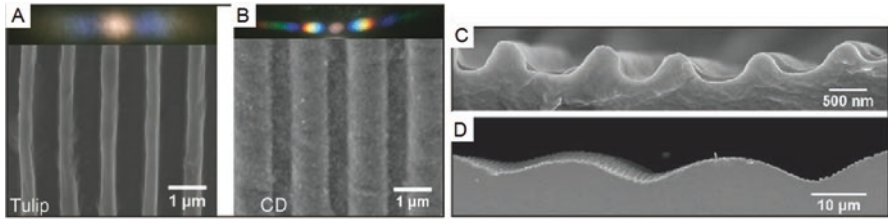
Fig. 3.7 (**a**) Top view of an epoxy cast of the tulip *T. kolpakowskiana*, showing striations resembling a line grating. Insert: the optical appearance of the flower in transmission under normal incident illumination. (**b**) Top view of an epoxy cast of a disassembled CD. The insert shows how similar the reflection properties of a CD are in comparison to the surface of the flower. (**c**, **d**) Cross-sectional views of the flower striations from (**a**), showing the disordered arrangement of the individual scattering elements. The individual elements are arranged in a hierarchical manner on a structure with much larger undulations. Both hierarchical levels influence the appearance (Figure reprinted with permission from Whitney et al. (2009))

and Caveney 1969). Nowadays, the widely accepted interpretation is that the effect originates from the presence of a birefringent anisotropic layer between two left-handed helicoids, which acts as a half-wave phase retarder: left-handed light is reflected by the first helicoid, while right-handed light, transmitted through to the retarding layer, changes its polarisation from right to left and impinges on the second helicoid. At this point, the light (being left-handed polarised) is reflected and transmitted through the plate, which changes its polarisation back. Right-handed light is transmitted by the first helicoid, providing the additional right-handed reflected polarisation (Caveney 1971; Hwang et al. 2005).

3.3.1.4 Diffraction Gratings

Gratings are periodic surface undulations that give rise to strong angle-dependent light reflection when the feature sizes are comparable to the wavelength of light. The visual effect from a grating is generally experienced as an abrupt change of colour with respect to viewing angle. A well-known example is the compact disc (CD), see Fig. 3.7b, where data is stored between periodically spaced grooves that constitute a diffraction grating.

Gratings in nature were first reported in a scarab beetle in 1942, observed via electron microscopy (Anderson and Richards 1942), and have found to be remarkably widespread in insects from the order Coleoptera. Not much attention has been given to understanding the role of disorder in these structures, even though there seems to be a wide diversity of arrangements. Whether the biological significance of the gratings is the optical function or not (it might for example be to reduce friction) is still not understood (Seago et al. 2009).

As seen in Fig. 3.7, disordered grating-like structures have also been found in flower petals (Whitney et al. 2009). While the development of these structures is still not understood (Vignolini et al. 2013), their function seems important for plant-

pollinator signalling (Whitney et al. 2009; Vignolini et al. 2015a, b). The effect of the iridescence is hard to assess due to the subtle effect of the grating compared to pigmentation underneath, and many open questions remain (van der Kooi et al. 2014, 2015).

3.3.2 Two-Dimensional Photonic Structures

In a two-dimensional (2D) photonic structure, the scattering elements vary in two dimensions while being invariant in the third one (Fig. 3.8a). If the structural variations are periodic, such as in Fig. 3.8a, the system is referred to as a photonic crystal. These photonic crystals give a specular reflection, but will also produce diffraction at a few discrete angles as exemplified in Fig. 3.2b, producing a glittering appearance that cannot be observed in one-dimensional multilayers (Fig. 3.9a).

The best known example of structural colour from a 2D structure is possibly the vivid appearance of peacock feathers (Zi et al. 2003), which originates from a regular packing of melanin rods and air channels in a keratin network that lies parallel to the surface of the barbule. Other examples of 2D regular and irregular packing with vastly different appearances are found in avian feathers (Prum et al. 1998), mammalian eyes and marine creatures (Starkey and Vukusic 2013). More recently, 2D photonic structures have also been observed in bacterial colonies (Fig. 3.9) (Kientz et al. 2016).

3.3.2.1 Modelling of Photonic Structures

Reflection maxima from periodic photonic structures (in two and three dimensions) can be computed by a so-called bandgap analysis using the open source tool MIT Photonic Bands (MPB) by the Massachusetts Institute of Technology (Johnson and Joannopoulos 2001) or commercially available software by Comsol or Lumerical.
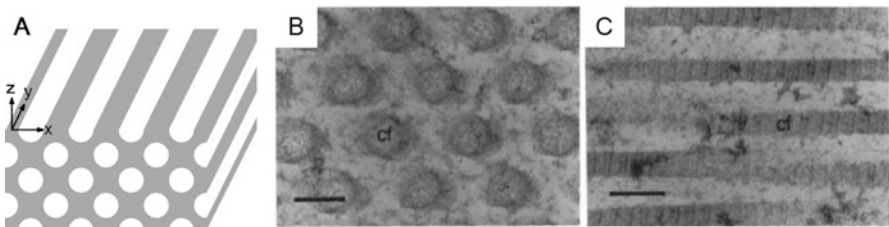
Fig. 3.8 (**a**) Scheme of a photonic crystal with a structure that is periodic in the *xz*-plane and invariant in the *y*-direction. (**b**) TEM of a cross-section of an array of collagen fibrils found in the structure around the eyes of the velvet asity (*Philepitta castanea*). Scale bar: 100 nm. (**c**) TEM of the longitudinal section of the collagen fibrils (with the distinct banding pattern being typical for collagen). Scale bar: 200 nm (Figure reproduced with permission from Prum et al. (1994))
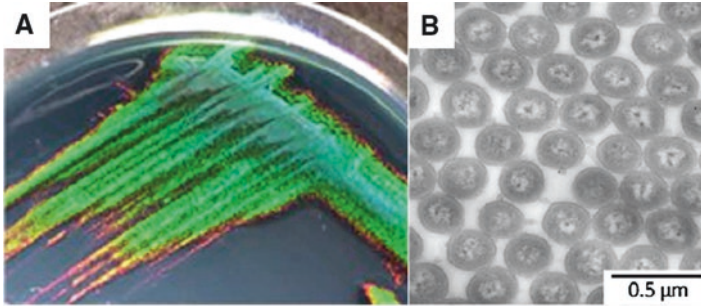
Fig. 3.9 The colourful appearance of a bacteria colony of *Cellulophaga lytica* (**a**) is caused by the rod-shaped bacteria packing in a roughly hexagonal photonic crystal arrangement as seen in (**b**). The effect is yet to be observed in a natural environment, but readily reproduced in the lab (Kientz et al. 2016) (Images from Kientz et al. (2016))

Such investigations provide a band diagram that indicates which wavelengths can be expected to be fully reflected (Eliason and Shawkey 2012). Even though this method does not provide the full spectral response, it provides a quick way to gain insight into a complex problem, and it constitutes a good starting point for understanding the optical response of a structure (Parker et al. 2001; Zi et al. 2003; Eliason and Shawkey 2012). More details on photonic crystals can be found in the book by Joannopoulos et al. (2008), which is freely available online from the authors, and also in Yablonovitch (1993).

In order to fully describe the optical response from nanostructures (ordered or disordered), a full wave electromagnetic solver is needed. A review of approaches deserves a chapter on its own, but it is worth mentioning that the Finite Difference Time Domain (FDTD) method is very popular within structural colour research, see for example Wilts et al. (2014a). The most popular tools are the open source software MIT Electromagnetic Equation Propagation (MEEP) (Oskooi et al. 2010) and the commercial software Lumerical FDTD.

3.3.2.2 Analysing Order and Disorder in 2D Structures

The effect of disorder in 2D natural photonic structures was first investigated in the structure surrounding the eye of the velvet asity *Philepitta castanea* (Fig. 3.10c) (Prum et al. 1994). The structure consists of a 2D array of collagen fibres as seen in Fig. 3.8b, c. In this work, the authors conclude that even if the system lacks perfect ordering, it is still capable of supporting constructive and destructive interference, as also demonstrated in Benedek (1971), due to correlation in the structure factor (see Sect. 3.2).

Since 2D structures are invariant in the third direction, a cross-sectional image of the material is adequate to assess the degree of disorder of the entire structure. Fourier transformation (Sect. 3.2) of cross-sectional electron microscope images (e.g. Fig. 3.8b) is therefore a good method to reveal the fundamental level of

periodicity in the structure. The approach was introduced (Prum et al. 1998) and further developed in the following decade by Prum and co-workers (Prum et al. 1999, Prum and Torres 2003a, b, 2013) and recently employed by other groups (Jordan et al. 2016).

The interplay between order and disorder in 2D photonic structures in birds is elucidated by Prum and Torres (2003b), who characterised an impressive number of species, showing a great diversity of optical effects (Fig. 3.10). The spectral responses were roughly estimated from the Fourier transform as well, whereas nowadays a better correlation can be obtained from the methods in Sect. 3.3.2.1. An interesting observation from the FFT spectra in Fig. 3.10g, h is the rotational symmetry. This implies that the periodicity of the system is the same in all directions perpendicular to the rods, which leads to decreased iridescence, and to an appear-
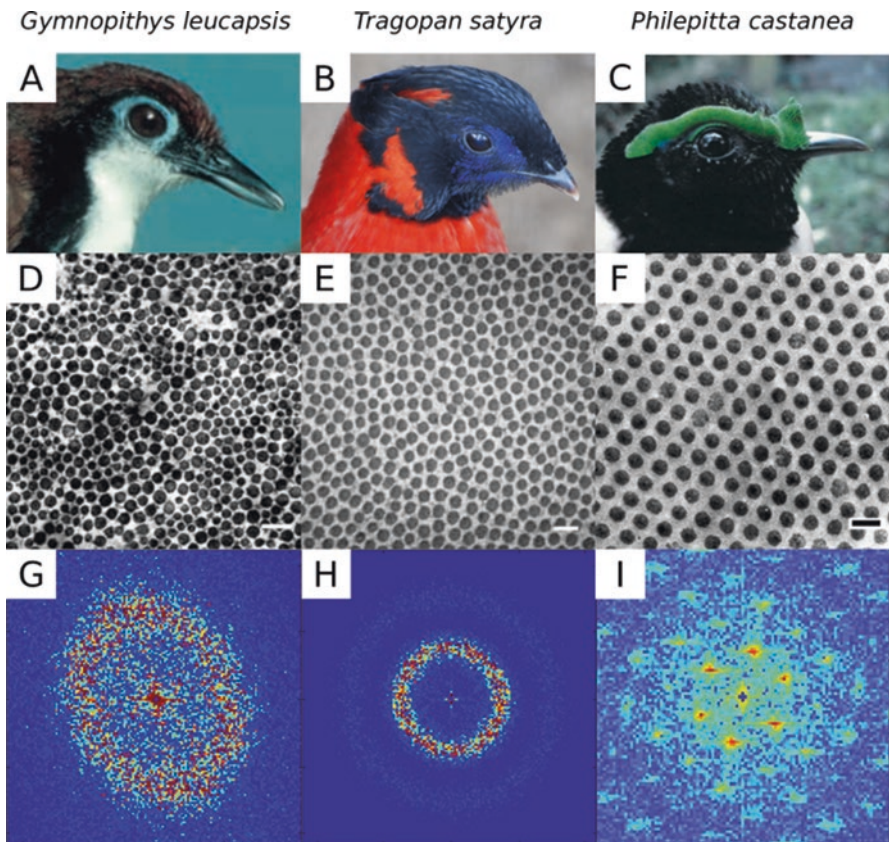
Fig. 3.10 (**a**, **b**, **c**) Photographs of three different avian species, whose feathers show photonic properties. (**d**, **e**, **f**) Electron micrograph of the 2D photonic arrangements found in the feathers. Scale bar: 200 nm. (**g**, **h**, **i**) Fast Fourier Transforms of the electron microscopy images in (**d**, **e**, **f**). The axis of the plots are all spanning −0.2 to 0.2 nm^{-1} (Images reproduced with permission from the author (Prum and Torres 2003b) apart from (**b**) from Wikimedia Commons (2008))

ance that will have the same reflection properties regardless of in-plane rotation. In contrast, the FFT in Fig. 3.10i shows a hexagonal pattern with clear spots, indicating direction dependence and a higher level of order, leading to a more angular dependent response. Such differences are hard to observe visually, since the overall optical appearance is affected by other factors such as pigmentation and feather orientation. The isolated photonic crystal response can, however, still be observed in small areas (Noh et al. 2010).

As an alternative to Fourier analysis for the investigation of disorder, Delaunay triangulation was used to determine centre-to-centre distances between inclusions in the *Pherusa* worm (Trzeciak and Vukusic 2009). This method provides additional statistical information about the relation between order and disorder in 2D natural photonic structures and can be more accessible for quantitative comparison than the Fourier transformed images. The approach is also used in Kientz et al. (2016) to assess the organisation of the bacteria colonies shown in Fig. 3.9.

By comparing the different examples presented in this section, it seems that for 2D photonic structures, disorder is not just an unavoidable feature in nature's photonic systems, but is used to control the optical response of the organisms.

3.3.2.3   Diatoms

A huge variety of photonic structures are found in the bio-mineralised silica cell wall of diatoms (Fig. 3.11) (Sumper and Brunner 2006); here we classify them as 2D structures but, as we will see, some species can be considered three-dimensional. However, it is important to highlight that this categorisation is debatable as the photonic properties of diatoms might be a concomitant effect of their geometry and ultrastructures (Noyes et al. 2008).
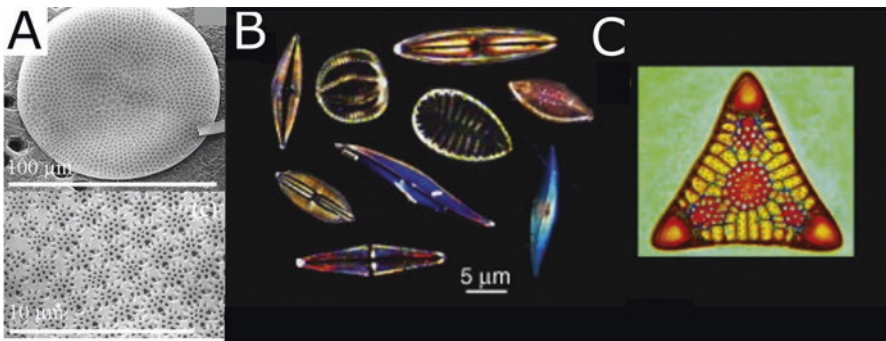
Fig. 3.11 (**a**) Scanning electron microscope images of the inner (top) and outer (bottom) valve of *C. wailesii*. (**b**) Micrographs of several pennate diatom species that show photonic properties. (**c**) Digitally enhanced Jamin-Lebedeff light microscopy image of the marine centric diatom fossil *Triceratium morlandii*. Cell width 120 mm ((**a**) adapted from De Tommasi et al. (2010), The Optical Society. (**b**) and (**c**) reprinted with permission from Elsevier, copyright (2009) (Gordon et al. 2009))

In 2004 it was reported that the pores on the surface of the cell wall of *Coscinodiscus granii* act as a photonic crystal, selectively enhancing the transport of light towards the chloroplasts in the cell (Fuhrmann et al. 2004).

However, De Tommasi et al. (2010) later suggested that, for a similar species, *Coscinodiscus wailesii*, the nano-structured silica contributes to light diffraction. Numerical modelling showed how light is selectively confined within the edges of the pores according to its wavelength. The same species of diatoms was studied by Kieu and co-workers (Kieu et al. 2014), who further investigated the role of the position of the pores. In fact, due to the imperfect periodicity of the pattern, the photonic structure in this system was defined as "quasi periodic" (Kieu et al. 2014).

Assessing disorder in diatoms' photonic structures can be challenging, however both Fourier analysis and X-ray diffraction experiments have been carried out (Almeida and Fujii 1979; Yun et al. 1987). In the first study, the Fourier analysis was used to distinguish various species of diatoms for taxonomic purposes. The latter study was, instead, one of the first reports of X-ray diffraction measured in a microscopic, biological specimen.

3.3.3   Three-Dimensional Photonic Structures

Disentangling the roles that order and disorder play in three-dimensional (3D) architectures is extremely challenging because sophisticated 3D tomography methods, such as 3D X-ray and electron tomography, are necessary to investigate the architectures (Noh et al. 2010). Hence, three-dimensional structures are typically approximated by a unit cell, which is repeated periodically to form a highly ordered stack. As in 1D and 2D structures, when the periodicity of a 3D photonic crystal is comparable to the wavelength of visible light, only certain wavelengths will be reflected. Thus, 3D photonic structures can give rise to brilliant colours, which vary depending on the orientation of the photonic crystal with respect to the angle of incidence of light. The analysis tools to investigate these structures are analogous to the ones presented in Sect. 3.3.2.1.

3.3.3.1   Polycrystalline Structures

In nature, such 3D structures are typically polycrystalline – meaning that the photonic structure is composed of a number of smaller crystallites (Seago et al. 2009). Each of the crystallites can be approximated to a perfectly repeating lattice, but the grains themselves can have different sizes and orientations. Hence, a polycrystalline structure has a high degree of order within each domain but no correlation between the domains, causing colour desaturation and a more angle-independent response. This may provide an evolutionary advantage due to a more consistent colour for signalling and camouflage (Michielsen and Stavenga 2008).

In nature, diamond-like 3D photonic structures have been observed inside the iridescent scales of the weevils *Lamprocyphus augustus* (Galusha et al. 2008) and *Entimus imperialis* (Wilts et al. 2012b). In both cases, micron-size domains which are differently oriented guarantee an almost entirely angle-independent optical response.

In 1970 Alan Shoen, an engineer at NASA, discovered a 3D periodic structure, based on the mathematical concept of minimal surfaces, that he named *gyroid* (Schoen 1970). This structure is composed of two distinct networks intertwined: one shows a sixfold geometry while the other is tetrahedral. Given the complexity and abstract nature of this crystal, the discovery of its occurrence in the cuticular structures of the lycaenid and papilionid butterflies is truly fascinating (Michielsen and Stavenga 2008). Later, similar structures have been found responsible for the optical responses in various species such as *Callophrys rubi* (Michielsen et al. 2010; Schröder-Turk et al. 2011), *Cyanophrys remus*, *Parides sesostris* (Wilts et al. 2012a), and *Thecla opisena* (Wilts et al. 2017b). Just like in the case of the weevils, the crystalline structure is constituted of multiple domains with variable size and orientation as shown in Fig. 3.12. In fact, the absence of circularly polarised reflection (expected due to the inherent chirality of the gyroid network) in the wing of *C. rubi* and *Teinopalpus imperialis* has been attributed to disorder (Saba et al. 2014).
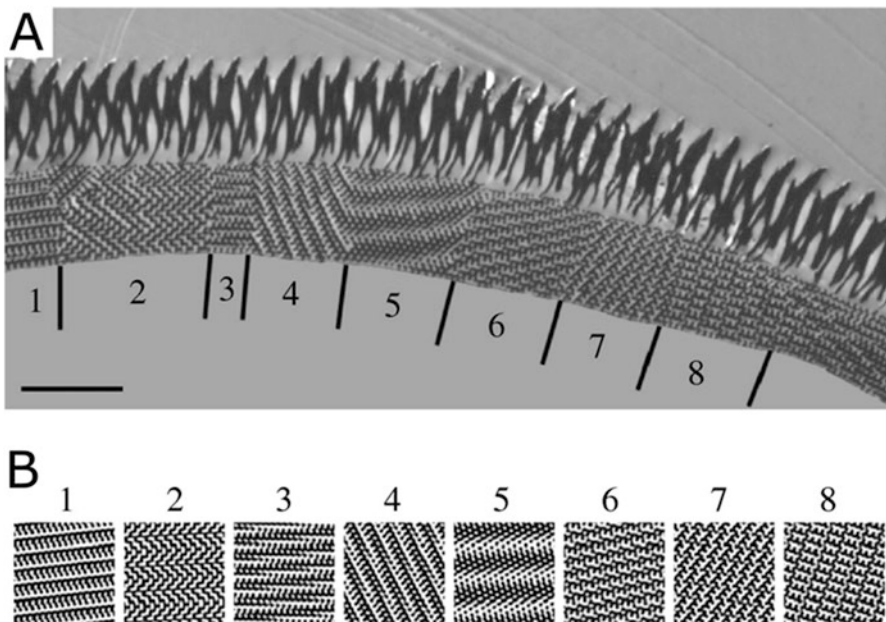
Fig. 3.12 (**a**) Cross-sectional view through the scale of *P. sesostris*. The numbers indicate the different domains in the cuticular crystal. The grain boundaries are indicated by vertical lines. Scale bar: 2.5 μm. (**b**) Projections of domains modelled computationally (Image reproduced from Michielsen and Stavenga (2008) licensed under CC-BY version 4.0)
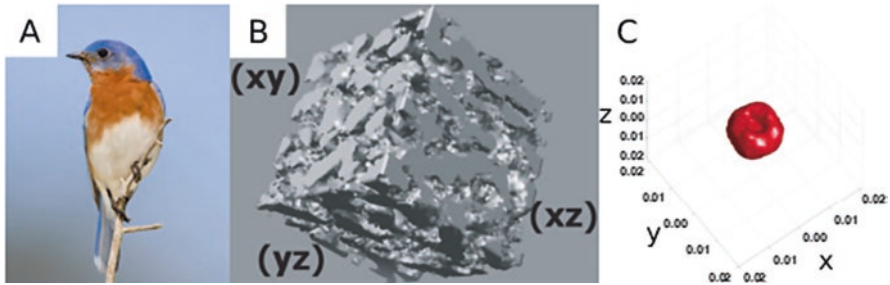
Fig. 3.13 (**a**) The eastern bluebird *S. sialis*. (**b**) 3D reconstruction of the keratin structure in the feathers. (**c**) 3D Fourier transform of the keratin structure. The doughnut shape reveals that the material is distributed periodically just like in Fig. 3.10g, h. This periodicity causes the blue colouration (Figure reproduced with permission from Shawkey et al. (2009) and Wikimedia Commons (2010))

3.3.3.2 Short-Range Ordered Structures

Even in the absence of long-range ordering, structural colours can be generated if short-range periodicity is present. The colouration is much more diffuse in this case as reported and studied in detail in the beetle *Anoplophora graafi* (Dong et al. 2010). Another example of colour produced by short-range order is the complex keratin network in the blue feathers of the eastern bluebird *S. sialis* (Fig. 3.13a) (Shawkey et al. 2009). A 3D reconstruction of the tissue was obtained by electron tomography, and a subsequent Fourier transformation revealed a periodic arrangement of the material for the reconstructed model (Fig. 3.13b, c).

Another way of probing complex networks is by small-angle X-ray scattering (SAXS), see Sect. 3.1. The method has been used to analyse bird feather barbs (Noh et al. 2010) as well as the wing scales of the butterfly *C. gryneus* (Sellers et al. 2017).

3.4 Random Photonic Structures

Light propagating through a completely disordered structure is scattered multiple times and exits the medium in random directions, thus giving a white, diffuse colouration (Wiersma 2013). We can understand this phenomenon by considering each inhomogeneity in the medium's refractive index as a scattering centre: when light impinges upon one of these obstacles, it is scattered at a random angle and propagates until another collision occurs (Fig. 3.14a).

Natural random media can be extremely difficult to study and model, as the knowledge of their 3D morphology is challenging to obtain. However, the understanding of these systems is growing with availability of advanced tomography techniques, such as focused ion beam (FIB) milling and high resolution X-ray
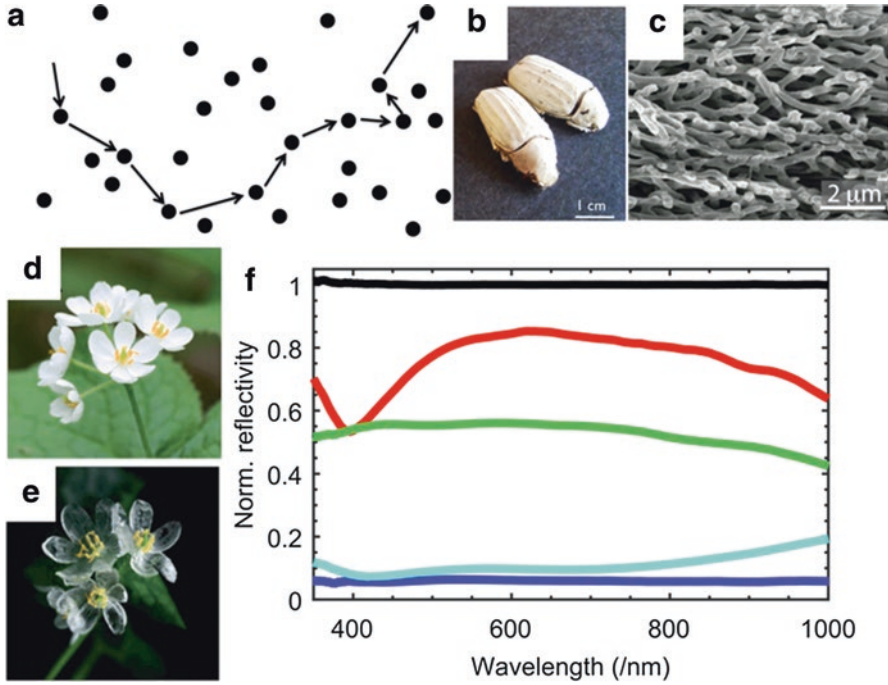
Fig. 3.14 (**a**) Light (represented by the arrow) is scattered multiple times by an inhomogeneous, complex medium (black dots). (**b**) *Cyphochilus* beetles with their chitin network shown in (**c**). Reproduced from Burresi et al. (2014) licensed under CC BY 4.0. (**d**, **e**) Petals of *Diphylleia grayi* in sunlight and in the rain, respectively (Reproduced from Yong et al. (2015) with permission from The Royal Society of Chemistry). (**f**) The reflectivity of various white materials compared to the white beetle *Cyphochilus* (red line). The green line corresponds to common filter paper (Whatman ®), the light blue to the hair of a polar bear (*Ursus maritimus*) and the dark blue to a transparent glass slide. The reflectivity was normalised with respect to a standard diffuser (black line). The numerical aperture of the microscope objective was 0.95

tomography that provide the required nm-resolution in three dimensions (Wilts et al. 2017a).

The scattering strength of a standard diffusive material can be quantified by the average step length between the collisions. This quantity is known as the *scattering mean free path* and is used to compare the whiteness in different materials: a short mean free path implies that the scattering is very efficient, giving a whiter appearance. In fact, a long step length (i.e. the scatterers are inefficient) implies that light is mostly unperturbed by the structure, leading to a transparent appearance of the material.

The scattering mean free path depends on three key parameters (Toninelli 2007):

1. The size and shape of the scatterers. By comparing the dimensions of the scatterers with respect to the light wavelength, we can identify different scattering regimes (Akkermans and Montambaux 2007). Intuitively, we see that if the

obstacles are very small (i.e. much smaller than the wavelength of the incident light), light does not interact with them but propagates as if the medium was homogeneous. Similarly, if the scattering centres are much larger than the wavelength, the medium appears homogeneous, and light propagates through it as in a bulk material.

2. The packing and density of the scatterers (or filling fraction). For efficient light scattering materials, the density of the scattering elements needs to be optimised. When the density of the scatterers is very low, the probability of having a scattering event decreases, making the material inefficient for scattering. However, if the density of the scatterers is too high, scattering from individual elements decreases as a consequence of the presence of others. This effect is known as optical crowding.

3. The refractive index ratio between the propagation medium and the scattering centres. If the difference between these two quantities is large, light is scattered more efficiently. On the other hand, if the two refractive indices are similar, the medium is effectively uniform.

3.4.1 *Refractive Index Matching:* Diphylleia grayi

The flower petals of the small herb *Diphylleia grayi* are white in dry weather. The numerous lacunae in between the cells on the petals are filled with air: the difference in refractive index between the two media causes light to be scattered and therefore produces a white colouration (Yong et al. 2015).

However, if it rains, the air gaps fill with water, whose refractive index is very similar to the one of cells. The petals become a uniform medium and light can propagate through them almost undeflected, giving a transparent appearance (Fig. 3.14d, e).

3.4.2 *The Whitest Natural Material: The* Cyphochilus *Genus*

Whiteness increases when there are a large number of scattering events. Thus, whiteness increases with thickness. In general, white materials are relatively thick, of the order of millimetres or larger. In the case of *Diphylleia grayi*, the scattering events are probably not very efficient, however the tissue is thick enough to provide a white response. Similarly, polar bear (*Ursus maritimus*) hairs appear white not because the scattering events are particularly efficient (each hair is only slightly more reflective than glass, Fig. 3.14f) but because the overall fur is composed of numerous hairs that are arranged in layers. White paper is in comparison much more reflective than a single hair (Fig. 3.14f).

However, some organisms have extremely well optimised whiteness. The scales of the beetle genus *Cyphochilus* show a brilliant white colouration whilst only being 5–7 μm thick (Fig. 3.14b, c). This makes them the whitest natural material known to date. The discovery was first reported in Vukusic et al. (2007) and it has been speculated that the white appearance helps the beetle camouflage amongst white fungi. Since then, many research groups have tried to explain how the *Cyphochilus* achieves such performance given that the biological material involved has a low refractive index and is therefore not well adapted for optimal whiteness. In fact, the scales are made up of long filaments of chitin, a long chain polysaccharide with a refractive index around 1.55–1.56.

By comparing *Cyphochilus* scales to other white beetles whose scattering efficiency is lower (*Lepidiota stigma* and *Calothyrza margaritifera*), it was observed that in all cases the filling fraction (i.e. the amount of chitin versus the amount of air) is optimised for scattering, but in *Cyphochilus* the scattering centres' spacing and diameters are particularly adapted to this function (Luke et al. 2010).

Time-resolved measurements confirmed that light is, indeed, scattered multiple times as it propagates through the scales (Burresi et al. 2014). The flux of photons through the scales was measured as a function of time elapsed from the illumination of the sample. This showed a significant time delay as compared to the time expected for light propagating ballistically (i.e. without being scattered). Later work demonstrated that the anisotropy of the chitin rod distribution was also important in the optical response (Cortese et al. 2015). In fact, the high filling fraction of the scales implies that some degree of angular correlation has to be introduced. In Fig. 3.14c it is possible to see such anisotropy as the chitin filaments are mostly distributed with a planar orientation.

Further measurements on *Cyphochilus insulanus* confirmed that the cuticle also shows a low degree of polarisation and gloss, which is a desirable characteristic in a camouflaging material (Åkerlind et al. 2015).

3.5 Hierarchical Structures at the Surface

So far we have described structures on a scale comparable to the wavelength of light. However, the reflection properties can also depend on the hierarchical ordering of photonic elements on a larger scale and how these are distributed across a surface. In this section, two (among many) very different types of disorder on a meso- and macro-scopic scale are described to exemplify the importance of hierarchical organisation for photonic properties and how disorder also plays a role here, namely diffractive surfaces and pixellated surfaces.

3.5.1   Diffractive Surfaces on the **Morpho** *Butterfly Wings*

The interplay between order and disorder in the photonic structures presented in the previous sections can be used to obtain different optical effects ranging from strong iridescence to matt, diffuse colouration. However, even by varying the degree of order in these photonic materials, little freedom is provided to fully design the angular response of reflected light. This limitation can be overcome by hierarchically structuring the surface of the photonic material. The most well-known example is found in the scales of the *Morpho* butterfly.

3.5.1.1   Wing Structure and Appearance

The most studied structural colouration strategy in nature is probably the one in the scales of several species of the *Morpho* butterfly, whose reflection properties were first quantified in 1999 (Vukusic et al. 1999). The colouration is mainly due to the distribution of long ridges of Christmas-tree-like structures on the wing scales (Fig. 3.15). The nanostructuring of the ridges provides a colour reflection similar to a standard multilayer structure (see Sect. 3.3.1). Several other features, such as multiple layers of scales, scale tilt angles, and an absorbing background also influence the striking visual appearance of the butterfly (Ingram and Parker 2008; Kinoshita et al. 2008; Giraldo et al. 2016). Vukusic et al. (1999) noticed that the reflection from the *Morpho* scales extended its blue colour roughly 100° along the longest direction and 15° along the shortest under normal illumination. This is illustrated by the elliptical shape in Fig. 3.16b. Such controlled reflectance properties are generally not easy to obtain.
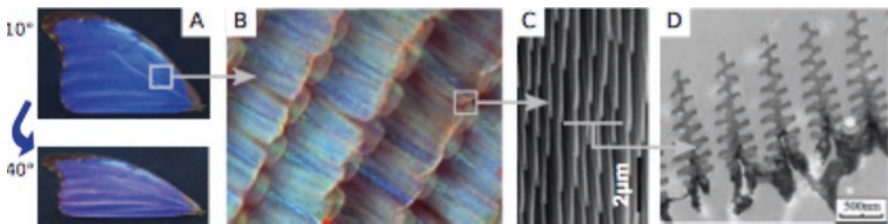
Fig. 3.15 Hierarchical structuring on a *Morpho didius* wing. The ordering is typical for several *Morpho* species. (**a**) Image of the wing from two different angles, showing iridescence caused by the structural colouration. (**b**) Optical microscopy of the wing scales. The blue scales are covered by transparent scales. (**c**) Top view of nanostructured ridges present on the blue scales. (**d**) Cross-sectional view of the ridges in (**c**), which are responsible for colour selectivity ((**a**, **c**) reproduced with permission from the author (Saito et al. 2013). (**b**, **d**) reprinted with permission from Elsevier from Jiang et al. (2014))

3.5.1.2 Hierarchical Organisation

The physical mechanism behind the *Morpho* colouration was proposed by Kinoshita et al. (2002) to mainly rely on multilayer interference and the height difference between the individual ridges, which can be seen in Fig. 3.15c. This interpretation inspired the fabrication of a surface mimicking the *Morpho*'s structural colouration only 2 years later (Saito et al. 2004). Since then, several contributions have uncovered more details in the understanding of the importance of disorder for the reflectance properties of the butterfly (Lee and Smith 2009; Saito et al. 2011; Johansen 2014).

In general, three disorder parameters seem crucial for reproducing the visual appearance of the *Morpho*: (i) the length distribution of the tree-like ridges (Fig. 3.15c), which controls the angular width of the reflection cone in the compressed direction (cf. Fig. 3.16b); (ii) the width of each individual ridge, which determines the angular size of the reflection cone in the other direction; (iii) and the distribution of height displacements, which suppresses the diffraction grating effect normally obtained from periodic structures (like the ridges in a Compact Disc) in order to give a smooth angular reflection (Saito et al. 2006).

The diversity of structural colouration strategies found in butterflies suggests a large degree of tunability of the structures through evolution (Nijhout 1985; Ghiradella 1991; Wickham et al. 2006; Ingram and Parker 2008), and there is also
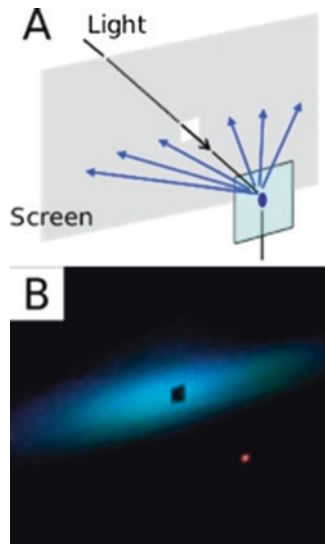
Fig. 3.16 Experiment to elucidate the reflection properties of the *Morpho* butterfly. (**a**) The wing is mounted on the sample holder (light blue square) and illuminated through a hole in a screen. (**b**) Photograph of screen in (**a**), where the reflection from the butterfly wing is seen. The elliptical shape is caused by the anisotropic disorder properties of the nanostructures of the wing. A circular shape is much more common, both for pigmented and structurally coloured structures (The figure is reproduced with permission from the author (Saito et al. 2013))

evidence that different types of disorder can provide similar results (Song et al. 2017). Given the impressive control of reflection properties that *Morpho* butterfly wings have, it is therefore likely that the scattering elements and disorder properties are highly optimised with respect to their optical response.

3.5.2   Pixellated Surfaces

Pixellated surfaces can give rise to vivid metallic as well as inconspicuous colourations. We define pixellated colouration as the phenomenon that occurs when the macroscopic appearance of an organism is constituted by the individual reflections of many small units that are differently coloured so that their appearance can be resolved individually when magnified but not by the naked eye. Such small areas of different colour could be individual cells in plants, or single iridocytes, or the differently coloured areas could be, for example, caused by the strong curvature of wing scales of a butterfly. To our knowledge, pixellated surfaces have not been summarised and reviewed before, so we decided to classify them as illustrated in the list below. Each strategy will be discussed in more detail later in this section. Briefly, different ultrastructures have been found to provide a pixellated colouration in cases where:

- Individual units, like plant cells or iridocytes, reflect different wavelengths, e.g. *Pollia condensata*, *Margaritaria nobilis*, and *Tridacna maxima*.
- Individual units, such as iridocytes, reflect varying wavelengths within them, e.g. *Tridacna derasa*.
- The surface has areas or patches that reflect different colours. For instance, this can be caused by different thicknesses in cuticular multilayers, e.g. *Cicindela oregona*, *Cicindela repanda*, and *Cicindela campestris*. This variation in layer thicknesses can also be linked to the structure of the surface, like in the elytra of *Chlorophila obscuripennis* where the layer thickness is higher at ridges but lower in the basins.
- The surface is structured in a way that reflects different colours from different features, for example concavities made up of multilayers, with different colours reflected from the tops or the walls of the concavities, like *Papilio palinurus*, or butterfly scales with a strong curvature, like in *Chrysiridia rhipheus*. This effect is based on the angular dependency of reflection of multilayers.

Examples of pixellated appearance are the fruits of *Pollia condensata* and *Margaritaria nobilis* (Vignolini et al. 2012, 2016). In these fruits, each individual cell in the pericarp reflects a slightly different colour by having a slightly different pitch in each cell, and the overall macroscopic appearance of the fruits is a metallic blue, see Sect. 3.3.1.3.

A similar example is the epithelium of certain clams (*Tridacna maxima*, *Tridacna derasa*), which has areas that show an intense white appearance, where individual

iridocytes (cells that are Bragg-like reflectors) reflect different wavelengths (Ghoshal et al. 2016a, b).

Whiteness can be caused either by the mixing of iridocytes of different colours, as in the case of *Tridacna maxima*, or by having different colours coming from just a single iridocyte, containing multiple Bragg stacks with different lamellar spacings, as in *Tridacna derasa*. Figure 3.17a, b shows a juvenile *Tridacna maxima,* where the reflective epithelium of the mantle overlapping the shell is visible, and a close-up of a white investigated area. The microscope image in Fig. 3.17e depicts an individual iridocyte, and a TEM of an individual iridocyte of the white area is shown in Fig. 3.17f, while a representative spectrum and the peak wavelength distribution are shown in Fig. 3.17g, h, respectively. A dissected *Tridacna derasa* and close-up of a white area are depicted in Fig. 3.17c, d.

The first example of colour mixing on pixellated surfaces was reported by Schultz and Bernard (1989) for tiger beetles. The dorsal wings of *Cicindela oregona* are covered by so-called alveoli, hexagonal pits of 13 µm across, consisting of cuticular multilayers. Figure 3.18a shows an SEM of the elytral surface with clearly visible alveoli. Two different morphs of *Cicindela oregona* were investigated, a brown and a black one. The surface of the brown morph is structured by such alveoli and has patches of blue-green surrounded by a red field. The surface of the black morph has magenta patches surrounded by a dull green field. These different colours are obtained by different spacing of the cuticular multilayers. The different patches can be resolved by microscopy. The spectra at the microscopic scale were collected in an area of 30–40 µm diameter, comprising 5–8 alveoli of the same colour. However, at the macroscopic scale, the colours of the patches and the surrounding field mix and an overall brown or black appearance is observed. The spectral
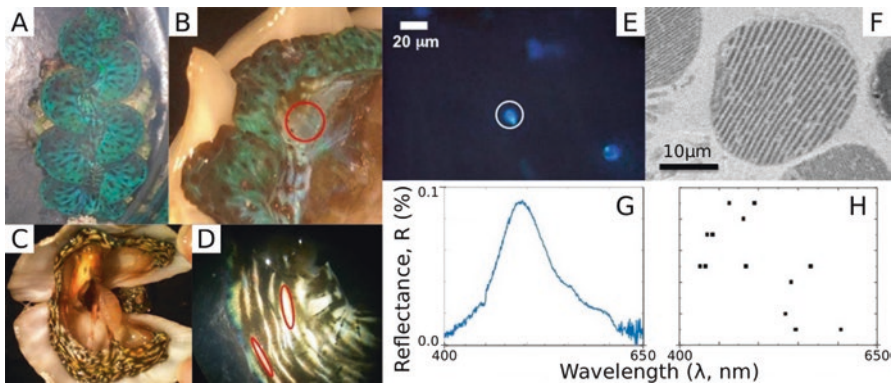
Fig. 3.17 Juvenile *Tridacna maxima* (the length of the clam is 6 cm) (**a**) and close-up (**b**). Photo (**c**) and close-up (**d**) of dissected *Tridacna derasa*. (**e–h**) *Tridacna maxima*: microscope image of an individual iridocyte (**e**), TEM of iridocyte (**f**), reflectance spectra (**g**) and colour distribution from individual iridocytes (**h**) ((**a–e, g, h**) reproduced with permission from Ghoshal et al. (2016a). (**f**) courtesy of Daniel E. Morse)
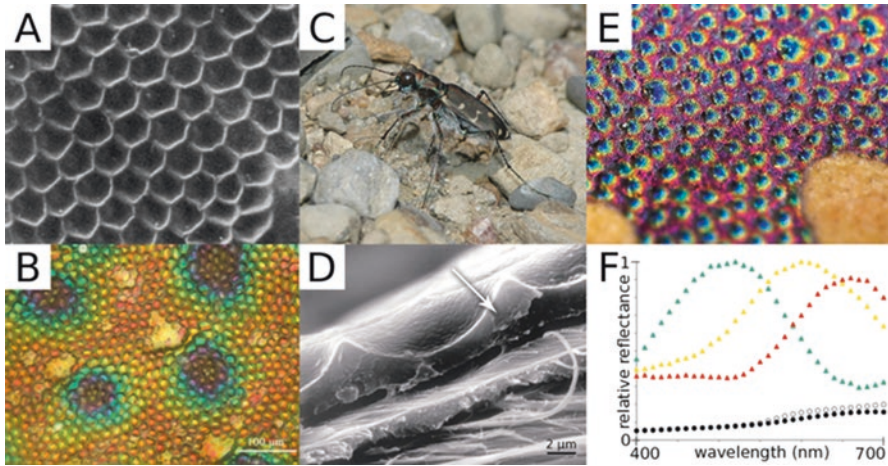
Fig. 3.18 (**a**) SEM of elytral surface of *Cicindela oregona*, each alveoli measures 13 μm across. (**b**) Dorsal surface of elytra of *Cicindela campestris*. (**c–f**) Photo, SEM, microscope image, and micro- and macro-scale spectra of *Cicindela repanda*, respectively ((**a**) reproduced with permission from Schultz and Bernard (1989). (**b**) reproduced with permission from Berthier et al. (2007). (**c–f**) adapted from Seago et al. (2009), courtesy of Thomas D. Schultz)

response at the macroscopic scale is measured on a 300 μm diameter area comprising around 530 alveoli and 7–8 colour patches. In this case, the reflectance is flat and unsaturated, giving the beetles a dull brown or black appearance, ideal for camouflage in their habitat.

The same macroscopic mixing effect is observed in the elytra of *Cicindela campestris*, see Fig. 3.18b (Berthier et al. 2007).

Finally, a similar mechanism is found in the elytra of *Cicindela repanda*, where blue-greenish *punctae*, surrounded by yellow circles in a red field (Fig. 3.18c–f) can be distinguished at the microscopic scale, while at the macroscopic scale, the colours mix and give a dull brown reflectance (filled circles), comparable to wet sand (open circles) (Fig. 3.18f), optimised for camouflage (Seago et al. 2009).

A similar effect is observed in the elytra of the beetle *Chlorophila obscuripennis* in Fig. 3.19a, which has a blue-green appearance. Here, the layer thicknesses of the chitin-melanoprotein multilayer are higher at the ridges than in the basins, so the bottom of the concavities reflects in the blue, while the sidewalls in the green (Fig. 3.19d), as depicted in Fig. 3.19a–d. SEM (Fig. 3.19b) and TEM (Fig. 3.19c) images show the concavities built up of cuticular multilayers with thicker layers at the ridges and smaller layers in the basins (Liu et al. 2008).

Another mechanism of pixellated colour is found in the butterfly *Papilio palinurus* (Fig. 3.20a) (Vukusic et al. 2000). In this case, the hierarchical surface structure consists of scales made up of multilayers. These multilayers are arranged in concavities of about 4–6 μm in diameter and 0.5–3 μm deep (Fig. 3.20b). The dimensions of the concavities are such that light reflected from the bottom of the structure shows a yellow reflection. In contrast, light impinging on the side walls of these
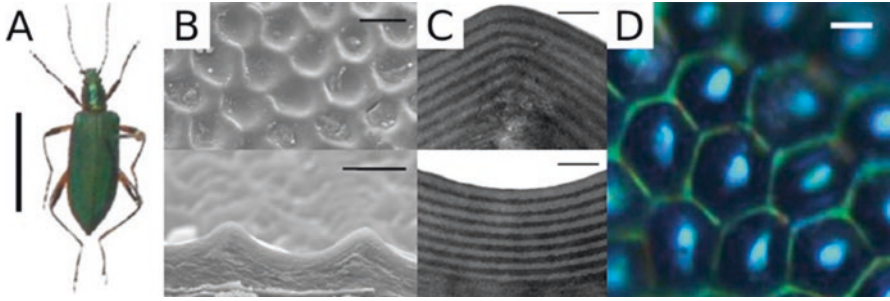
Fig. 3.19 *Chlorophila obscuripennis*. (**a**) Photo of *Chlorophila obscuripennis*, scale bar: 1 cm. (**b**) SEM of elytra: top view, and transverse cross-section, scale bars: 10 μm and 5 μm, respectively. (**c**) TEM cross-section of ridge and basin, scale bars: 0.5 μm. Note the layer thicknesses are smaller in the basin region. (**d**) Micrograph, scale bar: 5 μm (Reproduced with permission from Liu et al. (2008))
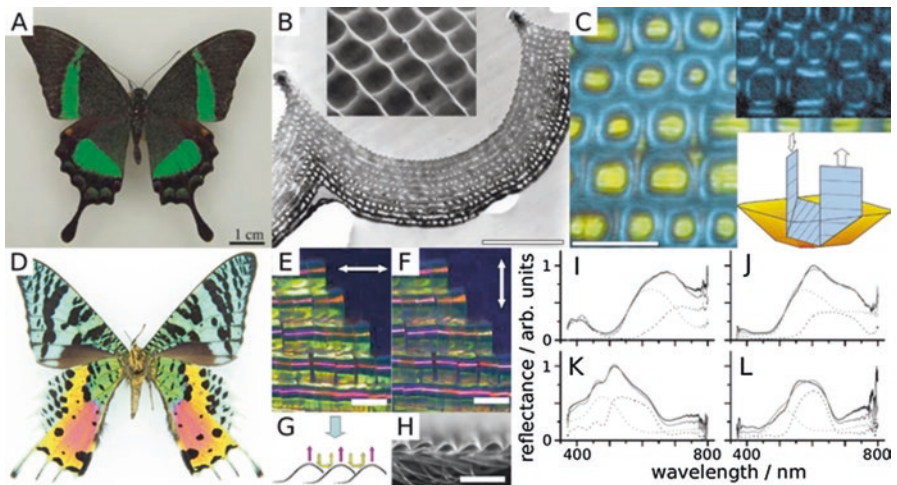
Fig. 3.20 (**a–c**) *Papilio palinurus*. (**a**) Photo of *Papilio palinurus*. (**b**) TEM of cross-section through the concavity of an iridescent scale. Inset: SEM image of same surface. Scale bars: 1 μm, inset 7 μm. (**c**) Micrographs with unpolarised light, inset same area between crossed polarisers, and scheme, scale bar: 12 μm, inset 6 μm. (**d–l**) *Chrysiridia rhipheus*. (**d–f**) Photo and microscope images (different polarisations) of *Chrysiridia rhipheus*, scale bar: 200 μm. (**g**) Scheme of reflection from top and sides of curvature, and (**h**) SEM cross-section, scale bar: 300 μm. (**i–l**) Reflectance spectra of purplish red, orange, pale blue, and green part of the wing, respectively. Individual (tops and bottoms of curvatures, black dashed and grey dashed lines) and additive spectra (taken by unfocusing the sample, black line, and summed from the individual spectra, grey line) ((**a**) reproduced with permission from Sun et al. (2013). (**b**, **c**) reproduced with permission from Vukusic et al. (2000). (**d–h**) reproduced with permission from Yoshioka and Kinoshita (2007). (**i–l**) reproduced with permission from Yoshioka and Kinoshita (2009))

concavities is reflected twice and yields an intense blue colouration, due to the different angle of incidence of the light with respect to the multilayer (Fig. 3.20c). Macroscopically, the contributions from the bottom and the side walls of these concavities cannot be resolved and the butterfly wings look green.

A similar effect is found in *Chrysiridia rhipheus* (Fig. 3.20d) where the wing scales have a strong curvature (Fig. 3.20h) leading to light being directly reflected from the top of the curvature, and dual reflection for light impinging in between (see scheme in Fig. 3.20g). The distance between these two reflected bands is only around 200 µm, so they cannot be resolved macroscopically (Yoshioka and Kinoshita 2007, 2009).

3.6 Outlook

In summary, disorder at different length scales adds functionalities to photonic structures in nature, providing control of colour and angular selectivity. In this chapter we reviewed examples of different types of disordered structures and their optical responses.

In contrast to perfectly periodic structures, where the knowledge of the unit cell is sufficient, the anatomical and theoretical description of disorder is very challenging because it requires the understanding of the structures on a large area (> tens of microns) with nm-scale precision.

Investigation of disorder is a useful tool for understanding evolution and aiding taxonomic classification, with more results to come in the next few decades. At the same time, many of these principles will provide bio-inspiration for fabrication of new optical materials and further research will not only benefit biological understanding but also lead to new discoveries in other areas of science.

References

Åkerlind, C., Arwin, H., Hallberg, T., Landin, J., Gustafsson, J., Kariis, H., & Järrendahl, K. (2015). Scattering and polarization properties of the scarab beetle *Cyphochilus insulanus* cuticle. *Applied Optics, 54*, 6037–6045.

Akkermans, E., & Montambaux, G. (2007). *Mesoscopic physics of electrons and photons*. Cambridge: Cambridge University Press.

Almeida, S. P., & Fujii, H. (1979). Fourier transform differences and averaged similarities in diatoms. *Applied Optics, 18*, 1663–1667.

Anderson, T. F., & Richards, A. G. (1942). An electron microscope study of some structural colors of insects. *Journal of Applied Physics, 13*, 748–758.

Arwin, H., Magnusson, R., Landin, J., & Järrendahl, K. (2012). Chirality-induced polarization effects in the cuticle of scarab beetles: 100 years after Michelson. *Philosophical Magazine, 92*, 1583–1599.

Bálint, Z., Kertész, K., Piszter, G., Vértesy, Z., & Biró, L. P. (2012). The well-tuned blues: The role of structural colours as optical signals in the species recognition of a local butterfly fauna (Lepidoptera: Lycaenidae: Polyommatinae). *Journal of the Royal Society Interface, 9*, 1745–1756.

Bell, G. R. R., Mäthger, L. M., Gao, M., Senft, S. L., Kuzirian, A. M., Kattawar, W. G., & Hanlon, R. T. (2014). Diffuse white structural coloration from multilayer reflectors in a squid. *Advanced Materials, 26*, 4352–4356.

Benedek, G. B. (1971). Theory of transparency of the eye. *Applied Optics, 10*, 459–473.

Berthier, S., Boulenguez, J., & Bálint, Z. (2007). Multiscaled polarization effects in *Suneve coronata* (Lepidoptera) and other insects: Application to anti-counterfeiting of banknotes. *Applied Physics A, 86*, 123–130.

Bossard, J. A., Lin, L., & Werner, D. H. (2016). Evolving random fractal Cantor superlattices for the infrared using a genetic algorithm. *Journal of the Royal Society Interface, 13*, 20150975.

Burresi, M., Cortese, L., Pattelli, L., Kolle, M., Vukusic, P., Wiersma, D. S., Steiner, U., & Vignolini, S. (2014). Bright-white beetle scales optimise multiple scattering of light. *Scientific Reports, 4*(6075).

Byrnes, S. J. (2016). Multilayer optical calculations. *arXiv e-prints, arXiv:1603.02720v2*.

Caveney, S. (1971). Cuticle reflectivity and optical activity in scarab beetles: The role of uric acid. *Proceedings of the Royal Society of London. Series B, 178*, 205–225.

Chandler, C. J., Wilts, B. D., Vignolini, S., Brodie, J., Steiner, U., Rudall, P. J., Glover, B. J., Gregory, T., & Walker, R. H. (2015). Structural colour in *Chondrus crispus*. *Scientific Reports, 5*, 11645.

Chandler, C. J., Wilts, B. D., Brodie, J., & Vignolini, S. (2017). Structural color in marine algae. *Advanced Optical Materials, 5*, 1600646.

Cortese, L., Pattelli, L., Utel, F., Vignolini, S., Burresi, M., & Wiersma, D. S. (2015). Light transport: Anisotropic light transport in white beetle scales. *Advanced Optical Materials, 3*, 1337–1341.

De Tommasi, E., Rea, I., Mocella, V., Moretti, L., De Stefano, M., Rendina, I., & De Stefano, L. (2010). Multi-wavelength study of light transmitted through a single marine centric diatom. *Optics Express, 18*, 12203–12212.

Del Río, L. F., Arwin, H., & Järrendahl, K. (2016). Polarizing properties and structure of the cuticle of scarab beetles from the *Chrysina* genus. *Physical Review E, 94*, 012409.

Dellieu, L., Cael, G., Louette, M., Herman, A., Deparis, O., & Sarrazin, M. (2017). Light coherence time modifies color perception of living beings. *Materials Today, 4*, 4952–4958.

Denton, E. J. (1970). Review lecture: On the organization of reflecting surfaces in some marine animals. *Philosophical Transactions of the Royal Society of London. B, 258*, 285–313.

Denton, E. J., & Land, M. F. (1971). Mechanism of reflexion in silvery layers of fish and cephalopods. *Proceedings of the Royal Society of London. Series B, 178*, 43–61.

Divitt, S., & Novotny, L. (2015). Spatial coherence of sunlight and its implications for light management in photovoltaics. *Optica, 2*, 95–103.

Dong, B. Q., Liu, X. H., Zhan, T. R., Jiang, L. P., Yin, H. W., Liu, F., & Zi, J. (2010). Structural coloration and photonic pseudogap in natural random close-packing photonic structures. *Optics Express, 18*, 14430–14438.

Donges, A. (1998). The coherence length of black-body radiation. *European Journal of Physics, 19*, 245–249.

Doucet, S. M., & Meadows, M. G. (2009). Iridescence: A functional perspective. *Journal of the Royal Society Interface, 6*, 115–132.

Eliason, C. M., & Shawkey, M. D. (2012). A photonic heterostructure produces diverse iridescent colours in duck wing patches. *Journal of the Royal Society Interface, 9*, 2279–2289.

Froufe-Pérez, L. S., Engel, M., Damasceno, P. F., Muller, N., Haberko, J., Glotzer, S. C., & Scheffold, F. (2016). Role of short-range order and hyperuniformity in the formation of band gaps in disordered photonic materials. *Physical Review Letters, 117*, 053902.

Fuhrmann, T., Landwehr, S., El Rharbi-Kucki, M., & Sumper, M. (2004). Diatoms as living photonic crystals. *Applied Physics B: Lasers and Optics, 78*, 257–260.

Galusha, J. W., Richey, L. R., Gardner, J. S., Cha, J. N., & Bartl, M. H. (2008). Discovery of a diamond-based photonic crystal structure in beetle scales. *Physical Review E, 77*, 050904.

Ghiradella, H. (1991). Light and color on the wing: Structural colors in butterflies and moths. *Applied Optics, 30*, 3492–3500.

Ghoshal, A., Eck, E., & Morse, D. E. (2016a). Biological analogs of RGB pixelation yield white coloration in giant clams. *Optica, 3*, 108–111.

Ghoshal, A., Eck, E., Gordon, M., & Morse, D. E. (2016b). Wavelength-specific forward scattering of light by Bragg-reflective iridocytes in giant clams. *Journal of the Royal Society Interface, 13*, 20160285.

Giraldo, M. A., Yoshioka, S., Liu, C., & Stavenga, D. G. (2016). Coloration mechanisms and phylogeny of *Morpho* butterflies. *The Journal of Experimental Biology, 219*, 3936–3944.

Glover, B. J., & Whitney, H. M. (2010). Structural colour and iridescence in plants: The poorly studied relations of pigment colour. *Annals of Botany, 105*, 505–511.

Gordon, R., Losic, D., Tiffany, M. A., Nagy, S. S., & Sterrenburg, F. A. S. (2009). The glass menagerie: Diatoms for novel applications in nanotechnology. *Trends in Biotechnology, 27*, 116–127.

Gould, K. S., & Lee, D. W. (1996). Physical and ultrastructural basis of blue leaf iridescence in four Malaysian understory plants. *American Journal of Botany, 83*, 45–50.

Graham, R. M., Lee, D. W., & Norstog, K. (1993). Physical and ultrastructural basis of blue leaf iridescence in two neotropical ferns. *American Journal of Botany, 80*, 198–203.

Gur, D., Leshem, B., Pierantoni, M., Farstey, V., Oron, D., Weiner, S., & Addadi, L. (2015). Structural basis for the brilliant colors of the sapphirinid copepods. *Journal of the American Chemical Society, 137*, 8408–8411.

Hébant, C., & Lee, D. W. (1984). Ultrastructural basis and developmental control of blue iridescence in *Selaginella* leaves. *American Journal of Botany, 71*, 216–219.

Hecht, E. (2017). *Optics* (5th ed.). Essex: Pearson.

Hunt, T., Bergsten, J., Levkanicova, Z., Papadopoulou, A., John, O. S., Wild, R., Hammond, P. M., Ahrens, D., Balke, M., Caterino, M. S., et al. (2007). A comprehensive phylogeny of beetles reveals the evolutionary origins of a superradiation. *Science, 318*, 1913–1916.

Hwang, J., Song, M. H., Park, B., Nishimura, S., Toyooka, T., Wu, J. W., Takanishi, J., Ishikawa, K., & Takezoe, H. (2005). Electro-tunable optical diode based on photonic bandgap liquid-crystal heterojunctions. *Nature Materials, 4*, 383–387.

Ingram, A. L., & Parker, A. R. (2008). A review of the diversity and evolution of photonic structures in butterflies, incorporating the work of John Huxley (The Natural History Museum, London from 1961 to 1990). *Philosophical Transactions of the Royal Society B, 363*, 2465–2480.

Jacobs, M., Lopez-Garcia, M., Phrathep, O. P., Lawson, T., Oulton, R., & Whitney, H. M. (2016). Photonic multilayer structure of *Begonia* chloroplasts enhances photosynthetic efficiency. *Nature Plants, 2*, 16162.

Jewell, S. A., Vukusic, P., & Roberts, N. W. (2007). Circularly polarized colour reflection from helicoidal structures in the beetle *Plusiotis boucardi*. *New Journal of Physics, 9*, 99.

Jiang, T., Peng, Z., Wu, W., Shi, T., & Liao, G. (2014). Gas sensing using hierarchical micro/nanostructures of *Morpho* butterfly scales. *Sensors and Actuators, A: Physical, 213*, 63–69.

Joannopoulos, J. D., Johnson, S. G., Winn, J. N., & Meade, R. D. (2008). *Photonic crystals: Molding the flow of light*. Princeton: Princeton University Press.

Johansen, V. E. (2014). Optical role of randomness for structured surfaces. *Applied Optics, 53*, 2405–2415.

Johansen, V. E., Thamdrup, L. H., Smistrup, K., Nielsen, T., Sigmund, O., & Vukusic, P. (2015). Designing visual appearance using a structured surface. *Optica, 2*, 239–245.

Johnson, S., & Joannopoulos, J. (2001). Block-iterative frequency-domain methods for Maxwell's equations in a planewave basis. *Optics Express, 8*, 173–190.

Jordan, T. M., Partridge, J. C., & Roberts, N. W. (2012). Non-polarizing broadband multilayer reflectors in fish. *Nature Photonics, 6*, 759–763.

Jordan, T. M., Wilby, D., Chiou, T.-H., Feller, K. D., Caldwell, R. L., Cronin, T. W., & Roberts, N. W. (2016). A shape-anisotropic reflective polarizer in a stomatopod crustacean. *Scientific Reports, 6*, 21744.

Kientz, B., Luke, S., Vukusic, P., Péteri, R., Beaudry, C., Renault, T., Simon, D., Mignot, T., & Rosenfeld, E. (2016). A unique self-organization of bacterial sub-communities creates iridescence in *Cellulophaga lytica* colony biofilms. *Scientific Reports, 6*, 19906.

Kieu, K., Li, C., Fang, Y., Cohoon, G., Herrera, O. D., Hildebrand, M., Sandhage, K. H., & Norwood, R. A. (2014). Structure-based optical filtering by the silica microshell of the centric marine diatom *Coscinodiscus wailesii*. *Optics Express, 22*, 15992–15999.

Kinoshita, S. (2008). *Structural colors in the realm of nature*. Singapore: World Scientific Publishing.

Kinoshita, S., & Yoshioka, S. (2005). Structural colors in nature: The role of regularity and irregularity in the structure. *ChemPhysChem, 6*, 1442–1459.

Kinoshita, S., Yoshioka, S., Fujii, Y., & Okamoto, N. (2002). Photophysics of structural color in the *Morpho* butterflies. *Forma, 17*, 103–121.

Kinoshita, S., Yoshioka, S., & Miyazaki, J. (2008). Physics of structural colors. *Reports on Progress in Physics, 71*, 076401.

Land, M. F. (1972). The physics and biology of animal reflectors. *Progress in Biophysics and Molecular Biology, 24*, 75–106.

Lathi, B. P. (1998). *Signal processing and linear systems*. Oxford: Oxford University Press.

Lee, D. W. (1991). Ultrastructural basis and function of iridescent blue colour of fruits in *Elaeocarpus*. *Nature, 349*, 260–262.

Lee, R. T., & Smith, G. S. (2009). Detailed electromagnetic simulation for the structural color of butterfly wings. *Applied Optics, 48*, 4177–4190.

Li, L., Kolle, S., Weaver, J. C., Ortiz, C., Aizenberg, J., & Kolle, M. (2015). A highly conspicuous mineralized composite photonic architecture in the translucent shell of the blue-rayed limpet. *Nature Communications, 6*, 6322.

Liu, F., Yin, H., Dong, B., Qing, Y., Zhao, L., Meyer, S., & Liu, X. (2008). Inconspicuous structural coloration in the elytra of beetles *Chlorophila obscuripennis* (Coleoptera). *Physical Review E, 77*(012901).

Lowry, J. B., & Lee, D. W. (1975). Physical basis and ecological significance of iridescence in blue plants. *Nature, 254*, 50–51.

Luke, S. M., Hallam, B. T., & Vukusic, P. (2010). Structural optimization for broadband scattering in several ultra-thin white beetle scales. *Applied Optics, 49*, 4246–4254.

Mason, C. W. (1923). Structural colors in feathers. I. *The Journal of Physical Chemistry, 27*, 201–251.

Mäthger, L. M., Denton, E. J., Marshall, N. J., & Hanlon, R. T. (2009). Mechanisms and behavioural functions of structural coloration in cephalopods. *Journal of the Royal Society Interface, 6*, 149–163.

Michelson, A. A. (1911). LXI. On metallic colouring in birds and insects. *Philosophical Magazine Series, 621*, 554–567.

Michielsen, K., & Stavenga, D. G. (2008). Gyroidcuticular structures in butterfly wing scales: Biological photonic crystals. *J. Royal Soc. Interface, 5*, 85–94.

Michielsen, K., De Raedt, H., & Stavenga, D. G. (2010). Reflectivity of the gyroidbiophotonic crystals in the ventral wing scales of the green hairstreak butterfly, *Callophrys rubi*. *Journal of the Royal Society Interface, 7*, 765–771.

Middleton, R., Steiner, U., & Vignolini, S. (2017). Bio-mimetic structural colour using biopolymers. In: *Bio-inspired polymers*, ed by Bruns, N., Kilbinger, A.F.M. Cambridge: The Royal Society of Chemistry, 555–585.

Mouchet, S. R., Van Hooijdonk, E., Welch, V. L., Louette, P., Colomer, J.-F., Su, B.-L., & Deparis, O. (2016). Liquid-induced colour change in a beetle: The concept of a photonic cell. *Scientific Reports, 6*(19322).

Nakamura, E., Yoshioka, S., & Kinoshita, S. (2008). Structural color of rock dove's neck feather. *Journal of the Physical Society of Japan, 77*, 124801.

Neville, A. C., & Caveney, S. (1969). Scarabaeid beetle exocuticle as an optical analogue of cholesteric liquid crystals. *Biological Reviews, 44*, 531–562.

Nijhout, H. F. (1985). The developmental physiology of color patterns in Lepidoptera. *Advances in Insect Physiology, 18*, 181–247.

Noh, H., Liew, S. F., Saranathan, V., Mochrie, S. G. J., Prum, R. O., Dufresne, E. R., & Cao, H. (2010). How noniridescent colors are generated by quasi-ordered structures of bird feathers. *Advanced Materials, 22*, 2871–2880.

Noyes, J. A., Vukusic, P., & Hooper, I. R. (2007). Experimental method for reliably establishing the refractive index of buprestid beetle exocuticle. *Optics Express, 15*, 4351–4358.

Noyes, J., Sumper, M., & Vukusic, P. (2008). Light manipulation in a marine diatom. *Journal of Materials Research, 23*, 3229–3235.

Onelli, O. D., van de Kamp, T., Skepper, J. N., Powell, J., dos Santos Rolo, T., Baumbach, T., & Vignolini, S. (2017). Development of structural colour in leaf beetles. *Scientific Reports, 7*, 1373.

Oskooi, A. F., Roundy, D., Ibanescu, M., Bermel, P., Joannopoulos, J. D., & Johnson, S. G. (2010). Meep: A flexible free-software package for electromagnetic simulations by the FDTD method. *Computer Physics Communications, 181*, 687–702.

Parker, A. R. (1998). The diversity and implications of animal structural colours. *The Journal of Experimental Biology, 201*, 2343–2347.

Parker, A. R. (2000). 515 million years of structural colour. *Journal of Optics A: Pure and Applied Optics, 2*, R15–R28.

Parker, A. R. (2005). A geological history of reflecting optics. *Journal of the Royal Society Interface, 2*, 1–17.

Parker, A. R., McPhedran, R. C., McKenzie, D. R., & Botten, L. C. (2001). Photonic engineering. Aphrodite's iridescence. *Nature, 409*, 36–37.

Prum, R.O. (2006). Anatomy, physics, and evolution of structural colors. In: *Bird coloration*, *Vol. 1,* ed. by Hill, G.E., McGraw, K. J. Cambridge: Harvard University Press, 295–353.

Prum, R. O., & Torres, R. H. (2003a). A fourier tool for the analysis of coherent light scattering by bio-optical nanostructures. *Integrative and Comparative Biology, 43*, 591–602.

Prum, R. O., & Torres, R. H. (2003b). Structural colouration of avian skin: Convergent evolution of coherently scattering dermal collagen arrays. *The Journal of Experimental Biology, 206*, 2409–2429.

Prum, R.O. and Torres, R.H. (2013). Fourier blues: Structural coloration of biological tissues. In: *Excursions in harmonic analysis,* Vol. 2, ed. by Andrews, T.D., Balan, R., Benedetto, J.J., Czaja, W., Okoudjou, K.A. New York: Springer, 401–421.

Prum, R. O., Morrison, R. L., & Ten Eyck, G. R. (1994). Structural color production by constructive reflection from ordered collagen arrays in a bird (*Philepitta castanea:* Eurylaimidae). *Journal of Morphology, 222*, 61–72.

Prum, R. O., Torres, R. H., Williamson, S., & Dyck, J. (1998). Coherent light scattering by blue feather barbs. *Nature, 396*, 28–39.

Prum, R. O., Torres, R., Williamson, S., & Dyck, J. (1999). Two-dimensional Fourier analysis of the spongy medullary keratin of structurally coloured feather barbs. *Proceedings of the Royal Society of London. Series B, 266*, 13–22.

Rayleigh, L. (1919). VII. On the optical character of some brilliant animal colours. *Philosophical Magazine Series, 6*(37), 98–111.

Saba, M., Wilts, B. D., Hielscher, J., & Schröder-Turk, G. E. (2014). Absence of circular polarisation in reflections of butterfly wing scales with chiral Gyroid structure. *Materials Today, 1*, 193–208.

Saito, A., Yoshioka, S.-Y., & Kinoshita, S. (2004). Reproduction of the *Morpho* butterfly's blue: Arbitration of contradicting factors. *Proceedings of SPIE – The International Society for Optical Engineering, 5526*, 188–194.

Saito, A., Miyamura, Y., Nakajima, M., Ishikawa, Y., Sogo, K., Kuwahara, Y., & Hirai, Y. (2006). Reproduction of the *Morpho* blue by nanocasting lithography. *Journal of Vacuum Science and Technology B, 24*, 3248–3251.

Saito, A., Yonezawa, M., Murase, J., Juodkazis, S., Mizeikis, V., Akai-Kasaya, M., & Kuwahara, Y. (2011). Numerical analysis on the optical role of nano-randomness on the *Morpho* butterfly's scale. *Journal of Nanoscience and Nanotechnology, 11*, 2785–2792.

Saito, A., Shibuya, T., Yonezawa, M., Akai-Kasaya, M., & Kuwahara, Y. (2013). Simulation analysis on the optical role of the number of randomly arranged nano-trees on the *Morpho* butterfly's scale. *Proceedings of SPIE – The International Society for Optical Engineering, 8686*. https://doi.org/10.1117/12.2012036.

Schoen, A. H. (1970). *Three dimensional Euclidean space partitioned into interpenetrating labyrinths by infinite periodic minimal surfaces without self intersections, NASA-TN-D-5541, C-98*. Cambridge: NASA Electronics Research Center.

Schröder-Turk, G. E., Wickham, S., Averdunk, H., Brink, F., Gerald, J. D. F., Poladian, L., & Hyde, S. T. (2011). The chiral structure of porous chitin within the wing-scales of *Callophrys rubi*. *Journal of Structural Biology, 174*, 290–295.

Schultz, T. D., & Bernard, G. D. (1989). Pointillistic mixing of interference colours in cryptic tiger beetles. *Nature, 337*, 72–73.

Seago, A. E., Brady, P., Vigneron, J. P., & Schultz, T. D. (2009). Gold bugs and beyond: A review of iridescence and structural colour mechanisms in beetles (Coleoptera). *Journal of the Royal Society Interface, 6*, 165–184.

Sellers, S. R., Man, W., Saba, M., & Florescu, M. (2017). Local self-uniformity in photonic networks. *Nature Communications, 8*, 14439.

Sharma, V., Crne, M., Park, J. O., & Srinivasarao, M. (2009). Structural origin of circularly polarized iridescence in jeweled beetles. *Science, 325*, 449–451.

Shawkey, M. D., Saranathan, V., Palsdottir, H., Crum, J., Ellisman, M. H., Auer, M., & Prum, R. O. (2009). Electron tomography, three-dimensional Fourier analysis and colour prediction of a three-dimensional amorphous biophotonic nanostructure. *Journal of the Royal Society Interface, 6*, 213–220.

Song, B., Johansen, V. E., Sigmund, O., & Shin, J. H. (2017). Reproducing the hierarchy of disorder for Morpho-inspired, broad-angle color reflection. *Scientific Reports, 7*, 46023.

Starkey, T., & Vukusic, P. (2013). Light manipulation principles in biological photonic systems. *Nanophotonics, 2*, 289–307.

Stavenga, D. G., Leertouwer, H. L., Marshall, N. J., & Osorio, D. (2011a). Dramatic colour changes in a bird of paradise caused by uniquely structured breast feather barbules. *Proceedings of the Royal Society of London. Series B, Biological Sciences 278*, 2098–2104.

Stavenga, D. G., Wilts, B. D., Leertouwer, H. L., & Hariyama, T. (2011b). Polarized iridescence of the multilayered elytra of the Japanese jewel beetle, *Chrysochroa fulgidissima*. *Philosophical Transactions of the Royal Society B: Biological Sciences, 366*, 709–723.

Steinbrecht, R. A., Mohren, W., & Schneider, D. (1985). Cuticular interference reflectors in the golden pupae of danaine butterflies. *Proceedings of the Royal Society of London. Series B, 226*, 367–390.

Strout, G., Russell, S. D., Pulsifer, D. P., Erten, S., Lakhtakia, A., & Lee, D. W. (2013). Silica nanoparticles aid in structural leaf coloration in the Malaysian tropical rainforest understorey herb *Mapania caudata*. *Annals of Botany, 112*, 1141–1148.

Sumper, M., & Brunner, E. (2006). Learning from diatoms: Nature's tools for the production of nanostructured silica. *Advanced Functional Materials, 16*, 17–26.

Sun, J., Bhushan, B., & Tong, J. (2013). Structural coloration in nature. *RSC Advances, 3*, 14862–14889.

Thomas, K. R., Kolle, M., Whitney, H. M., Glover, B. J., & Steiner, U. (2010). Function of blue iridescence in tropical understorey plants. *Journal of the Royal Society Interface, 7*, 1699–1707.

Toninelli, C. (2007). *Light transport in photonic structures: Interplay between order and disorder* (PhD thesis). Florence: Lens.

Trzeciak, T. M., & andVukusic, P. (2009). Photonic crystal fiber in the polychaete worm *Pherusa* sp. *Physical Review E, 80*, 061908.

van der Kooi, C. J., Wilts, B. D., Leertouwer, H. L., Staal, M., Elzenga, J. T. M., & Stavenga, D. G. (2014). Iridescent flowers? Contribution of surface structures to optical signaling. *The New Phytologist, 203*, 667–673.

van der Kooi, C. J., Dyer, A. G., & Stavenga, D. G. (2015). Is floral iridescence a biologically relevant cue in plant-pollinator signaling? *The New Phytologist, 205*, 18–20.

Vignolini, S., Rudall, P. J., Rowland, A. V., Reed, A., Moyroud, E., Faden, R. B., Baumberg, J. J., Glover, B. J., & Steiner, U. (2012). Pointillist structural color in *Pollia* fruit. *Proceedings of the National Academy of Sciences of the United States of America, 109*, 15712–15715.

Vignolini, S., Moyroud, E., Glover, B. J., & Steiner, U. (2013). Analysing photonic structures in plants. *Journal of The Royal Society Interface, 10*, 20130394.

Vignolini, S., Moyroud, E., Hingant, T., Banks, H., Rudall, P. J., Steiner, U., & Glover, B. (2015a). Is floral iridescence a biologically relevant cue in plant-pollinator signalling? A response to van der Kooi et al. (2014b). *The New Phytologist, 205*, 21–22.

Vignolini, S., Moyroud, E., Hingant, T., Banks, H., Rudall, P. J., Steiner, U., & Glover, B. J. (2015b). The flower of *Hibiscus trionum* is both visibly and measurably iridescent. *The New Phytologist, 205*, 97–101.

Vignolini, S., Gregory, T., Kolle, M., Lethbridge, A., Moyroud, E., Steiner, U., Glover, B. J., Vukusic, P., & Rudall, P. J. (2016). Structural colour from helicoidal cell-wall architecture in fruits of *Margaritaria nobilis*. *Journal of The Royal Society Interface, 13*, 20160645.

Vukusic, P., & Sambles, J. R. (2003). Photonic structures in biology. *Nature, 424*, 852–855.

Vukusic, P., & Stavenga, D. G. (2009). Physical methods for investigating structural colours in biological systems. *Journal of The Royal Society Interface, 6*, 133–148.

Vukusic, P., Sambles, J. R., Lawrence, C. R., & Wootton, R. J. (1999). Quantified interference and diffraction in single *Morpho* butterfly scales. *Proceedings of the Royal Society B, 266*, 1403–1411.

Vukusic, P., Sambles, J. R., & Lawrence, C. R. (2000). Structural colour: Colour mixing in wing scales of a butterfly. *Nature, 404*, 457.

Vukusic, P., Hallam, B., & Noyes, J. (2007). Brilliant whiteness in ultrathin beetle scales. *Science, 315*, 348.

Whitney, H. M., Kolle, M., Andrew, P., Chittka, L., Steiner, U., & Glover, B. J. (2009). Floral iridescence, produced by diffractive optics, acts as a cue for animal pollinators. *Science, 323*, 130–133.

Wickham, S., Large, M. C. J., Poladian, L., & Jermiin, L. S. (2006). Exaggeration and suppression of iridescence: The evolution of two-dimensional butterfly structural colours. *Journal of The Royal Society Interface, 3*, 99–109.

Wiersma, D. S. (2013). Disordered photonics. *Nature Photonics, 7*, 188–196.

Wikimedia Commons, Kuribo (2008). *Satyr Tragopan, captive, Osaka*. Satyr Tragopan Osaka.jpg, licensed under CC BY-SA 3.0.

Wikimedia Commons, & William H. Majoros (2010). *Eastern Bluebird*. 7Z1E5531.jpg, licensed under CC BY-SA 3.0.

Wilts, B. D., Michielsen, K., De Raedt, H., & Stavenga, D. G. (2012a). Iridescence and spectral filtering of the gyroid-type photonic crystals in *Parides sesostris* wing scales. *Interface Focus, 2*, 681–687.

Wilts, B. D., Michielsen, K., Kuipers, J., De Raedt, H., & Stavenga, D. G. (2012b). Brilliant camouflage: Photonic crystals in the diamond weevil, *Entimus imperialis*. *Proceedings of the Royal Society B, 279*, 2524–2530.

Wilts, B. D., Michielsen, K., De Raedt, H., & Stavenga, D. G. (2014a). Sparkling feather reflections of a bird-of-paradise explained by finite-difference time-domain modeling. *Proceedings of the National Academy of Sciences of the United States of America, 111*, 4363–4368.

Wilts, B. D., Whitney, H. M., Glover, B. J., Steiner, U., & Vignolini, S. (2014b). Natural helicoidal structures: Morphology, self-assembly and optical properties. *Materials Today, 1*, 177–185.

Wilts, B. D., Sheng, X., Holler, M., Diaz, A., Guizar-Sicairos, M., Raabe, J., Hoppe, R., Liu, S. H., Langford, R., Onelli, O. D., et al. (2017a). Evolutionary-optimized photonic network structure in white beetle wing scales. *Advanced Materials, 1702057*.

Wilts, B. D., Zubiri, B. A., Klatt, M. A., Butz, B., Fischer, M. G., Kelly, S. T., Spiecker, E., Steiner, E., & Schröder-Turk, G. E. (2017b). Butterfly gyroid nanostructures as a time-frozen glimpse of intracellular membrane development. *Science Advances, 3*, e1603119.

Wolf, E. (2007). *Introduction to the theory of coherence and polarization of light*. Cambridge: Cambridge University Press.

Yablonovitch, E. (1993). Photonic band-gap structures. *Journal of the Optical Society of America B: Optical Physics, 10*, 283–295.

Yong, J., Chen, F., Yang, Q., Du, G., Shan, C., Bian, H., Farooq, U., & Hou, X. (2015). Bioinspired transparent underwater superoleophobic and anti-oil surfaces. *Journal of Materials Chemistry, A3*, 9379–9384.

Yoshioka, S., & Kinoshita, S. (2007). Polarization-sensitive color mixing in the wing of the Madagascan sunset moth. *Optics Express, 15*, 2691–2701.

Yoshioka, S., & Kinoshita, S. (2009). Optical effects of highly curved multilayer structure found in the scale of structurally colored moth. *Proceedings of SPIE, 7401*, 740105. https://doi.org/10.1117/12.824861.

Yun, W.-B., Kirz, J., & Sayre, D. (1987). Observation of the soft X-ray diffraction pattern of a single diatom. *Acta Crystallographica. Section A, 43*, 131–133.

Zi, J., Yu, X., Li, Y., Hu, X., Xu, C., Wang, X., Liu, X., & Fu, R. (2003). Coloration strategies in peacock feathers. *Proceedings of the National Academy of Sciences of the United States of America, 100*, 12576–12578.

Part III
Wetting Phenomena

Chapter 4
Moisture-Harvesting Reptiles: A Review

Anna-Christin Joel, Gerda Buchberger, and Philipp Comanns

Abstract Reptiles can live in arid environments due to special adaptations of their integument to such habitats. So called moisture-harvesting reptiles show behavioral and morphological adaptations, as their diet often does not cover the complete water demand and rain is scarce. The collection of water from various sources by moisture-harvesting reptiles is often accompanied by a stereotypical behavior: snakes coil up in the open and show a dorso-ventral flattening of their body to increase the surface area. Lizards also show a flattening of their body, but additionally raise their abdomen by splaying and extending their legs and lowering their head and tail. A similar behavior is observed in tortoises. Though there are several behavioral descriptions of moisture-harvesting reptiles, there are only few investigations about the physical principles enabling a passive collection of water. Special skin structures, comprising a micro structured surface with capillary channels in between imbricate overlapping scales, enable lizards to collect water efficiently. In some lizards, such as the Texas horned lizard *Phrynosoma cornutum*, water droplets applied to their body surface show a preferred spreading direction, transporting the water towards their mouth for ingestion. This passive directional transport is enabled by asymmetric and interconnected channels between the scales. Elucidation of the physical principles behind the directional water spreading has inspired a biomimetic transfer to optimize future applications in liquid handling, e.g. in fields of microfluidics.

A.-C. Joel (✉)
Institute of Zoology, RWTH Aachen University, Aachen, Germany

Westphalian Institute of Biomimetics, Westphalian University of Applied Science, Bocholt, Germany
e-mail: joel@bio2.rwth-aachen.de

G. Buchberger
Institute of Biomedical Mechatronics, JKU Linz, Linz, Austria

P. Comanns
Institute of Zoology, RWTH Aachen University, Aachen, Germany

4.1 The Integument's Diverse Functions

The integument, i.e. the skin and its derivates like scales, hairs or feathers, is the organ separating an animals' body from its environment. As a barrier and external display, the integument has to accomplish several functions for adaptation of the animal to its ecological niche (Fig. 4.1). A very prominent function is its color display: brightly colored skin is often used for communication or attraction of the other sex (Cooper and Burns 1987; Thompson and Moore 1991; Ligon and McGraw 2013). Color can also play a role in camouflage or disguise to avoid predation (Sherbrooke 2002; Stuart-Fox et al. 2006; Cooper and Sherbrooke 2012; Pfennig 2012). Being ectothermic, some reptiles use the color of their skin for thermoregulation. By darkening their skin, for example, they can heat up their bodies and vice versa, hence maintain vital functions (Cole 1943; Pearson 1977; Walton and Bennett 1993; Sherbrooke 1997). Instead of changing their integuments' color, some reptiles show behavioral adaptations like basking in the sun to increase or burrowing in the soil to decrease their body temperature (Heath 1962; Douglass and Layne 1978; Powell and Russell 1985; Bulova 2002; Cloudsley-Thompson 1991).

One important function of the reptiles' integument is, however, the regulation of water balance, especially the inhibition of water loss. The evolution of a more water-proof integument was a critical step for the transition of amphibians to reptiles, hence from anamniotes to amniotes (Alibardi 2003; Lillywhite 2006). With notable exceptions, like the xerophilic desert rain frog *Breviceps macrops*, amphibians need permanent access to water (Channing and Wahlberg 2011). In contrast, reptiles have evolved a more water-proof skin, enabling them to inhabit not only rainforests but also deserts (Roberts and Lillywhite 1980). However, inhabitation of deserts requires more adaptations of an animal than just a water-proof skin.
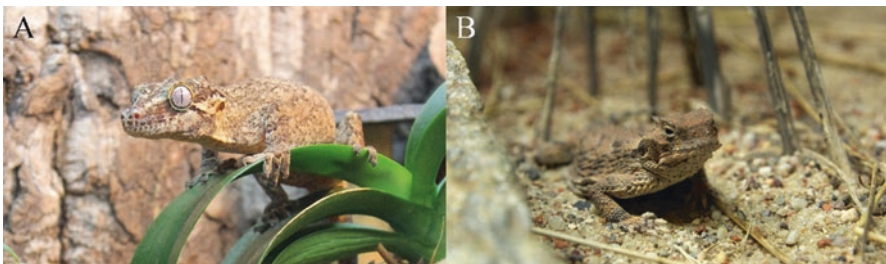
Fig. 4.1 Two reptiles adapted to their different ecological niches. The gecko *Rhacodactylus auriculatus* (**A**) lives in the forests of New Caledonia, whereas the lizard *Phrynosoma platyrhinos* (**B**) originally inhabits deserts in North America

4.2   Moisture-Harvesting Reptiles

Wet habitats like rainforests necessitate antibacterial and antifungal properties of the integument, i.e. by being superhydrophobic and showing self-cleaning ability (Watson et al. 2015a, b), whereas animals in arid regions have to prevent water loss from their body and simultaneously absorb, withhold and/or drink any water available. It has often been discussed whether the water content of the consumed food is already sufficient to sustain all vital functions of desert reptiles. For example land tortoises probably indefinitely survive on a vegetable diet without any additional water, with their fat acting as a source for metabolic water (Cloudsley-Thompson 1971). Likewise, it is suggested that the snakes which live on a diet of lizards (containing approximately 75% water) consume additional water only opportunistically rather than obligatorily (Robinson and Hughes 1978).

Not all desert reptiles are able to rely on water obtained from food (Nagy 1987). Some reptiles, such as thorny devils, *Moloch horridus*, or horned lizards, *Phrynosoma* ssp., mainly feed on ants. Although the water content of these insects is not exceptionally low, they cause the excretion of high concentrations of electrolytes. This way, a myrmecophagous diet can deprive a lizard of vitally needed water (Bradshaw and Shoemaker 1967; Minnich and Shoemaker 1972; Withers and Dickman 1995; Peterson 1998). Typically in desert reptiles water loss through feces and urine is very low as nitrogen excretion takes place by insoluble uric acid instead of urea (Weese 1917, 1919). To excrete the surplus of electrolytes without increasing the excreted substance, horned lizards possess nasal salt glands (Sherbrooke 1981). Other ant-feeding lizards can retain elevated sodium ion concentrations in their body fluids, thus conserving water which would otherwise be required for excretion (Bradshaw 1986; Bradshaw and Shoemaker 1967). The typical level of blood plasma sodium is reestablished after these lizards had access to water, e.g. in form of rain.

Whether or not requiring freely accessible water for survival, many desert reptiles show extensive use of available water, such as rain, puddles after rainfall, the morning dew or even moist sand (Bentley and Blumer 1962; Pianka and Pianka 1970; Louw 1972; Gans et al. 1982; Withers 1993; Sherbrooke 2004; Repp and Schuett 2008; Comanns et al. 2016). Western diamond-backed rattlesnakes (*Crotalus atrox*) were observed to leave the safety of their den to drink rain, sleet or snow even if ambient temperatures are far below their physiological temperature (Repp and Schuett 2008). It is also suggested that reptiles can harvest moisture from air after a cold night by thermally facilitated condensation (Lasiewski and Bartholomew 1969; Gans et al. 1982; Comanns et al. 2011).

Because the skin of desert reptiles has been found to be almost impermeable for water to minimize water loss by evaporation, absorption of water through the integument is not possible (Weese 1917; Bentley and Blumer 1962). This leads to a major challenge: not only must the water in its available form be found and collected, this water has to be also transported to the mouth for drinking. Most reptiles usually just lick and drink water from stones or vegetation. The desert turtle, *Gopherus agassizii*, drinks rain from ditches which it has dug itself (Medica et al. 1980). Besides the typical adaptations of reptiles inhabiting arid regions, some

Table 4.1 Moisture-harvesting reptiles

	Species	References
Lizards	*Moloch horridus*	Bentley and Blumer (1962) and Sherbrooke (1993)
	Phrynocephalus arabicus	Schwenk and Greene (1987)
	Phrynocephalus helioscopus[a]	Schwenk and Greene (1987)
	Phrynocephalus horvathi[a]	Yenmiş et al. (2015)
	Phrynosoma cornutum[a]	Sherbrooke (1990)
	Phrynosoma modestum[a]	Sherbrooke (2004)
	Phrynosoma platyrhinos[a]	Peterson (1998) and Sherbrooke (2004)
	Pogona vitticeps	Fitzgerald (1983) and Sherbrooke (1993)
	Saara hardwickii	Seshadri (1957)
	Smaug giganteus	Mertens (1960)
	Trapelus flavimaculatus[a]	Vesely and Modry (2002)
	Trapelus mutabilis[a]	Vesely and Modry (2002)
	Trapelus pallidus[a]	Vesely and Modry (2002)
	Uromastix aegyptia	Ditmars (1933)
Snakes	*Bitis peringueyi*	Louw (1972) and Robinson and Hughes (1978)
	Bothrops asper	Greene (1986)
	Bothrops moojeni[a]	Andrade and Abe (2000)
	Crotalus atrox[a]	Repp and Schuett (2008)
	Crotalus lepidus[a]	Mata-Silva et al. (2014)
	Crotalus pyrrhus[a]	Glaudas (2009)
	Crotalus oreganus concolor	Ashton and Johnson (1998)
	Crotalus s. scutulatus[a]	Cardwell (2006)
	Gloydius blomhoffii[a]	Sasaki and Duvall (2003)
	Nerodia c. compressicauda	Miller (1985)
Tortoises	*Homopus areolatus*[a]	Auffenberg (1963)
	Kinixys homeana[a]	Auffenberg (1963)
	Psammobates t. trimeni[a]	Auffenberg (1963)

[a]Including an accompanying stereotypic behavior

desert reptiles are "moisture harvesters" (Table 4.1). These reptiles display specific behaviors and integumental peculiarities to efficiently harvest water with their body surface. The specializations developed in different reptilian species of lizards, tortoises and snakes.

4.3   Stereotypical Moisture-Harvesting Behavior

To collect water and make it accessible for drinking, many moisture-harvesting reptiles display an innate stereotypic behavior, differing between the groups of reptiles (Robinson and Hughes 1978; Sherbrooke 2004). Moisture-harvesting snakes, for example, emerge from their den or any potential roofing during rain showers and coil up in the open (Fig. 4.2, middle). By coiling up, they bring their body loops in
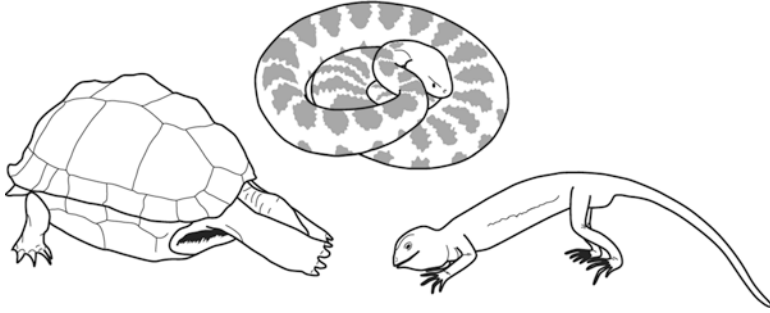
Fig. 4.2 Stereotypical moisture-harvesting body positions of different reptiles. Left: western tent tortoise (*P. t. trimeni*), redrawn after Auffenberg (1963). Middle: Mojave rattlesnake (*C. s. scutulatus*), after Cardwell (2006). Right: Horvath's toad-headed agama (*P. horvathi*), after Yenmiş et al. (2015)

close contact with each other and water is retrained in the formed shallows between the loops (Louw 1972; Robinson and Hughes 1978; Andrade and Abe 2000; Cardwell 2006; Glaudas 2009). Some species also exhibit a dorso-ventral flattening of the body, probably to increase the exposed surface area. With the snout continuously in contact with the shallows and the head moving contrary to scales' overlap, the collected water is ingested.

In contrast to snakes, several lizards are not able to lick water from their body. They likewise flatten their body surface to enlarge the exposed area (Schwenk and Greene 1987; Sherbrooke 1990; Peterson 1998; Vesely and Modry 2002). Furthermore, they raise their abdomen by splaying and extending their legs and lowering their head and tail (Fig. 4.2, right). Due to gravity, any striking droplet thus runs down the body towards head and snout to be ingested. A similar posture is adopted by moisture-harvesting tortoises. However, they press the front limbs against their head, probably to lead the water from their shell towards their snout (Fig. 4.2, left) (Auffenberg 1963). Any flattening of their body is, apparently, inhibited by their rigid protection.

Besides a behavioral description, a more detailed insight into the principles behind moisture-harvesting of most reptiles is missing so far. More detailed studies have only been performed for lizards, especially for the thorny devil, *M. horridus*, and the Texas horned lizard, *P. cornutum*. Hence, these will be in focus in the following parts.

4.4 Adaptations of the Integument to Enable Moisture-Harvesting

The integument of lizards consists of an outer beta-keratin layer, an inner alpha-layer built up mainly from the corresponding keratins and a meso layer separating both (Fig. 4.3) (Maderson et al. 1998; Alibardi and Maderson 2003). The outer layer is covered by the "Oberhäutchen", which often exhibits a micro structure. In moisture-harvesting lizards, but also in some lizard species for which
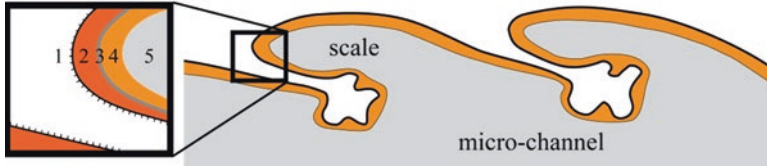
Fig. 4.3 Cross section through the skin of a moisture-harvesting lizard. *1* Oberhäutchen with micro structure, *2* beta-keratin layer, *3* meso layer, *4* alpha-layer, *5* dermis

moisture-harvesting is not described, this micro structure has a honeycomb pattern with diameters of about 10–30 μm and a few micrometers in depth (Peterson 1998; Vesely and Modry 2002; Sherbrooke et al. 2007; Comanns et al. 2011).

Another unusual morphological feature of the integument of moisture-harvesting lizards is the existence of micro-channels formed by partially (imbricate) overlapping scales (Fig. 4.3). Morphological studies found a width of 100–250 μm in their basal part, and narrower openings towards the surface, i.e. 100–150 μm (Withers 1993; Sherbrooke et al. 2007). These narrow channels form a semi-tubular network of interconnected channels over the entire lizard's body (Gans et al. 1982; Sherbrooke et al. 2007; Comanns et al. 2015). Both, the honeycomb-shaped micro structure as well as the channels in between the scales allow these lizards to collect and transport water more efficiently to their mouth for drinking (Withers 1993; Vesely and Modry 2002; Sherbrooke et al. 2007; Comanns et al. 2011, 2015).

4.4.1 Improved Wettability by Micro Structure

At a rough estimate the ability to collect water improves with a more hydrophilic surface. Hence, the wettability of the Oberhäutchen is important for lizards to harvest water. Experiments showed that on a rather smooth keratin surface, e.g. the inner side of a scale, the contact angle (measurement of wettability; the higher the contact angle the less wettable the surface) is about 70°, whereas the scale surface appeared superhydrophilic with a contact angle of less than 10° (Fig. 4.4) (Comanns et al. 2011). The major difference between both scale sides is the micro structure on the scale's surface.

On smooth and homogenous surfaces, the contact angle θ is described by the Young's law (de Gennes et al. 2004; Berthier and Silberzan 2010; Bormashenko 2013)

$$\cos\theta = \left(\gamma_{sg} - \gamma_{sl}\right) / \gamma_{lg} \tag{4.1}$$

with γ_{lg}, γ_{sg} and γ_{sl} characterizing the liquid-gas, substrate-gas, and substrate-liquid surface tensions (Fig. 4.5, left). However, wettability changes as soon as the substrate is no longer smooth and homogenous. In case of a surface roughness
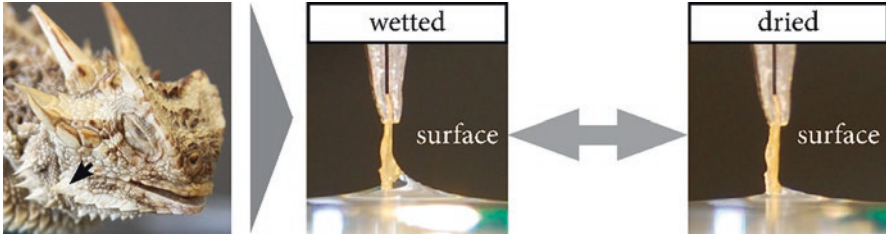
Fig. 4.4 Taking a scale from the sublabial region (left picture) of the Texas horned lizard (*P. cornutum*), its surface is superhydrophilic though consisting of roughly the same material as its inner side. This improved wettability of the scale's surface is only established after pre-wetting and vanishes after drying. After Comanns et al. (2011)
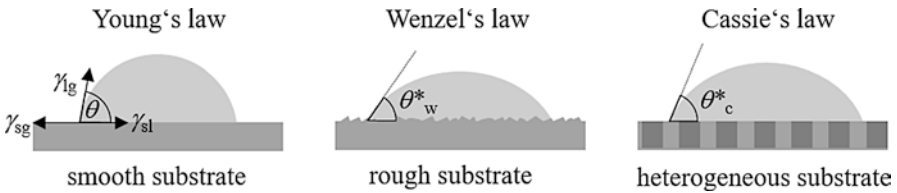
Fig. 4.5 Different wetting conditions of a liquid droplet on a surface. Young's law describes the contact angle of a liquid on a smooth substrate. The contact angle of a liquid droplet on a rough surface is changed following the Wenzel's law. Cassie's law quantifies the contact angle on a smooth but chemically heterogeneous substrate

considerably smaller than the droplet size, Wenzel's law describes the apparent contact angle θ_{w}^{*} (Wenzel 1936; de Gennes et al. 2004; Berthier and Silberzan 2010; Bormashenko 2013)

$$\cos\theta_{w}^{*} = r\cos\theta \qquad (4.2)$$

with θ being the Young's contact angle (Fig. 4.5, middle). The roughness r is defined as the ratio of the actual surface to the projected (unstructured) surface. For a hydrophilic contact with $\theta < 90°$ wetting is increased by roughness. Hence, the micro structure on the Oberhäutchen of the scales can already lower the contact angle due to roughness factors between $r \approx 1.4$ and $r \approx 3$ (Comanns et al. 2011).

Though the surface roughness can already decrease the contact angle on the scale's surface, its superhydrophilicity depends on a pre-wetted status: it has been observed that the contact angle is similar on both sides of a dried scale. Only after pre-wetting, the scale's surface becomes superhydrophilic (Fig. 4.4) (Comanns et al. 2011).

Based on this observation, the hypothesis has been derived that a water film can be held by the micro structure (Fig. 4.6) (Comanns et al. 2011). In view of its wetting properties, the skin's surface becomes a composite material of keratin (material 1) and water (material 2) (Figs. 4.5 and 4.6). On chemically heterogeneous surfaces
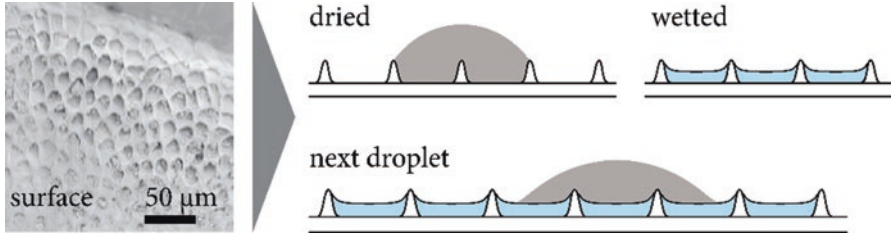
Fig. 4.6 Wetting behavior of micro structure on moisture-harvesting lizard's skin. Left: SEM image of surface honeycomb-shaped micro structure. Right: improving wettability by pre-wetting. After Comanns et al. (2014)

consisting of two types of surface materials Cassie's law[1] is used to describe the contact angle θ^*_c (Fig. 4.5, right) (Cassie 1948)

$$\cos\theta^*_c = f_1 \cos\theta_1 + f_2 \cos\theta_2 \tag{4.3}$$

In Eq. (4.3) f_1 and f_2 are the surface fractions of the two different materials, and θ_1 and θ_2 are the corresponding contact angles on these materials at a macroscopic size. Like the Wenzel's law, Cassie's law was derived under the assumption that the scale of the heterogeneities is small compared to the dimensions of the droplet.

Applying Cassie's law to the lizard's skin, a water area fraction of 73% is required to obtain a superhydrophilic surface. In case all indentations built by the micro structure are completely covered with water, 73% corresponds to a hexagonal model of the surface micro structure with a diameter of 15.86 μm (filled with water) and a wall width of 2 μm (as keratin area). These calculated values are within the natural size range observed for the Oberhäutchen's micro structure (Comanns et al. 2016). Hence, the honeycomb-shaped micro structure on the skin of moisture-harvesting lizards most likely results in a superhydrophilic surface by maintaining a pre-wetted status. Such increased wettability allows for more rapid spreading of any additional droplets and the collection of greater amounts of water with the skin.

For thorny devils collecting additional water as little as 0.2% of their body weight (82.7 mg) has been found to be sufficient to fill the surface micro structure of 1.7 times their body surface (Comanns et al. 2016). A yet unresolved question is how lizards exactly access this water and pre-wet their skin. One hypothesis is that the micro structure as well as the spiny scales of moisture-harvesting lizards act as condensation foci yielding thermally-facilitated condensation in the early morning (Lasiewski and Bartholomew 1969; Gans et al. 1982; Comanns et al. 2011). Moist sand could also enable pre-wetting: Thorny devils have been observed to rub their ventral body surface on moist substrate and/or shovel moist sand onto their back (Sherbrooke 1993). These behaviors most likely reflect a mechanism to collect

---

[1] In educational books Cassie's law is often denoted as Cassie-Baxter law, although the original Cassie-Baxter law describes a droplet on a rough surface with entrapped air (Cassie and Baxter 1944).

small amounts of water. Especially the sand-shoveling behavior should result in a pre-wetting of the skin: it increases the contact area between lizard's skin and moist sand and additionally reduces the matric potential and utilizes gravitational force to absorb water from sand (Comanns et al. 2016).

4.4.2 Directional Water Transport in Channels

A rapid collection of water for drinking is essential in desert environments where temperatures increase rapidly in the morning and water starts to evaporate. However, a lizard's skin is relatively impervious to water, so it must have a means of drinking any water collected with the skin surface. The physical ability to harvest moisture includes a network of channels in between the imbricate overlapping scales. Capillary forces acting on the water within the channels result in a passive and typically symmetrical water spreading on the lizards' skin. To finally reach the mouth, hence enable drinking, the channels must be filled to a sufficient extent (Comanns et al. 2016). Lizard species have adapted to this demand differently: to facilitate drinking in the common case of collecting only droplets of water, the skin channels of thorny devils (*M. horridus*) exhibit convoluted features of their walls that greatly increase the internal surface area of the semi-tubular network. An enlargement of surface area by convolutions of the surrounding skin is considered to result in greater capillary forces and farther transport of the fluid (Sherbrooke et al. 2007; Comanns et al. 2016). On the other hand, the Texas horned lizard (*P. cornutum*) and the Horvath's toad-headed agama (*P. horvathi*) show a pre-determined flow direction towards the mouth (Comanns et al. 2015; Yenmiş et al. 2015). In case of the Texas horned lizard, this directionality leads to a 70% farther spreading towards the mouth compared to the opposed direction in the first 5 s (Comanns et al. 2015). The ecological role of this ability seems to be an efficient collection of water for drinking when harvesting even smaller amounts than necessary to fill the complete network of capillary channels.

The phenomenon of directional water transport on the Texas horned lizards' skin has been found to result from two geometric principles, namely the principles of "longitudinal asymmetry" and "interconnections" (Comanns et al. 2015). The asymmetry contributes to the liquid transport on a local level. Here, the liquid transport can be theoretically modeled with the Young-Laplace equation, also called Laplace's law (Berthier and Silberzan 2010; Comanns et al. 2015). One can abstract the lizard's channels between the scales into saw-tooth shaped capillaries with infinite depth[2], the simplest periodic, asymmetrically narrowing and widening capillary structure (Fig. 4.7A). A liquid droplet applied to this structure develops a meniscus at each free liquid-air interface, mainly depending on the surface tension γ between liquid and air (resulting in the contact angle θ) and on the geometry (angle α of the

---

[2] The influence of finite depth on the driving pressure difference is discussed in Buchberger et al. (2015).
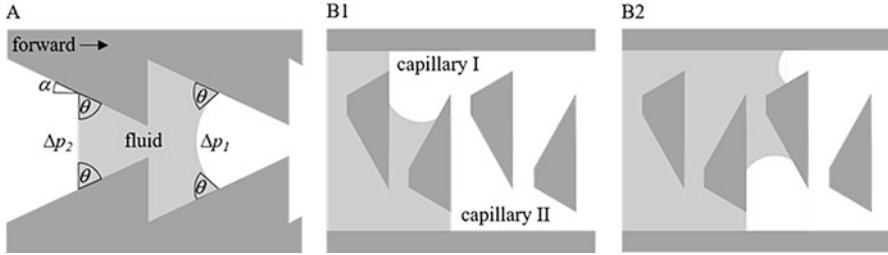
Fig. 4.7 Physical model of directional water spreading. (**A**) Functional principle of "longitudinal asymmetry" illustrated by a capillary channel of saw-tooth shape (top view). Here, the special case of $\Delta p_2 = 0$ is shown. (**B**) Functional principle of "interconnections" depicted for a two-capillary-network of saw tooth shaped channels (top view). (**B1**) The liquid front halts at the abrupt widening while it continues to flow in the neighbored capillary. (**B2**) The nearby interconnection between the capillaries results in merging with the halted liquid front for further liquid spreading. This "picking up" leads to an alternating fluid flow. Redrawn after Comanns et al. (2015)

capillary side wall). Passive transport of this liquid requires a positive capillary pressure difference Δp across the liquid interface. This capillary driving pressure can be calculated for narrowing sections (positive angle α of the capillary side wall) and widening sections (negative angle α) yielding

$$\Delta p = 2\gamma \cos(\theta - \alpha)\mathrm{d}(x)^{-1} \tag{4.4}$$

assuming a saw-tooth shaped capillary channel with a width $\mathrm{d}(x)$. For a concave curvature ($\Delta p > 0$), the liquid slug will move forward in the capillary, whereas a convex curvature ($\Delta p < 0$) retards the flow. When describing a liquid slug in the middle of the capillary channel, the curvatures of the liquid-air interfaces at the two sides (1 and 2) must be taken into account. As long as $\Delta p_1 > 0$ and $\Delta p_2 \leq 0$ liquid is transported unidirectional into the forward direction and halted in backward direction, respectively. If $\Delta p_1 > 0$ and $\Delta p_1 > \Delta p_2$, liquid will flow faster in forward than in backward direction.

The model of a saw-tooth shaped capillary channel allows only a local description of the observed liquid transport. In this structure the liquid would stop at the abrupt widening at the end of each narrowing section, a behavior not observed in nature. Interconnections, i.e. the capillary network found in moisture-harvesting lizards, facilitate an overcoming of the above mentioned stopping points (Fig. 4.7B) (Comanns et al. 2015). Thus, the principle of "interconnection" contributes to the directional water transport on a global level. This global transport can be physically modelled by combining a Poiseuille flow profile between two parallel plates with the model of a porous body, i.e. Washburn's law (Comanns et al. 2015).

The network of capillary micro-channels with their micro structured surface on the integument of lizards enables a rapid spreading of water, and is also adapted to the limited amount of water in arid regions: collected water is channeled to the snout for ingestion with the lowest possible loss. This is facilitated either by convolutions

reducing the channel width or by ensuring a preferred spreading direction towards the snout through asymmetric channels. Only a few species have been studied regarding such exploitation of collected water (Yenmiş et al. 2015; Comanns et al. 2015, 2016). Whether other lizards, snakes or turtles deploy similar mechanisms for extensive water usage has to be examined in future studies.

4.5   Outlook: Biomimetical Transfer

The directional water transport found in the Texas horned lizard results from two functional principles: (1) asymmetric channels with (2) specific interconnection. Using a biomimetic approach, these principles have been transferred to design a variety of artificial surfaces (in polymers and metal) that mimic the directional liquid transport (Buchberger et al. 2015; Comanns et al. 2015). Such surface functionality has much potential for various technical applications. For example, a more precise lubrication could lead to reduction of lubricants, hence to economic and environmental benefits. This applies for corresponding applications as well as fabrication processes. In fields of micro fluidics the half-open capillary system provides free access to the liquid and directional transport, no matter where the liquid is applied.

References

Alibardi, L. (2003). Adaptation to the land: The skin of reptiles in comparison to that of amphibians and endotherm amniotes. *Journal of Experimental Zoology Part B: Molecular and Developmental Evolution, 298*, 12–41.

Alibardi, L., & Maderson, P. F. (2003). Observations on the histochemistry and ultrastructure of the epidermis of the tuatara, *Sphenodon punctatus* (Sphenodontida, Lepidosauria, Reptilia): A contribution to an understanding of the lepidosaurian epidermal generation and the evolutionary origin of the squamate shedding complex. *Journal of Morphology, 256*, 111–133.

Andrade, D. V., & Abe, A. S. (2000). Water collection by the body in a viperid snake, Bothrops moojeni. *Amphibia-Reptilia, 21*, 485–492.

Ashton, K., & Johnson, J. (1998). *Crotalus viridis concolor* (Midget faded rattlesnake): Drinking from skin. *Herpetological Review, 29*, 170.

Auffenberg, W. (1963). A note on the drinking habits of some land tortoises. *Animal Behaviour, 11*, 72–73.

Bentley, P. J., & Blumer, W. F. C. (1962). Uptake of water by the lizard, *Moloch horridus*. *Nature, 194*, 699–700.

Berthier, J., & Silberzan, P. (2010). *Microfluidics for biotechnology*. London/Boston: Artech House.

Bormashenko, E. Y. (2013). *Wetting of real surfaces*. Berlin: Walter de Gruyter.

Bradshaw, S. D. (1986). *Ecophysiology of desert reptiles*. London: Academic.

Bradshaw, S. D., & Shoemaker, V. H. (1967). Aspects of water and electrolyte changes in a field population of *Amphibolurus* lizards. *Comparative Biochemistry and Physiology, 20*, 855–865.

Buchberger, G., Hischen, F., Comanns, P., Baumgartner, R., Kogler, A., Buchsbaum, A., Bauer, S., & Baumgartner, W. (2015). Bio-inspired microfluidic devices for passive, directional liquid transport: Model-based adaption for different materials. *Procedia Engineering, 120*, 106–111.

Bulova, S. J. (2002). How temperature, humidity, and burrow selection affect evaporative water loss in desert tortoises. *Journal of Thermal Biology, 27*, 175–189.

Cardwell, M. D. (2006). Rain-harvesting in a wild population of *Crotalus s. scutulatus* (Serpentes: Viperidae). *Herpetological Review, 37*, 142–144.

Cassie, A. B. D. (1948). Contact angles. *Discussions of the Faraday Society, 3*, 11–16.

Cassie, A. B. D., & Baxter, S. (1944). Wettability of porous surfaces. *Journal of the Chemical Society, Faraday Transactions, 40*, 546–551.

Channing, A., & Wahlberg, K. (2011). Distribution and conservation status of the desert rain frog *Breviceps macrops*. *African Journal of Herpetology, 60*, 101–112.

Cloudsley-Thompson, J. L. (1971). *The temperature and water relations of reptiles*. Watford: Merrow Publishing Co.

Cloudsley-Thompson, J. L. (1991). *Ecophysiology of desert arthropods and reptiles*. Berlin: Springer.

Cole, L. C. (1943). Experiments on toleration of high temperature in lizards with reference to adaptive coloration. *Ecology, 24*, 94–108.

Comanns, P., Effertz, C., Hischen, F., Staudt, K., Bohme, W., & Baumgartner, W. (2011). Moisture harvesting and water transport through specialized micro-structures on the integument of lizards. *Beilstein Journal of Nanotechnology, 2*, 204–214.

Comanns, P., Winands, K., Arntz, K., Klocke, F., & Baumgartner, W. (2014). Laser-based biomimetic functionalization of surfaces: From moisture harvesting lizards to specific fluid transport systems. *International Journal of Design & Nature and Ecodynamics, 9*, 206–215.

Comanns, P., Buchberger, G., Buchsbaum, A., Baumgartner, R., Kogler, A., Bauer, S., & Baumgartner, W. (2015). Directional, passive liquid transport: The Texas horned lizard as a model for a biomimetic 'liquid diode'. *Journal of the Royal Society Interface, 12*, 20150415.

Comanns, P., Withers, P. C., Esser, F. J., & Baumgartner, W. (2016). Cutaneous water collection by a moisture-harvesting lizard, the thorny devil *Moloch horridus*. *The Journal of Experimental Biology, 219*, 3473–3479.

Cooper, W. E., & Burns, N. (1987). Social significance of ventrolateral coloration in the fence lizard, *Sceloporus undulatus*. *Animal Behaviour, 35*, 526–532.

Cooper, W. E., & Sherbrooke, W. C. (2012). Choosing between a rock and a hard place: Camouflage in the round-tailed horned lizard *Phrynosoma modestum*. *Current Zoology, 58*, 541–548.

de Gennes, P., Brochard-Wyart, F., & Quéré, D. (2004). *Capillarity and wetting phenomena: Drops, bubbles, pearls, waves*. New York: Springer.

Ditmars, R. L. (1933). *Reptiles of the world*. New York: The MacMillan Company.

Douglass, J. F., & Layne, J. N. (1978). Activity and thermoregulation of the gopher tortoise (*Gopherus polyphemus*) in southern Florida. *Herpetologica, 34*, 359–374.

Fitzgerald, M. (1983). A note on water collection by the bearded dragon *Amphibolurus vitticeps*. *Herpetofauna, Sydney, 14*, 93.

Gans, C., Merlin, R., & Blumer, W. (1982). The water-collecting mechanism of *Moloch horridus* re-examined. *Amphibia-Reptilia, 3*, 57–64.

Glaudas, X. (2009). Rain-harvesting by the Southwestern Speckled Rattlesnake (*Crotalus mitchellii pyrrhus*). *The Southwestern Naturalist, 54*, 518–521.

Greene, H. W. (1986). *Natural history and evolutionary biology. Predator-prey relationships*. Chicago: Chicago Press.

Heath, J. E. (1962). Temperature-independent morning emergence in lizards of the genus *Phrynosoma*. *Science, 138*, 891–892.

Lasiewski, R. C., & Bartholomew, G. A. (1969). Condensation as a mechanism for water gain in nocturnal desert Poikilotherms. *Copeia, 1969*, 405–407.

Ligon, R. A., & McGraw, K. J. (2013). Chameleons communicate with complex colour changes during contests: Different body regions convey different information. *Biology Letters, 9*, 20130892.

Lillywhite, H. B. (2006). Water relations of tetrapod integument. *The Journal of Experimental Biology, 209*, 202–226.

Louw, G. N. (1972). The role of advective fog in the water economy of certain Namib Desert animals. *Symposia of the Zoological Society of London, 31*, 297–314.

Maderson, P. F. A., Rabinowitz, T., Tandler, B., & Alibardi, L. (1998). Ultrastructural contributions to an understanding of the cellular mechanisms involved in lizard skin shedding with comments on the function and evolution of a unique lepidosaurian phenomenon. *Journal of Morphology, 236*, 1–24.

Mata-Silva, V., Johnson, J. D., Rocha, A., & Dilks, S. (2014). Rainwater-harvesting by the rock rattlesnake, *Crotalus lepidus*, in the Chihuahuan Desert of western Texas. *The Southwestern Naturalist, 59*, 303–304.

Medica, P. A., Bury, R. B., & Luckenbach, R. A. (1980). Drinking and construction of water catchments by the desert tortoise, *Gopherus agassizii*, in the Mojave Desert. *Herpetologica, 36*, 301–304.

Mertens, R. (1960). *The world of amphibians and reptiles*. New York: McGraw-Hill.

Miller, D. (1985). Rain water drinking by the mangrove water snake, *Nerodia fasciata compressicauda*. *Herpetological Review, 16*, 71.

Minnich, J. E., & Shoemaker, V. H. (1972). Water and electrolyte turnover in a field population of the lizard, *Uma scoparia*. *Copeia, 1972*, 650–659.

Nagy, K. A. (1987). How do desert animals get enough water. In L. Berkofsky & M. G. Wurtele (Eds.), *Progress in desert research* (pp. 89–98). Totowa: Rowman and Littlefield.

Pearson, O. P. (1977). The effect of substrate and skin color on thermoregulation of a lizard. *Comparative Biochemistry and Physiology, 58*, 353–358.

Peterson, C. C. (1998). Rain-harvesting behavior by a free-ranging desert horned lizard (*Phrynosoma platyrhinos*). *The Southwestern Naturalist, 43*, 391–394.

Pfennig, D. (2012). Mimicry: Ecology, evolution, and development. *Current Zoology, 58*, 604–607.

Pianka, E. R., & Pianka, H. D. (1970). The ecology of *Moloch horridus* (Lacertilia: Agamidae) in Western Australia. *Copeia, 1970*, 90–103.

Powell, G. L., & Russell, A. P. (1985). Field thermal ecology of the eastern short-horned lizard (*Phrynosoma douglassi brevirostre*) in Southern Alberta. *Canadian Journal of Zoology, 63*, 228–238.

Repp, R. A., & Schuett, G. W. (2008). Western diamond-backed rattlesnakes, *Crotalus atrox* (Serpentes: Viperidae), gain water by harvesting and drinking rain, sleet, and snow. *The Southwestern Naturalist, 53*, 108–114.

Roberts, J. B., & Lillywhite, H. B. (1980). Lipid barrier to water exchange in reptile epidermis. *Science, 207*, 1077–1079.

Robinson, M. D., & Hughes, D. A. (1978). Observations on the natural history of Peringuey's adder, *Bitis peringueyi* (Boulenger) (Reptilia: Viperidae). *Annals of the Transvaal Museum, 31*, 189–193.

Sasaki, K., & Duvall, D. (2003). Rainwater drinking by free-ranging Japanese pitvipers, *Gloydius blomhoffii*. *Current herpetology, 22*, 43–44.

Schwenk, K., & Greene, H. W. (1987). Water collection and drinking in *Phrynocephalus helioscopus*: A possible condensation mechanism. *Journal of Herpetology, 21*, 134–139.

Seshadri, C. (1957). Water conservation in *Uromastix hardwickii* (Gray), with a note on the presence of Mullerian ducts in the male. *Journal of the Zoological Society India, 9*, 103–113.

Sherbrooke, W. C. (1981). *Horned lizards: Unique reptiles of Western North America*. Globe: Southwest Parks and Monuments Association.

Sherbrooke, W. C. (1990). Rain-harvesting in thelizard, *Phrynosoma cornutum*: Behavior and integumental morphology. *Journal of Herpetology, 24*, 302–308.

Sherbrooke, W. C. (1993). Rain-drinking behaviors of the Australian Thorny Devil (Sauria: Agamidae). *Journal of Herpetology, 27*, 270–275.

Sherbrooke, W. C. (1997). Physiological (rapid) change of color in horned lizards (*Phrynosoma*) of arid habitats: Hormonal regulation, effects of temperature, and role in nature. *Amphibia -Reptilia, 18*, 155–175.

Sherbrooke, W. C. (2002). Do vertebral-line patterns in two horned lizards (*Phrynosoma* spp.) mimic plant-stem shadows and stem litter? *Journal of Arid Environments, 50*, 109–120.

Sherbrooke, W. C. (2004). Integumental water movement and rate of water ingestion during rain harvesting in the Texas horned lizard, Phrynosoma cornutum. *Amphibia -Reptilia, 25*, 29–39.

Sherbrooke, W. C., Scardino, A. J., de Nys, R., & Schwarzkopf, L. (2007). Functional morphology of scale hinges used to transport water: Convergent drinking adaptations in desert lizards (*Moloch horridus* and *Phrynosoma cornutum*). *Zoomorphology, 126*, 89–102.

Stuart-Fox, D., Whiting, M. J., & Moussalli, A. (2006). Camouflage and colour change: Antipredator responses to bird and snake predators across multiple populations in a dwarf chameleon. *Biological Journal of the Linnean Society, 88*, 437–446.

Thompson, C. W., & Moore, M. C. (1991). Throat color reliably signals status in male tree lizards, *Urosaurus ornatus*. *Animal Behaviour, 42*, 745–753.

Vesely, M., & Modry, D. (2002). Rain-harvesting behavior in agamid lizards (*Trapelus*). *Journal of Herpetology, 36*, 311–314.

Walton, B. M., & Bennett, A. F. (1993). Temperature-dependent color change in Kenyan chameleons. *Physiological Zoology, 66*, 270–287.

Watson, G. S., Cribb, B. W., Schwarzkopf, L., & Watson, J. A. (2015a). Contaminant adhesion (aerial/ground biofouling) on the skin of a gecko. *Journal of the Royal Society Interface, 12*, 20150318.

Watson, G. S., Green, D. W., Schwarzkopf, L., Li, X., Cribb, B. W., Myhra, S., & Watson, J. A. (2015b). A gecko skin micro/nano structure – A low adhesion, superhydrophobic, anti-wetting, self-cleaning, biocompatible, antibacterial surface. *Acta Biomaterialia, 21*, 109–122.

Weese, A. O. (1917). An experimental study of the reactions of the horned lizard, *Phrynosoma modestum* Gir., a reptile of the semi-desert. *The Biological Bulletin, 32*, 98–116.

Weese, A. O. (1919). Environmental reactions of *Phrynosoma*. *The American Naturalist, 53*, 33–54.

Wenzel, R. N. (1936). Resistance of solid surfaces to wetting by water. *Industrial and Engineering Chemistry, 28*, 988–994.

Withers, P. C. (1993). Cutaneous water acquisition by the thorny devil (*Moloch horridus*, Agamidae). *Journal of Herpetology, 27*, 265–270.

Withers, P. C., & Dickman, C. R. (1995). The role of diet in determining water, energy and salt intake in the thorny devil *Moloch horridus* (Lacertilia: Agamidae). *Journal of the Royal Society of Western Australia, 78*, 3–11.

Yenmiş, M., Ayaz, D., Sherbrooke, W. C., & Veselý, M. (2015). A comparative behavioural and structural study of rain-harvesting and non-rain-harvesting agamid lizards of Anatolia (Turkey). *Zoomorphology, 135*, 137–148.

Chapter 5
The Velamen Radicum of Orchids: A Special Porous Structure for Water Absorption and Gas Exchange

Anita Roth-Nebelsick, Frank Hauber, and Wilfried Konrad

Abstract Aerial roots of epiphytic orchids cannot absorb water from the soil but supply the plant by collecting atmospheric water together with dissolved nutrients. A special outer tissue layer, the velamen radicum (VR), consisting of dead cells, is crucial for water interception and absorption. In this contribution, the VR is explored as an intricate porous material whose surface and structure is evolutionarily fine-tuned for water capture and absorption. After wetting, the VR is usually completely drained after less than two hours, as demonstrated by MRI (Magnetic Resonance Imaging). Furthermore, the MRI results indicate that the VR is drained homogeneously in such a way that no isolated water-filled parts occur. Interspecific differences in drainage time can be explained at least partially by differences in thickness and structure of the considered taxa: dehydration time of an aerial root increases with increasing thickness of the VR. Drainage behavior is, however, not completely dependent on thickness alone. Also porosity of the VR walls and the size of the single pores are of relevance. Aerial roots of leafless orchids are particularly astounding, because they conduct two tasks, water absorption and photosynthesis and show a very thin VR. Here, the exodermis, situated underneath the VR, probably contracts during dehydration, thereby restricting evaporation. The variability of external layers of aerial roots, VR and exodermis, very likely played a major role during the successful radiation of epiphytic orchids into various niches and habitats, and many functional features and special adaptations are still not well understood or are even undetected.

A. Roth-Nebelsick (✉)
State Museum of Natural History, Stuttgart, Germany
e-mail: anita.rothnebelsick@smns-bw.de

F. Hauber · W. Konrad
Department of Geosciences, University of Tübingen, Tübingen, Germany
e-mail: wilfried.konrad@uni-tuebingen.de

5.1 The Velamen Radicum

Many tropical orchids do not grow in soil but live as epiphytes on trees or bushes, with their roots attached to the bark or hanging freely in the air. These "aerial roots" can therefore not absorb water from the ground but are nonetheless responsible for water supply. In fact, aerial roots of epiphytic orchids are able to collect atmospheric water (rain, fog, mist, dew), together with dissolved nutrients (Barthlott and Capesius 1975; Benzing et al. 1983; Zotz and Winkler 2013). A special outer layer, the velamen radicum (VR), is crucial for the ability of aerial roots to procure water from the atmosphere (Fig. 5.1). The velamen radicum consists of dead cells and serves as an absorptive sheath from which the water is conducted into the living cortex.

Since the VR is composed of cell walls, which are the only structures left from the dead cells making up this layer, it is a "passive" tissue, meaning that no metabolic activities can be involved in its functional tasks. Despite its vital importance for water interception, functional details of the VR with respect to water absorption and conduction attracted not much scientific attention (Zotz and Winkler 2013). In fact, it was even suggested that the ability of the VR to absorb water would be quite limited (Dycus and Knudson 1957).

Orchids which rely on aerial roots as source of water supply occur in a wide variety of habitats, from shady and moist environments, such as the lower strata of rainforests, to exposed positions on rocks or woody plant stems in open and sunny environments. Under these different conditions, type and frequency of procurable atmospheric humidity differs greatly. Particularly in open environments with high potential evaporation, the occurrence of orchids with aerial roots appears to be astounding, because roots cannot regulate the gas permeability of their surface, as

Fig. 5.1 SEM (Scanning Electron Microscopy) picture showing a cross-section of an aerial root of *Dendrobium nobile*. The letters indicate the principal tissues of the aerial root: *E* Exodermis, *C* Cortex, *V* Vascular cylinder, *VR* Velamen radicum
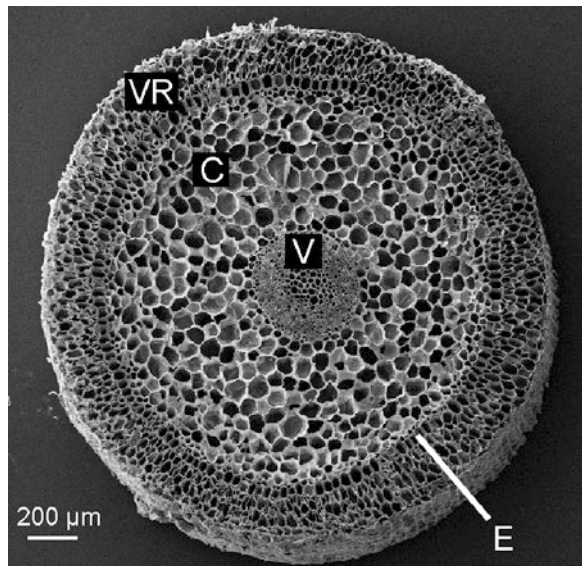
leaves are able to do. Additionally, in various groups leafless species have evolved all over the globe which entirely rely on aerial roots both for water and nutrient absorption as well as for photosynthesis – a unique role for roots.

Given the high selective pressure that acts on aerial roots with respect to their ability to water supply, it is to be expected that the structure of the "passive" velamen radicum is highly adapted in the various epiphytic orchid species to provide adequate water procurements. In this contribution, the velamen radicum will be explored as an intricate porous material whose surface and structure is evolutionarily fine-tuned for water capture and absorption.

5.2   The Structure of the Velamen Radicum

Aerial roots usually show an axisymmetric structure, with the VR as outermost layer, followed by the exodermis, cortex and the vascular cylinder (Fig. 5.1) (all SEM samples were prepared by critical point drying). The VR consists of one to several layers of dead cells from which only the cell walls remained (Fig. 5.2). The cells can be elongated, oriented parallel to the long axis of the root, or inclined. The VR cell walls are distinctly perforated, rendering the VR a basket-like appearance. The structure of the VR cells and their orientiation are species-specific (Fig. 5.2). In
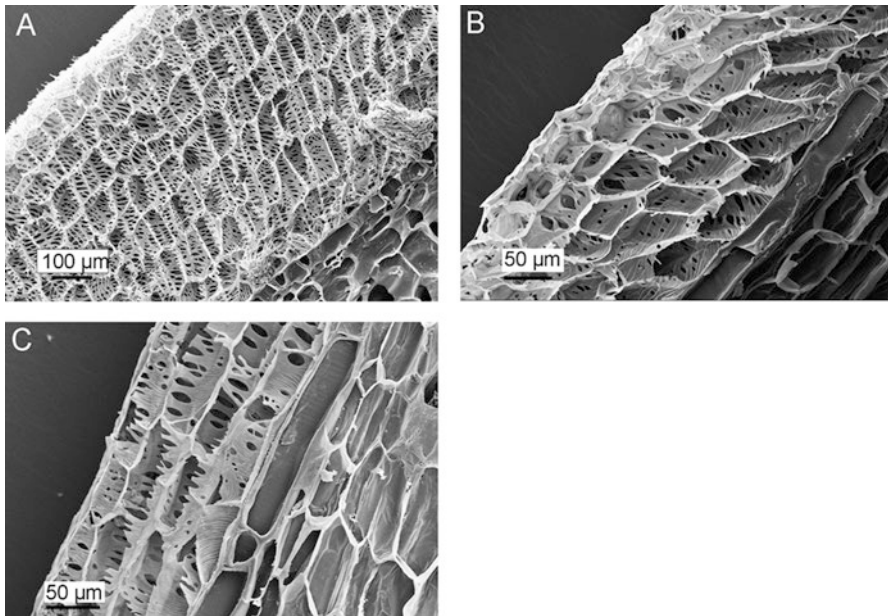
Fig. 5.2 SEM images of longitudinal sections of aerial roots, showing the VR. (**a**) *Dendrobium densiflorum*. (**b**) *D. nobile*. (**c**) *Epidendrum secundum*

Fig. 5.3 Aerial roots of *Microcoelia exilis*, in the dry state (upper picture) and after wetting (lower picture). The arrows indicate unwettable patches within the VR, termed as pneumathodes.

some species, the uppermost layer of the VR has a special structure, and is then termed as epivelamen.

In the dry state, aerial roots have a whitish-silvery appearance, due to total reflexion caused by air filling the VR cells (Fig. 5.3). Upon wetting and subsequent absorption of water into the VR, aerial roots of orchids turn green, revealing the existence of chloroplasts inside the living cortex cells (Fig. 5.3). All green aerial roots of orchids are capable of photosynthesis, but their assimilation rate is usually low and the roots are still dependent on the assimilating leaves for their sustenance (Goh et al. 1983), with the exception of leafless orchids whose aerial roots supply the plant not only with water but also with assimilates and which will be considered in the next section.

In contrast, special cells within the underlying layer, the exodermis, which conduct the water from the VR into the cortex, are vital, and various studies focus on their physiological functions that are probably essential for passing on water and nutrients.

In many groups, algae can be found in the VR which might represent – at least partially – symbiotic partners (Fig. 5.4) (Sanford and Adanlawo 1973; Carlsward et al. 2006a).

How fast is water drawn from the VR into the cortex, and in which way does the water flow? Figure 5.5 shows an exemplary MRI sequence (Magnetic Resonance Imaging, Siemens, 1.5T Magnetom Vision). Two aerial roots were scanned before and after wetting, and during the process of VR dehydration. One root was scanned at the middle region and the other one closer to the apex. The latter shows a brighter picture, indicating a somewhat higher water content. Upon wetting, the roots appear to become much wider because VR is visible on the MRI images after water absorption (Fig. 5.5). This process occurs rapidly. On later images, the diameter of the roots appears to decrease again, indicating the gradual dehydration of the VR. Rapid

Fig. 5.4 A VR cell of an aerial root of *Microcoelia exilis* showing unicellular green algae in its interior
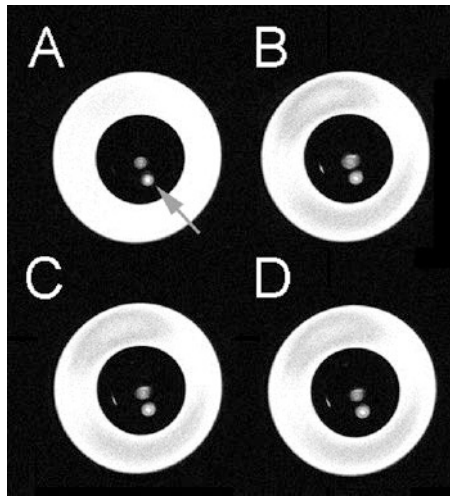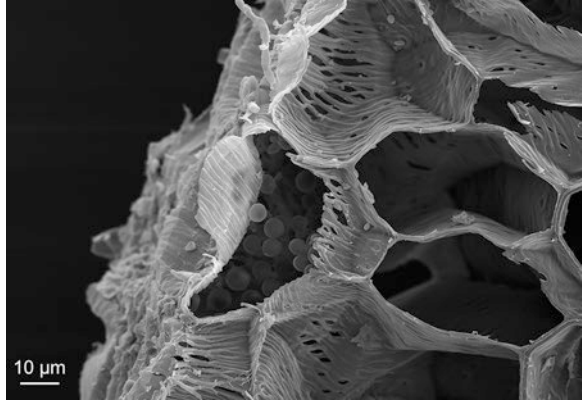
Fig. 5.5 MRI images of two aerial roots of *Dendrobium nobile* during water absorption. The two smaller circular objects in the centre are the aerial roots, showing a diameter of about 2 mm. One root is scanned closer to the apex (grey arrow in **a**), the other one within the middle region. Brightness increases with increasing water content. For imaging, 20 layers with a pixel size of 0.1 × 0.1 mm and a thickness of 0.5 mm were scanned. (**a**) Before wetting. (**b**) 30 min after wetting. (**c**) 60 min after wetting, (**d**) 120 min after wetting

water absorption of the VR was also demonstrated gravimetrically by Zotz and Winkler (2013), while water loss from the VR took much longer times.

Water loss from the VR can be either due to evaporation or conduction into the cortex. In the MRI images, particularly the diameter of that root which appeared to show a lower water content decreases, indicating water uptake by the cortex (Fig. 5.5). This interpretation is also supported by the circumstance that the centre of the originally less hydrated root becomes brighter when the visible part of the VR starts to shrink (Fig. 5.5).
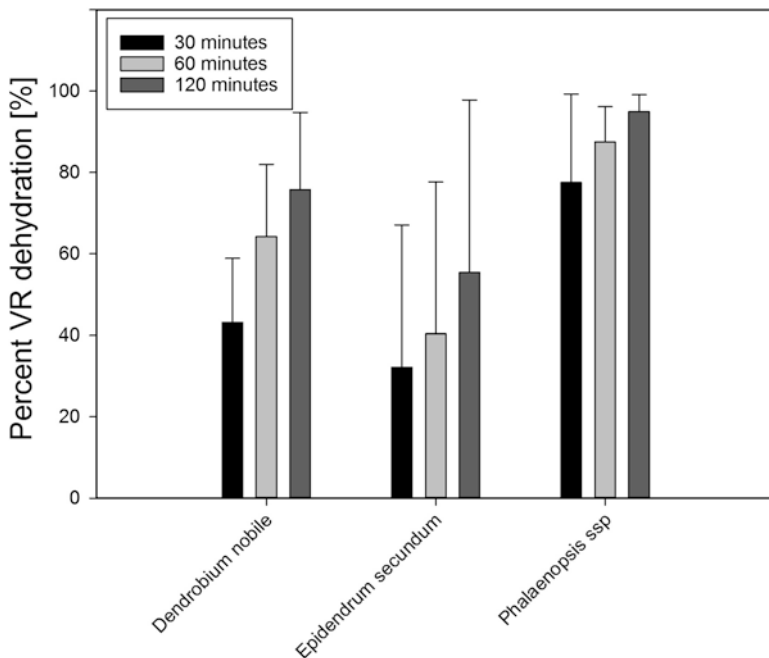
Fig. 5.6 Dehydration dynamics of the aerial roots of three different species, determined by image analysis of MRI images. The columns represent mean values, and the whiskers within the columns indicate standard deviation

Table 5.1 Thickness of the VR and number of VR cell layers of the taxa for which MRI imaging studies of the VR drainage process were conducted

Species	VR thickness [μm]	Number of cell layers
Dendrobium nobile	245	5
Epidendrum secundum	192	4
Phalaenopsis ssp.	72	2

After less than 2 h, the VR is usually completely drained in all considered species (Fig. 5.6). As indicated by the MRI images, the VR is drained homogeneously in such a way that no isolated water-filled parts occur.

Data obtained by image analysis of MRI series indicate substantial differences between aerial roots of different species which can be explained at least partially by the structure of the VR. The differences in the drainage times are due to differences in thickness and structure of the considered taxa (Table 5.1).

An aerial root with a shallow VR dehydrates rapidly, as was already shown experimentally (Zotz and Winkler 2013) and in agreement with results showing positive correlation between VR thickness and dry habitat (Sanford and Adanlawo 1973). There can be, however, considerable differences between aerial roots showing thicker VR, and the drainage time is not completely dependent on the thickness

Fig. 5.7 Size of pores within the cell walls of the VR of various orchid species. Because the pores are not circular, their size is shown as area, and plotted as $\log_{10}$. The data are shown as box plots spanning the 50% interquartile, with the horizontal line representing the median value, the whiskers the highest and lowest value. Single outliers are drawn as dots
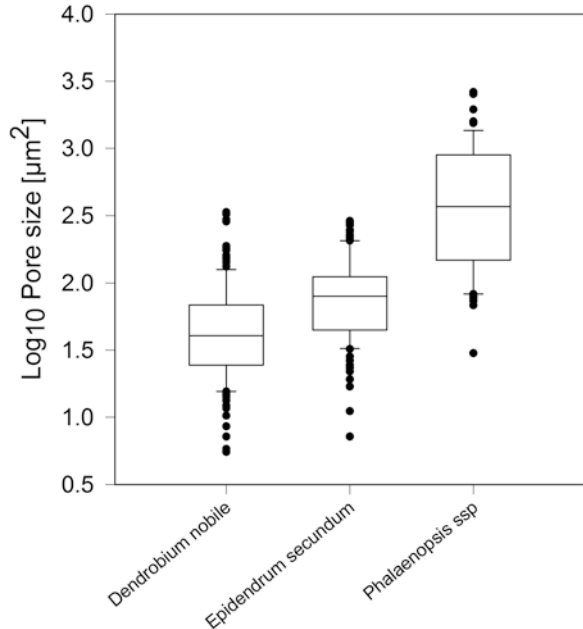
alone. When placed upon aerial roots of the three taxa, drops with a volume of about 9 µl are absorbed faster by *D. nobile* than by *E. secundum*, despite the latter showing a somewhat thicker VR (Fig. 5.6). The VR of *D. nobile* and *E. secundum* differ with respect to the porosity of their cell walls (Fig. 5.7). In *E. secundum*, the VR walls show larger pores, leading to a higher permeability and therefore to a lower drainage time, while *Phalaenopsis ssp.* not only shows a thinner VR but also the largest pores in the VR walls (Fig. 5.7).

5.3 The Special Case of Leafless Orchids

In leafless epiphytic orchids, aerial roots represent the only autotrophic parts of the plants, and have therefore to be fully functional with respect to both photosynthesis and water procurement (Fig. 5.8) (Benzing et al. 1983; Carlsward et al. 2006b). Particularly aerial roots of leafless orchids are astounding plant organs, because they are able to fully conduct two tasks, water absorption and photosynthesis which are partially in conflict with each other and are therefore usually assigned to separate plant organs: roots (water and nutrient absorption) and leaves (photosynthesis). Because photosynthesis requires gas exchange with the air to let CO_2 diffuse into the leaf interior, leaves are generally equipped with a cuticle (a wax layer showing a low permeability) and stomata (micropores which can be opened and closed). Both structures allow for a controlled gas exchange.

Fig. 5.8 *Microcoelia exilis*, a leafless orchid

Cuticle and stomata are also absent from aerial roots of leafless orchids, making their ability to serve both as water-absorbing and assimilating organ particularly remarkable. This concerns not only the ability to avoid dehydration of the cuticle-less aerial root, but to reconcile gas exchange and water absorption, because a moist VR hampers diffusion of CO_2 into the root interior. In fact, the ability of aerial roots of leafless orchids to conduct sufficient photosynthesis as well as to serve as water-absorbing organ has puzzled researchers for quite a long time (Haberlandt 1914; Jonsson 1981).

In leafless orchids, adaptations to reconcile the conflicting tasks of photosynthesis and water absorption should therefore be particularly promoted. At this point, a special type of photosynthetic pathway should be mentioned which is utilized also by aerial orchid roots: Crassulaceaen Acid Metabolism, or CAM photosynthesis. CAM is characterized by nocturnal uptake of CO_2 and its storage into malic acid, conducted by the PEP carboxylase using hydrocarbonate as substrate. The CO_2, which is stored in this way during the night, is released the following day by de-acidification, and subsequently fixed by Rubisco.

Leaves of CAM plants usually show a diurnal course of gas permeability, their stomata are open during the night, and close after dawn. The advantage of this process is that gas exchange occurs during conditions which provide usually a much lower humidity gradient between atmosphere and plant interior, due to the higher nocturnal air humidity. A plant utilizing CAM loses less water vapor during CO_2 uptake, and, consequently, CAM is characteristic for plants living under drier conditions. The Crassulaceae, the plant group after which this special photosynthesis type was named, are typical inhabitants of dry and hot places, often with poor or shallow substrate. CAM, however, comes at a price since the pre-fixation process needs metabolic energy, and so CAM is only economic when water supply is limited.

In the following we will focus on *M. exilis* as a representative of leafless orchids. *M. exilis* can be found in different habitats in tropical South East Africa including Madagascar, mostly in riverine forests and woodland (Fig. 5.8). There it is usually located on smaller branches of understorey trees and bushes at partially exposed
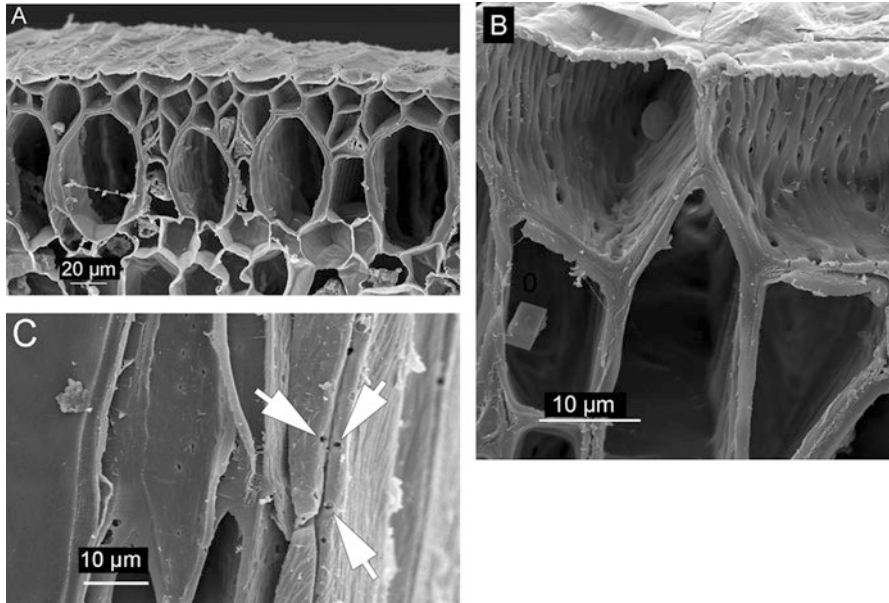
Fig. 5.9 SEM images showing the VR of *M. exilis.* (**a**) Cross-section, with the uppermost layer forming an epivelamen. (**b**) Detail of two epivelamen cells, showing pores in their lateral walls. (**c**) Longitudinal section through the VR, showing small pores (arrows)

positions (Jonsson 1981), being thus exposed to quite dry air and various insolation conditions during the day.

A cross-section of the aerial roots of *M. exilis* reveals a very thin VR of the Vanda type (Porembski and Barthlott 1998; Carlsward et al. 2006a), consisting of only 2–3 cell layers, with an epivelamen as the uppermost layer (Fig. 5.9a). Additionally, the VR cells are quite narrow, and the total thickness of the VR amounts to about 20–30 μm. The shallowness of the VR is astounding, considering the typical habitats of *M. exilis*, and the circumstance that various data indicate evaporative water loss from the VR to decrease with increasing VR thickness (Benzing et al. 1983; Zotz and Winkler 2013). So how do the aerial roots of *M. exilis* maintain their hydrated state and reconcile water absorption and photosynthesis?

Inspection of the surface of the VR reveals that the outer epivelamen wall is quite thin, with the internal side showing a finely fibrillar structure (Fig. 5.9b). The lateral walls of the VR show quite small pores (Fig. 5.9a, b). Pores at the surface edges of lateral walls are partially visible in top view or in longitudinal sections (Fig. 5.9c). In *M. exilis*, the cell walls are thus much less perforated than in aerial roots of leaf-bearing orchids, probably to reduce gas permeability of the thin VR. The shallowness of the VR, which appears at first sight to be problematic for an aerial root with respect to water conservation, represents very likely an adaptation to prevent the development of a thick water-filled layer, and to minimize the distance between atmosphere and assimilating cortex cells.

Fig. 5.10 SEM image showing details from the exodermis of the aerial root of *M. exilis*. *P* Passage cell, *U* U-cells. Arrow shows cover cell between the passage cell and the VR
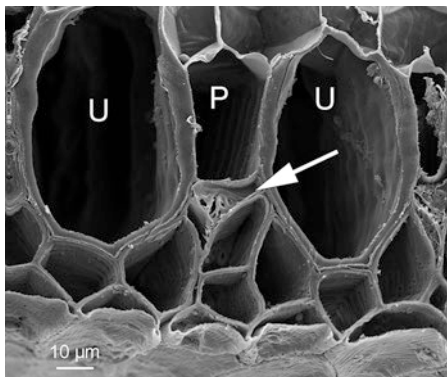
The storage capacity of the VR is, however, small and humidity has to be absorbed as fast as possible by the passage cells. Water absorption occurs in fact quite rapidly, and the VR becomes dry again after less than 10 min of complete wetting or earlier, indicated by regaining total reflexion. Furthermore, the pneumathode areas are quite dense and spacious, maintaining unrestricted gas exchange under humid conditions (Fig. 5.3). It was shown by Jonsson (1981) that the unwettability of the pneumathode areas is due to membranes closing the pores in the walls of the epivelamen cells.

The exodermis cells are thickened and impermeable to water, and the transfer of water into the cortex is performed by living passage cells, as in other orchids (Fig. 5.10). These cells are connected to the VR via specially structured cells, the cover cells (Fig. 5.10, arrow). Above the passage cells, VR cells become smaller and more angular, showing a graded structure towards the water-absorbing spots. This structure very likely supports rapid and continuous absorption of water and nutrients by forming a wick-like passage conducting water towards the passage cells.

All in all, the VR structure of *M exilis* appears to be designed in such a way as to reconcile rapid absorption of humidity with reducing risk of evaporation and therefore water loss from the VR. Is this, however, sufficient to compensate for the shallow VR? The VR and the underlying exodermis are functionally coupled, not only with regard to the passage cells which are specialized exodermis cells. The main cell type, making up most of the exodermis, is dead in its functional state. This cell type shows a conspicuous structure, with the outer (= facing the VR) and lateral cell walls massively thickened (Figs. 5.10 and 5.11). According to this structure, these cells are termed "U-cells" (Carlsward et al. 2006a). The inner (= facing the cortex proper) edges of the thickened lateral cell walls which are attached to the outer cortex cells form conspicuous angular contact zones (Fig. 5.11b, arrow), providing obviously a tight and rigid fixation mechanism. The U-cells and the cortex are mechanically coupled. The inner cell wall of the U-cells is unthickened and can therefore bend and possibly stretch (Figs. 5.10 and 5.11).
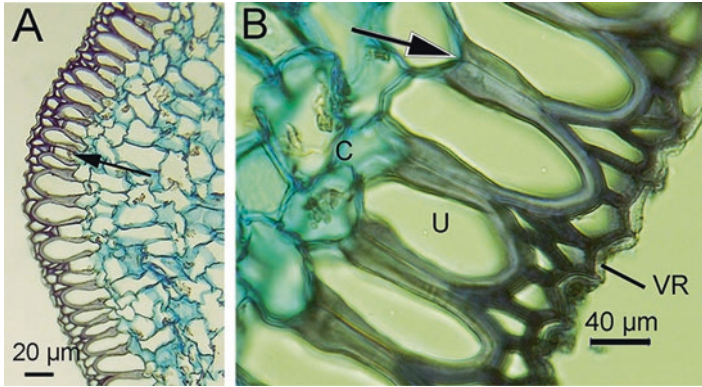
Fig. 5.11 Light microscope images showing details from the peripheral region of cross-sections of the aerial roots of *M. exilis*. (**a**) Exodermis, showing U-cells which make up the majority of this layer, and a passage cell (arrow) seated within. (**b**) A magnification showing U-cells (U) and their thickened cell walls (lateral walls and the bow-shaped wall facing the VR). The thickened lateral walls are tightly connected to the cortex cells (arrow)
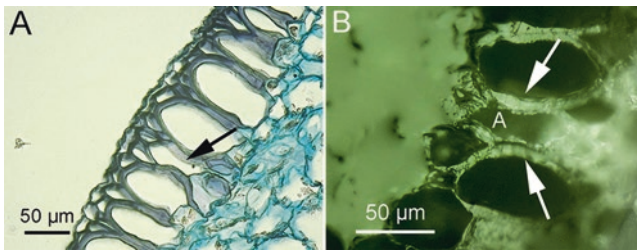
Fig. 5.12 Light microscope images, showing aeration cells within the exodermis of *M. exilis*. (**a**) Direct light image. The aeration cell is indicated by the black arrow, seated between two U-cells. The walls of the aeration cells are not thickened, and the lateral walls of the neighbouring U-cells are bulging into the aeration cell. (**b**) Incident light image, showing a surface view onto a freshly aerial root of *M. exilis*. The aeration cell is marked by "A". White arrows indicate the walls of U-cells which are adjacent to the aeration cell

Besides the passage cells, the exodermis comprises another special exodermis cell type, located underneath the pneumathode areas (Fig. 5.12). These cells are also dead in the functional state, and will be termed as "aeration cells" in the following, because they very probably conduct air (Haberlandt 1914; Benzing et al. 1983; Carlsward et al. 2006a).

In cross-sections, aeration cells appear as bottle-shaped elements inserted between U-cells, with the "bottleneck" oriented towards the cortex proper (Fig. 5.12). The thickened lateral walls of the adjacent U-cells appear to be bow-shaped and bulging into the lumen of the aeration cells. The special structure of the U-cells may allow for transferring a deformation of the cortex, caused by hydration and dehydration, to the exodermis. Upon dehydration, the cortex will lose volume,
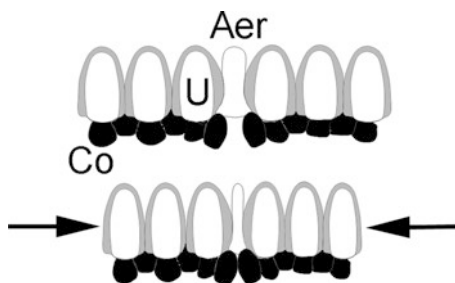
Fig. 5.13 Schematic drawing of the putative closing mechanism of the aeration cell (Aer). When the cortex cells (Co) shrink due to water loss, the exodermis will contract since the U-cells (U) are tightly connected to one another and to the cortex. This contraction pinches together the lateral walls of the aeration cell. Furthermore, intercellular spaces below the aeration cell will shrink because the cortex cells will come closer to each other

and the exodermis will contract. As already suggested by Benzing et al. (1983), a shrinking cortex may trigger a mechanism which closes the aeration cell. When the exodermis contracts, the adjacent lateral U-cell walls will come closer to each other, thereby closing the "bottleneck" of the aeration cells by pinching it together (Fig. 5.13). In this way, the permeability of the gas-conducting pathway will be reduced. The aerial roots of *M. exilis* may therefore be equipped with a simple but effective gas permeability control system which differs completely from the stomatal system of leaves.

5.4   Final Remarks

The strong selective pressure acting upon the aerial roots of orchids has led to the evolution of surfaces with impressing functional structures and strategies for water absorption, conservation and gas exchange. The VR and the underlying exodermis together form a surface unit with a high constructional diversity. Since the cells of the VR are dead in the functional state, as well as most cell types of the exodermis, with the exception of the passage cells, the working mechanisms run without the activities of living cells, solely based on processes such as capillarity within a graded porous structure (the VR) which promotes rapid water absorption but decreasing evaporation, and dehydration-triggered deformations.

Considering the wide differences in habitat conditions of epiphytic orchids and their structural variety, it is probable that various novel functional principles are still undetected. This concerns also quite "straightforward" and basic processes, such as the processes of water interception and water absorption. Are there VR types which are particularly fine-tuned to absorb different kinds of atmospheric water (dew, rain, mist)? What exactly is the functional background of the different porosity structures

and angular cell wall arrangements which can be found in the VR? The VR and the exodermis as external layers which regulate and mediate the contact of the aerial root to its surroundings and simultaneously protect it from harmful influences, have, however, to fulfil multiple tasks, such as protection against UV, pathogens and also mechanical abrasion (Chomicki et al. 2014). It is quite probable that the external layers of their aerial roots, VR and exodermis, with their variability and adaptability, played a major role during the successful radiation into various niches and habitats of epiphytic orchids, and many functional features and special adaptations of the VR and the exodermis are still not well understood or even undetected.

References

Barthlott, W., & Capesius, I. (1975). Mikromorphologische und funktionelle Untersuchungen am Velamen radicum der Orchideen. *Berichte Deutsche Botanische Gesellschaft, 88*, 379–390.

Benzing, D. H., Friedman, W. E., Peterson, G., & Renfrow, A. (1983). Shootlessness, velamentous roots, and the pre-eminence of Orchidaceae in the epiphytic biotope. *American Journal of Botany, 70*, 121–133.

Carlsward, B. S., Stern, W. L., & Bytebier, B. (2006a). Comparative vegetative anatomy and systematics of the angraecoids (Vandeae, Orchidaceae) with an emphasis on the leafless habit. *Botanical Journal of the Linnean Society, 151*, 165–218.

Carlsward, B. S., Whitten, W. M., Williams, N. H., & Bytebier, B. (2006b). Molecular phylogenetics of Vandeae (Orchidaceae) and the evolution of leaflessness. *American Journal of Botany, 93*, 770–786.

Chomicki, G., Bidel, L. P. R., Ming, F., Coiro, M., Zhang, X., Wang, Y., Baissac, Y., Jay-Allemand, C., & Renner, S. S. (2014). The velamen protects photosynthetic orchid roots against UV-B damage, and a large dated phylogeny implies multiple gains and losses of this function during the Cenozoic. *The New Phytologist, 205*, 1330–1341.

Dycus, A. M., & Knudson, L. (1957). The role of the velamen of the aerial roots of orchids. *Botanical Gazette, 119*, 78–87.

Goh, C. J., Arditti, J., & Avadhani, P. N. (1983). Carbon fixation in orchid aerial roots. *The New Phytologist, 95*, 367–374.

Haberlandt, G. F. J. (1914). *Physiological plant anatomy*. London: McMillan.

Jonsson, L. (1981). *A monograph of the genus Microcoelia (Orchidaceae)*, *Symbolae Botanicae Upsalienses XXII (4)*. Stockholm: Almqvist & Wiksell International.

Porembski, S., & Barthlott, W. (1998). Velamen radicum micromorphology and classification of Orchidaceae. *Nordic Journal of Botany, 8*, 117–137.

Sanford, W. W., & Adanlawo, I. (1973). Velamen and exodermis characters of West African epiphytic orchids in relation to taxonomic grouping and habitat tolerance. *Botanical Journal of the Linnean Society, 66*, 307–321.

Zotz, G., & Winkler, U. (2013). Aerial roots of epiphytic orchids: The velamen radicum and its role in water and nutrient uptake. *Oecologia, 171*, 733–741.

Chapter 6
Sucking the Oil: Adsorption Ability of Three-Dimensional Epicuticular Wax Coverages in Plants As a Possible Mechanism Reducing Insect Wet Adhesion

Elena V. Gorb, Philipp Hofmann, Alexander E. Filippov, and Stanislav N. Gorb

Abstract Primary aerial surfaces of terrestrial plants are very often covered with three-dimensional epicuticular waxes. Such wax coverages play an important role in insect-plant interactions. Wax blooms have been experimentally shown in numerous previous studies to be impeding locomotion and reducing attachment of insects. Among the mechanisms responsible for these effects, a possible adsorption of insect adhesive fluid by highly porous wax coverage has been proposed (adsorption hypothesis). Recently, a great decrease in insect attachment force on artificial adsorbing materials was revealed in a few studies. However, adsorption ability of plant wax blooms was still not tested. Using a cryo scanning electron microscopy approach and high-speed video recordings of fluid drops behavior, followed by numerical analysis of experimental data, we show here that the three-dimensional epicuticular wax coverage in the waxy zone of *Nepenthes alata* pitcher adsorbs oil: we detected changes in the base, height, and volume of the oil drops. The wax layer thickness, differing in samples with untreated two-layered wax coverage and treated one-layered wax, did not significantly affect the drop behavior. These results provide strong evidence that three-dimensional plant wax coverages due to their adsorption capability are in general anti-adhesive for insects, which rely on wet adhesion.

E. V. Gorb (✉) · P. Hofmann · S. N. Gorb
Department of Functional Morphology and Biomechanics, Zoological Institute, Kiel University, Kiel, Germany
e-mail: egorb@zoologie.uni-kiel.de

A. E. Filippov
Department of Functional Morphology and Biomechanics, Zoological Institute, Kiel University, Kiel, Germany

Department N5, Donetsk Institute for Physics and Engineering, Donetsk, Ukraine

6.1 Introduction

Epicuticular waxes are cuticular lipids, which are complex mixture of cyclic (e.g. triterpenoids) and long-chain aliphatic compounds, such as primary and secondary alcohols, primary aldehydes, fatty acids, and alkanes (Barthlott et al. 1998; Jetter et al. 2006), deposited onto the plants surface (Jeffree 2006). They cover all aerial primary surfaces of higher plants in the form of relatively smooth two-dimensional films or layers, from which also three-dimensional projections can emerge (Jeffree 1986). Two-dimensional waxes vary in thickness from extremely thin films consisting of a few molecular layers in aquatic plants to noticeable crusts up to 0.5 mm thick in land plants. Three-dimensional wax projections, which originate by self-assembly (e.g. Jeffree et al. 1975; Jetter and Riederer 1994, 1995; Meusel et al. 2000; Koch and Ensikat 2008), range in size from 0.5 to 100 μm (Barthlott et al. 1998; Koch et al. 2010) and show various morphologies ─ platelets, rodlets, tubules, threads etc. (Barthlott et al. 1998). The morphology of wax projections depends on the chemical composition of the wax and is determined by the dominating chemical compound or compound class (Barthlott et al. 1998; Jetter et al. 2006; Bargel et al. 2006).

Epicuticular waxes play an important role in interactions between plants and their environment, also in insect-plant interactions. They protect plants against herbivory, are involved in the so called greasy pole syndrome preventing the robbery of nectar and other resources by ants, serve as a selective barrier protecting associated ants against non-specialised ant species on stems of myrmecophylic species, impair attachment, locomotion, and foraging behaviour of predatory and parasitoid insects, contribute to temporary capture of pollinators in plants with kettle trap flowers, and play a key role in prey capturing and retention by trapping organs (pitchers) of carnivorous plants (reviewed by Gorb and Gorb (2013)).

It is a well-known fact that plant surfaces bearing wax projections decrease the insect locomotion (reviews by Eigenbrode (1996) and Müller (2006)). The effect of the three-dimensional wax coverages on insect attachment has been experimentally studied using different approaches with a number of insect species and some plant species. Insects usually showed successful attachment to the smooth surfaces without wax or with removed wax bloom, but performed poorly on the surfaces covered with wax projections (see review by Gorb and Gorb (2013)). Not only the presence of wax, but also the projection size and density of the wax coverage may affect insect attachment. This was observed on plant surfaces and additionally revealed on bio-inspired artificial wax-covered surfaces (Gorb et al. 2008, 2014b). However, most plant wax surfaces studied only temporarily reduced the attachment ability of insects (Gorb and Gorb 2002).

We have previously proposed four hypotheses explaining the mechanisms of insect adhesion reduction on plant surfaces covered with three-dimensional epicuticular waxes (Gorb and Gorb 2002). (1) Wax projections create micro-roughness, which greatly decreases the real contact area between the plant surface and insect attachment organs called adhesive pads (roughness hypothesis). (2) Wax projections are easily detachable structures contaminating insect pads (contamination hypoth-

esis). (3) Highly porous wax coverage may absorb the fluid secretion from the insect pad surface (fluid absorption hypothesis). (4) Insect pad secretion may dissolve epicuticular plant waxes (wax dissolving hypothesis). This would result in the appearance of a thick layer of fluid, making the plant surface slippery.

Recently, only the first two hypotheses have been experimentally tested. The effect of surface roughness on insect attachment has been revealed in a number of studies showing the worst insect attachment on rough substrates with a nominal asperity size of 0.3 and 1.0 μm (e.g. Gorb 2001; Peressadko and Gorb 2004; Voigt et al. 2008; Bullock and Federle 2009) corresponding to those in most wax-covered plant surfaces. Also the contamination of insect pads by the plant waxes has been detected for several insect and plant species (Juniper and Burras 1962; Stork 1980; Eigenbrode et al. 1999; Gaume et al. 2004; Gorb et al. 2005; Gorb and Gorb 2006a). It has been found that plants differ in their contaminating effects on insect pads: the contaminating ability depended on the micro-morphology of the wax projections and was related to both the largest dimension and the aspect ratio of the projections (Gorb and Gorb 2006a).

As for the fluid adsorption hypothesis, only a very few relevant studies demonstrating the effect of the fluid reduction on the insect attachment to artificial surfaces have been performed. The essential reduction or even the loss of the attachment ability on smooth substrates after treating the pads of the bug *Rhodnius prolixus* with lipid solvent or after walking of the aphid *Aphis fabae* on silica gel for a certain time were recorded (Edwards and Tarkanian 1970; Dixon et al. 1990). A significant attachment force reduction caused by a decrease of the pad secretion was measured in the stick insect *Carausius morosus* on smooth polyimide substrates that selectively adsorbed the watery component of the secretion (Dirks et al. 2010). Also rough nano-porous substrates highly reduced the attachment forces of the beetle *Coccinella septempunctata* if compared to smooth solid substrates (Gorb et al. 2010). Since the comparison of the changes in contact angles of water and oil between solid and nano-porous surfaces indicated a strong adsorption ability of the nano-porous samples for both polar and non-polar fluids, it was concluded that due to their high porosity, the nano-porous samples can adsorb the fluid from insect pads, thereby reducing insect attachment.

However, information on the adsorption ability of three-dimensional epicuticular waxes in plants is lacking in literature. The aim of the present study was to test whether the wax coverage of the waxy zone in the pitcher of the carnivorous plant *Nepenthes alata* is able to adsorb fluids. The wax bloom of *N. alata* was used here as a model plant system because it has been comprehensively studied previously in regards to its micro-morphology (Gorb et al. 2005, 2013; Gorb and Gorb 2009; Benz et al. 2012) as well as physicochemical (Gorb and Gorb 2006b) and material properties (Gorb et al. 2005, 2014a). The main functions of this pitcher surface are prey trapping and retention fulfilled through the reduction of insect attachment (e.g. Gaume et al. 2002, 2004; Gorb et al. 2005; Scholz et al. 2010). Additionally, the two-layered structure of the wax coverage (Fig. 6.1a) made it possible to vary the porous layer thickness.
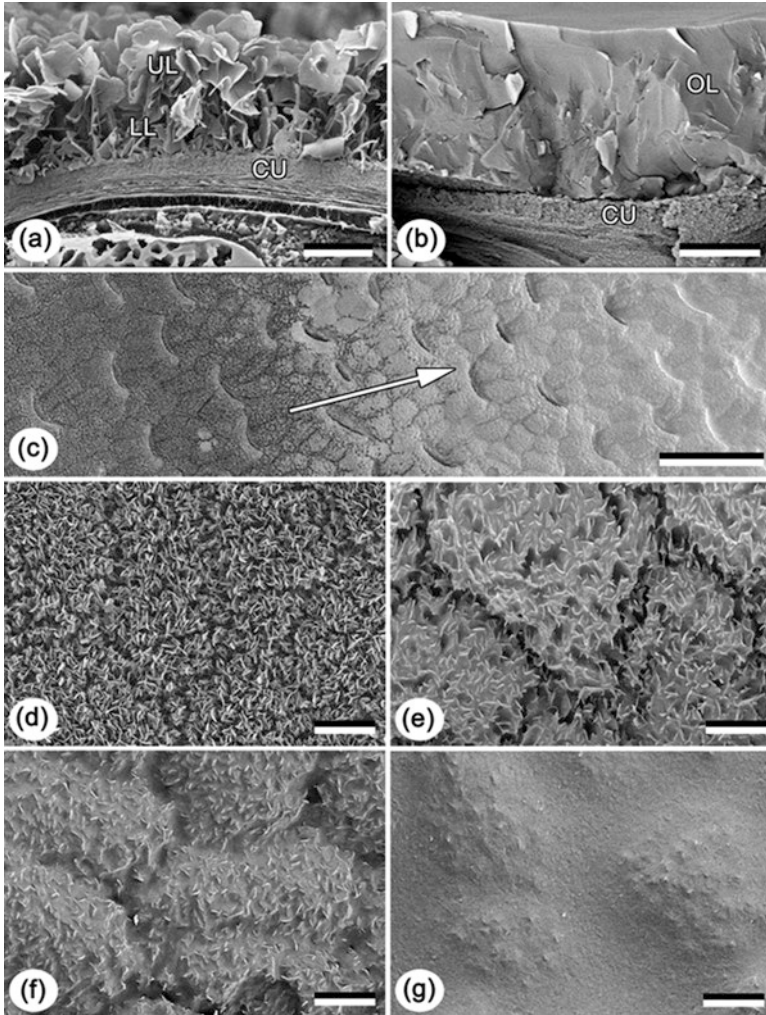
Fig. 6.1 Cryo scanning electron microscopy (SEM) images of the wax coverage in the *Nepenthes alata* pitcher. (**a**) intact; (**b–g**) after applying the oil drops onto the pitcher surface. (**a**, **b**): cryo fracture; (**c–g**): view from above. Arrow in (**c**) indicates the gradient from uncovered (dark) to completely wetted/oil-adsorbing (bright) regions shown at high magnifications in (**d–g**), respectively. *CU* cuticle; *LL* lower wax layer; *OL* oil adsorbed by the wax coverage; *UL* upper wax layer. Scale bars: 2 μm (**a**, **b**), 10 μm (**d–g**) and 100 μm (**c**)

We performed experiments with the *N. alata* pitcher surfaces bearing either intact, two-layered wax coverage (UL) or only one, lower wax layer (LL) after the upper wax projections were mechanically removed. As in nature, the upper wax projections can be dislodged from the waxy zone by insects trying to escape from the trap, we used both UL and LL pitcher samples in this study. The artificial smooth solid sample (SS) served as a reference surface. We measured adsorption rates of

two fluids—polar double-distilled water and non-polar mineral oil. Water was used to simulate the watery phase of the bi-phasic (water-oil emulsion) adhesive pad secretion reported for locusts, stick insect, ants, and flies (e.g. Gorb 2001; Vötsch et al. 2002; Drechsler and Federle 2006; Dirks and Federle 2011; Gerhardt et al. 2015, 2016; Reitz et al. 2015; Betz et al. 2016). The oil was employed as a rough approximation of the oily pad secretion found previously in beetles (e.g. Ishii 1987; Kosaki and Yamaoka 1996; Eisner and Aneshansley 2000; Attygalle et al. 2000; Geiselhardt et al. 2009).

6.2   Results

6.2.1   Modification of the Water Drops

With the only exception of the contact angles ($94.50 \pm 1.09°$ on SS, $140.76 \pm 3.67°$ on UL, $151.60 \pm 2.84°$ on LL) (Fig. 6.2a), the behavior of the water drops was very similar on all tested surfaces. We observed no changes in the drop shape during the experimental time of 30 s. The drop base usually remained the same. The drop height either did not change or was reduced by up to 1.5% of the initial value on both UL and LL or by 0.5–5.0% of the initial value on SS. The loss of the drop volume accounted for 0.5–2% of the initial value. The volume V decreased gradually and showed similar linear dependence on time t for all tested surfaces: $V = -0.001\,t$ (n = 7) on SS, $V = -0.0013\,t$ (n = 6) on UL and $V = -0.0008\,t$ (n = 6) on LL (one way ANOVA: $F_{2,18} = 3.118$, P = 0.072) (Fig. 6.2b).

6.2.2   Modification of the Oil Drops

In the case of the oil, which readily wetted all test surfaces (Fig. 6.3, upper row), the drops behaved differently during 30 s of the experiment depending on the surface (Fig. 6.3). On SS (Fig. 6.4), the spreading was accompanied by the continuous growth of the drop base (by 21–38% of the initial value) and continuous decrease in the drop height (by 25–40% of the initial value) (Figs. 6.3 (SS) and 6.4a, b). These processes occurred much faster at small times and were slower at large times. Some reduction in the drop volume (by 5–8.5% of the initial value) happened at three different regimes/stages: the initial stage 1 at small times (up to 3–6 s), some intermediate stage 2 and the stage 3 at large times (Fig. 6.4c). The relative loss of the volume V/V_0 showed the exponential character $\ln(V/V_0) = \gamma t$ with $\gamma = -0.0020 \pm 0.0025$ during the "quick" stage 1, whereas it could be described well by the power-law function $\ln(V/V_0) = \alpha\ln(t)$ with $\alpha = -0.0121 \pm 0.0103$ during the "slow" stage 3 (Fig. 6.4d, e).
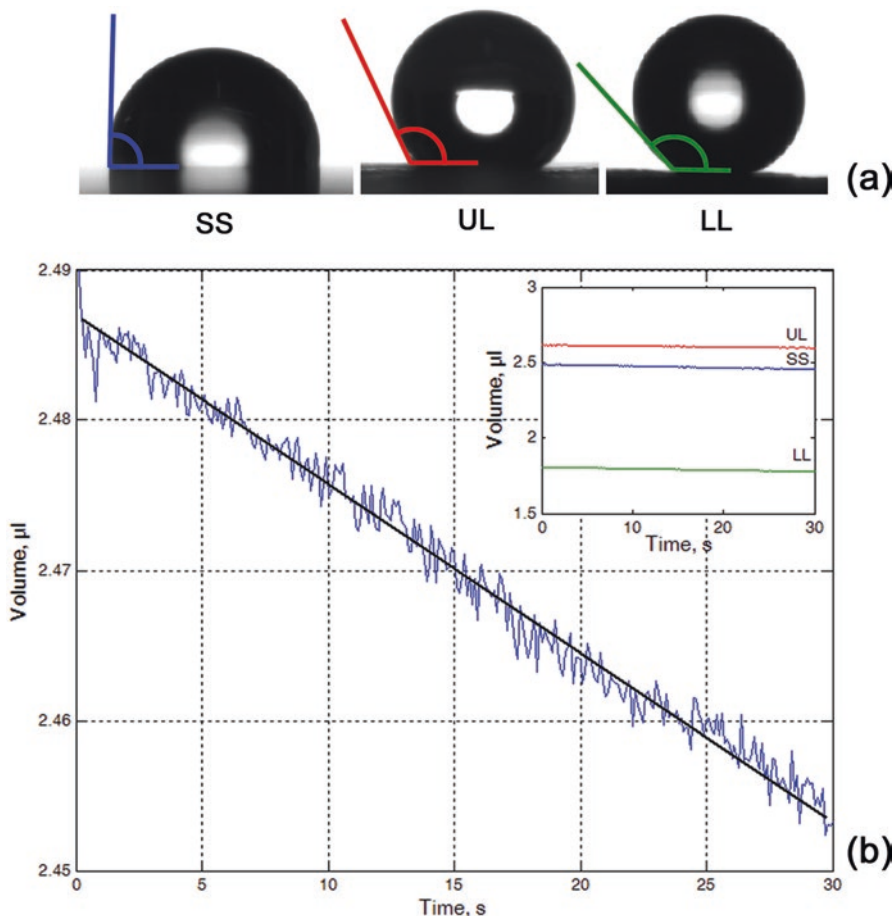
Fig. 6.2 The water drops on the test surface samples. (**a**) Contact angles on the artificial smooth solid sample SS and two *Nepenthes alata* pitcher samples with two wax layers UL and one wax layer LL. (**b**) Time-dependant values of the volume of the water drop on the smooth solid sample SS. The straight black line indicates the linear fitting function $V = -0.001\ t$. The inset shows the change of the volume on all tested surfaces: the smooth solid sample (SS) and the pitcher samples with one (LL) and two wax layers (UL)

Cryo SEM investigations of the oil drops applied onto the pitcher wax coverage revealed the high affinity between oil and the wax material: fluid readily wetted and completely penetrated the wax coverage down to the cuticle (Fig. 6.1b–g).

The oil drops showed extremely quick spreading over the UL surface during the first several seconds; then after a certain time without observable changes, they sunk in either over the same drop base or with its shrinkage (Fig. 6.3 (UL)). The intensive spread of the drop base (by 30–220% of the initial value) occurred extremely fast during the first several seconds, then the base either almost did not change or went down (by 33–57% of the highest value) (Fig. 6.5a). The drop height decreased by
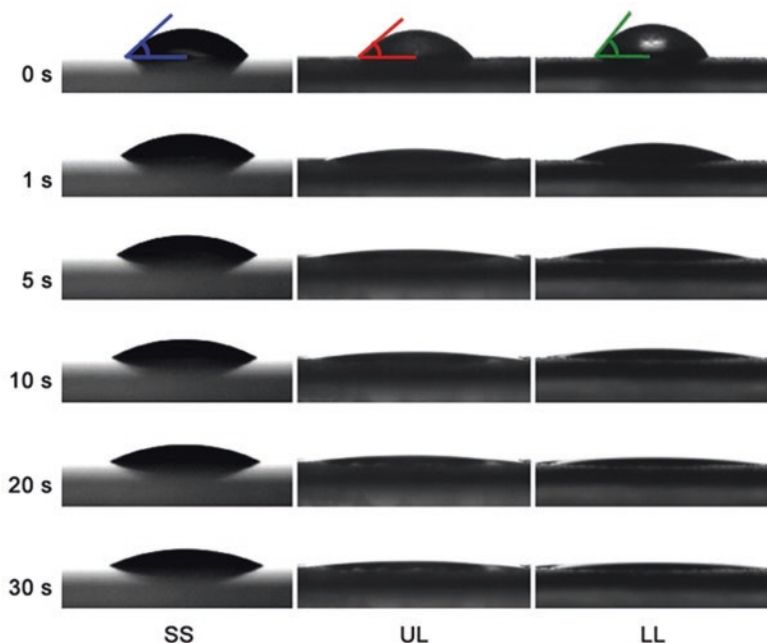
Fig. 6.3 Modification of the oil drops on the test surface samples. Video sequences of the drop behavior on the smooth solid sample SS and the pitcher samples with the two-layered wax UL and one-layered wax LL during 30 s of the experiments: at 0 s, 1 s, 5 s, 10 s, 20 s and 30 s after deposition of the drops on the sample surface

62–88% of the initial value exceedingly quickly at the very beginning and much slower at larger times (Fig. 6.5b). The great reduction in the drop volume, which accounted by 40–88% of the initial value, happened through three stages: the "quick" stage 1 at small (first 2–5 s, up to 10 s) times (exponential function $\ln(V/V_0) = \gamma t$, $\gamma = -0.0783 \pm 0.0513$), some intermediate stage 2 and the "slow" stage 3 at large times (power-law function $\ln(V/V_0) = \alpha \ln(t)$ with $\alpha = -0.4525 \pm 0.1993$) (Fig. 6.5c–e).

On LL, the oil drops spread very quickly over the surface during the first several up to 10 s, then did not change in shape for a short time and afterwards started to shrink/disappear (Fig. 6.3 (LL)). The drop base increased extremely fast during the first few (up to maximum 10) seconds by 41–160% of the initial value, then decreased either slightly (only by 10% of the maximal value) or greatly (by 40–75% of the maximal value) (Fig. 6.6a). The drop height decreased by 73–95% of the initial value: first (from several to up to 10 s) faster, then slower (Fig. 6.6b). The great decrease in the drop volume (by 32–94% of the initial value) occurred during the "quick" stage at small (0–10 s) times (exponential function $\ln(V/V_0) = \gamma t$ with $\gamma = -0.0644 \pm 0.0262$) and the "slow" stage at larger times (power-law function $\ln(V/V_0) = \alpha \ln(t)$ with $\alpha = -0.5100 \pm 0.1790$) (Fig. 6.6c–e). The intermediate stage 2 was either not present or very short.
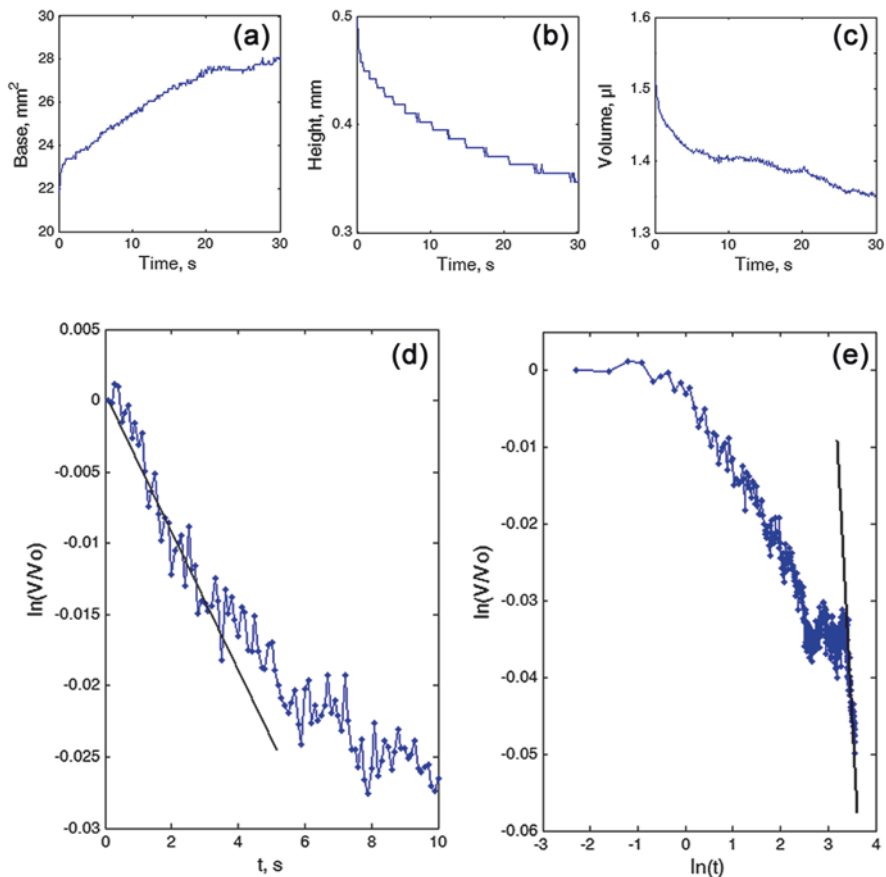
Fig. 6.4 Modification of the oil drops on the smooth solid sample SS. (**a**–**c**) Time-dependant values of the base (**a**), height (**b**) and volume of the drop (**c**). (**d**, **e**) Log-linear (**d**) and log-log plots (**e**) of the time-dependence of the change in the oil drop volume V/V_0. The straight black lines touching the experimental curves in (**d**) and (**e**) correspond to the exponential and scaling dependencies in different time intervals, respectively

The comparisons of γ-values in the exponential functions (for the "quick" stage at small times) and α-values in the power-law functions (for the "slow" stage at large times) (Fig. 6.7) showed significant differences between surfaces (γ: $H_{2,22} = 12.904$, $P = 0.002$; α: $H_{2,22} = 10.857$, $P = 0.002$; both Kruskal-Wallis one way ANOVA on ranks). Both values were considerably lower on SS compared to both UL and LL and did not differ between the latter two surface samples (Table 6.1).
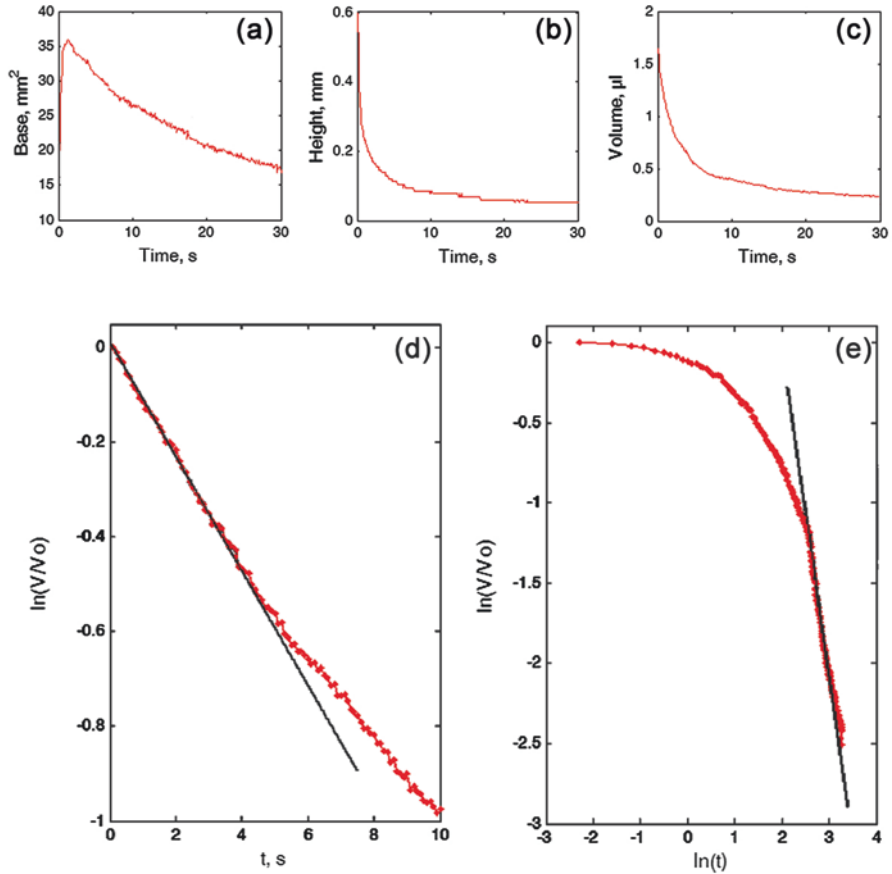
Fig. 6.5 Modification of the oil drops on the two-layered wax sample of the pitcher UL. (**a–c**) Time-dependant values of the base (**a**), height (**b**) and volume of the drop (**c**). (**d, e**) Log-linear (**d**) and log-log plots (**e**) of the time-dependence of the change in the oil drop volume V/V_0. The straight black lines touching the experimental curves in (**d**) and (**e**) correspond to the exponential and scaling dependencies in different time intervals, respectively

6.3 Discussion

Our experiments with the water drops on the artificial smooth solid sample (SS) and two *N. alata* pitcher samples with either one (LL) or two wax layers (UL) demonstrated very similar behavior of the fluid, despite of some differences in the surface wettability between the samples. Permanence of the drop shape and base as well as very little, linear decrease in the drop height and volume during the experimental time indicate that neither spreading nor adsorption of water took place on the tested samples. Little changes in the drop height and volume resulted most likely from the evaporation of the fluid. Hence, non-significant difference in k-values ($V = kt$)
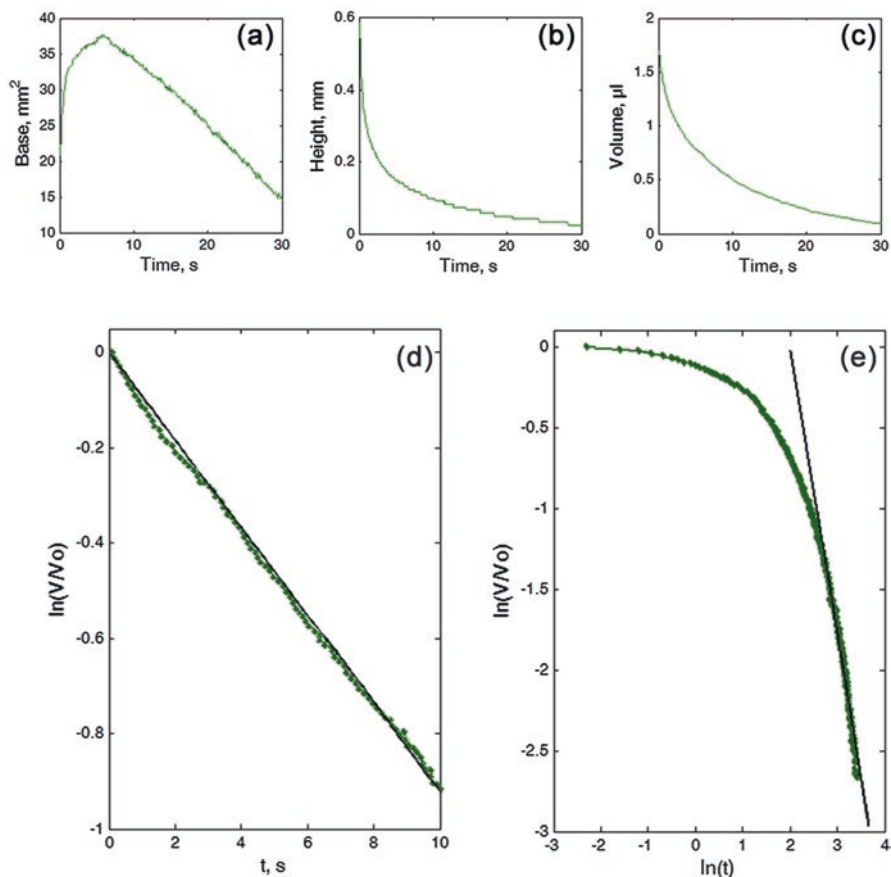
Fig. 6.6 Modification of the oil drops on the one-layered wax sample of the pitcher LL. (**a–c**) Time-dependant values of the base (**a**), height (**b**) and volume of the drop (**c**). (**d, e**) Log-linear (**d**) and log-log plots (**e**) of the time-dependence of the change in the oil drop volume V/V_0. The straight black lines touching the experimental curves in (**d**) and (**e**) correspond to the exponential and scaling dependencies in different time intervals, respectively

between different samples means that similar processes, apparently evaporation of water, occur at similar rates on the tested surfaces.

We have found that performance of the oil drops differed essentially from that of the water drops. On all tested surfaces, distinct changes in shape of the oil drops as well as growth of the drop base together with the reduction of the drop height were clearly seen, especially at small times, and losses of the drop volume were revealed. We also detected certain dissimilarities in the drop behavior if compare SS with both UL and LL.

The continuous, but relatively moderate spreading of the oil drop over SS, which was relatively rapid at the beginning and slow at high times, resulted in the expanding drop base and the reducing drop height. Changes in both drop parameters were
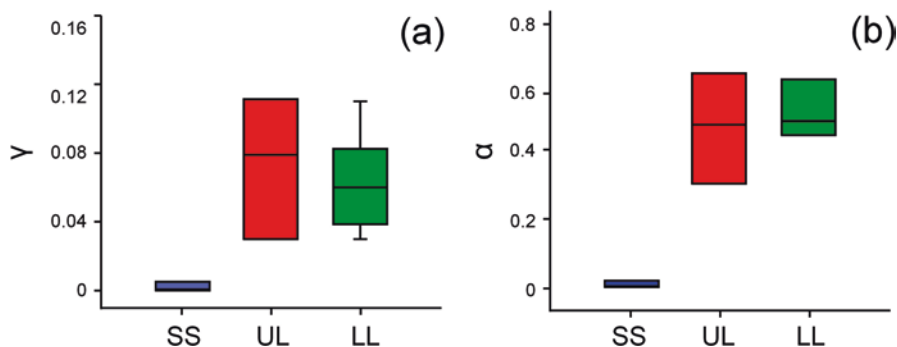
Fig. 6.7 γ- and α-values obtained for the test samples. The γ- (**a**) and α- (**b**) values were calculated for fits for the exponential $\ln(V/V_0) = \gamma t$ and power-law $\ln(V/V_0) = \alpha \ln(t)$ functions, respectively, obtained for the artificial smooth solid sample SS (n = 6) and pitcher samples with two wax layers UL (n = 8) and one wax layer LL (n = 9)

Table 6.1 Results of multiple pairwise comparisons (Dunn's method) of γ-values and α-values obtained for the relative volume change of the oil drops on different samples

comparison	DF	Q	P < 0.05
γ			
SS vs UL	12.125	3.310	Yes
SS vs LL	10.944	3.062	Yes
UL vs LL	1.182	0.358	No
α			
SS vs UL	9.563	2.832	Yes
SS vs LL	10.500	3.031	Yes
UL vs LL	0.938	0.306	No

DR difference on ranks, *LL* pitcher sample with only lower wax layer, *P* probability value, *SS* smooth solid sample, *Q* test statistics, *UL* pitcher sample with both wax layers

essentially lower than those in UL and LL. The obtained decrease in the oil drop volume on SS appeared to be higher than the expected one caused by the evaporation of oil. This happened possibly due to errors of experimental and/or calculation methods used in the study. However, taking into account great differences in the volume loss values between SS compared to both UL and LL, these errors can be neglected. As both γ-value $(\ln(V/V_0) = \gamma t)$ and α-value $(\ln(V/V_0) = \alpha \ln(t))$ in SS were nearly 35 times lower than those in UL and LL, we can conclude that SS did not adsorb oil, whereas both UL and LL could do this.

For the oil drops on both UL and LL, we suggest the following scenario. During the initial stage, which was usually shorter (just several seconds) in UL and longer (up to 10 s) in LL, the liquid simultaneously quickly penetrated into the porous media located under the drop and spread over the surface. This stage contributed to the most decrease of the drop volume observed in the experiments, especially on UL. At large times (starting from ca. 10th s after the drop deposition on the surface),

mainly imbibition of the liquid to lateral directions into the porous media, which resulted in the shrinkage of the drop base (more pronounced on LL compared to UL) and the expanding of the wetted region inside the porous layer, took place. During the intermediate stage, which was noticeable in UL, the pores under the drop base became saturated and the adsorption of the fluid towards the lateral directions into the porous media started. At that time, the drop base did not expand or even slightly decreased. The presence of this stage on UL may be explained by the higher thickness of the porous layer and, consequently, longer pores (both 2–3 times larger than those in LL (Gorb and Gorb 2009)). We assume that the evaporation of the oil, which should occur at all stages, had probably a minimal effect on the loss of the drop volume compared to the adsorption of the fluid by the porous layer. Large values of the drop volume loss and non-significant differences in both γ- and α-values on UL and LL indicate that both one-layered and two-layered waxes of the *N. alata* pitcher were equally effective in adsorbing oil.

Our results on the behavior of the oil drops on both *N. alata* pitcher samples (with one wax layer LL and with the two-layered wax UL) are in line with the previous results on the spreading of small liquid drops of silicone oil over dry porous layers in the case of complete wetting (Starov et al. 2003). Our observations also clearly showed that the drop motion was caused by the fluid adsorption through the porous media (see a great decrease in the drop volume in Figs. 6.5c and 6.6c) resulting in the spreading of the drop over already saturated regions of the porous substrates (growth of the drop base) and the imbibition of the liquid from the drop into the porous materials (decrease of the drop base) (see Figs. 6.5a and 6.6a).

Our previous study on the insect attachment to nano-porous artificial samples, showing the pronounced ability to oil adsorption, revealed extremely poor attachment of ladybird beetles *Coccinella septempunctata* to these substrates due to possible absorption of the secretion fluid from insect adhesive pads by the porous media (Gorb et al. 2010). In the case of epicuticular plant waxes, due to the high affinity between the wax material and oily insect pad secretion, the fluid disappears rapidly from the contact. That is why all kinds of forces contributing to the wet adhesion (capillary interactions and viscous adhesion) will be reduced or even completely eliminated. This will cause a great reduction in the attachment of insect to such substrates. Since the amount of the fluid secreted by insects is extremely small (average amount in the footprint is 0.986 μm^3 in the beetle and 0.019 μm^3 in the fly (Peisker and Gorb 2012)) and much smaller than the adsorption capability of the waxy zone in *Nepenthes* pitcher shown in the present paper, the fluid will be immediately and completely absorbed from the insect pad by the plant wax. The results of the present study provide strong evidence that three-dimensional epicuticular wax coverages in plants are in general anti-adhesive for insects, which rely on wet adhesion.

6.4   Methods

6.4.1   Samples

Three types of surface samples were used in the study: (1) the *N. alata* pitcher sample with one wax layer of the three-dimensional epicuticular wax coverage (LL), (2) the pitcher sample with the two-layered wax (UL), and (3) the artificial smooth solid sample (SS) served as a reference surface.

Pitchers of the carnivorous plant species *N. alata* Blanco (Nepenthaceae), endemic to the Philippines (McPherson 2009), were obtained from plants grown in the greenhouse at the Botanical Garden of the Kiel University (Kiel, Germany). The waxy zone of the freshly harvested pitchers was used to get both UL and LL. The untreated pitcher surface bearing both wax layers (Gorb et al. 2005, 2014a; Gorb and Gorb 2009; Benz et al. 2012) was used as UL (Fig. 6.1a). The LL was obtained after mechanical removal of the upper wax layer by treating the waxy zone with a two-component polyvinylsiloxane (Coltène Whaledent Dentalvertriebs GmbH, Konstanz, Germany). For this purpose, the fluid polyvinylsiloxane was applied to the pitcher surface and then peeled off after 5 min of polymerization. As SS, we used the epoxy resin sample obtained from a smooth clean glass slide by applying a two-step molding method according to Gorb (2007).

6.4.2   Experiments

6.4.2.1   Cryo Scanning Electron Microscopy

Pieces of ca. 5 × 5 mm were cut out of the central part in the waxy zone of the *N. alata* pitcher using a razor blade. Two types of the pitcher samples were examined: (1) with the intact epicuticular wax coverage and (2) after applying a small droplet of mineral oil (light oil (neat) BioReagent M8410, Sigma-Aldrich Chemie GmbH, Munich, Germany; density 0.84 g/cm^3 at 25 °C, viscosity 20.5 mm^2/s at 40 °C, Brookfield viscosity 30.0 cps at 25 °C) onto the wax coverage. This oil was selected, because its viscosity corresponds to that previously estimated experimentally for the footprints of beetles (Peisker et al. 2014). The total mount specimens with the inner pitcher surface facing up and fractured samples were examined in a scanning electron microscope Hitachi S-4800 (Hitachi High-Technologies Corp., Tokyo, Japan) equipped with a Gatan ALTO 2500 cryo preparation system (Gatan Inc., Abingdon, UK). Sample preparation and mounting are described in detail by Gorb and Gorb (2009) and Benz et al. (2012).

6.4.2.2 Apparent Contact Angle Measurements

Contact angles of double-distilled water (surface tension = 72.1 mN/m, dispersion component = 19.9 mN/m, polar component = 52.2 mN/m) (Busscher et al. 1984) on test samples were measured by using a high-speed optical contact angle measuring device OCAH 200 (DataPhysics Instruments GmbH, Filderstadt, Germany) according to the sessile drop method. For a detailed description of the method, see Gorb and Gorb (2006b). We applied 2 µl drops and circle or ellipse fitting for evaluation of the apparent contact angles. On each surface, the contact angles of 10 drops were measured. Data are given as mean ± SD.

6.4.2.3 Adsorption Experiments

In the adsorption experiments, we used the sessile drops (ca. 2 µl) of two fluids—polar double-distilled water and non-polar mineral oil (light oil (neat) BioReagent M8410, Sigma-Aldrich Chemie GmbH, Munich, Germany). The behavior of the drops during the first 30 s after the drop deposition on the test surfaces was video recorded (10 frames per second) using the contact angle measuring device mentioned above. On each sample type, 6–9 experiments were carried out with each fluid. By applying the numerical analysis of the experimental results, described below, we obtained time-dependencies for the drop base, height and volume.

6.4.2.4 Numerical Analysis of Experimental Data

Numerical analysis of the experimental results was organized as follows. We copied the sequence of graphic images from an experimentally recorded movie to MatLab software and transformed them into black and white maps. Numerically, these black and white maps corresponded to the matrices, which contained only 0 and 1 values. This allowed one to determine formally borders of the visualized liquid drops. As during our numerous experiments on contact angles measurements, both previous (Gorb and Gorb 2006b, 2009) and performed in this study, we observed mostly symmetric drops, we treated here every liquid drop as cylindrically symmetric.

In a further numerical procedure, the instant height of the drop *h* was divided into a large number of as small as possible layers *dh* « 1. In fact, the number of the layers was defined by the number of pixels in the recorded HD-movie. Each layer in an instant drop image had a diameter, which was determined by the borders of its projection on the vertical plane. It can be formally done in MatLab, where a black and white image corresponded to a matrix containing 0 and 1 elements only.

Using the obtained array of the diameters for all layers, one can easily calculate the areas of the circles corresponding to each layer. In particular, the lowest (first) layer of this array defined instant contact area (drop base).

One could also multiply the area of every layer by the height *dh* to calculate its volume and thus collecting the volumes of all the layers up to the total volume of the drop, performing a numerical summation on all of them.

The above procedure could be easily repeated for every frame of the movie. As a result, we obtained time-dependant values of the drop volume, base and height (see Figs. 6.4a–c, 6.5a–c and 6.6a–c). In the numerically generated movies, mutual correspondence between the real image of the process, black and white map of the vertical drop projection (with its borders marked by the colored points), and time-dependant volume, base and height of the drop were directly seen from a comparison between different subplots of the movie frames.

In particular, it could be seen directly from the frames that different stages of the process had different rates and different (functional) time dependence. Because of this, it was also useful to plot all time-dependant values in the log-log scale (see Figs. 6.4e, 6.5e and 6.6e). It allowed us to separate the time intervals, where the corresponding values behaved as a linear, exponential or scaling (power-law) function of time.

As for determination of different functional time-dependencies in log-linear and log-log plots, straight lines touching the experimental curves in Figs. 6.4d, 6.5d, 6.6d and Figs. 6.4e, 6.5e, 6.6e correspond to the exponential and scaling hypothetic functional dependencies in different time intervals, respectively.

References

Attygalle, A. B., Aneshansley, D. J., Meinwald, J., & Eisner, T. (2000). Defense by foot adhesion in a chrysomelid beetle (*Hemisphaerota cyanea*): Characterization of the adhesive oil. *Zoology, 103*, 1–6.

Bargel, H., Koch, K., Cerman, Z., & Neinhuis, C. (2006). Structure–function relationships of the plant cuticle and cuticular waxes—A smart material? *Functional Plant Biology, 33*, 893–910.

Barthlott, W., Neinhuis, C., Cutler, D., Ditsch, F., Meusel, I., Theisen, I., & Wilhelmi, H. (1998). Classification and terminology of plant epicuticular waxes. *Botanical Journal of the Linnean Society, 126*, 237–260.

Benz, M. J., Gorb, E. V., & Gorb, S. N. (2012). Diversity of the slippery zone microstructure in pitchers of nine carnivorous *Nepenthes* taxa. *Arthropod-Plant Interactions, 6*, 147–158.

Betz, O., Verheyden, A. N., Maurer, A., Schmitt, C., Braun, J., Kowalik, T., Grunwald, I., Hartwig, A., & Neuenfeldt, M. (2016). Peptide mass analyses of the tarsal adhesive secretion in the desert locust *Schistocerca gregaria* and the Madagascar hissing cockroach *Gromphadorhina portentosa*. *Insect Molecular Biology, 25*, 541–549.

Bullock, J. M., & Federle, W. (2009). Division of labour and sex differences between fibrillar, tarsal adhesive pads in beetles: Effective elastic modulus and attachment performance. *The Journal of Experimental Biology, 212*, 1876–1888.

Busscher, H. J., Vanpert, A. W. J., Deboer, P., & Arends, J. (1984). The effect of the surface roughening of polymers on measured contact angle of liquids. *Colloids and Surfaces, 9*, 319–331.

Dirks, J.-H., & Federle, W. (2011). Fluid-based adhesion in insects—Principles and challenges. *Soft Matter, 7*, 11047–11053.

Dirks, J.-H., Clemente, C. J., & Federle, W. (2010). Insect tricks: Two-phasic foot pad secretion prevents slipping. *Journal of the Royal Society Interface, 7*, 587–593.

Dixon, A. F. G., Croghan, P. C., & Gowing, R. P. (1990). The mechanism by which aphids adhere to smooth surfaces. *The Journal of Experimental Biology, 152*, 243–253.

Drechsler, P., & Federle, W. (2006). Biomechanics of smooth adhesive pads in insects: Influence of tarsal secretion on attachment performance. *Journal of Comparative Physiology A, 192*, 1213–1222.

Edwards, J. S., & Tarkanian, M. (1970). The adhesive pads of Heteroptera: A re-examination. *Proceedings of the Royal Entomological Society of London. Series A, General Entomology, 45*, 1–5.

Eigenbrode, S. D. (1996). Plant surface waxes and insect behavior. In G. Kerstiens (Ed.), *Plant cuticles—An integrated functional approach* (pp. 201–222). Oxford: BIOS Scientific Publishers.

Eigenbrode, S. D., Castognola, T., Roux, M. B., & Steljes, L. (1999). Mobility of three generalist predators is greater on cabbage with glossy leaf wax than on cabbage with a wax bloom. *Entomologia Experimentalis et Applicata, 81*, 335–343.

Eisner, T., & Aneshansley, D. J. (2000). Defense by foot adhesion in a beetle (*Hemisphaerota cyanea*). *Proceedings of the National Academy of Sciences of the United States of America, 97*, 6568–6573.

Gaume, L., Gorb, S., & Rowe, N. (2002). Function of epidermal surfaces in the trapping efficiency of *Nepenthes alata* pitchers. *The New Phytologist, 156*, 479–489.

Gaume, L., Perret, P., Gorb, E., Gorb, S., Labat, J.-J., & Rowe, N. (2004). How do plant waxes cause flies to slide? Experimental tests of wax-based trapping mechanisms in three pitfall carnivorous plants. *Arthropod Structure & Development, 33*, 103–111.

Geiselhardt, S. F., Geiselhardt, S., & Peschke, K. (2009). Comparison of tarsal and cuticular chemistry in the leaf beetle *Gastrophysa viridula* (Coleoptera: Chrysomelidae) and an evaluation of solid-phase microextraction and solvent extraction techniques. *Chemoecology, 19*, 185–193.

Gerhardt, H., Schmitt, C., Betz, O., Albert, K., & Lämmerhofer, M. (2015). Contact solid-phase microextraction with uncoated glass and polydimethylsiloxane-coated fibers versus solvent sampling for the determination of hydrocarbons in adhesion secretions of Madagascar hissing cockroaches *Gromphadorrhina portentosa* (Blattodea) by gas chromatography-mass spectrometry. *Journal of Chromatography A, 1388*, 24–35.

Gerhardt, H., Betz, O., Albert, K., & Lämmerhofer, M. (2016). Similarities, dissimilarities and classification of molecular (hydrocarbon) profiles of insect secretions in dependence of species, sex, and sampled body region. *Journal of Chemical Ecology, 42*, 725–738.

Gorb, S. N. (2001). *Attachment devices of insect cuticle*. Dordrecht/Boston/London: Kluwer Academic Publishers.

Gorb, S. N. (2007). Visualisation of native surfaces by two-step molding. *Microscopy Today, 15*, 44–46.

Gorb, E. V., & Gorb, S. N. (2002). Attachment ability of the beetle *Chrysolina fastuosa* on various plant surfaces. *Entomologia Experimentalis et Applicata, 105*, 13–28.

Gorb, E. V., & Gorb, S. N. (2006a). Do plant waxes make insect attachment structures dirty? Experimental evidence for the contamination hypothesis. In A. Herrel, T. Speck, & N. P. Rowe (Eds.), *Ecology and biomechanics—A mechanical approach to the ecology of animals and plants* (pp. 147–162). Boca Raton: CRC Press.

Gorb, E. V., & Gorb, S. N. (2006b). Physicochemical properties of functional surfaces in pitchers of the carnivorous plant *Nepenthes alata* Blanco (Nepenthaceae). *Plant Biology, 8*, 841–848.

Gorb, E., & Gorb, S. (2009). Functional surfaces in the pitcher of the carnivorous plant Nepenthes alata: A cryo-SEM approach. In S. N. Gorb (Ed.), *Functional surfaces in biology: Adhesion related effects* (pp. 205–238). Dordrecht/Heidelberg/London/New York: Springer.

Gorb, E. V., & Gorb, S. N. (2013). Anti-adhesive surfaces in plants and their biomimetic potential. In P. Fratzl, J. W. C. Dunlop, & R. Weinkamer (Eds.), *Materials design inspired by nature: Function through inner architecture* (pp. 282–309). Cambridge: RSC Publishing.

Gorb, E., Haas, K., Henrich, A., Enders, S., Barbakadze, N., & Gorb, S. (2005). Composite structure of the crystalline epicuticular wax layer of the slippery zone in the pitchers of the carnivorous plant *Nepenthes alata* and its effect on insect attachement. *The Journal of Experimental Biology, 208*, 4651–4662.

Gorb, E., Voigt, D., Eigenbrode, S. D., & Gorb, S. (2008). Attachment force of the beetle *Cryptolaemus montrouzieri* (Coleoptera, Coccinellidae) on leaf surfaces of mutants of the pea *Pisum sativum* (Fabaceae) with regular and reduced wax coverage. *Arthropod-Plant Interactions 2*, 247–259.

Gorb, E. V., Hosoda, N., Miksch, C., & Gorb, S. N. (2010). Slippery pores: Anti-adhesive effect of nanoporous substrates on the beetle attachment system. *Journal of the Royal Society Interface, 7*, 1571–1579.

Gorb, E. V., Baum, M. J., & Gorb, S. N. (2013). Development and regeneration ability of the wax coverage in *Nepenthes alata* pitchers: A cryo-SEM approach. *Scientific Reports, 3*, 3078.

Gorb, E. V., Purtov, J., & Gorb, S. N. (2014a). Adhesion force measurements on the two wax layers of the waxy zone in *Nepenthes alata* pitchers. *Scientific Reports, 4*, 5154.

Gorb, E. V., Böhm, S., Jacky, N., Maier, L.-P., Dening, K., Pechook, S., Pokroy, B., & Gorb, S. N. (2014b). Insect attachment on crystalline bioinspired wax surfaces formed by alkanes of varying chain lengths. *Beilstein Journal of Nanotechnology, 5*, 1031–1041.

Ishii, S. (1987). Adhesion of a leaf feeding ladybird *Epilachna vigintioctomaculta* (Coleoptera: Coccinellidae) on a vertically smooth surface. *Applied Entomology and Zoology, 22*, 222–228.

Jeffree, C. F. (1986). The cuticle, epicuticular waxes and trichomes of plants, with reference to their structure, function and evolution. In B. Juniper & R. Southwood (Eds.), *Insects and the plant surface* (pp. 23–64). London: Edward Arnold Publishers.

Jeffree, C. E. (2006). The fine structure of the plant cuticle. In M. Riederer & C. Müller (Eds.), *Biology of the plant cuticle* (pp. 11–125). Oxford: Blackwell.

Jeffree, C. E., Baker, E. A., & Holloway, P. J. (1975). Ultrastructure and recrystallisation of plant epicuticular waxes. *The New Phytologist, 75*, 539–449.

Jetter, R., & Riederer, M. (1994). Epicuticular crystals of nanocosan-10 ol: *In vitro* reconstitution and factors influencing crystal habits. *Planta, 195*, 257–270.

Jetter, R., & Riederer, M. (1995). *In vitro* reconstitution of epicuticular wax crystals: Formation of tubular aggregates by long chain secondary alkanediols. *Botanica Acta: Journal of the German Botanical Society, 108*, 111–120.

Jetter, R., Kunst, L., & Samuels, A. L. (2006). Composition of plant epicuticular waxes. In M. Riederer & C. Müller (Eds.), *Biology of the plant cuticle* (pp. 145–181). Oxford: Blackwell.

Juniper, B. E., & Burras, J. K. (1962). How pitcher plants trap insects. *New Scientist (1971), 269*, 75–77.

Koch, K., & Ensikat, H. J. (2008). The hydrophobic coatings of plant surfaces: Epicuticular wax crystals and their morphologies, crystallinity and molecular self-assembly. *Micron, 39*, 759–772.

Koch, K., Bhushan, B., & Barthlott, W. (2010). Multifunctional plant surfaces and smart materials. In B. Bhushan (Ed.), *Handbook of nanotechnology* (pp. 1399–1436). Heidelberg: Springer.

Kosaki, A., & Yamaoka, R. (1996). Chemical composition of footprints and cuticula lipids of three species of lady beetles. *Japanese Journal of Applied Entomology and Zoology, 40*, 47–53.

McPherson, S. (2009). *Pitcher plants of the old world*. Poole: Redfern Natural History Productions.

Meusel, I., Neinhuis, C., Markstadter, C., & Barthlott, W. (2000). Chemical composition and recrystallization of epicuticular waxes: Coiled rodlets and tubules. *Plant Biology, 2*, 462–470.

Müller, C. (2006). Plant-insect interactions on cuticular surfaces. In M. Riederer & C. Müller (Eds.), *Biology of the plant cuticle* (pp. 398–422). Oxford: Blackwell.

Peisker, H., & Gorb, S. N. (2012). Evaporation dynamics of tarsal liquid footprints in flies (*Calliphora vicina*) and beetles (*Coccinella septempunctata*). *The Journal of Experimental Biology, 215*, 1266–1271.

Peisker, H., Heepe, L., Kovalev, A., & Gorb, S. N. (2014). Comparative study of the fluid viscosity in tarsal hairy attachment systems of flies and beetles. *Journal of the Royal Society Interface, 11*, 1–7.

Peressadko, A., & Gorb, S. (2004). Surface profile and friction force generated by insects. In I. Boblan & R. Bannasch (Eds.), *Proceedings of the first international industrial conference bionik* (pp. 257–263). Düsseldorf: VDI Verlag.

Reitz, M., Gerhardt, H., Schmitt, C., Betz, O., Albert, K., & Laemmerhofer, M. (2015). Analysis of chemical profiles of insect adhesion secretions by gas chromatography-mass spectrometry. *Analytica Chimica Acta, 854*, 47–60.

Scholz, I., Bückins, M., Dolge, L., Erlinghagen, T., Weth, A., Hischen, F., Mayer, J., Hoffmann, S., Riederer, M., Riedel, M., & Baumgartner, W. (2010). Slippery surfaces of pitcher plants: *Nepenthes* wax crystals minimize insect attachment via microscopic surface roughness. *The Journal of Experimental Biology, 213*, 115–1125.

Starov, V. M., Zhdanov, S. A., Kosvintsev, S. R., Sobolev, V. D., & Velarde, M. G. (2003). Spreading of liquid drops over porous substrates. *Advances in Colloid and Interface Science, 104*, 123–158.

Stork, N. E. (1980). Role of waxblooms in preventing attachment to brassicas by the mustard beetle, *Phaedon cochleariae*. *Entomologia Experimentalis et Applicata, 26*, 100–107.

Voigt, D., Schuppert, J. M., Dattinger, S., & Gorb, S. N. (2008). Sexual dimorphism in the attachment ability of the Colorado potato beetle *Leptinotarsa decemlineata* (Coleoptera: Chrysomelidae) to rough substrates. *Journal of Insect Physiology, 54*, 765–776.

Vötsch, W., Nicholson, G., Müller, R., Stierhof, Y.-D., Gorb, S. N., & Schwarz, U. (2002). Chemical composition of the attachment pad secretion of the locust *Locusta migratoria*. *Insect Biochemistry and Molecular Biology, 32*, 1605–1613.

Part IV
Adhesion

Chapter 7
Examples of Bioadhesives for Defence and Predation

Janek von Byern, Carsten Müller, Karin Voigtländer, Victoria Dorrer, Martina Marchetti-Deschmann, Patrick Flammang, and Georg Mayer

Abstract Bioadhesives are widely used in nature, not only for settlement but also for defence, prey capture, nest construction or mobility. These glues are superbly adapted in terms of chemical composition and biomechanical properties to the requirements of those organisms producing them. More than 100 marine and terrestrial organisms are known to produce adhesives, some of them since 500 million years. However, only little is known about the composition, production, secretion mechanisms and mechanical properties of the vast majority of these glues.

Attaching to a substratum, as done by bacteria, plants and animals, surely is the most common function of bioadhesives and has been extensively described in various organisms such as mussels, acorn barnacles, sandcastle worms or slugs.

This chapter focuses on animals that use adhesive secretions for defence and predation, as these functions require specialized behaviours and adhesive properties, such as fast curing process in the millisecond range, squirting over distance, protection against own glue, or bonding to various sorts of substrata with varying

J. von Byern (✉)
Ludwig Boltzmann Institute for Experimental and Clinical Traumatology, Vienna, Austria
e-mail: vbyern@freenet.de

C. Müller
University of Greifswald, Greifswald, Germany
e-mail: carstmue@uni-greifswald.de

K. Voigtländer
Senckenberg Museum für Naturkunde Görlitz, Görlitz, Germany
e-mail: karin.voigtlaender@senckenberg.de

V. Dorrer · M. Marchetti-Deschmann
Technische Universität Wien, Vienna, Austria
e-mail: martina.marchetti-deschmann@tuwien.ac.at

P. Flammang
Université de Mons, Mons, Belgium
e-mail: Patrick.Flammang@umons.ac.be

G. Mayer
University of Kassel, Kassel, Germany
e-mail: gmayer@onychophora.com

surface chemistry or texture. The depicted organisms cover a large environmental and phylogenetic diversity. In addition to marine animals such as hagfish and comb jellies, many terrestrial species like centipedes, salamanders, spitting spiders and velvet worms use adhesives for defence or prey capture. With its subterranean life-style, the glowworm exhibits a highly specialized adhesive system combined with prey-attracting bioluminescence.

Bioadhesion research is challenging but also offers understanding of bioadhesive evolution and mechanisms, and to identify commonalities and functional principles.

7.1   Introduction

The use of bioadhesives as means to cling to a support surface, be it a rock, a plant or another animal, is surely its most common function among bacteria, plants and animals. However, the sticky secretions also fulfil other purposes, such as defence, predation, locomotion or nest construction. Bioadhesives are perfectly adapted mor-phologically, biologically, chemically and physically to the needs and requirements of the organism. In particular those used for defence and predation exhibit a fast secretion and curing process, being swifter than that of any synthetic system, while others can be exposed for weeks in the environment without losing their bonding capability.

In the following chapter we shall describe some properties of the sticky secre-tions used for defence and predation, focusing on organisms that produce them. Major emphasis will be on gland morphology, release mechanisms, chemical com-position and purpose. A detailed knowledge of these systems not only helps under-standing their fast hardening process, but could also assist designing fast-reacting artificial systems in the future.

7.2   Defence

"The defensive form of war is in itself stronger than the offensive". (Carl von Clausewitz, Selection from "On War", Book 6, Chapter 1, Offence and Defence)

Animals have evolved a wide variety of antipredator mechanisms, such as cam-ouflage, warning colouration, mimicry, immobile defensive structures including spines, hairs and bristles, unpalatability, the secretion of noxious chemicals, and various behavioural patterns. Although adhesives are rarely used as a weapon of defence, in contrast to other mechanisms listed in the chapters above, they still dem-onstrate a high degree of effectiveness against larger predators.

While some defence tools, such as the dorsal mucus of the slug *Arion subfuscus* (Draparnaud 1805), the Cuverian tubules in holothurians, and the epithelial secretions in the frog *Notaden bennettii* (Günther 1873), have recently been

described in detail elsewhere (see respective chapters in Smith (2016)), it is the goal of this review to provide a short description of some as yet incompletely character-ised bioadhesive systems used as part of a defensive reaction.

7.2.1 Centipedes

Centipedes or Chilopoda are well known for their ability to capture a wide variety of prey, such as insects, spiders, amphibians, reptiles and even mammals, using lethal venoms (Undheim et al. 2015) secreted by aggregated epidermal glands located in the forcipules (maxillipedes). There are numerous observations, publica-tions and medical reports on the composition of the different types of toxins (Undheim et al. 2015) and their venomous effect on invertebrates as well as verte-brates (for more details, see the related book chapters by Rosenberg (2009a) and Rosenberg et al. (2011)).

However, although some data are available regarding the offensive venom glands and the venoms' chemical compositions, little is known about the adhesive secre-tions used for defence in some of the chilopods. Their milky-white sticky secretions are released from defence glands (named telopodal glands in Lithobiomorpha or sternal glands in Geophilomorpha) and harden immediately when the animal is, for example, attacked and bitten by a predator or irritated artificially (Fig. 7.1a, b).

At morphological level, the two glue-secreting glands (telopodal and sternal) share similar general cellular organisation with the venom glands. This type of gland, referred to as a recto-canal epidermal gland, as recently defined by Müller et al. (2014), consists of a multitude of closely packed (aggregated) morphological and functional modules, which contain a subset of four to five constitutive cells.
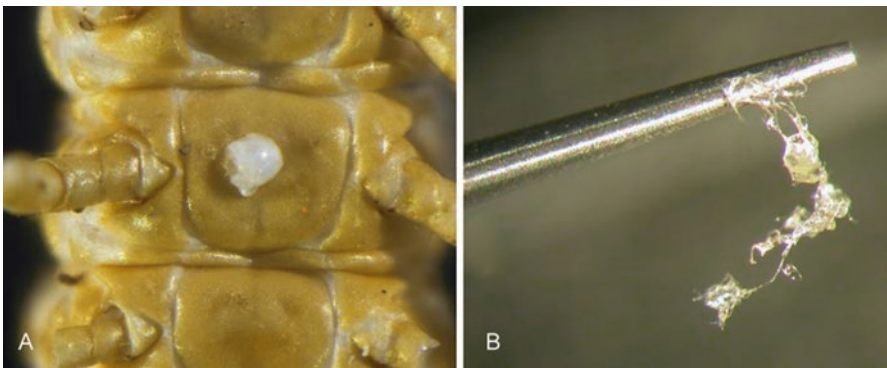
Fig. 7.1 (**a**) Chilopods, such as *Haplophilus subterraneus* (Shaw 1794), release a milky-white glue droplet through the ventral sternal glands (see also Fig. 7.3 for details). (**b**) The secretion adheres to any material within seconds and exhibits a glossy surface (Images from **Janek von Byern,** Ludwig Boltzmann Institute for Experimental and Clinical Traumatology (Austria), and reproduced with his permission)

Among them are two secretory cells of unequal size, an intermediary cell of hitherto unknown function, and one or two canal cells making up the cuticle-lined duct (Fig. 7.2a–f).

The secretory cell is extremely elongated and surrounds a tubular, deep-reaching reservoir filled with fibrillous substance. Through the narrow passage the secretion is first squeezed into a widened, drop-shaped space, termed "atrium" (Rosenberg and Hilken 2006; Dugon and Arthur 2012). This structure is separated from more proximal parts of the conducting canal (= duct) by a conspicuous, valve-like structure (cf., Fig. 4.8D in Rosenberg et al. (2011)). The gland furthermore contains a cuticle-enforced duct (calyx) before it reaches particular surface areas of the body cuticle like, for instance, the sternal pore plates in case of geophilomorph sternal (defence) glands (Fig. 7.2) or the inner rim of the tarsungulum of the forcipule as in case of chilopod venom glands (Dugon and Arthur 2012; Dugon 2017). Accompanying muscle fibres individually lining each gland module may support the release of the secretion. They are present in sternal glands of Geophilomorpha (see Fig. 4.10 in Rosenberg et al. (2011) and Fig. 7.2a in this review), but seem to be absent in lithobiomorph telopodal as well as venom glands (compare Rosenberg et al. (2011)).

Interestingly, the aggregated recto-canal epidermal glands reviewed in this chapter do not resemble each other at topological level; however they may share the same evolutionary origin. For instance, Dugon and Arthur (2012) assumed that the venom glands of Chilopoda might have derived from the internalisation of a formerly exposed glandular epithelium located at the inner rim of the tarsungulum or an appendage gradually transforming into proper forcipules. This assumption is based (a) on observations on early postembryonic stages in the development of the venom gland, namely the successive invagination of a grooved glandular epithelium and the final closure into a circular, internalised calyx (Dugon et al. 2012), and (b) the occurrence of a cuticular crest tying the calyx to the lateral cuticle of the tarsungulum (Dugon and Arthur 2012). Thus, it is perfectly possible that chilopod venom gland modules are homologous to telopodal-like glands present on the anterior trunk and/or head appendages.

7.2.1.1 Lithobiomorpha – Telopodal Glands

All species of Lithobiomorpha possess so-called telopodal glands (Keil 1975; = "periatrial glands" *sensu* Carcupino (1996)), located on the inner face of the femur and tibia of the 14th pair of walking legs in addition to those of the 15th pair of legs, the ultimate or terminal legs, which are no longer used for locomotion (telopodites XII-XV *sensu* Rilling (1968) and Rosenberg et al. (2011)). Keil (1975) described solitary recto-canal epidermal glands from the antennae as showing an arrangement of cells similar to those of the modules of the aggregated telopodal glands. Either solitary or as modules in aggregated formation, each telopodal gland consists of either one secretory cell type (on the antennae) or two closely append secretory
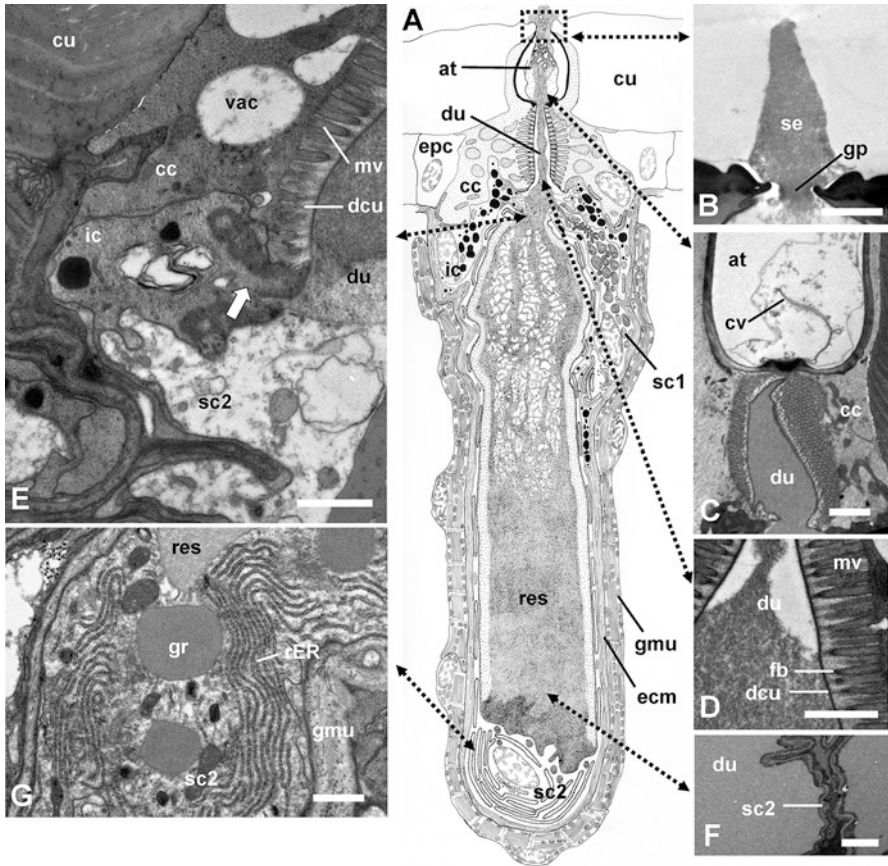
Fig. 7.2 General organization of aggregated modules in sternal (defensive) glands of geophilomorph centipedes using the example of *Himantarium gabrielis* (Linnaeus 1767). (**a**) Semischematic reconstruction of the cellular anatomy of a 4-cell sternal gland module (in mediolongitudinal view) comprising a canal cell (cc), an intermediary cell (ic), as well as two types of secretory cells, a short, granulated cell (sc1) and an extremely elongated, poorly granulated cell (sc2) forming the bulk of the repellent secretion (se) stored in a long tubular reservoir (res). A gland module is surrounded by longitudinal muscle fibres (gmu). (**b–g**) Module ultrastructure as revealed by TEM on selected section levels from distal to proximal gland areas, with section levels indicated in (**a**) by dashed, double-pointed arrows. (**b**) Gland pore (gp), note the secretion fixed in moment of discharge. (**c**) Longitudinal section of the two duct compartments formed by the canal cell, the distal, drop-shaped atrium (at) and the proximal part characterized by canal cell microvilli (mv) subjacent to duct wall cuticle (dcu). Note the cuticular valve structure (cv) preventing a secretion reflux during expulsion. (**d**) Proximal compartment of the gland duct (du) surrounded by microvilli with tips of microvilli are attached to the duct wall cuticle by a brush of filaments. (**e**) Apices of canal cell, intermediary cell and the elongated secretory cell; note that the duct wall cuticle covers only part of the apex of the intermediary cell (arrow). (**f**) Peripheral sector of the tubular reservoir and thin cytoplasmic sheath of the sc2 surrounding it. (**g**) The major part of the secretion is produced in the basal part of the sc2 indicated by numerous cisternae of the rough endoplasmatic reticulum (rER) and some secretory granules (gr). Further abbreviations: *cu* cuticle, *ecm* extracellular matrix, *epc* epidermal cell. Scale bars: 1 μm (**d–e**, **g**); 2 μm (**b**, **c**); 10 μm (**f**) (Image from Carsten Müller, University of Greifswald (Germany), and reproduced with his permission)

cells (on the posterior legs) as well as an intermediary cell (cf. Table 2 in Müller et al. (2014)). While their role in the production of pheromones had been discussed over 100 years ago (Verhoeff 1905), subsequent analyses have shown that the telopodal glands have a defensive function (Panic 1963; Simon 1964; Keil 1975; Rosenberg 2009b).

The species *Lithobius forficatus* (Linnaeus 1758) synthesizes and releases viscous threads, which consist of proteins and lipids (positive reaction to Millon, Sudan black and ninhydrin; Rilling 1968). When attacked by a spider or an ant, this centipede lifts its most posterior leg pairs, catapulting the threads emanating from its telopodal glands against the predators and thus binding the offender to the ground, entangling or at least hampering the attacker severely (Rilling 1968). However, the definite mechanisms of secretion still remain unclear. A release by muscle contraction has been excluded, as the telopodal glands are not surrounded by muscles, and a release by haemolymph pressure remains uncertain, although it may play a role (Rilling 1968; Keil 1975). In addition, contracting microvilli projecting into the reservoir and the various levels of the highly diversified conducting canal may also create micro-currents propelling the secretion along the canal to the gland pore.

7.2.1.2   Geophilomorpha – Sternal (Defensive) Glands

Geophilomorph centipedes such as *Henia vesuviana* (Newport 1845) produce glowing and gluing substances in the so-called sternal glands (Rosenberg et al. 2011). These epidermal glands are also of the recto-canal type and are thus comparable to the *telopodal glands of Lithobiomorpha and the venom glands of Chilopoda*. Sternal glands include aggregated units comprising four to five cells: one or two type(s) of canal cells, eventually stacked onto each other (then termed distal and proximal canal cell), an intermediary cell, and two types of secretory cells, a "regular" but small secretory cell (termed type-1 secretory cell) containing many ER cisternae, Golgi stacks and secretory granules released into the gland duct at the microvilli-equipped apex (Fig. 7.2a) and an extremely elongated, poorly granulated secretory cell (type-2 secretory cell). The existence of a type-2 secretory cell in geophilomorph sternal glands is recorded here for the first time, using the example of *Himantarium gabrielis* (Fig. 7.2). Previous descriptions only documented type-2 secretory cells (Rosenberg et al. 2011). This failure may be easily explained by the small size of the type-1 secretory cells which can be easily overlooked, even during careful examination of related TEM section series.

Sternal glands are located on the ventral surface of each or only particular sternite(s) of a given geophilomorph species (Hopkin and Anger 1992). They are clearly identifiable by a large (2–4 μm) depressed pore patch (Fig. 7.3), also called ventral/sternal pore areas (Turcato and Minelli 1990; Turcato et al. 1995) or ventral pore fields (Bonato et al. 2010, Rosenberg et al. 2011). Up to 200 gland pores are found on each either circular or ovoid patch, coinciding with the occurrence of the same number of glandular units forming a connection to the related pores via a small duct to the ventral surface. Due to the extreme length of the secretory cell and
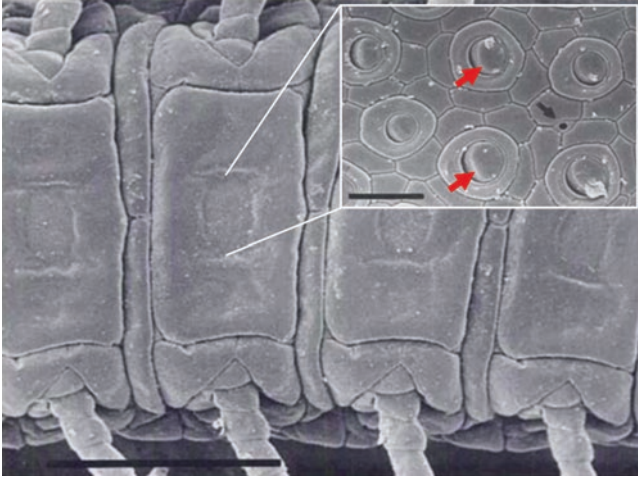
Fig. 7.3 Sternal gland pores (inset) located on the ventral side of several sternites of *Henia vesuviana*. Each pore (red arrows in the insert) is associated with one glandular unit/gland. In between these are pores indicating the presence of smaller, non-gluing epidermal glands (black arrow). Scale bar: 1 mm, inset 10 μm (Image from Hopkin et al. (1990) and reproduced with permission of the original proceedings editor and publisher)

the tubular reservoir (Fig. 7.2), the glandular units reach deep into the perineural sinus, where they touch the ventral nerve cord at the centre of a trunk segment (cf. Fig. 4.10B in Rosenberg et al. (2011)). The secretory cell, or type-2 secretory cell, has been described as "a huge sac, surrounded by a thin layer of cytoplasm from which the glue is derived" (Hopkin and Anger 1992; Müller et al. 2014) (Fig. 7.4). Distal to the secretory cell there is a single intermediary cell, which presumably serves as an accessory secretory cell adding further components to an immature secretion discharged mainly by the type-2 secretory cell (cf. Rosenberg et al. 2011; Müller et al. 2014).

In the geophilomorph genus *Henia*, a distal, spacious, and slender-cylindrical compartment of the gland duct (atrium), close to the pore, includes a valve-like structure that may regulate the amount of secretion to be released from each unit (Hopkin and Anger 1992). In *Pleurogeophilus mediterraneus (Meinert 1870), however,* an internal plug of solidified glue in the duct serves to close the pore opening (Turcato and Minelli 1990; Turcato et al. 1995). In addition to the valve-based regulation of the amount of glue secreted, only those thoracic segments with legs that have been stimulated externally, either by a needle or a predator's bite, show signs of glue secretion (Fig. 7.5). It is proposed that this stimulus results in a hydrostatic and/or muscular pressure on the glands of the respective segment and, thus, initiates a fast release of the glue. It remains an open question as to how geophilomorphs avoid being affected by their own glue. Hopkin and Anger (1992) assumed that additional, small solitary epidermal glands, located between the sternal glands (black arrows in Fig. 7.3), may produce an anti-adhesive secretion.
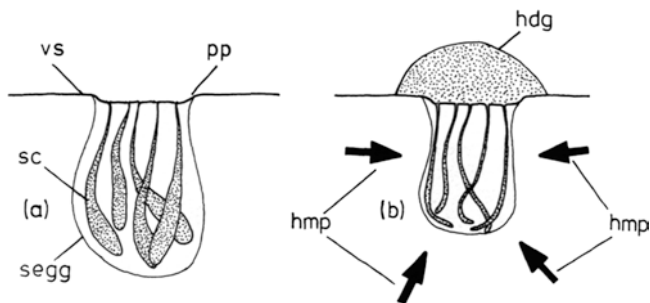
Fig. 7.4 Schematic drawing of the sternal gland system in the centipede *Henia vesuviana* with the glandular units (**a**) accumulating secretion or (**b**) exhausted after secretion (Hopkin and Read Hopkin and Anger 1992). Each glue-secretion glandular unit, and the dominant (type-2) secretory cell (sc) in particular, is embedded in a distinctive, sac-like structure (segg) containing associated muscle fibres, other glandular units, and the small, repellent-producing epidermal glands; the sac is lined by a basal matrix devoid of a basal labyrinth. Each cell secretes through a duct to the pore patch (pp), located on the sternite at the medial ventral surface (vs). According to the authors, secretion is effected by hydrostatic and/or muscular pressure (hmp), resulting in a hemispherical droplet of glue (hdg) (Image by Hopkin and Anger (1992) and republished with permission of the Naturwissenschaftlich-Medizinischer Verein in Innsbruck (Austria))

Fig. 7.5 Stimulation of a leg (st) by a needle (n) in the centipede *Henia vesuviana* results in the secretion of a glue droplet (dg) in the corresponding segment, while the neighbouring segments remain unaffected (Image from Hopkin and Anger (1992) and republished with permission of the Naturwissenschaftlich-Medizinischer Verein in Innsbruck (Austria))
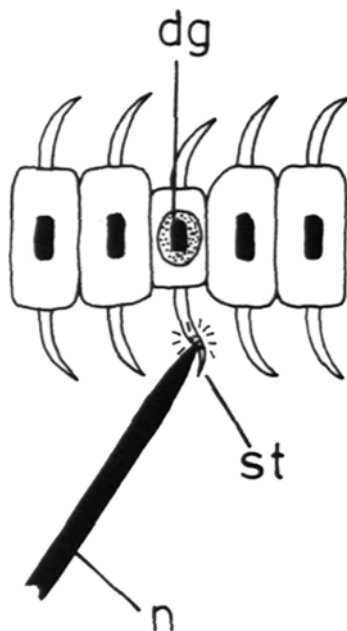
Biochemical analyses of the adhesive secretion of *Henia* sp. indicate the presence of two major (12 kDa and 130 kDa) and several other minor proteins (molecular weight not specified) in the 1D–PAGE (Hopkin et al. 1990). Amino acid analyses of the glue secretion indicate that the glue protein content bears slightly more nonpolar than polar or hydrophobic side groups (Hopkin et al. 1990), similar to the defensive glue secreted by salamanders (see the section Salamanders further below for details).

While *Henia vesuviana* is currently the only species known to contain only proteins in its sternal gland secretions (Hopkin et al. 1990), in three out of thirteen investigated geophilomorph centipedes (Linotaeniidae, Geophilidae and Himantariidae) hydrogen cyanide (HCN) as well as other cyanogenic derivatives and precursors (benzoyl nitrile, benzaldehyde, mandelonitrile and others) may also be present in the viscid secretions (Schildknecht et al. 1968; Jones et al. 1976; Maschwitz et al. 1979; see also Table 2 in Vujisic et al. (2013)). However, while the protein composition has not yet been analysed for most geophilomorph centipedes, only in *Himantarium gabrielis* one major protein with a molecular weight of 55 kDa was detected (Vujisic et al. 2013) in contrast to the two proteins found in *Henia* sp. (Hopkin et al. 1990). This may raise the question if the constant part of the secretions consists of the cyanogenic components, while the proteomic content may vary among the geophilomorph subclades.

Apart from their chemical composition, the sternal secretions also differ in their pH values; for example, in *Pachymerium ferrugineum* (Koch 1835) the secretion has a low pH (3.5–4.0) (Schildknecht et al. 1968), while in *Geophilus vittatus* (Rafinesque 1820) it is almost neutral (pH 6.0–6.5) (Jones et al. 1976). Colour differences have also been observed; in *Geophilus carpophagus* (Leach 1815) the secretion fluid is "more watery and clear", in *Himantarium gabrielis* it appears rosered (Brade-Birks and Brade-Birks 1920), whereas in *Strigamia crassipes* (De Geer 1778) it looks milky white (Koch 1927). In several species, such as *Geophilus flavus* (De Geer 1778)*, H. gabrielis*, *S. crassipes* and others, the secretions are furthermore bioluminescent (Koch 1927, Rosenberg and Meyer-Rochow 2009) and may be used as an *aposematic defence strategy by these nocturnal centipedes.*

In addition to the repellent effect of the cyanogenic components in the sternal glands of various geophilomorph centipedes (Schildknecht et al. 1968; Jones et al. 1976), the adhesive secretions also serve for defence against small arthropods such as ants and beetles (Hopkin and Gaywood 1987; Hopkin et al. 1990). The glue of representatives of *Henia* hardens within a few seconds when exposed to air and "physically immobilises large insects such as the Devil's Coach Horse beetle (*Staphylinus olens* Müller 1764) for more than 20 minutes" (observation cited by Hopkin and Anger (1992)). However, this bonding ability of the secretion only occurs during direct and immediate contact with the substratum and is an irreversible process.

7.2.2 Salamanders

Amongst the amphibians, urodeles have evolved a wide variety of antipredator mechanisms (Brodie and Gibson 1969; Brodie 1977, 1983; Ducey and Brodie (1983); Ducey et al. 1993; Duellman and Trueb 1994). The most effective strategies are immobile posture, tail autotomy, colour patterns, various behavioural responses, and the release of toxic, noxious or adhesive skin secretions (Nowak and Brodie 1978; Brodie and Smatresk 1990; Heiss et al. 2010).

In addition to toxic or noxious secretions some salamanders also use adhesives to defend themselves (Arnold 1982; Evans and Brodie 1994); behavioural observations in the plethodontid salamander *Batrachoseps attenuatus* (Eschscholtz 1833) have demonstrated the effectiveness of its gluing strategy. Once attacked and grasped by a predator like, for example, a snake, the salamander loops its tail around the snake's head and coats it with a sticky viscous fluid (Fig. 7.6a). The glue in the secretion hardens within seconds upon exposure to air (Brodie and Gibson 1969; Williams and Anthony 1994) and immobilizes the snake immediately (Fig. 7.6b). The salamander escapes, and the snake is unable to free itself for up to 48 h (Arnold 1982).

To date, this adhesive antipredator strategy has only been reported in a few North American (*Ambystoma* spp., *Plethodon* spp., *Batrachoseps* spp. and *Bolitoglossa* spp.; Brodie and Gibson 1969; Williams and Larsen 1986; Evans and Brodie 1994) and Japanese species (*Hynobius* spp.; Brodie 1977), and to some extent has been characterized in *Plethodon shermani* Stejneger 1906 (Largen and Woodley 2008; von Byern et al. 2015). Many of these species do not display obvious warning colours like, for example, *Salamandra salamandra* (Linnaeus 1758) or *Pseudotriton*

Fig. 7.6 Defence strategy of the salamander (*Batrachoseps* sp.) (*) towards a snake (+) attack using glue. (**a**) Typical defence reaction. Note the salamander's tail wrapped around the snake's neck. (**b**) In this case, the mouth of the snake has been glued open (Image from Arnold (1982) and reproduced with permission of the American Society of Ichthyologists and Herpetologists)
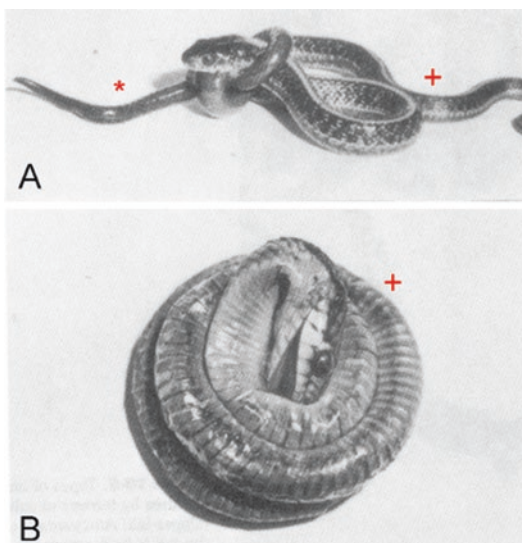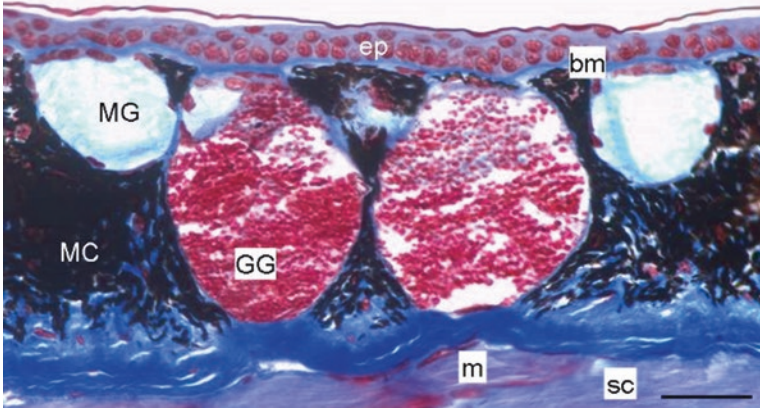
Fig. 7.7 The skin of the salamander *Plethodon shermani* contains two layers: a thin epidermis (ep) with the underlying basement membrane (bm) and a thick dermis. The two gland types, mucous glands (MG) and granular glands (GG), as well as the melanocytes (MC) are located within the stratum spongiosum, above the stratum compactum (sc), which is made up largely of subcutaneous muscle tissue (m). The secretory material of the granular glands (GG) contains spherical granules, while in the mucous gland the content has a flocculent appearance. Scale bar: 50 μm (Image from von Byern et al. (2015) and reproduced with permission)

ruber (Sonnini de Manoncourt and Latreille 1801) do (Mebs 2000; Mitchell and Gibbons 2010). They rather appear relatively dark, i.e. for *Plethodon shermani, Plethodon glutinosus (Green 1818), Ambystoma opacum (Gravenhorst 1807), with a few* yellowish-orange spots as *Ambystoma maculatum (Shaw 1802)* (Mitchell and Gibbons 2010), *or are generally pale green as Hynobius dunni Tago 1931* (Brodie 1977), and secrete their adhesives only as a last resort of defence when provoked over a relatively long period of time (von Byern et al. 2015).

Morphological and histochemical studies of *Plethodon shermani* have shown that the adhesive glands are mainly distributed along the lateral edges of the tail ridge and in the parotid region. Two gland types occur in the dermal layer of the skin in *Plethodon shermani* (Fig. 7.7). The mucous glands are densely packed with flocculent material and contain mostly acidic glycoproteins (positive staining with Alcian blue, pH 2.5 as well as with Periodic acid-Schiff reaction - PAS) (von Byern et al. 2015). The granular glands secrete various granules of different sizes and densities that contain only basic proteinaceous material (strong staining with Biebrich scarlet at pH 6.0 and weakly at pH 8.5, but no reactivity at pH 9.5 and 10.5) and lack the glycan fraction (von Byern et al. 2015). Additionally, there is another glandular region named the granular gland area, which is adjacent to the granular gland and shows a similar composition to the mucous gland; however, its function remains as yet undetermined (von Byern et al. 2015).

Microanatomical analyses show that the secretory material of both gland types is not homogenous but varies considerably in size, density and content (Fig. 7.8). Some granules have up to three layers and contain small to large inclusions which appear electron-lucent, electron-dense or empty. This suggests that a "cocktail" of
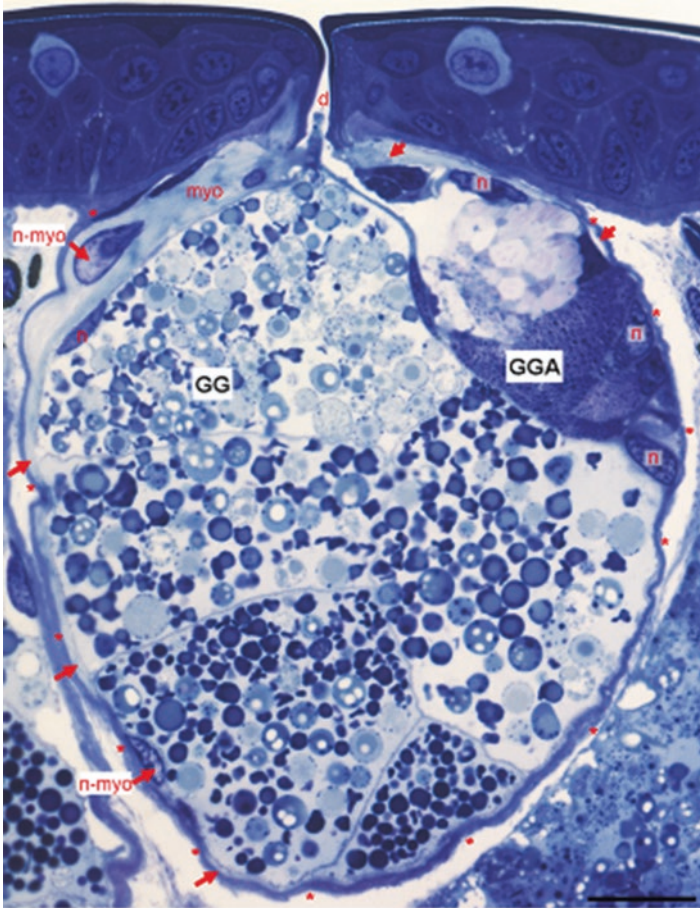
Fig. 7.8 Semi-thin section of the granular gland (GG) and granular gland area (GGA) in the salamander *Plethodon shermani*. The GG and GGA share a secretion duct (d) and are commonly enclosed by a myoepithelium (red arrows) and connective tissue layer (red asterisks). However, the GG and GGA differ in view of their secretory content and chemical composition. Generally, the gland nucleus (n) in salamanders is a peripherally oriented nucleus; n-myo marks the nuclei of the myoepithelium layer. Scale bar: 10 μm (Image from von Byern et al. (2015) and reproduced with permission)

substances is present even within one gland type, which is nevertheless able to form a rapid and highly stable glue seconds after being released. Unfortunately, due to the size differences of the glandular content a detailed characterisation of single granules could not be performed. Hence the acidic and basic protein contents remain uncertain (von Byern et al. 2015).

Protein identification strategies revealed proteins with pIs between 5.0 and 8.0 and molecular masses between 10 and 170 kDa from the glue of *Plethodon shermani* (von Byern et al. 2017a). As positive reactions for acidic and basic proteins are given in the isolated secretions, it can be concluded that both glands contribute to

glue formation. Prominent spots around 15, 25, and 30 kDa can be found in the 2D–PAGE, while the respective peptide mass fingerprint analyses and *de novo* peptide sequencing indicate similarities to different NADH dehydrogenase subunits (von Byern et al. 2017a). However, only short sequence tags were identified and homology with these proteins may not reflect the real function of the proteins.

Besides a high protein ratio (>70% of dry weight, based on amino acid analysis), the salamander glue also contains sugar moieties such as mannose (stained with lectin GNA), α-L-fucose (stained with lectin UEA) and N-acetyl-D-glucosamine (stained with lectin WGA) as well as lipids (von Byern et al. 2015). The glue of *Plethodon shermani* further exhibits only a relatively low water content of ~ 70% compared with other glue-producing animals, such as the Australian frog *Notaden bennetti* (water content 85–90%; Graham et al. 2005), the marine goose barnacle *Dosima fascicularis* (Ellis and Solander 1786) (water content 92%; Zheden et al. 2014), the terrestrial gastropod *Arion subfuscus* (water content 97%; Smith 2016) or the prey capture threads of the larvae of the New Zealand glowworm larvae *Arachnocampa luminosa* (Skuse 1890) (water content 99%; von Byern et al. 2016); see also the section Glowworm further below for more details). Upon release, the glue of *Plethodon shermani* cures immediately, enabling an irreversible and strong bonding of the adhesive to biological (human skin) and artificial (wood, glass, metal) but not hydrophobic surfaces.

Skin alkaloids present in many other amphibians (Daly et al. 2005; Mina et al. 2015; Jeckel et al. 2015) are lacking in the *Plethodon* skin (von Byern et al. 2017a); furthermore, the cured adhesives appear to be biocompatible in cell culture (von Byern et al. 2017b). Nevertheless, cell culture tests also show that the adhesive secretions of other glue-producing salamanders (e.g. *Ambystoma maculatum* and *Plethodon glutinosus*) are cytotoxic, as has been shown for toxin-producing species (von Byern et al. 2017b). This confirms that some glue-producing salamanders not only defend themselves exclusively through their sticky secretions (Fig. 7.6), but additionally use other approaches, mechanisms and strategies to survive an attack.

As was the case for the centipedes mentioned above, it remains unclear how salamanders avoid being glued by their own weapon. Unpublished data from *Plethodon shermani* indicate that the glue appears to be hydrophilic directly after secretion, but becomes hydrophobic during the curing stage. As the salamanders always have a moist skin, this water barrier may ensure that the glue cannot bond to the salamander's skin, but rather adheres to the snake's scaly and dry skin. Further studies are in progress to confirm this hypothesis. Such a wettability avoidance strategy is unlikely to exist in centipedes, as in contrast to salamanders these animals do not have a moist skin.

7.2.3 Hagfish

Hagfish (Myxinidae), also known as slime eels, are slender up to 60 cm long eel-shaped fish (Fig. 7.9). Their skin lacks scales and varies in colour from white or rose to darker reddish-brown and their tiny eyes appear unpigmented. As these fishes

Fig. 7.9 Photograph of the New Zealand hagfish species *Eptatretus cirrhatus* (Forster 1801), which inhabits the east coast of Australia including Tasmania as well as New Zealand (Image courtesy of **Dr. Paddy Ryan** (www.ryanphotographic.com) and reproduced with his permission)

lack bones and instead possess cartilaginous skeletal elements, hagfishes are extremely flexible and can form a knot with their body, which works as a leverage mechanism for feeding or prey capture (Clark and Summers 2007; Zintzen et al. 2011). There are slime pores (around 150 in total) present prebranchially and caudally on the lateral body side (Weinrauch et al. 2017), which the animals use as part of a defence system (see below for details). Hagfishes are mostly demersal opportunistic scavengers (Martini 1998; Clark and Summers 2007), but myxine predatory behaviour has also been observed (Zintzen et al. 2011). Hagfishes are cosmopolitan and are found exclusively in marine waters at depths of 30–2000 m and even occur around hydrothermal vents (Martini 1998; Clark and Summers 2007).

Hagfishes are known to secrete large amounts of slime when threatened by predators, such as marine mammals, sharks and seabirds, or to deter feeding competitors (Lim et al. 2006; Zintzen et al. 2011). This slime is produced in specialised epidermally-derived slime glands (see below) and is instantaneously released (with a jet velocity of 0.18 ms^{-1}) (Lim et al. 2006) as milky droplets (in amounts of around 90 mg) (Fudge et al. 2005). The total content of the slime glands constitutes up to 3–4% of the hagfish body mass (Fudge et al. 2005). Once in contact with seawater, the droplets increase substantially in volume (up to around 900 ml) and form a large mucus-like cohesive mass, interspersed irregularly with threads.

Analyses have shown that this slime mass consists mostly of water (>99.9%) and a very low amount of exudate (mucin content 0.0015% and thread content 0.002%) (see below for details) (Fudge et al. 2005). Observations confirm that the slime is extruded when the animal has been directly threatened (bitten or engulfed) by the predator or stressed by nearby competitors (Martini 1998; Zintzen et al. 2011). The extruded slime does not show an adhesive effect as is given for the salamander secretion (see Fig. 7.6), but rather functions like a mesh, clogging the gills and mouths of the predators and thus impairing the flow of water (Lim et al. 2006).

The predator is only able to clear the slime from the mouth and gills by choking (Zintzen et al. 2011). There are no toxins in the slime and bitter substances also seem to be absent as the extruded slime is neutral (pH 7.3) when dissolved in water (Herr et al. 2010).

Unlike many other fish and lampreys, hagfish undergo direct development with no larval stages. The slime gland appears at a late embryonic stage (stage 14 of a total of 19) (Miyashita and Coates 2017), although it is not clear whether the gland is already functionally active at this early stage of development. Morphological studies indicate that the slime is produced by a deeply invaginated epithelial gland type (known as the slime gland, diameter up to 5 mm) (Terakado et al. 1975; Fudge et al. 2015), which contains two different cells: the gland thread cells (GTC) and the gland mucus cells (GMC) (Downing et al. 1981; Fudge and Schorno 2016). Each slime gland is connected to the epidermal surface by a short duct and the release occurs through a gland pore (Fig. 7.10).

The slime gland is surrounded by a connective tissue capsule and striated muscle, the *musculus decussatus* (Lametschwandtner et al. 1986), which affects the simultaneous release of the GTC and the GMC onto the epidermal surface. Both glands produce a different content, with a long coiled, proteinaceous thread from the GTC and mucin vesicles from the GMC (Fudge et al. 2015). During holocrine secretion, the content of both gland types becomes disrupted in the pore duct and is released as a large white droplet of mucus (Downing et al. 1981) on the epidermal surface. The intermediate filament unwinds itself and the mucin vesicles coalesce, rapidly forming a mass of viscous mucus (see below) (Koch et al. 1991).

The gland mucus cells (GMC) derive from stem cells in the gland epithelium and increase in size during maturation, finally reaching a diameter of up to 150 μm, with a centrally orientated, shrunken nucleus (Terakado et al. 1975). Within a slime gland there are numerous GMCs, each filled with vesicles, which stain slightly positive for PAS, Alcian blue at pH 2.5 and Gomori's aldehyde fuchsin, confirming the presence of acidic sulphated glycoproteins (Terakado et al. 1975; Salo et al. 1983; Fudge et al. 2015). The gland thread cells (GTC) are oval-shaped, up to 180 μm × 80 μm in size (length × width), and embedded between the GMC within the slime gland (Fudge et al. 2015) (Fig. 7.10). Within a slime gland, both immature and mature GTCs can be found, with the immature ones being clustered at the periphery of the gland and the mature ones in the centre (Terakado et al. 1975). The round nucleus appears inconspicuous in the mature cells, but plays an important role during cell maturation (see below). As indicated by the name, each GTC is filled with a single coiled and densely packed intermediate filament (IF) (Fudge and Schorno 2016). This bi-directionally tapered thread, 150 mm in length and with a diameter of 2 μm (Terakado et al. 1975), stains positively with the Alloxan-Schiff reaction (Spitzer et al. 1984) and consists of three polypeptides (see below for details) (Terakado et al. 1975; Koch et al. 1991; Spitzer and Koch 1998).

In addition to the GMC and GTC, a third cell type, the gland interstitial cell (GIC), can be observed in the immature slime glands (Winegard 2012). This cell type completely occupies the spaces between the two gland types. The cells contain a large Golgi apparatus and a fusion of vesicles at the GTC and GMC membrane
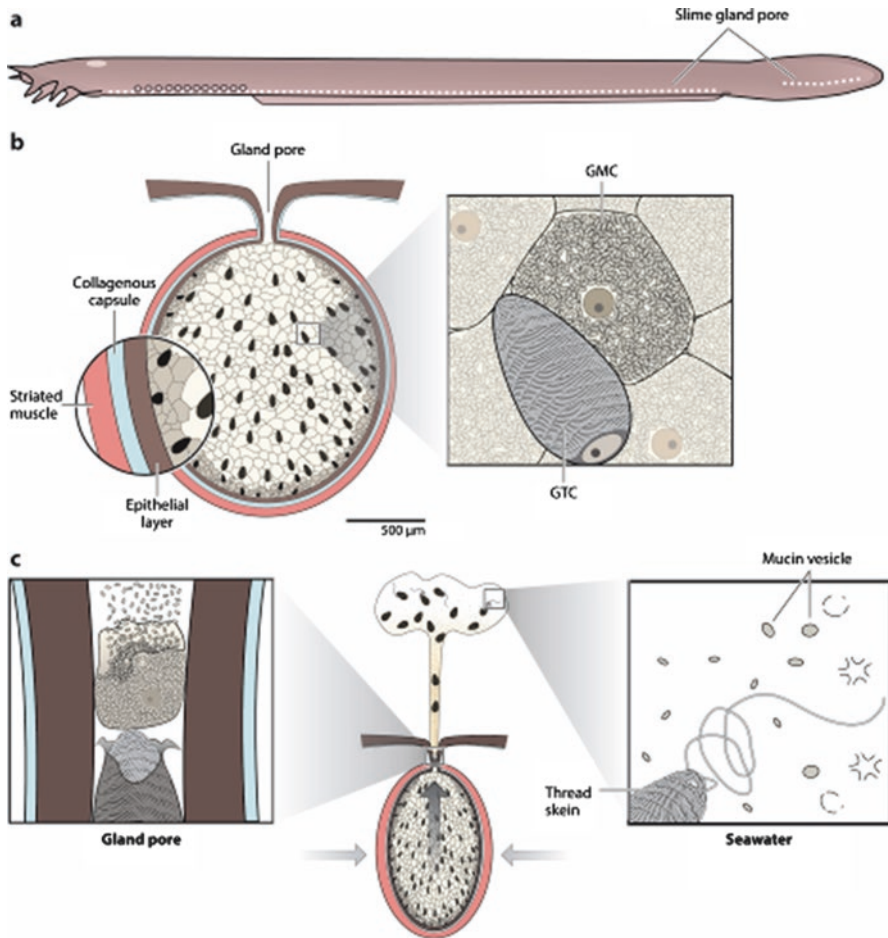
Fig. 7.10 Slime glands of the hagfish *Myxine glutinosa* (Linnaeus 1758). (**a**) The pores of the slime glands are easy recognizable along the lateral sides of the trunk. (**b**) The gland is encapsulated by an epithelial layer, collagen and striated muscle and contains the gland mucus cells (GMC) and gland thread cells (GTC). A third cell type, the gland interstitial cells (GIC), is interspersed between the developing GMC and GTC, however its function remains unclear (Winegard 2012). (**c**) Upon secretion, the GMC and GTC are disrupted within the duct and release mucin vesicles (from the GMC) and a coiled thread (from the GTC) into the seawater (Image from Fudge et al. (2015) and republished with permission)

can be observed, suggesting a supportive function for both gland types. So far, no GIC has been observed in the expelled slime glands, but it cannot be excluded that the cells become damaged during the holocrine release (Winegard 2012).

While the slime glands are concentrated in specific regions and limited in number (see above), other gland cells dominate the hagfish integument, namely the small mucous cells (SMC) (91%) and, to a minor extent, the large mucous cells (LMC) (1%) as well as the epidermal thread cells (ETC) (7%) (Spitzer and Koch 1998). In comparison to the slime gland cells, the normal epidermal cells are smaller

in size (SMC: 15 μm × 8 μm, LMC: 60 μm × 35 μm, ETC: 35–20 μm), isolated, and not encapsulated by connective tissue and muscle layers (Spitzer and Koch 1998). Nevertheless, each ETC is surrounded by SMCs and the two cells types interconnect via interdigitating plasma membranes, and the ETC thread binds with desmosome-like structures to these membranes (Whitear 1986). However, common properties of the content have not been described for the SMC and ETC as it has for the GMC and GTC of the slime gland. Mucous glands (SMC, LMC) and thread cells (ETC) are not limited to the hagfish integument but have also been found in other fishes such as the goblet cells (mucous cells) or the club cells (thread cells) in teleosts (Lane and Whitear 1980) or "skein cells" in lampreys (Leppi 1968; Rahemtulla et al. 1976).

Although the small and large mucous cells (SMC and LMC) also produce mucus and stain histochemically for acidic glycoproteins similar to the GMC (Subramanian et al. 2008), a higher enzyme activity (lysozyme, alkaline phosphatase, cathepsin B and proteases) and three additional proteins (13–16 kDa, matching haemoglobulin-3, histone H3 and H2B protein) can be observed in the extruded slime (Subramanian et al. 2008). In addition to the different mucous cells (GMC, SMC, LMC) to which they are associated in the hagfish integument, the thread cells of the normal epithelium (ETC) and those in the slime gland (GTC) also display differences. While the threads in the GTC are tightly wound and increase in thickness and length during gland maturation (Fig. 7.10), those of the ETC appear to be shorter and less organized. Radiolabelling tests furthermore support the assumption that more than one thread are produced in the different regions of the ETC, while there is only a single thread in the GTC.

While the predator-defensive function of the slime glands has been clearly documented (see above), the epithelial normal mucus is continuously released. It serves as a physical and biological barrier to the aquatic environment as well as pathogens (Lane and Whitear 1980) but does not contribute to slime production. The function of the threads from the ETC is unclear. Although also secreted, the threads do not participate in the slime formation; they may instead serve to "provide support against distortion in the soft mucigenic epidermis […]" (Fudge and Schorno 2016).

GMCs and GTCs are hypothesised to arise from a basal epithelial cell layer and form the slime gland as they grow and mature (Downing et al. 1984; Fudge et al. 2015). Further studies may be necessary to determine the stem cells and process of gland formation. Detailed studies are, however, available for the formation of the tightly coiled thread of the GTC. Initially, the nucleus of an immature GTC is roughly spherical and fills a large part of the cell. With further maturation, the cell becomes ellipsoidal in shape, with one end becoming pointed and the other more blunted. The nucleus also changes its shape, assuming a conical to elongate spindle form with a wide base at the blunt side of the cell (Downing et al. 1984). At this premature stage there is no thread formation, however, at this thread formation zone (also named the mitochondrial-rich zone – MRZ) (Downing et al. 1984) the cytoplasm is rich in mitochondria, ribosomes and polyribosomes. At maturation, the MRZ has disappeared and is occupied almost entirely by the formed thread, and the nucleus has retreated to the basal end of the cell (Fig. 7.11).
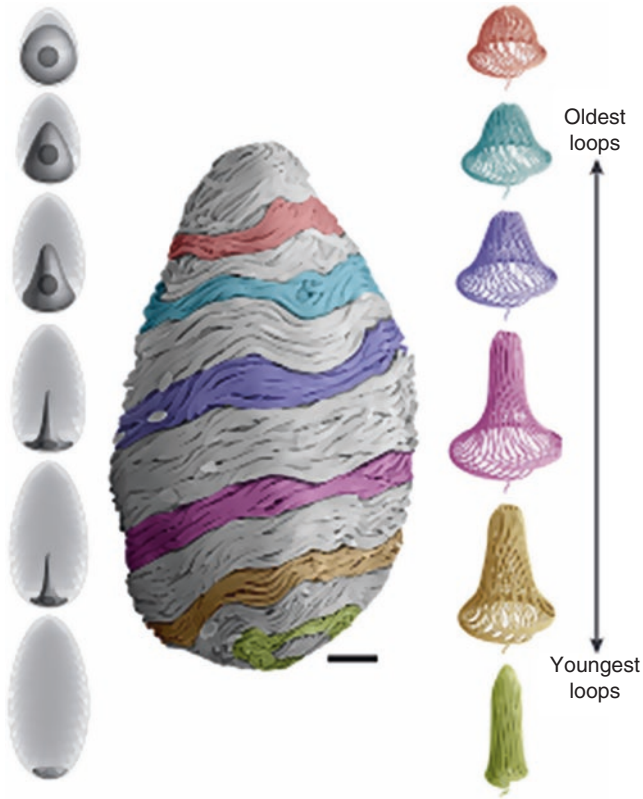
Fig. 7.11 Growth of the gland thread cells (GTC) in the hagfish *Myxine glutinosa*. On the left column, the growth of the GTC is shown from an early stage to the full mature stage (upper to lower arrangement). With maturation, the nucleus (darker area) shrinks in size and becomes slender, while in parallel the number of thread layers (light grey) increases. The centre and right column of the figure shows the maturation of the threads depending on the cell developmental stage. Initially, a cap-like thread coil (upper apricot-coloured thread) is formed in the mitochondria-rich zone, but with maturation the thread acquires a compact, ovoid form (lower green-coloured thread). Scale bar: 10 μm (Image from Winegard et al. (2014) and republished with permission)

Images of the immature thread show that it is formed from a few (6–12) parallel bundled intermediate filaments (IF) (10–12 nm in diameter) of indeterminate length (Terakado et al. 1975), separated by an electron-lucent space and partly interconnected by fine fibrous structures associated with polyribosomes (Winegard et al. 2014). With the maturation of the GTC, the thread diameter increases through the addition of more IFs to the thread. The younger threads are around 30 nm in diameter. The younger threads are around 30 nm in diameter (about 2–3 IFs only) (Terakado et al. 1975) and the mature ones are about 2 μm (incorporating 50–300 filaments) (Downing et al. 1984). Furthermore, microtubules (MTs) (~25 nm in diameter) are incorporated into these bundles (Fudge and Schorno 2016) or penetrate
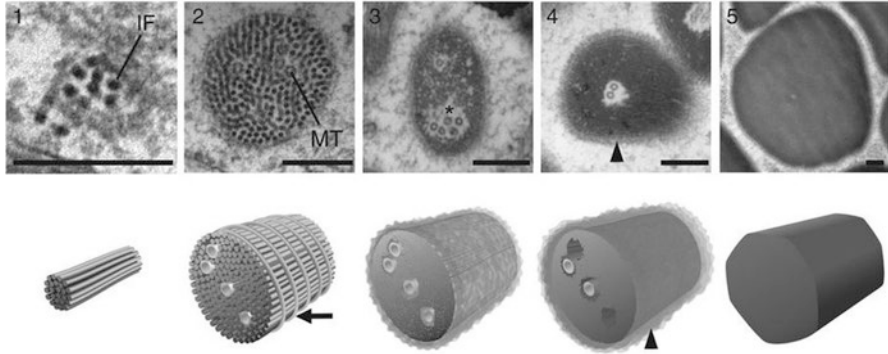
Fig. 7.12 Subsequent growth and maturation of the thread (from left to right) formed by the gland thread cells (GTC) in the hagfish *Myxine glutinosa*. The upper row shows TEM images and the lower row the corresponding schematic drawings. Starting with a few intermediate filaments (IFs) in the first section on the left, further IFs and microtubules (MTs) are incorporated into these bundles (second section). Furthermore, a filamentous-like structure (black arrow) wrapped around the IFs-MTs bundle and zones of exclusion can be observed around the MTs. With further maturation, the IFs become tightly packed and the outer filamentous structure becomes replaced by a rind. In a fairly mature thread cell (fourth section from the left), the IFs condensate into a unitary super-structure; the MTs and their halos as well as the fluffy rind around the thread disappear and the superstructure eventually appears as a mature thread in the fifth section from the left (Images from Winegard et al. (2014) and republished with permission)

from the side (Fudge and Schorno 2016), either to deliver IFs and/or IF subunits, or to increase the thread's girth (Terakado et al. 1975). Furthermore, in this intermediate stage the filament-to-filament spaces within the thread decrease, while in the filament-to-MT space, a zone of exclusion, named a halo, can be observed (Terakado et al. 1975; Downing et al. 1984; Fudge et al. 2015). Besides the addition of IF and MT to the thread, there is also a filamentous-like structure wrapped around the IF-MT bundle (Fudge et al. 2015) (Fig. 7.12).

With further development, the IFs are very tightly packed together and can hardly be separated visually, while a fluffy rind appears on the thread surface, where the filamentous-like structure is wrapped around the bundle (Fudge et al. 2015). In a fairly mature thread cell, the IFs condensate into a single IF superstructure and the MT and its halos as well as the fluffy rind around the thread disappear (Winegard et al. 2014). As these modifications to the threads (loss of MT and rind, condensation of IF) appear to happen in all parts of the thread simultaneously, Spitzer et al. (1984) assumed that these processes might be triggered by chemical signalling. Besides the morphological changes of the IFs, the ratio of the three polypeptides (Spitzer et al. 1988) also changes and with the GTC maturation a progressive increase in the β/γ value could be measured, while the $\alpha/(\beta + \gamma)$ ratios remain near 1 (Winegard et al. 2014). However, this IF condensation does not represent the final stage of thread maturation, as the thread continues to increase in diameter subsequently.
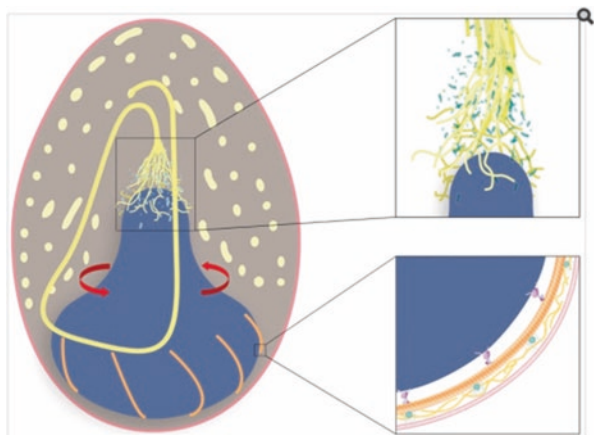
Fig. 7.13 Thread formation by the gland thread cells in the hagfish *Myxine glutinosa*. The intermediate filaments (yellow) are synthesized and arranged in the mitochondria-rich zone (light blue) near the apical tip of the nucleus (dark blue). In parallel, the nucleus rotates unidirectionally, driven by dynein molecule motors (purple), which process along the microtubules (orange) of the cell membrane (see Fudge and Schorno (2016)) (Image from Fudge and Schorno (2016) and republished with permission)

In addition to the aspect of thread maturation, questions remain as to how the coiling of the thread with about 500 thread loops is achieved. Fudge and Schorno (2016) have shown that the arrangement of thread loops is correlated with the changing morphology of the nucleus, whereby the oldest loops are located apically and the youngest ones basally (Fig. 7.11). As a specific wheel-like structure, which would enable the almost perfect coiling of the thread, has so far not been observed in the cytoplasm, it is hypothesized that the nucleus, with the thread attached to it, rotates around its own axis instead (Fig. 7.13) (Terakado et al. 1975).

Although the thread maturation of the GTC has quite extensively been described in the literature, no knowledge of its development period has so far been mentioned. Further open questions remain not only with regard to the mucin production in the GMC, but also more generally as to whether (and how fast) a re-synthesis of the slime gland takes place or if the gland actually degrades after having expelled its slimy content.

Chemical analyses of the extruded slime indicate a ratio of 77% protein, 12% carbohydrate, 5% lipid, and 6% sulphates (dry weight) (Salo et al. 1983). One part of this amount is surely produced by the GMC, whose mucin vesicles stain positively with Alcian blue and PAS (Salo et al. 1983; Spitzer et al. 1984), as well as for sugar moieties like *N*-acetylgalactosamine (lectin soybean agglutinin – SBA) (Winegard and Fudge 2010), indicating the presence of acidic sulphated glycoproteins in the slime. In the thread, three abundant IF proteins (α, β, and γ) have been confirmed, with a similar molecular mass (63 kDa) but distinct pI values (α = pI 7.56, β = pI 5.67, γ = pI 5.31) (Spitzer et al. 1984; Schaffeld and Schultess 2006).

In earlier studies the hagfish thread was determined to be keratin-like, because of its low sequence identity with other IF proteins (Koch et al. 1991; Fudge et al. 2003) and mechanical properties different from mammalian hard α-keratins (Fudge and Gosline 2004). However, later genome analyses have confirmed that the γ thread protein is a member of the type I keratin family (although it shows structural congruence with the type III IF proteins), while the α thread protein appears to be homolog of the type II keratins (Schaffeld and Schultess 2006). Moreover, both hagfish IF proteins contain glycine-rich segments; these loops may contribute to the mechanical flexibility of the IFs (Schaffeld and Schultess 2006).

In addition to sugars and proteins, a substantial quantity of inorganic ions such as chloride (191 mmol l^{-1}), potassium (143 mmol l^{-1}) and, to a lower extent, sodium (41 mmol l^{-1}) could be confirmed in the slime in relation to its body fluid. The extruded slime furthermore contains organic osmolytes such as trimethylamine oxide (TMAO, 101.3 mmol l^{-1}), glycine (79.9 mmol l^{-1}) and others (Herr et al. 2010). However, it may be likely that these compounds serve mainly as osmoprotectants for the tissue. Hagfishes are osmoconformers, and their plasma, tissue and extruded slime (888 mOsm l^{-1}) have a similar osmolarity to that of sea water (1000 mOsm l^{-1}) (Herr et al. 2010).

Directly after the secretion of the thread the mucin vesicles swell and burst, forming strands which bind to the unravelled and elongating thread (Fig. 7.14), whereby a 3D mesh net is formed. So far it has remained unresolved as to what exactly triggers the rupture of the mucin vesicles, since some vesicles remain intact when released into the medium while others swell and burst more slowly or more quickly (Herr et al. 2010). As is the case for hagfish tissues generally, the vesicles also have the same osmolarity as seawater (Luchtel et al. 1991). Tests with inorganic ions, organic compounds and membrane channel inhibitors confirm that the majority of the vesicles rupture in the presence of Ca^{2+}, indicating Ca^{2+}-activated membrane transporters and aquaporins (Herr et al. 2014).

Differences in the unravelling of the thread could be observed in different hagfish species. The threads of the Atlantic species (*Myxine glutinosa*) do not uncoil spontaneously, but require the presence of the mucin and the mixing effect (Winegard and Fudge 2010) to trigger the fast maturation (about 100 ms) of the slime. In contrast, the GTC of the Pacific species *Eptatretus stoutii* (Lockington 1878) only unravel at a certain sodium chloride concentration (1.5 mol l^{-1}) and specific temperature, but in the absence of the mucin vesicles and the mixing effect (Koch et al. 1991; Bernards et al. 2014).

The third component, water, does not bind to this thread/mucin net, but is physically entrapped as in a fine sieve (Fudge et al. 2005). The stability of the slime is ensured by the long threads, as the mucin viscosity is too low to form stable linkages between the threads (Fudge et al. 2005).

This slime appears to be an elastic and coherent soft gel with a thread extensibility of 2.2, similar to that of orb-web spiders (see Table 7.1 for comparison), as well as a tensile strength of up to 180 MPa (Fudge et al. 2003). At a certain strain point, however, the threads do not return to their original length but remain deformed.
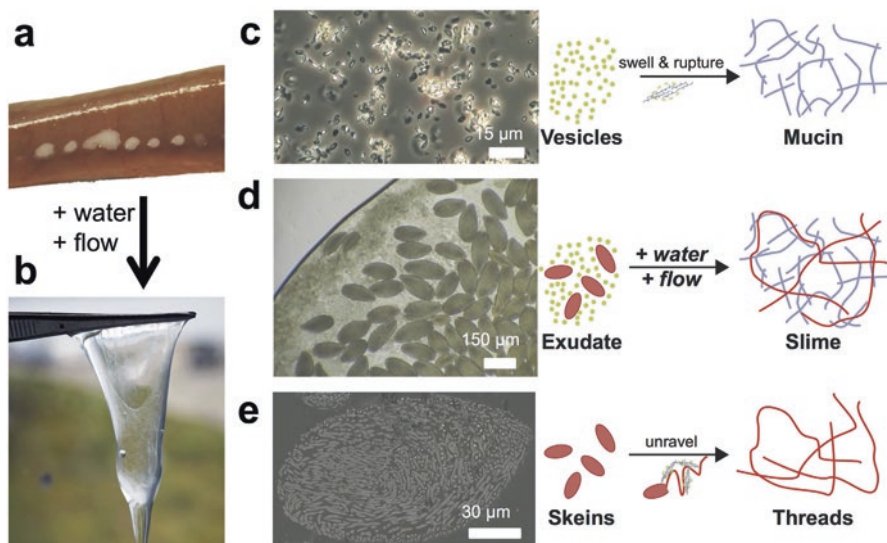
Fig. 7.14 Slime glands and slime formation in the hagfish *Myxine glutinosa*. (**a**) Photograph of slime gland pores and its isolated secretion. (**b**) Light micrograph of the two components. (**c**) Secreted mucin vesicles from the gland mucus cells. (**d**) Final slime (also named exudate) including mucin vesicles and threads from the gland thread cells. (**e**) Isolated threads (also named skeins) (Image from Boni et al. (2016a) and republished with permission)

This behaviour is caused by an irreversible transition of the α-helices within the thread proteins towards a β-sheet confirmation (Fudge et al. 2003), effecting this high breaking stress value.

The hagfish slime itself is not adhesive, as is the case for the other animals described in this study. Nevertheless, the hagfish system provides a good basis for the study of food-relevant aspects (Bocker et al. 2016; Boni et al. 2016b) or the development of artificial protein-based fibres (Negishi et al. 2012; Dance 2016; Fu et al. 2017). Similarly, bioadhesives mostly also have a low sugar ratio (von Byern et al. 2017a), bind a high amount of water (von Byern et al. 2016), and assemble into fibrous 3D structures when released into sea water (Zheden et al. 2014, 2015). However, contrary to hagfish slime, these systems are currently far from being fully understood. Finally, characterizing the hagfish survival strategy may provide a new indication of how the animals avoid being trapped in their own slime, current data indicating that the elongational extrusion of the slime towards the predator causes a thickening of the slime, effective in clogging gills. On the other hand, shearing off the slime from its body by making a movable knot results in a slime thinning and by this the hagfish avoids being clogged by its own secretion (Boni et al. 2016a). Thus, hagfish slime could be a good model to understand the effects and mechanisms of a defensive system.

Table 7.1 Comparison of the glowworm *Arachnocampa luminosa* prey capture system with that of orb-web spiders, showing large differences regarding the materials (silk and glue) used

	Arachnocampa	Orb-web spider
Usage	Prey capture	Prey capture
Environment conditions	Humidity >90%	Humidity 20–90%[d, e]
	Temp. 13–18 °C[a]	
Silk production region	Labial gland[b]	Abdominal silk spinning organ[f, g]
Silk type	Cross-β-sheet[b]	β-spiral, 310 helix[f, g]
Major silk amino acids	Lys, Pro, Ser[b]	Gly, Pro[f, g]
Major silk fibroin size (kDa)	~1000[b]	200–500[f, g]
Silk extensibility	0.47[c]	2.7–5.0[h]
		Max. 27% major ampullate fiber[h]
Silk tensile strength	1.9 MPa single fishing line[c]	0.5 GPa viscid fibre[h]
		1.1 GPa major ampullate fiber[h]
Droplet size	<1185 × 785 µm[a]	4.4 × 4.5 µm *Mangora maculata* (Keyserling 1865)
		67 × 50 µm *Araneus marmoreus* Clerck 1757[i]
Glue composition	Water (99%)	N-acetylgalactosamine
	Protein	Glycoprotein
	Fatty acids	Lipids
	Salts (maybe urea/uric acid)[a]	Salts
		Choline, GABamide and others[j]
Droplet model	2 layers[a]	3 layers[k]
	1. Central core region	1. Central anchoring granule
	2. Outer water hull	2. Larger glycoprotein glue region
		3. Outer fluid cover

Further details of both systems can be found elsewhere:[a]von Byern et al. (2016),[b]Walker et al. (2015),[c]Unpublished data by von Byern,[d]Opell et al. (2013),[e]Opell et al. (2011),[f]Hayashi and Lewis (1998),[g]Hu et al. (2006),[h]Gosline et al. (1999),[i]Opell and Hendricks (2009),[j]Amarpuri et al. (2015),[k]Opell and Hendricks (2010)

7.3 Predation

"Invincibility lies in the defence; *the possibility of victory in the attack"*. (Sun Tzu, "The Art of War")

Prey capture by adhesive secretion may take place passively through trap mechanism (e.g. silk web, mucus net or tentacle fan). Additionally a few species are known to directly attacks and capture prey by their sticky secretion.

7.3.1 Trapping Approach

Orb-weaving spiders are quite possibly the model organism when discussing the use of adhesives to trap prey. With their large, impressive, highly structured webs and the different types of silk involved in building and maintaining these, while also enabling them to resist abiotic and biotic factors, these animals are highly specialised at prey capture. Studies on the viscid capture threads and the glue involved have recently been reviewed by Opell (2013). Therefore, we do not aim to provide a comprehensive summary of the review, but rather discuss and correlate the data given for orb-web spiders with an as yet poorly known web structure system, namely that of the New Zealand glowworm *Arachnocampa luminosa*.

7.3.1.1 Glowworm

Glowworms are the larval form of a fungus gnat of the Keroplatidae family (Matile 1981; Meyer-Rochow 2007; Baker et al. 2008). *Arachnocampa* (Edwards 1924) is a world-renowned glowworm genus, endemic to New Zealand and Australia (Merritt and Baker 2001; Evenhius 2006; Baker et al. 2008). Species of this genus are known for their ability to capture prey by means of adhesive droplets on vertical threads (Fig. 7.15) in combination with auto-bioluminescence (Richards 1960; Meyer-Rochow 2007; Willis et al. 2010). The habitat of this group of insects is limited to places with a high humidity and low air movement such as rainforest patches or tree fern-lined gullies, but the animals can also be found in wet boulder caves
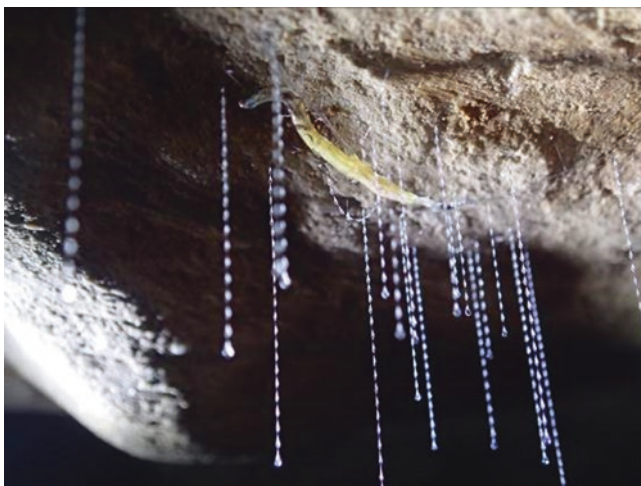
Fig. 7.15 In situ image of a larva of the glowworm *Arachnocampa luminosa* and the curtain of fishing lines along its nest (Image from Janek von Byern, Ludwig Boltzmann Institute for Experimental and Clinical Traumatology (Austria), and reproduced with his permission)
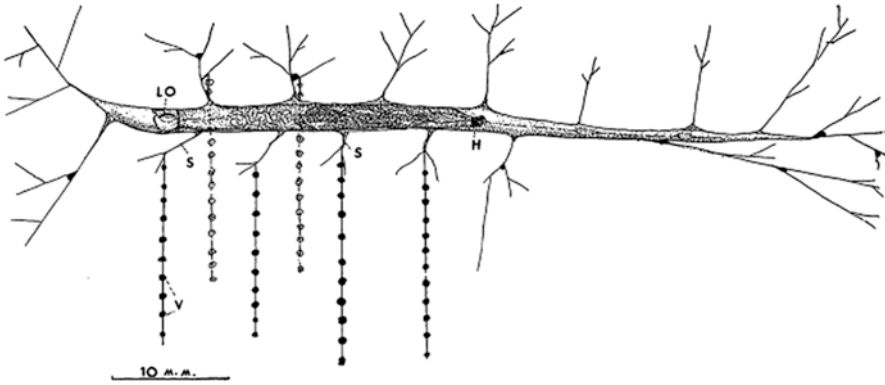
Fig. 7.16 Larva of the glowworm *Arachnocampa luminosa* within its tube, with its head (h) on the right figure side and its posterior light organ (LO) on the left side. The larva attracts the prey with its emitting bioluminescence and then catches it with adhesive threads made of silk (s) and adhesive vesicles (v) (Image originally by Gatenby (1959), modified by von Byern et al. (2016), and republished with permission by the Royal Society of New Zealand)

(Pugsley 1984; Broadley 2015). Not all caves in New Zealand and Australia have glowworms, but in particular the world-famous Waitomo Cave (Humphries 1889) and Spellbound Cave on New Zealand's North Island have populations of thousands of individuals, enabling a spectacular glowworm viewing experience at any time.

The larvae construct a nest composed of a mucous tube attached by a network of threads to the rocky substratum (Fig. 7.16) (Gatenby and Cotton 1960; Meyer-Rochow 2007). From this "hammock", long fishing lines with evenly spaced adhesive droplets (von Byern et al. 2016) hang down, forming an adhesive curtain (Richards 1960) similar in function to orb-web spider webs (Meyer-Rochow 1990, 2007; Walker et al. 2012) The *Arachnocampa* larvae have adopted a "sit-and-lure" predatory strategy to catch phototropic flying insects.

To attract prey, bioluminescence (peak emission wavelength at 488 nm) (Lee 1976) is emitted from the larva's posterior light organ, which is composed of several large modified Malpighian tubuli (Green 1978; Sivinski 1998; Willis et al. 2010; Merritt and Clarke 2011; Sharpe et al. 2015). With this blue light projecting downwards, the larva attracts potential prey, catching small flying (e.g, moths, gnats, sand- and stoneflies, or other *Arachnocampa* adults) or crawling animals (isopods, ants, amphipods, millipedes or even small land snails) (Richards 1960; Stringer 1967; Pugsley 1984; Broadley and Stringer 2001, 2009). In addition, larger insects such as Hymenoptera (bees and wasps) and Coleoptera (beetles) are also occasionally found within the fishing lines, but it is questionable whether these insect groups are actually and specifically attracted to the glowworms' bioluminescence (Broadley and Stringer 2001).

The adhesive droplets are evenly spaced along a silk thread produced by *Arachnocampa* and are spindle shaped (Fig. 7.17) with a heavier double-sized droplet at the thread's end (von Byern et al. 2016).

Fig. 7.17 The droplets in the fishing lines of the glowworm *Arachnocampa luminosa* are ellipsoid in shape and uniformly distributed along the thread (Image from Janek von Byern, Ludwig Boltzmann Institute for Experimental and Clinical Traumatology (Austria), and reproduced with his permission)

The droplets consist mostly of water (99%) and display hygroscopic properties at varying humidity levels (von Byern et al. 2016). So far, only free fatty acids (low concentration dodecanoic acid, tetracosanoic acid, pentadecanoic acid; higher concentration hexadecanoic acid, octadecanoic acid) and proteins (MW range of 58–62 kDa and a pI of 4.2–5.5) were investigates by GC-MS, 2D–PAGE while there is no indication for the presence of monosaccharides (unpubl. Data by V. Dorrer, J. von Byern and M. Marchetti-Deschmann). The glue furthermore appears weakly acidic (pH 4). The hygroscopic properties of the *Arachnocampa* glue indicate that additional compounds must be present. After drying, crystals appear in the droplet region, which attract water with increasing humidity (von Byern et al. 2016). In the past, it was assumed that glowworms use oxalic acid or barbiturate-like compounds in their adhesive droplets to kill and predigest their prey (Fulton 1941; Meyer-Rochow 2007). However, later analyses (Pugsley 1980; von Byern et al. 2016) rather speak against this; instead, the excretory products urea and/or uric acid (von Byern et al. 2016) may be present in the droplets and might be responsible for these hygroscopic properties.

Although it is named "*Arachno*" ("spider-like"), the prey capture system of *Arachnocampa* differs substantially in its origin, composition, strength and behaviour from the well-known orb-web spider system (Table 7.1). The glowworm thread is composed mainly of cross-β-sheet crystallites, as seen in other silks (Craig 1997; Walker et al. 2012, 2015) produced by paired labial glands (Gatenby 1960) and released through the mouth part. Orb-web spiders produce parallel-β-sheets to compose their silk threads (Craig 1997) with different mechanical properties and

molecular structures (Blackledge and Hayashi 2006) through a complex abdominal silk spinning organ named a spinneret (Vollrath 1999; Vollrath and Knight 2001). Besides the divergence in the silk structure, the *Arachnocampa* fishing lines and viscid threads of orb-web spiders also differ in their overall structure and adhesive droplet composition (Table 7.1).

In *Arachnocampa*, so far only a two-layered droplet could be confirmed, with a low number of components present. The droplets only show a bonding ability at humidity values higher than 80% (unpubl. data by von Byern). In contrast, a three-layered droplet model with quite a complex composition exists in spiders. Moreover, at low humidity (>20%; Opell and Hendricks, Opell et al. 2011, 2015; Stellwagen et al. 2014), the spiders' droplets are still visible and adhesive.

The silk of spiders is known to show a high extensibility and tensile strength, comparable to artificial materials such as nylon (Gosline et al. 1999). The prey capture system of *Arachnocampa* lacks such strong mechanical properties (unpubl. data by von Byern). However, it should be noted that these animals live in a cave or forest throughout their life cycle. Hence, they have adapted to the very constant habitat conditions characterised by low turbidity and a lack of UV influence and humidity variation unlike spiders. The prey spectrum is also rather constant in size and impact force. Unpublished data may indicate that glowworms have developed a predetermined thread failure force limit. This would ensure that too many prey items or too heavy prey result in a breakage and loss of one fishing line, thus preventing the whole nest from being torn from the cave ceiling.

While some fungus gnats, such as *Arachnocampa*, have become a national and tourist celebrity and have been well described, the larval biology of most other fungus gnat species remains marginally investigated. South American *Neoditomyia* spp. (Sturm 1973) and the Jamaican species *Neoditomyia farri* (Coher 1996) likewise inhabits caves and captures prey by fishing lines (Stringer and Meyer-Rochow 1993, 1996) similar to *Arachnocampa*. However, *Neoditomyia* spp. appear to have longer fishing lines (of up to at least 17 cm) than *Arachnocampa* and these are coated with a thin layer of glue instead of distinct adhesive droplets (Stringer and Meyer-Rochow 1993, 1996; Meyer-Rochow 2007). Moreover, *Neoditomyia* spp. capture their prey "passively", meaning that they do not attract prey through bioluminescence as do *Arachnocampa* spp. (Meyer-Rochow and Stringer 1998). Besides *Arachnocampa* and *Neoditomyia*, there are more carnivorous (Fulton 1939, 1941; Fisher (1940); Meyer-Rochow 2007) and non-carnivorous fungus gnats (Schmitz 1912; Sevcik et al. 2012; Osawa et al. 2014), whose adhesive and mucus secretions are currently far from being fully characterised.

7.3.1.2   Comb Jellies

The sea gooseberry *Pleurobrachia pileus* (Müller 1776) (Fig. 7.18) is a small (upto 4 cm) oval to ovoid ctenophore, occurring worldwide in the upper water column (Greve 1974, van Walraven et al. 2017). *Pleurobrachia* is a carnivorous species and catches actively swimming planktonic organisms, such as gammarid amphipods,
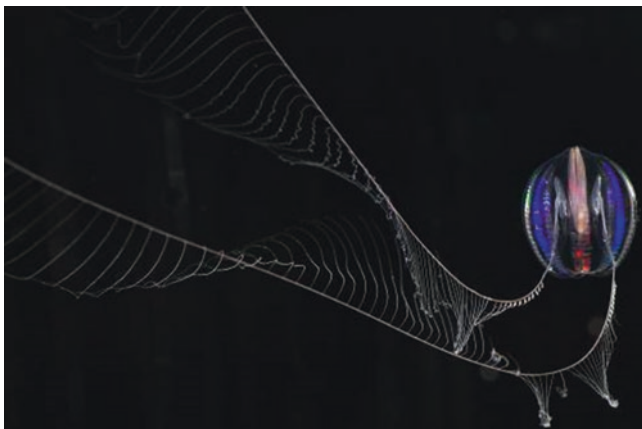
Fig. 7.18 The cydippid comb jelly *Pleurobrachia pileus* with its two tentacles and the numerous branching tentilla (Image courtesy of Lodewijk van Walraven, Netherlands Institute for Sea Research Texel (Netherlands), and reproduced with his permission)

crab larvae, barnacle cyprids and copepods, with its two long tentacles. Unlike jellyfish of the phylum Cnidaria, the sea gooseberry does not use poisonous substances or nettle cells (cnidocytes) (Östman 2000), but instead uses an adhesive for prey capture (Bargmann et al. 1972). The two long retractable tentacles are branched into small thread-like filaments, so-called tentilla, which can fan out during swimming to spread over a large area (up to 400 cm^2) for prey capture (Greve 1975). Both the tentacles and tentilla consist of central muscle cells surrounded by an outer epidermal layer. The latter comprises sensory cells and a large accumulation of fungiform-like secretory cells (the so-called "Lassozellen" or colloblasts) (Vences 1988), in which the glue is produced. Like the cnidarian cnidocystes (Anderson and Deban 2010, 2012; Anderson et al. 2012), the colloblasts in ctenophores are released and projected towards the external stimulus (Carré and Carré 1993) and bond to the prey at the moment of contact. This mechanism is comparable with the spin tongue of amphibians and some reptiles.

The size and morphology of the colloblasts vary between and within species (Benwitz 1978). In *Pleurobrachia*, they are about 10 μm long and 4 μm wide (Benwitz 1978), while in *Eucharis multicornis* (Eschscholtz 1928) the cells reach a size of 25 μm by 8–10 μm (length by width) (Franc 1978). Other species such as *Minictena luteola* (Carré and Carré 1993) bear five different types of colloblasts, differing in size and cellular content, on a single tentillum (Benwitz 1978). As it could be excluded that these five colloblast types only represent different maturation phases, the functional significance of this high variability so far remains unclear (Benwitz 1978).

Colloblasts (Fig. 7.19) consist of a hemispherical head (the collosphere) and a helical filament (the collopod), which coils several times around the central stalk-like nucleus and is rooted in the mesoglea (Carré and Carré 1993). In *Pleurobrachia*, two types of granules can be distinguished: a layer of small osmiophilic external

Fig. 7.19 Schematic drawing of the colloblast in the comb jelly *Pleurobrachia pileus* and its neighbouring cells in a tentillum. Abbreviations: *ec* epithelial cell, *eg* external granules, *f* fibre of the mesoglea, *ig* internal granules, *m* muscle, *n* nucleus, *np* nerve plexus, *ps* perimuscular space, *r* radius, *rm* root membrane, *ro* root, *sb* spheroidal body (Image originally from Benwitz (1978) and modified by von Byern et al. (2010), reproduced with permission)
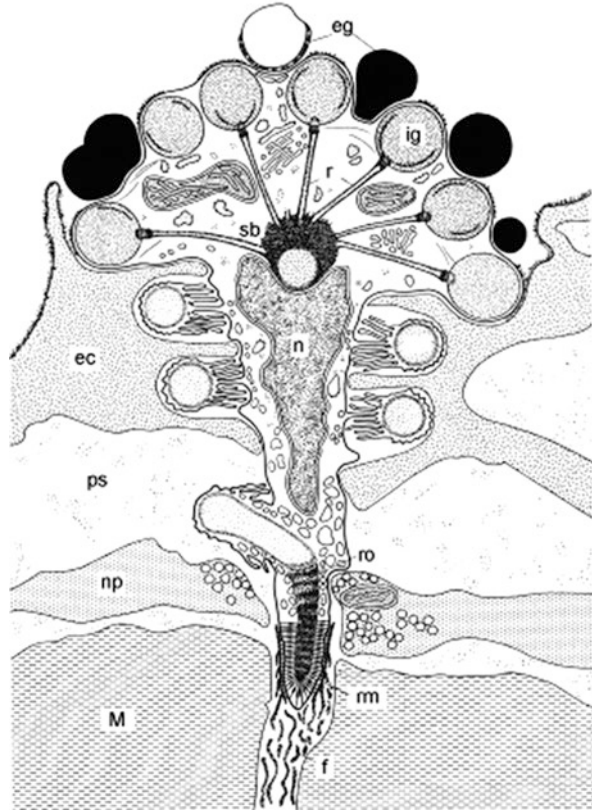
granules (0.8–0.9 μm in diameter) located on the outer side of the collosphere (Benwitz 1978) and another layer of membrane-bound internal granules ("eosinophilic granules", likewise around 0.8 μm in diameter) located inside the collosphere, enclosing a fine-grained content (von Byern et al. 2010). In the centre of the collosphere is the spheroidal body, a star-shaped structure from which up to 20 connecting strands (also called "radii") radiate towards the internal granules. These strands, however, are not directly connected to the granules and end in a stamp-like plate from which tubular rods bind to the granules (Benwitz 1978). The function of this star-shaped body remains unclear. Carré and Carré 1993 assumed a nucleation centre for the spiral filament or an involvement in collosphere development. It is also conceivable that the strands determine the position of the internal vesicles and push them against the colloblast membrane.

Detailed descriptions of the development and differentiation of the colloblasts are given by Benwitz (1978) and Mackie et al. (1988). Based on their observations, colloblasts develop from choanocyte-like precursor cells through three intermediate stages. Moreover, the external granules are not formed by the colloblast itself but

rather by another cell type, namely the cap cells (Weill 1935; Hovasse and de Puytorac 1962, 1963; Bargmann 1972; Bargmann et al. 1972; Storch and Lehnert-Moritz 1974; Benwitz 1978; Franc 1978; Emson and Whitfield 1991; Carré and Carré 1993). These cap cells appear at an early stage of the colloblast development and degenerate later, leaving the granules as "residual" droplets on the external membrane of the collosphere (von Byern et al. 2010). As a consequence, the mature external granules possess two membrane layers, an inner strongly osmiophilic vesicle membrane and the outer cap cell membrane (Moore 2001).

Although numerous studies are available on the anatomy of the colloblasts in different ctenophore species (McAlister 1960; Gilbert and Rayor 1983), many questions remain concerning glue synthesis and composition and its involvement in prey capture. Previous ultrastructural observations indicate that the external granules contain "osmiophilic lipoproteins" (Bargmann et al. 1972; preliminary studies by von Byern et al. (2010)) furthermore confirm the presence of neutral sugars (*periodic acid-Schiff* reaction) and proteins at pH 6.0–8.5 (Biebrich scarlet staining) in both the internal and/or external granules. Latest genome analyses identify a specific gene named "tentillin", which exhibits cell-specific expression patterns in the tentacles, tentillae and mature colloblasts (Moroz et al. 2014).

Like the cnidarian cnidocytes, the colloblast in Ctenophora can only be used once as the spiral filament cannot be retracted and rewound. Also, the external granules are only synthesised by cap cells during colloblast development. In cnidarians, it is known that approximately 25% of the existing cnidocytes are used for prey capture. However the animals are able to replace and renew used cnidocytes within 48 h (von Byern et al. 2010). For ctenophores such as *Pleurobrachia*, there is as yet no information about the colloblast or tentilla replacement.

7.3.2   Direct Attack

7.3.2.1   Spitting Spider

In addition to the trapping mechanisms described for orb-web spiders, ground spiders (Gnaphosidae) (Wolff et al. 2017) or bolas spiders (Yeargan 1994) others like the so-called "spitting spiders" (Bürgis 1980, 1990) use another approach for prey capture. As its name suggests, *Scytodes* sp. (Scytodidae, Arachnida) does not produce adhesive webs but actively expels sticky silk onto its prey to ensnare it (Fig. 7.20) (Monterosso 1927, 1928; Kovoor and Zylberberg 1972). This system is also used as self-defence against predators (Bristowe 1931; Dabelow 1958; McAlister 1960; Valerio 1981; Jackson et al. 1998).

The genus *Scytodes* contains several species of small spiders, about 3–6 mm in length, whose females are slightly larger (4–6 mm) than the males (about 4 mm) (Robinson 2005). The animals are shiny and hairless but with short setae covering the body (Fig. 7.21). The body colour is mid-brown to pale yellow-reddish with black stripes on the cephalothorax that somewhat resemble a lyre (Jackson et al. 1998).

Fig. 7.20 The spider *Scytodes* sp. spits the adhesive threads in a zigzag pattern using either one or both chelicerae to expel the threads (Image from Foelix (1996) and republished with permission)
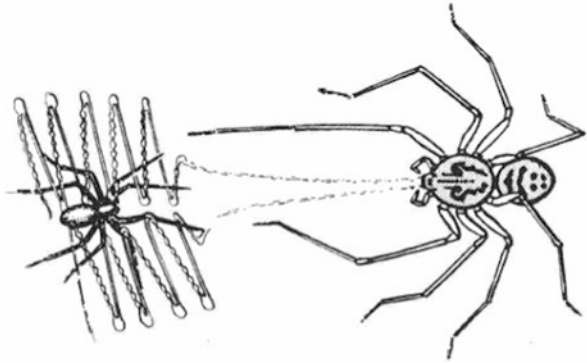
Fig. 7.21 Image of the spider *Scytodes thoracica* (Image courtesy of Pierre Oger (http://arachno. piwigo.com/) and reproduced with his permission)

The legs, which slowly taper in size, are long and black banded. The abdomen, of roughly the same circular shape as the cephalothorax, slopes downwards towards the thin pedicel (waist-like connector) and bears paired black spots, of which the first pair is fused (Nentwig 1985). *Scytodes thoracica* (Latreille 1802) is the most prominent and best characterized species within the family Scytodidae. The animals prefer a concealed lifestyle and can commonly be found in shady areas in houses (cellars, dark areas, closets) and outside under bark, among tree leaves or beneath overhanging stones and slopes (Nentwig 1985; Suter and Stratton 2005). Although *Scytodes* spp. are ecribellate spiders and do not produce a dragnet as orb-web spiders do, they can be observed in a woven non-sticky web (Nentwig 1985).

The spitting spiders are solitary and actively hunt their prey at night by wandering around. During the day, the animals hide in a cryptic posture and avoid light (Nentwig 1985). The spiders are slow-moving and have extremely poor eyesight (Gilbert and Rayor 1985). Instead, they use their front legs, which are covered with sensory setae, to explore the environment and detect potential prey through vibrations or direct tactile sensation (Nentwig 1985). All types of prey, e.g. Formicidae, Lepidoptera, Diptera, Araneae, Heteroptera, Mantodea and others, are caught as long as they are within the same size range or slightly larger than the spider (Dabelow 1958; McAlister 1960; Nentwig 1985), but weakly chitinized prey seems to be preferred (Dabelow 1958).

Fig. 7.22 Spitted thread of the spider *Scytodes thoracica* on a glass slide, imaged by differential interference contrast microscopy. The varying thickness of the threads appears to be a result of bundled threads deposited together during the spitting process rather than different silk types (Image from Suter and Stratton (2010) and republished with permission)
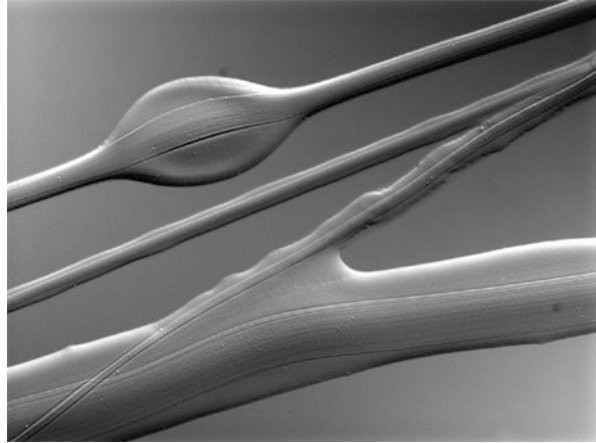
In close proximity to a potential victim, the spider orients itself towards the prey (defined as an alert posture) and slowly taps its front legs until the prey is centred between the legs (Dabelow 1958; Gilbert and Rayor 1985; Bürgis 1990; Suter and Stratton 2010). Then the spider spits one (using only one chelicera) or two sticky threads in a zigzag pattern over the prey to trap it, moves forward, and wraps the prey in the drying threads with the first and second pair of legs.

This spitting process occurs within milliseconds (<35 ms) (Dabelow 1958), covering a distance of 5–20 mm (Suter and Stratton 2010). The zigzag pattern (Fig. 7.20) is controlled by a lateral-medial oscillation of the fangs with a ventral-to-dorsal extension of the chelicerae (Suter and Stratton 2010) and by this covers the prey completely with liquid (Fig. 7.22). Usually, the animals expel around 5–17 bands, whereas the right and left block contain an unequal number of bands (Gilbert and Rayor 1985) with a maximum length of up to 0.9 m (Suter and Stratton 2010). The animals are able to control the glue amount and only use more spit for prey that shows an increased "struggling intensity" (Clements and Li 2008). After being trapped by the silky bands, the prey is then paralysed with a venomous bite and wrapped in silk thread produced by the spinnerets (Dabelow 1958).

The glue glands are located in the cephalothorax (prosoma) and initially separated into three parts (Fig. 7.23), namely (1) a larger, posterior glue gland (defined as "fond séricigéne") containing the adhesive components, (2) a smaller, anterior poison gland (defined as "ampoule") containing the venom, and (3) the secreting canal in the cheliceres (Millot 1930). Later, Kovoor and Zylberberg (1972) furthermore separated the poison glands according to their gland cells and content and defined five distinct regions in total (Fig. 7.24):

I. The glue gland (defined as lobe I) synthesises the silk threads surrounded by glycoprotein microfibrils. The glands contain large nuclei and a high density of rough endoplasmatic reticulum. Gland cells, being closely related to lobe III of the poison gland (Fig. 7.24), furthermore contain small Golgi vesicles and are rich in proteins and acidic glyocoproteins.

Fig. 7.23 The gland system (highlighted in grey) of the spider *Scytodes thoracica* consists of into three parts: the posterior glue gland (GG), the anterior poison gland (PG), and the secretion channel (Ca) located in the chelicerae (Ch). The glands as well as the channel are enclosed by massive muscle fibres (Mu) (Image from Millot (1930) and republished with permission of the *Société Zoologique de France*)

II. The posterior part of the poison gland is defined as lobe II and consists of gland cells with fibrillar, granular and paracristalline content, which stain for proteins and acidic glycoproteins. The glands contain organelles such as rER, Golgi vesicles and small mitochondria. Together with the anterior part (lobe III), these gland cells are thought to be responsible for the production of the toxic components.

III. The smaller lobe III, situated between the glue gland and lobe II, contains cells with electron-dense vesicles. However, these are located near the rER and Golgi apparatus and show no signs of contributing to the glue and/or toxin formation. Histochemically, these cells react to carboxylated glycoproteins.

IV. The content of lobe IV stains for neutral glycoproteins and, ultrastructurally, a "constant association of mitochondria with ER lamellae" can be detected in the gland cells. An involvement of this lobe in toxin production has not been determined, and its "functional role […] is not clear" (Kovoor and Zylberberg 1972).

V. The intracheliceral part (earlier defined as "canal", labelled as Ca in Fig. 7.24) comprises different cell types: the canal itself is composed of muscle layers and its outer epithelium is covered by a cuticle. Internally, the ventral side of the canal is lined by a single epithelial cell layer, while the dorsal side is divided into the following different gland types (Fig. 7.24): (a) this gland type covers most parts and contains ergastoplasmic parasomes and glycogen accumulations; (b) these are neighbouring elongated cells, clearly distinguishable by their apical, club-shaped microvilli and the presence of microtubules in the cytoplasm. As some signs of pinocytosis activity can be observed, Kovoor and Zylberberg (1972) assume an involvement of this cell type in resorption, ionic
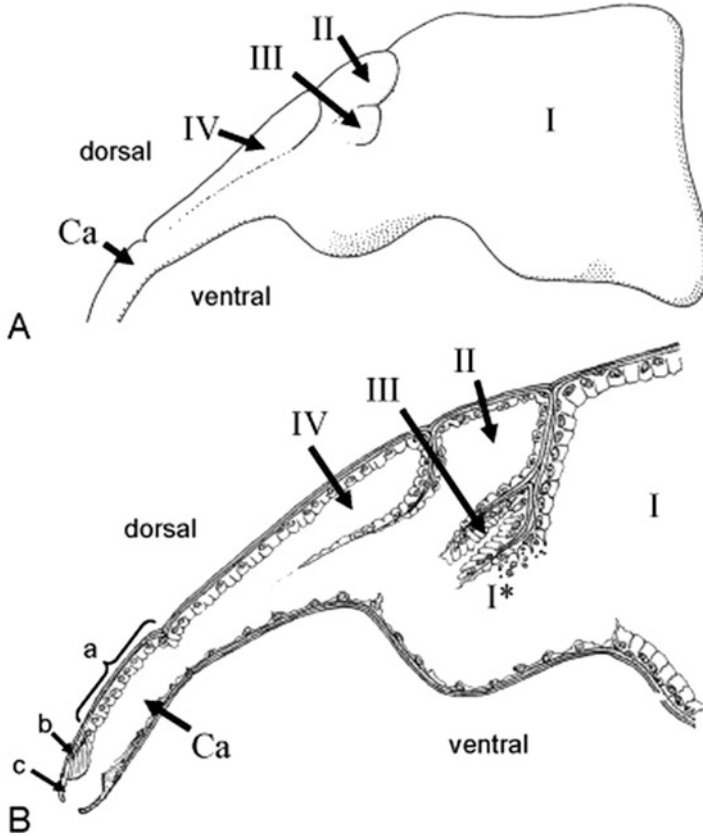
Fig. 7.24 Anatomy of the spitting glands in the spider *Scytodes thoracica*. (**a**) Outer morphology of the isolated spitting gland. The glue gland is labelled as I, following the nomenclature of Kovoor and Zylberberg (1972), the poison gland is subdivided into the lobes II, III and IV. The glue is expelled through the channel (Ca) in the cheliceres. (**b**) Cross-section of the spitting gland; the gland cells mostly appear dorsally, while ventrally a non-secretory cell layer can be observed. The glue glands (marked as I*) neighbouring lobe III of the poison gland show a difference in secretory content compared to the remaining glue glands in lobe I. In the dorsal region of the channel (Ca), three different cells (a, b and c) can be distinguished based on their morphology and secretory content (Image from Kovoor and Zylberberg (1972) and republished with permission)

regulation and transport of substances from the canal lumen to the cells and vice versa; (c) the last cell type connects the canal lumen with the outer cuticle; no information is given about any secretory activity for this cell (Kovoor and Zylberberg 1972).

So far it remains unclear whether *Scytodes* sp. spit already contains toxic components from lobes II and III or if they are released afterwards for the bite. Behavioural observation with prey covered with the glue of *Scytodes* sp. for a period of 24 h showed that it survived, and that the prey was also able to eat the hardened glue without any negative side effects (Clements and Li 2008).

The latest chemical characterization of the poison/adhesive glands confirms a cocktail of toxins (35% of the proteome) present in this prey-capture system. Some of these components show a high homology to other spider toxins, e.g., those of *Phoneutria nigriventer* (Keyserling 1891), *Psalmopoeus cambridgei* (Pocock 1895), *Dysdera erythrina* (Walckenaer 1802) and others (Zobel-Thropp et al. 2014). The authors assume that the small (3.5–7 kDa) glycine-rich and diglutamine/dityrosine motif-containing peptides found by transcriptome and proteome analyses may contribute to the formation of the *Scytodes* glue. Unfortunately, Zobel-Thropp et al. (2014) characterized the complete gland system without separating the adhesive from the poison gland and without using the ejected spit for comparison. Therefore, it needs to be confirmed that toxins are absent from the spit and that the glue contains these small peptides found in the tissue samples (Zobel-Thropp et al. 2014).

Biomechanical data indicate that the *Scytodes* thread shortens by 40–60% directly after ejection, generating a force of 0.1–0.3 mN (Poinar 1996, Suter and Stratton 2010). As a consequence, the prey is not only arrested by the adhesive spit but is also immobilized onto the substratum by the contracting threads.

7.3.2.2 Velvet Worms

Onychophorans are carnivorous, exclusively terrestrial invertebrates that occur in tropical and temperate forests of the southern hemisphere and around the equator (Ruhberg 1985; Reid 1996; Mayer 2007; Oliveira et al. 2016). Their common name refers to the velvety appearance of their skin, which is water-repellent (Storch and Ruhberg 1993; Ruhberg and Mayer 2013). To date, 191 valid onychophoran species have been described, namely 76 peripatids from Central and South America, Western Africa and South-East Asia, and 115 peripatopsids from Chile, South Africa and Australasia (Mayer and Oliveira 2011; Oliveira et al. 2012; Oliveira and Mayer 2017). Representatives of most species do not exceed 5–6 cm in length, but some neotropical species reach body lengths of 20 cm or more (Morera-Brenes and Monge-Nájera 2010). Onychophorans possess a more or less cylindrical body with 13–43 pairs of unjointed legs called lobopods. At the anterior end, the lobopods have been modified to form three pairs of cephalic appendages, including the frontal antennae, the jaws located within the mouth cavity, and the slime papillae, which are used for slime ejection (Mayer et al. 2010, 2015).

The animals occur mostly in or under decaying logs and leaf litter of humid tropical and temperate forests, where they feed on small invertebrates such as termites, cockroaches, crickets and woodlice (Read and Hughes 1987; Barclay et al. 2000; Reinhard and Rowell 2005). Onychophorans are slow-moving animals and do not actively hunt their prey over a long distance or time, but instead localize their prey at a short distance using their sensory antennae (Read and Hughes 1987). In order to catch their potential prey, the animals typically eject two streams of a sticky secretion via the paired slime papillae (Fig. 7.25). The ideal distance for squirting and entangling the prey is 0.5–4.0 cm (Röper 1977; Read and Hughes 1987),

Fig. 7.25 Specimen of the velvet worm species *Principapillatus hitoyensis* (Oliveira et al. 2013) squirting its sticky slime. Note the two jets of slime, which are ejected via the paired slime papillae (Image courtesy of Alexander Baer and Ivo Oliveira, University of Kassel (Germany), and reproduced with their permission)

Fig. 7.26 Extruded slime threads of the velvet worm *Principapillatus hitoyensis* (Peripatidae), forming an adhesive trap (Image courtesy of Georg Mayer, University of Kassel (Germany), and reproduced with his permission)

but squirting distances of up to "almost a foot" (Sedgwick 1895), i.e. 30 cm, have also been reported.

Immediately after release, the slime hardens and entangles the prey in a net of sticky threads (Fig. 7.26). Read and Hughes (1987) observed that the animals direct additional focused slime squirts at the prey's limbs and fangs if it is still violently struggling. The onychophoran glue-like slime lacks toxins or anaesthetics; instead, the velvet worm bites the immobilised prey and injects digestive saliva into its body (Heatley 1936; Storch et al. 1979; Nelson et al. 1980), leading to a rapid death and partial digestion of the victim (Read and Hughes 1987; Mayer et al. 2015). During the prey digestion process, the velvet worm also ingests its own squirted slime, often along with attached soil particles. In addition to prey capture, the glue-like slime is also used for defence against predators (Reinhard and Rowell 2005; Baer et al. 2014).

The slime is produced in long, slender, paired glands that are located within the main body cavity (central sinus) and extend along each side of the gut (Fig. 7.27). Each gland is subdivided into two major regions: the posterior glandular portion associated with numerous endpieces, in which the slime is produced, and the
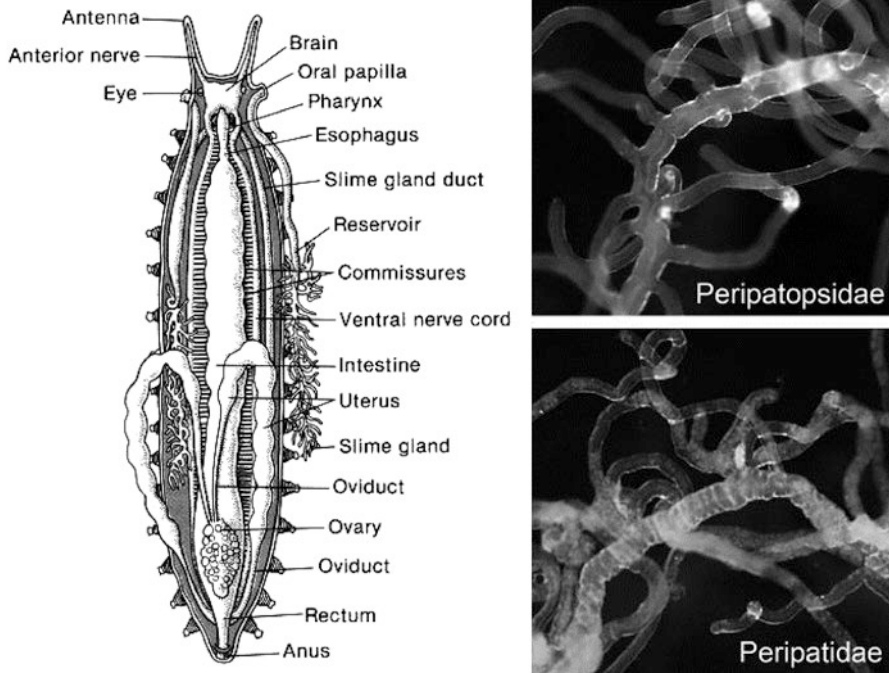
Fig. 7.27 Position and structure of slime glands in velvet worms. The left-hand drawing illustrates the internal anatomy of a representative of Peripatopsidae. The light micrographs on the right show details of the slime glands of the two major onychophoran subgroups, Peripatopsidae and Peripatidae (Diagram from Brusca and Brusca (2002) and republished with permission. Light micrographs by courtesy from Alexander Baer, University of Kassel (Germany), and reproduced with his permission)

anterior reservoir, from which the slime is released via the opening of the slime papilla (Baer and Mayer 2012). The slime gland opening is surrounded by denticle-like scales of an unknown function (Figs. 8D, F in Oliveira et al. (2012)). While the numerous endpieces of the slime gland directly open into the central secretory duct in representatives of Peripatopsidae, the endpieces are arranged in rosettes of four in Peripatidae, so that the slime is first collected in an atrium before being processed further into the central duct (Baer and Mayer 2012). The prismatic gland cells lining the cavity of the endpieces are densely packed with tubules of rough endoplasmic reticulum (rER) and Golgi vesicles (Ruhberg and Storch 1977). Furthermore, the nuclei and nucleoli of the gland cells are clearly larger than those of the surrounding tissue (Ruhberg and Storch 1977; Baer and Mayer 2012). The secretory vesicles in the glands are electron-dense (Ruhberg and Storch 1977) and either appear as an "usual granular structure" (Moseley 1874) or "are not concentrated in granules, rather they are released in a diffuse form" (Lavallard and Campiglia 1971). Also, there are differences between authors regarding their secretion into the cavity. According to Moseley (1874), the vesicles swell and finally burst the glandular content into the cavity, while Lavallard and Campiglia (1971) observed an apocrine

secretion. Transmission electron microscopy has revealed membrane residues and micellar particles in freshly secreted droplets, while such particles were absent in droplets fixed 12 min after secretion and these also lacked adhesiveness (Ruhberg and Storch 1977). The presence of micellar nanoglobules was indeed confirmed in a recent multiscale structural and compositional analysis of the onychophoran slime (Baer et al. 2017). Apart from this granular material, α-glycogen and lipid inclusions were observed within the glands, but not in the secreted droplets (Ruhberg and Storch 1977).

According to Ruhberg and Storch (1977), there are some differences between the adults and juveniles at the cellular level. Besides a higher amount of rER and free ribosomes, the young individuals apparently have a lower amount of Golgi vesicles and secretory inclusions in their glands. Also, species-related differences with respect to the number and length of the gland tubes and endpieces have been recorded, in addition to differences in protein band patterns (Baer and Mayer 2012; Baer et al. 2014). The glands are surrounded by an outer layer of connective tissue and muscle fibres; the latter, however, are lacking around the endpieces (Baer and Mayer 2012). The central secretory duct is formed by a single layer of epithelial cells that bear numerous apical microvilli. The duct is surrounded by a thick layer of collagen and muscle fibres towards the body cavity. In the transition area between the duct and the slime reservoir, a valve-like structure may be present, which might serve for preventing the backflow of the slime during the ejection event. Interestingly, this structure was only observed in the investigated representatives of Peripatopsidae, but not in the Peripatidae species (Baer and Mayer 2012).

The reservoir of the slime gland differs from the central secretory duct in that its lumen is lined by a thin cuticle, indicating an ectodermal origin (Ruhberg and Storch 1977). Only a few organelles are present in its cells, including a large nucleus and electron-lucent lipid inclusions. Additionally, the reservoir is enclosed by several layers of interlacing muscle and collagen fibres, most probably to facilitate a fast ejection of the slime (Baer and Mayer 2012). Further observations by the authors show that in dissected specimens kept in physiological saline, peristaltic contractions of the reservoir occur. The slime reservoir comprises around 11% of the entire body mass, but still contains slime even after several ejection events and is replenished within one day (Read and Hughes 1987).

The ejected slime consists of a small translucent thread (diameter 0.02 mm) along which clear and scentless droplets are aligned (Benkendorff et al. 1999) (Figs. 7.26 and 7.28). The droplets are similar in their appearance to those observed in orb-web spiders and glowworms (see sections above). However, in contrast to spiders and glowworms, the onychophoran thread consists of glue (Haritos et al. 2010) and does not contain silk (Craig 1997) or collagen (Benkendorff et al. 1999). The thread-like appearance of the slime is most likely a result of the jet-like propulsion during the ejection process and the re-arrangement and crosslinking of the proteins towards gelation (Haritos et al. 2010). Recent mechanoresponsive analyses of the onychophoran slime indeed suggest that the biopolymeric fibre assembly is facilitated via mono-disperse lipid-protein nanoglobules (Baer et al. 2017). These nanoglobules might self-assemble into nano- and microfibrils by shear forces,
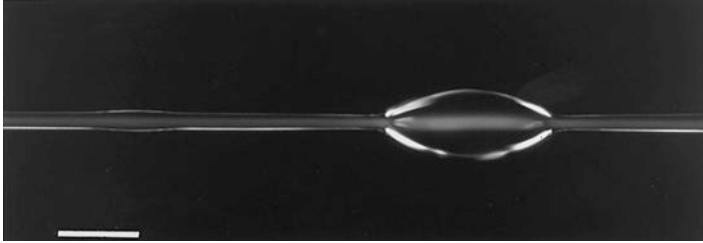
Fig. 7.28 Light micrograph of a slime thread from the onychophoran *Euperipatoides kanangrensis* (Reid 1996) with an attached droplet. Both the thread and the droplet are clear and transparent. Scale bar: 0.1 mm (Image from Benkendorff et al. (1999) and republished with permission)

which results in the formation of macroscopic fibres with a protein-enriched core and lipid-rich coating. This process seems to be reversible, as dissolution of dried fibres in water leads to re-formation of nanoglobules (Baer et al. 2017). Hence, the supramolecular assembly of proteins might be mediated by reversible non-covalent interactions within the slime.

Chemically, the onychophoran slime consists largely of water, around 84% (Röper 1977) in *Peripatopsis moseleyi* (Wood-Mason 1879) and up to 90% (Benkendorff et al. 1999) in *Euperipatoides kanangrensis*. There are also differences between the two species regarding the reported protein and sugar contents. However, it remains to be clarified whether these differences are species-specific, influenced by the prey items they consume or due to more sensitive analysis tools that were used in the study by Benkendorff et al. (1999). In *P. moseleyi*, a protein content of 16% (amino acids such as Gly = 41%, Glx = 11%, Lys = 1.3%) but no sugar was reported (Röper 1977). The slime of *E. kanangrensis* in contrast consists of 55% protein (amino acids such as Gly =27%, Glx = 5%, Pro =13%, Lys = 7%), lipids, nonylphenol and 1.3% glycan residues such as *N*-acetylgalactosamine (GalNAc), mannose and galactose (Benkendorff et al. 1999). In general, the onychophoran slime comprises proteins in a wide molecular mass range from 8 to 1300 kDa (Mora et al. 1996; Haritos et al. 2010; Baer et al. 2014). Benkendorff et al. (1999) classified the glue proteins into at least "two groups: high molecular weight (>600 kDa) monomers and low molecular weight dimers (25–28 kDa)" after gel electrophoretic separation. More detailed analyses of some major proteins (Er_P1 = 250, 350 kDa; Er_P2a and Er_P2b = 80 kDa) bear a high amount (>20%) of the amino acid proline. Both proteins are supposed to be responsible for the gelation of slime through cross-linking mechanisms involving covalent, ionic and/or hydrophobic bonds (Haritos et al. 2010). The low molecular weight proteins present in the onychophoran slime instead show a high homology to carbohydrate-binding proteins and protease inhibitors and are assumed to serve as antimicrobial agents within the slime glands (Haritos et al. 2010).

As stated above, the glandular systems of the two major onychophoran subgroups, the Peripatidae and Peripatopsidae, differ with respect to their structure. Also, on the proteomic level a clear species-related pattern can be observed, suitable

for species identification and phylogenetic evaluation (Mora et al. 1996; Baer et al. 2014). On the one hand, a high interspecific similarity has been detected for the high molecular weight proteins (350 kDa and ~ 780 kDa) maybe responsible for the formation and gelation of slime. On the other hand, in particular the low molecular weight (8–25 kDa) that have been proposed to serve as antimicrobial agents, allow a clear distinction at the species level (Baer et al. 2014). Slight differences in the gel electrophoretic protein pattern between specimens of the same species but from two neighbouring localities, albeit a similar habitat, could not yet be explained as an environmental adaptation (Baer et al. 2014).

Beyond species profiling, the major slime protein (Er_P1) of *Euperipatoides rowelli* (Reid 1996) also indicates a similarity to an amphibian glue protein (Nb-1R), namely that of the frog *Notaden bennetti* (Graham et al. 2013). According to the authors, Er_P1 and Nb-1R proteins are very large (260–500 kDa), rich in glycine (16–17 mol%), proline (7–12 mol%) and 4-hydroxyproline (4 mol%) and, beyond this, they have "oddly 'turbulent' bands" in gel electrophoretic separations (Graham et al. 2013). This proteinic congruence is interesting, in particular because the two glue-producing animals are not closely related to each other (a vertebrate versus a panarthropod/ecdysozoan). Also, in view of their glue gland locality and morphology as well as the usage of the adhesive, the animals clearly differ: the frog produces the defensive glue in its skin glands (Tyler 2010), as do the salamanders, while the onychophorans use their secretion for offence/defence and produce it in an internal gland system. Further studies would be necessary to confirm the hypothesis of a convergent evolution of adhesive components and common mechanisms of curing and adhesion and to compare this with the data given for other terrestrial, but also marine, glue-producing animals.

References

Amarpuri, G., Chaurasia, V., Jain, D., Blackledge, T. A., & Dhinojwala, A. (2015). Ubiquitous distribution of salts and proteins in spider glue enhances spider silk adhesion. *Scientific Reports, 5*, 90301–90307.

Anderson, C. V., & Deban, S. M. (2010). Ballistic tongue projection in chameleons maintains high performance at low temperature. *Proceedings of the National Academy of Sciences of the United States of America, 107*(12), 5495–5499.

Anderson, C. V., & Deban, S. M. (2012). Thermal effects on motor control and in vitro muscle dynamics of the ballistic tongue apparatus in chameleons. *The Journal of Experimental Biology, 215*(Pt 24), 4345–4357.

Anderson, C. V., Sheridan, T., & Deban, S. M. (2012). Scaling of the ballistic tongue apparatus in chameleons. *Journal of Morphology, 273*(11), 1214–1226.

Arnold, S. J. (1982). A quantitative approach to antipredator performance: Salamander defense against snake attack. *Copeia, 1982*(2), 247–253.

Baer, A., & Mayer, G. (2012). Comparative anatomy of slime glands in Onychophora (velvet worms). *Journal of Morphology, 273*(10), 1079–1088.

Baer, A., Oliveira, I. S., Steinhagen, M., Beck-Sickinger, A. G., & Mayer, G. (2014). Slime protein profiling: A non-invasive tool for species identification in Onychophora (velvet worms). *Journal of Zoological Systematics and Evolutionary Research, 52*, 265–272.

Baer, A., Schmidt, S., Haensch, S., Eder, M., Mayer, G., & Harrington, M. J. (2017). Mechanoresponsive lipid-protein nanoglobules facilitate reversible fibre formation in velvet worm slime. *Nature Communications, 8*, 974.

Baker, C. H., Graham, G. C., Scott, K. D., Cameron, S. L., Yeates, D. K., & Merritt, D. J. (2008). Distribution and phylogenetic relationships of Australian glow-worms *Arachnocampa* (Diptera, Keroplatidae). *Molecular Phylogenetics and Evolution, 48*, 506–514.

Barclay, S. D., Rowell, D. M., & Ash, J. E. (2000). Pheromonally mediated colonization patterns in the velvet worm *Euperipatoides rowelli* (Onychophora). *Journal of Zoology, 250*, 437–446.

Bargmann, W. (1972). Zur Architektur der Mesogloea – Untersuchungen an der Rippenqualle *Pleurobrachia pileus*. *Zeitschrift für Zellforschung und Mikroskopische Anatomie, 123*(1), 66–81.

Bargmann, W., Jacob, K., & Rast, A. (1972). Über Tentakel und Colloblasten der Ctenophore *Pleurobrachia pileus*. *Zeitschrift für Zellforschung und Mikroskopische Anatomie, 123*(1), 121–152.

Benkendorff, K., Beardmore, K., Gooley, A. A., Packer, N. H., & Tait, N. N. (1999). Characterization of the slime gland secretion from the peripatus, *Euperipatoides kanangrensis* (Onychophora: Peripatopsidae). *Comparative Biochemistry and Physiology. B, 124*, 457–465.

Benwitz, G. (1978). Elektronenmikroskopische Untersuchungen der Colloblasten-Entwicklung bei der Ctenophora *Pleurobrachia pileus* (Tentaculifera, Cydippea). *Zoomorphologie, 89*, 257–278.

Bernards, M. A., Oke, I., Heyland, A., & Fudge, D. S. (2014). Spontaneous unraveling of hagfish slime thread skeins is mediated by a sewater-soluble protein adhesive. *The Journal of Experimental Biology, 217*, 1263–1268.

Blackledge, T. A., & Hayashi, C. Y. (2006). Silken toolkits: Biomechanics of silk fibers spun by the orb web spider *Argiope argentata* (Fabricius 1775). *The Journal of Experimental Biology, 209*(Pt 13), 2452–2461.

Bocker, L., Ruhs, P. A., Boni, L., Fischer, P., & Kuster, S. (2016). Fiber-enforced hydrogels: Hagfish slime stabilized with biopolymers including k-carrageenan. *ACS Biomaterials Science & Engineering, 2*, 90–95.

Bonato, L., Edgecombe, G. D., Lewis, J. G., Minelli, A., Pereira, L. A., Shelley, R. M., & Zapparoli, M. (2010). A common terminology for the external anatomy of centipedes (Chilopoda). *Zookeys, 69*, 17–51.

Boni, L., Fischer, P., Bocker, L., Kuster, S., & Ruhs, P. A. (2016a). Hagfish slime and mucin flow properties and their implications for defense. *Scientific Reports, 6*, 30371.

Boni, L., Ruhs, P. A., Windhab, E. J., Fischer, P., & Kuster, S. (2016b). Gelation of soy milk with hagfish exudate creates a flocculated and fibrous emulsion- and particle gel. *PLoS One, 1*(1), e0147022.

Brade-Birks, H. K., & Brade-Birks, S. (1920). Notes on Myriapoda – XX. Luminous chilopoda, with special refence to *Geophilus carpophagus*, Leach. *Annals and Magazine of Natural History, 9*(5), 1–30.

Bristowe, B. A. (1931). LXIII. – Notes on the biology of spider – VI. Spitting as a means of capturing prey by spiders. *Annals and Magazine of Natural History, 8*(10), 469–471.

Broadley, R. A. (2015). Notes on pupal behaviour, eclosion, mate attraction, copulation and predation of the New Zealand glowworm *Arachnocampa luminosa* (Skuse) (Diptera: Keroplatidae), at Waitomo. *New Zealand Entomologist, 35*(1), 1–9.

Broadley, R. A., & Stringer, I. A. N. (2001). Prey attraction by larvae of the New Zealand glowworm, *Arachnocampa luminosa* (Diptera: Mycetophilidae). *Invertebrate Biology, 120*(2), 170–177.

Broadley, R. A., & Stringer, I. A. N. (2009). Larval behaviour of the New Zealand glowworm, *Arachnocampa luminosa* (Diptera: Keroplatidae), in bush and caves. In V. B. Meyer-Rochow (Ed.), *Bioluminescence in focus – A collection of illuminating essays* (pp. 325–355). Kerala: Research Signpost.

Brodie, E. D. (1977). Salamander antipredator postures. *Copeia, 3*, 523–535.

Brodie, E.D. (1983). Antipredator adaptations of salamanders: Evolution and convergence among terrestical species. In N. S. Margaris, M. Arianoutsou-Faraggitaki, & R. J. Reiter (Eds.), *Plant, animal and microbial adaptations to terrestrial environment* (pp, 109–133). New York: Plenum Publishing Corporation.

Brodie, E. D., & Gibson, L. S. (1969). Defensive behavior and skin glands of the northwestern salamander, *Ambystoma gracile*. *Herpetologica, 25*, 187–194.

Brodie, E. D., & Smatresk, N. J. (1990). The antipredator arsenal of fire salamanders: Spraying of secretions from highly pressurized dorsal skin glands. *Herpetologica, 46*(1), 1–7.

Brusca, R. C., & Brusca, G. J. (2002). *Invertebrates*. Sunderland: Sinauer Associates Inc.

Bürgis, H. (1980). Eine Spinne, die spuckt. *Mikrokosmos, 69*, 342–349.

Bürgis, H. (1990). Die Speispinne *Scytodes thoracica* (Araneae: Sicariidae): ein Beitrag zur Morphology und Biologie. *Mitteilungen der Pollichia, 77*, 289–313.

Carcupino, M. (1996). Morphological characterization of female accessory sex glands of *Eupolybothrus fasciatus* (Newport) (Chilopoda Lithobiomorpha). *Journal of Morphology, 228*, 61–75.

Carré, D., & Carré, C. (1993). Five types of colloblast in a cydippid ctenophore *Minictena luteola* Carré and Carré: An ultrastructural study and cytological interpretation. *Philosophical Transactions of the Royal Society B, 341*, 437–448.

Clark, A. J., & Summers, A. P. (2007). Morphology and kinematics of feeding in hagfish: Possible functional advantages of jaws. *The Journal of Experimental Biology, 210*(Pt 22), 3897–3909.

Clements, R., & Li, D. (2008). Regulation and non-toxicity of the spit from the pale spitting spider *Scytodes pallida* (Araneae: Scytodidae). *Ethology, 111*, 311–321.

Craig, C. L. (1997). Evolution of arthropod silks. *Annual Review of Entomology, 42*, 231–267.

Dabelow, S. (1958). Zur Biologie der Leimschleuderspinne *Scytodes thoracica* (Latreille). *Zoologische Jahrbücher Abteilung für Systematik, Geographie und Biologie der Tiere, 86*, 85–126.

Daly, J. W., Spande, T. F., & Garraffo, H. M. (2005). Alkaloids from amphibian skin: A tabulation of over eight-hundred compounds. *Journal of Natural Products, 68*, 1556–1575.

Dance, A. (2016). Will hagfish yield the fibers of the future? *Proceedings of the National Academy of Sciences of the United States of America, 113*(26), 7005–7006.

Downing, S. W., Salo, W. L., Spitzer, R. H., & Koch, E. A. (1981). The hagfish slime gland: A model system for studying the biology of mucus. *Science, 214*, 1143–1144.

Downing, S. W., Spitzer, R. H., Koch, E. A., & Salo, W. L. (1984). The hagfish slime gland thread cell I. A unique cellular system for the study of intermediate filaments and intermediate filament-microtubule interactions. *The Journal of Cell Biology, 98*(2), 653–669.

Ducey, P. K., & Brodie, E. D. (1983). Salamanders respond selectively to contacts with snakes: Survival advantage to alternative antipredator strategies. *Copeia, 1983*(4), 1036–1041.

Ducey, P. K., Brodie, E. D., & Baness, E. A. (1993). Salamander tail autonomy and snake predation: Role of antipredator behavior and toxicity for three neotropical *Bolitoglossa* (Caudata: Plethodontidae). *Biotropica, 25*(3), 344–349.

Duellman, W. E., & Trueb, L. (1994). *Biology of amphibians*. Baltimore: John Hopkins University Press.

Dugon, M. M. (2017). Evolution, morphology, and development of the centipede venom system. In P. Gopalakrishnakone, & A. Malhotra (Eds.), *Evolution of venomous animals and their toxins* (pp. 261–278). Dordrecht: Springer.

Dugon, M. M., & Arthur, W. (2012). Comparative studies on the structure and development of the venom-delivery system of centipedes, and a hypothesis on the origin of this evolutionary novelty. *Evolution & Development, 14*(1), 128–137.

Dugon, M. M., Hayden, L., Black, A., & Arthur, W. (2012). Development of the venom ducts in the centipede *Scolopendra*: An example of recapitulation. *Evolution & Development, 14*(6), 515–521.

Emson, R. H., & Whitfield, P. J. (1991). Behavioural and ultrastructural studies on the sedentary platyctenean ctenophore *Vallicula multiformis*. *Hydrobiologia, 216*(217), 27–33.

Evans, C. M., & Brodie, E. D. (1994). Adhesive strength of amphibian skin secretions. *Journal of Herpetology, 4*(499), 502.

Evenhius, N. L. (2006). *Catalog of the Keroplatidae of the world (Insecta: Diptera)*. Honolulu: Bishop Museum Press.

Fisher, E. G. (1940). New Mycetophilidae from North Carolina (Diptera). *Entomological News, 51*, 243–247.

Foelix, R. F. (1996). *Biology of spiders*. New York: Oxford University Press.

Franc, J. M. (1978). Organization and function of ctenophore colloblasts: An ultrastructural study. *The Biological Bulletin, 155*, 527–541.

Fu, J., Guerette, P. A., Pavesi, A., Horbelt, N., Lim, C. T., Harrington, M. J., & Miserez, A. (2017). Artificial hagfish protein fibers with ultra-high and tunable stiffness. *Nanoscale, 9*(35), 12908–12915.

Fudge, D. S., & Gosline, J. M. (2004). Molecular design of the alpha-keratin composite: Insights from a matrix-free model, hagfish slime threads. *Proceedings of the Biological Sciences, 271*(1536), 291–299.

Fudge, D. S., & Schorno, S. (2016). The hagfish gland thread cell: A fiber-producing cell involved in predator defense. *Cell, 5*(2), 25.

Fudge, D. S., Gardner, K. H., Forsyth, V. T., Riekel, C., & Gosline, J. M. (2003). The mechanical properties of hydrated intermediate filaments: Insights from hagfish slime threads. *Biophysical Journal, 85*(3), 2015–2027.

Fudge, D. S., Levy, N., Chiu, S., & Gosline, J. M. (2005). Composition, morphology and mechanics of hagfish slime. *The Journal of Experimental Biology, 208*(Pt 24), 4613–4625.

Fudge, D. S., Schorno, S., & Ferraro, S. (2015). Physiology, biomechanics, and biomimetics of hagfish slime. *Annual Review of Biochemistry, 84*, 947–967.

Fulton, B. B. (1939). Lochetic luminous dipterous larvae. *Journal of the Elisha Mitchell Scientific Society, 55*(2), 289–294.

Fulton, B. B. (1941). A luminous fly larva with spider traits (Diptera, Mycetophilidae). *Annals of the Entomological Society of America, 34*, 289–302.

Gatenby, J. B. (1959). Notes on the New Zealand glow-worm, *Bolitophila* (*Arachnocampa*) *luminosa*. *Transactions of the Royal Society of New Zealand, 87*(3 & 4), 291–314.

Gatenby, J. B. (1960). The New Zealand glow-worm. *Tuatara, 8*(2), 86–92.

Gatenby, J. B., & Cotton, S. (1960). Snare building and pupation in *Bolitophila luminosa*. *Transactions of the Royal Society of New Zealand, 88*(1), 149–156.

Gilbert, C., & Rayor, L. S. (1983). First record of mantisfly (Neuroptera: Mantispidae) parasitizing a spitting spider (Scytodidae). *Journal of the Kansas Entomological Society, 56*(4), 578–580.

Gilbert, C., & Rayor, L. S. (1985). Predatory behavior of spitting spiders (Araneae: Scytodidae) and the evolution of prey wrapping. *Journal of Arachnology, 13*, 231–241.

Gosline, J. M., Guerette, P. A., Ortlepp, C. S., & Savage, K. N. (1999). The mechanical design of spider silks: From fibroin sequence to mechanical function. *The Journal of Experimental Biology, 202*(Pt 23), 3295–3303.

Graham, L. D., Glattauer, V., Huson, M. G., Maxwell, J. M., Knott, R. B., White, J. W., Vaughan, P. R., Peng, Y., Tyler, M. J., Werkmeister, J. A., et al. (2005). Characterization of a protein-based adhesive elastomer secreted by the Australian frog *Notaden bennetti*. *Biomacromolecules, 6*(6), 3300–3312.

Graham, L. D., Glattauer, V., Li, D., Tyler, M. J., & Ramshaw, J. A. (2013). The adhesive skin exudate of *Notaden bennetti* frogs (Anura: Limnodynastinae) has similarities to the prey capture glue of *Euperipatoides* sp. velvet worms (Onychophora: Peripatopsidae). *Comparative Biochemistry and Physiology. B, 165*(4), 250–259.

Green, L. F. B. (1978). *Thesis: Structure and function of the Malphighian tubules of the larva of the New Zealand glow-worm* Arachnocampa luminosa *(Skuse)*. Auckland: University of Auckland.

Greve, W. (1974). Organisation der Rippenqualle *Pleurobrachia pileus* (Ctenophora). *Institut für wissenschaftlichen Film, C1186*(1972), 3–13.

Greve, W. (1975). Verhaltensweisen der Rippenquallen *Pleurobrachia pileus* (Ctenophora). *Institut für wissenschaftlichen Film, C1181*(1975), 3–10.

Haritos, V. S., Niranjane, A., Weisman, S., Trueman, H. E., Sriskantha, A., & Sutherland, T. D. (2010). Harnessing disorder: Onychophorans use highly unstructured proteins, not silks, for prey capture. *Proceedings of Biological Society of Washington, 277*(1698), 3255–3263.

Hayashi, C. Y., & Lewis, R. V. (1998). Evidence from flagelliform silk cDNA for the structural basis of elasticity and modular nature of spider silks. *Journal of Molecular Biology, 275*(5), 773–784.

Heatley, N. G. (1936). The digestive enzymes of the Onychophora (*Peripatopsis* spp.) *The Journal of Experimental Biology, 13*, 329–343.

Heiss, E., Natchev, N., Salaberger, D., Gumpenberger, M., Rabanser, A., & Weisgram, J. (2010). Hurt yourself to hurt your enemy: New insights on the function of the bizarre antipredator mechanism in the salamandrid *Pleurodeles waltl*. *Journal of Zoology, 280*, 156–162.

Herr, J. E., Winegard, T. M., O'Donnell, M. J., Yancey, P. H., & Fudge, D. S. (2010). Stabilization and swelling of hagfish slime mucin vesicles. *The Journal of Experimental Biology, 213*(Pt 7), 1092–1099.

Herr, J. E., Clifford, A. M., Goss, G. G., & Fudge, D. S. (2014). Defensive slime formation in Pacific hagfish requires Ca2+− and aquaporin-mediated swelling of released mucin vesicles. *The Journal of Experimental Biology, 217*(Pt 13), 2288–2296.

Hopkin, S. P., & Anger, H. S. (1992). On the structure and function of the glue-secreting glands of *Henia vesuviana* (Newport, 1845) (Chilopoda: Geophilomorpha). *Berichte des naturwissenschaftlich-medizinischen Vereins in Innsbruck Supplement, 10*, 71–79.

Hopkin, S. P., & Gaywood, M. J. (1987). Encounters between the geophilid centipede *Henia* (*Chaetechelyne*) *vesuviana* Newport and the devil's coach horse beetle *Staphylinus olens* (Mueller). *Bullettin of the Britain Myriapadology Group, 4*, 22–26.

Hopkin, S. P., Gaywood, M. J., Vincent, J. F. V., & Mayes-Harris, E. L. V. (1990). Defensive secretion of proteinaceous glues by *Henia (Chaetechelyne) vesuviana* (Chilopoda Geophilomorpha). In A. Minelli (Ed.), *Proceedings of the 7th international congress of myriapodology* (pp. 175–181). Leiden: E.J. Brill.

Hovasse, R., & de Puytorac, P. (1962). Contributions á la connaissance du colloblaste, grace á la microscopie électronique. *Comptes Rendus. Academy of Sciences, 255*, 3223–3225.

Hovasse, R., & de Puytorac, P. (1963). Le colloblaste des ctenophores: Ultrastructure, signification. In J. A. Moore (Ed.), *Proceedings of the XVI international congress of zoology*, 20–27 August 1963, Washington, 27.

Hu, X., Vasanthavada, K., Kohler, K., McNary, S., Moore, A. M., & Vierra, C. A. (2006). Molecular mechanisms of spider silk. *Cellular and Molecular Life Sciences, 63*(17), 1986–1999.

Humphries, T. (1889). The Waitomo caves, King Country, *Appendices to the Journals of the House of Representatives, V*(III), H-18.

Jackson, R. R., Li, D., Fijn, N., & Barrion, A. (1998). Predator-prey interactions between aggressive-mimic jumping spiders (Salticidae) and araneophagic spitting spiders (Scytodidae) from the Philippines. *Journal of Insect Behavior, 11*(3), 319–342.

Jeckel, A. M., Grant, T., & Saporito, R. A. (2015). Sequestered and synthesized chemical defenses in the poison frog *Melanophryniscus moreirae*. *Journal of Chemical Ecology, 41*(5), 505–512.

Jones, T. H., Conner, W. E., Meinwald, J., Eisner, H. E., & Eisner, T. (1976). Benzoyl cyanide and mandelonitrile in the cynogenetic secretion of a centipede. *Journal of Chemical Ecology, 2*(4), 421–429.

Keil, T. (1975). *Thesis: Die Antennensinnes- und Hautdrüsenorgane von* Lithobius forficatus *L. – Eine licht- und elektronenmikroskopische Untersuchung.* Berlin: Freie Universität.

Koch, A. (1927). Studien an leuchtenden Tieren. I. Das Leuchten der Myriapoden. *Zeitschrift für Morphologie und Ökologie der Tiere, 8*(1/2), 241–270.

Koch, E. A., Spitzer, R. H., Pithawalla, R. B., & Downing, S. W. (1991). Keratin-like components of gland thread cells modulate the properties of mucus from hagfish (Eptatretus stouti). *Cell and Tissue Research, 264*(1), 79–86.

Kovoor, P. J., & Zylberberg, L. (1972). Histologie et infrastructure de la glande chélicérienne de *Scytodes delicatula* Sim. (Araneidae, Scytodidae). *Annales des Sciences Naturelles – Zoologie et Biologie Animale, 14*, 333–388.

Lametschwandtner, A., Lametschwandtner, U., & Patzner, R. (1986). The different vascular patterns of slime glands in the hagfishes, *Myxine glutinosa* Linnaeus and *Eptatretus stoutii* Lockington: A scanning electron microscope study of vascular corrosion casts. *Acta Zoologica, 67*, 243–248.

Lane, E. B., & Whitear, M. (1980). Skein cells in lamprey. *C. Journal of Zoology, 58*(3), 450–455.

Largen, W., & Woodley, S. K. (2008). Cutaneous tail glands, noxious skin secretions, and scent marking in a terrestrial salamander (*Plethodon shermani*). *Herpetologica, 64*(3), 270–280.

Lavallard, R., & Campiglia, S. (1971). Données cytochimiques et ultrastructurales sur les tubes sécréteurs des glandes de la glu chez *Peripatus acacioi* Marcus et Marcus (Onychophore). *Zeitschrift für Zellforschung und Mikroskopische Anatomie, 118*, 12–34.

Lee, J. (1976). Bioluminescence of the Australian glow-worm, *Arachnocampa richardsae* Harrison. *Photochemistry and Photobiology, 24*, 279–285.

Leppi, T. J. (1968). Morphochemical analysis of mucous cells in the skin and slime glands of hagfishes. *Histochemie, 15*(1), 68–78.

Lim, J., Fudge, D. S., Levy, N., & Gosline, J. M. (2006). Hagfish slime ecomechanics: Testing the gill-clogging hypothesis. *The Journal of Experimental Biology, 209*(Pt 4), 702–710.

Luchtel, D. L., Deyrup-Olsen, I., & Martin, A. W. (1991). Ultrastructure and lysis of mucin-containing granules in epidermal secretions of the terrestrial slug *Ariolimax columbianus* (Mollusca: Gastropoda:Pulmonata). *Cell and Tissue Research, 266*, 375–383.

Mackie, G. O., Mills, C. E., & Singla, C. L. (1988). Structure and function of the prehensile tentilla of *Euplokamis* (Ctenophora, Cydippida). *Zoomorphology, 107*, 319–337.

Martini, F. (1998). The ecology of hagfishes. In: *The biology of hagfishes,* ed. by Jørgensen, J.M., Lomholt, J.P., Weber, R.E. and Malte, H. London: Chapman & Hall, 57–77.

Maschwitz, U., Lauschke, U., & Würmli, M. (1979). Hydrogen cyanide-producing glands in a scolopender, *Asanada* n.sp. (Chilopoda, Scolopendridae). *Journal of Chemical Ecology, 5*(6), 901–907.

Matile, L. (1981). Description d'un Keroplatidae du crétacé moyen et données morphologiques et taxinomiques sur les Mycetophiloidea (Diptera). *Annales de la Société Entomologique de France, 17*(1), 99–123.

Mayer, G. (2007). *Metaperipatus inae* sp. nov. (Onychophora: Peripatopsidae) from Chile with a novel ovarian type and dermal insemination. *Zootaxa, 1440*(1), 21–37.

Mayer, G. and Oliveira, I.S. (2011). Phylum Onychophora Grube, 1853. In: *Animal biodiversity: An outline of higher-level classification and survey of taxonomic richness,* ed. by Zhang, Z.Q. Auckland: Magnolia Press.

Mayer, A. M., Glaser, K. B., Cuevas, C., Jacobs, R. S., Kem, W., Little, R. D., McIntosh, J. M., Newman, D. J., Potts, B. C., & Shuster, D. E. (2010). The odyssey of marine pharmaceuticals: A current pipeline perspective. *Trends in Pharmacological Sciences, 31*(6), 255–265.

Mayer, G., Oliveira, I. S., Baer, A., Hammel, J. U., Gallant, J., & Hochberg, R. (2015). Capture of prey, feeding, and functional anatomy of the jaws in velvet worms (Onychophora). *Integrative and Comparative Biology, 55*(2), 217–227.

McAlister, W. H. (1960). The spitting habit in the spider *Scytodes intricata* banks (Family Scytodidae). *Texas Journal of Science, 12*, 17–20.

Mebs, D. (2000). *Gifttiere*. Stuttgart: Wissenschaftliche Verlagsgesellschaft.

Merritt, D. J., & Baker, C. (2001). Australian glow-worms in caves. *Newcaves Chronicles, 16*, 42–44.

Merritt, D. J., & Clarke, A. K. (2011). Synchronized circadian bioluminescence in cave-dwelling *Arachnocampa tasmaniensis* (glowworms). *Journal of Biological Rhythms, 26*(1), 34–43.

Meyer-Rochow, V. B. (1990). *The New Zealand glowworm*. Otorohanga: Waitomo Caves Museum Society.

Meyer-Rochow, V. B. (2007). Glowworms: A review of *Arachnocampa* spp. and kin. *Luminescence, 22*, 251–265.

Meyer-Rochow, V. B., & Stringer, I. A. N. (1998). Underjordisk i Jamaica – tropeoens fasciner-ende huleverden going underground in Jamaica: The fascinating world of caves. *Naturens Verden, 8*, 297–302.

Millot, J. (1930). Glandes venimeuses et glandes sericigenes chez les Sicariides. *Bulletin de la Société Zoologique de France, 55*, 150–175.

Mina, A. E., Ponti, A. K., Woodcraft, N. L., Johnson, E. E., & Saporito, R. A. (2015). Variation in alkaloid-based microbial defenses of the dendrobatidpoison frog *Oophaga pumilio*. *Chemoecology, 25*(4), 169–178.

Mitchell, J., & Gibbons, W. (2010). *Salamanders of the Southeast*. Athens, GA: University of Georgia Press.

Miyashita, T. and Coates, M.I. (2017). Hagfish embryology: Staging table and relevance to the evolution and development of vertebrates. In: *Hagfish biology,* ed. by Edwards, S.L. and Goss, G.G. Boca Raton: CRC Press, 95–128.

Moore, J. (2001). Cnidaria. In *An introduction to the invertebrates* (pp. 30–46). Cambridge: Cambridge University Press.

Mora, M., Herrera, A., & Leon, P. (1996). Análisis electroforético de las secreciones adhesivas de onicóforos del género *Epiperipatus* (Onychophora: Peripatidae). *Revista de Biología Tropical, 44*(1), 147–152.

Morera-Brenes, B., & Monge-Nájera, J. (2010). A new giant species of placented worm and the mechanism by which onychophorans weave their nets (Onychophora: Peripatidae). *Revista de Biología Tropical, 58*(4), 1127–1142.

Moroz, L. L., Kocot, K. M., Citarella, M. R., Dosung, S., Norekian, T. P., Povolotskaya, I. S., Grigorenko, A. P., Dailey, C., Berezikov, E., Buckley, K. M., et al. (2014). The ctenophore genome and the evolutionary origins of neural systems. *Nature, 510*(7503), 109–114.

Moseley, H. N. (1874). XXII. On the structure and development of *Peripatus capensis*. *Philosophical Transactions of the Royal Society of London, 164*, 757–782.

Müller, C. H. G., Rosenberg, J., & Hilken, G. (2014). Ultrastructure, functional morphology and evolution of recto-canal epidermal glands in Myriapoda. *Arthropod Structure & Development, 43*(1), 43–61.

Negishi, A., Armstrong, C. L., Kreplak, L., Rheinstadter, M. C., Lim, L. T., Gillis, T. E., & Fudge, D. S. (2012). The production of fibers and films from solubilized hagfish slime thread proteins. *Biomacromolecules, 13*(11), 3475–3482.

Nelson, L., van der Lande, V., & Robson, E. A. (1980). Fine structural and histochemical studies on salivary glands of *Peripatoides novae-zealandiae* (Onychophora) with special reference to acid phosphatase distribution. *Tissue & Cell, 12*(2), 405–418.

Nentwig, W. (1985). Feeding ecology of the tropical spitting spider *Scytodes longipes* (Araneae, Scytodidae). *Oecologia, 65*, 284–288.

Nowak, R. T., & Brodie, E. D. (1978). Rib penetration and associated antipredator adaptations in the salamander *Pleurodeles waltl* (Salamandridae). *Copeia, 1978*, 424–429.

Oliveira, I. S., & Mayer, G. (2017). A new giant egg-laying onychophoran (Peripatopsidae) reveals evolutionary and biogeographical aspects of Australian velvet worms. *Organisms, Diversity and Evolution, 17*(2), 375–391.

Oliveira, I. S., Read, V. M. S., & Mayer, G. (2012). A world checklist of Onychophora (velvet worms), with notes on nomenclature and status of names. *Zookeys, 211*, 1–70.

Oliveira, I. S., Bai, M., Jahn, H., Gross, V., Martin, C., Hammel, J. U., Zhang, W., & Mayer, G. (2016). Earliest onychophoran in amber reveals Gondwanan migration patterns. *Current Biology, 26*(19), 2594–2601.

Opell, B.D. (2013). Cribellar thread. In: *Spider ecophysiology,* ed. by Nentwig, W. Heidelberg: Springer, 303–315.

Opell, B. D., & Hendricks, M. L. (2010). The role of granules within viscous capture threads of orb-weaving spiders. *The Journal of Experimental Biology, 213*(2), 339–346.

Opell, B. D., Karinshak, S. E., & Sigler, M. A. (2011). Humidity affects the extensibility of an orb-weaving spider's viscous thread droplets. *The Journal of Experimental Biology, 214*, 2988–2993.

Opell, B. D., Andrews, S. F., Karinshak, S. E., & Sigler, M. A. (2015). The stability of hygroscopic compounds in orb-web spider viscous thread. *Journal of Arachnology, 43*, 152–157.

Osawa, K., Sasaki, T., & Meyer-Rochow, V. B. (2014). New observations on the biology of *Keroplatus nipponicus* Okada, 1938 (Diptera: Mycetophiloidea; Keroplatidae), a bioluminescent fungivorous insect. *Entomologie heute, 26*, 139–149.

Östman, C. (2000). A guideline to nematocyst nomenclature and classification and some notes on the systematic value of nematocysts. *Scientia Marina, 64*(Suppl. 1), 31–46.

Panic, J. (1963). Das Verhalten von Ameisen gegenüber bodenbewohnenden Kleinarthropoden. *Pedobiologia, 2*, 223–234.

Poinar, G. (1996). Fossil velvet worms in Baltic and Dominican amber: Onychophoran evolution and biogeography. *Science, 273*, 1370–1371.

Pugsley, C. (1980). *Thesis: Ecology of the New Zealand* Arachnocampa luminosa *(Skuse) (Diptera: Mycetophilidae) in tourist caves at Waitomo.* Auckland: University of Auckland.

Pugsley, C. (1984). Ecology of the New Zealand glowworm, *Arachnocampa luminosa* (Diptera: Keroplatidae), in the Glowworm cave, Waitomo. *Journal of the Royal Society of New Zealand, 14*(4), 387–407.

Rahemtulla, F., Hoglund, N. G., & Lovtrup, S. (1976). Acid mucopolysaccharides in the skin of some lower vertebrates (hagfish, lamprey and chimaera). *Comparative Biochemistry and Physiology. B, 53*(3), 295–298.

Read, V., & Hughes, R. (1987). Feeding behaviour and prey choice in *Macroperipatus torquatus* (Onychophora). *Proceedings of the Zoological Society of London. B, 230*, 483–506.

Reid, A. (1996). Review of the Peripatopsidae (Onychophora) in Australia, with comments on peripatopsid relationships. *Invertebrate Taxonomy, 10*(4), 665–936.

Reinhard, J., & Rowell, D. M. (2005). Social behaviour in an Australian velvet worm, *Euperipatoides rowelli* (Onychophora: Peripatopsidae). *Journal of Zoology, 267*, 1–7.

Richards, A. M. (1960). Observations on the New Zealand glow-worm *Arachnocampa luminosa* (Skuse) 1890. *Transactions of the Royal Society of New Zealand, 88*(3), 559–574.

Rilling, G. (1968). *Lithobius forficatus.* Stuttgart: Gustav Fischer Verlag.

Robinson, W. H. (2005). *Urban insects and arachnids – A handbook of urban entomology.* Cambridge: Cambridge University Press.

Röper, H. (1977). Analytical investigations on the defensive secretions from *Peripatopsis moseleyi* (Onychophora). *Zeitschrift für Naturforschung C: A Journal of Biosciences, 32*, 57–60.

Rosenberg, J. (2009a). Giftdrüsen und Giftwirkung. In: *Die Hundertfüsser – Chilopoda,* ed. by Rosenberg, J., Voigtländer, K. and Hilken, G. Hohenwarsleben: Westarp Wissenschaften, 311–323.

Rosenberg, J. (2009b). Wehrdrüsen. In: *Die Hundertfüsser – Chilopoda,* ed. by Rosenberg, J., Voigtländer, K. and Hilken, G. Hohenwarsleben: Westarp Wissenschaften, 324–328.

Rosenberg, J., & Hilken, G. (2006). Fine structural organization of the poison gland of *Lithobius forficatus* (Chilopoda, Lithobiomorpha) *Nor. Journal of Entomology, 53*, 119–127.

Rosenberg, J. and Meyer-Rochow, V.B. (2009). Luminescent myriapoda: A brief review. In: *Bioluminescence in focus – A collection of illuminating essays,* ed. by Meyer-Rochow, V.B. Thiruvananthapuram: Research Signpost, 139–146.

Rosenberg, J., Müller, C.H.G. and Hilken, G. (2011). Chilopoda – Integument and associated organs. In: *Treatise on zoology – Anatomy, taxonomy, biology,* ed. by Minelli, A. Leiden: E.J. Brill, 67–111.

Ruhberg, H. (1985). Die Peripatopsidae (Onychophora). Systematik, Ökologie, Chorologie und phylogenetische Aspekte. In: *Zoologica,* ed. by Schaller, F. Stuttgart: E. Schweizerbart'sche Verlagsbuchhandlung, 1–183.

Ruhberg, H. and Mayer, G. (2013). Onychophora, Stummelfüßer. In: *Spezielle Zoologie,* ed. by Westheide, W. And Rieger, G. Berlin: Springer, 457–464.

Ruhberg, H., & Storch, V. (1977). Über Wehrdrüsen und Wehrsekret von *Peripatopsis moseleyi* (Onychophora) – Electron microscopical investigations and live observations. *Zoologischer Anzeiger, 198*(1/2), 9–19.

Salo, W. L., Downing, S. W., Lidinsky, W. A., Gallagher, W. H., Spitzer, R. H., & Koch, E. A. (1983). Fractionation of hagfish slime gland secretions: Partial characterization of the mucous vesicle fraction. *Preparative Biochemistry, 13*(2), 103–135.

Schaffeld, M., & Schultess, J. (2006). Genes coding for intermediate filament proteins closely related to the hagfish "thread keratins (TK)" alpha and gamma also exist in lamprey, teleosts and amphibians. *Experimental Cell Research, 312*(9), 1447–1462.

Schildknecht, H., Maschwitz, U., & Krauss, D. (1968). Blausäure im Wehrsekret des Erdläufers *Pachymerium ferrugineum*. *Naturwissenschaften, 55*(5), 230.

Schmitz, H. (1912). Biologisch-anatomische Untersuchungen an einer höhlenbewohnenden Mycetophilidenlarve (*Polylepta leptogaster* Winn.) *Jaarboek van het Natuurhistorisch Genootschap in Limburg*, 65–96.

Sedgwick, A. (1895). Peripatus. In: *The Cambridge natural history, Vol. 5,* ed. by Sedgwick, A., Sinclair, F.G. And Sharp, D. London: Macmillan and Co., 3–26.

Sevcik, J., Kjaerandsen, J., & Marshall, S. A. (2012). Revision of *Speolepta* (Diptera: Mycetophilidae), with description of new Neartic and oriental species. *Canadian Entomologist, 144*(1), 93–107.

Sharpe, M. L., Dearden, P. K., Gimenez, G., & Krause, K. L. (2015). Comparative RNA seq analysis of the New Zealand glowworm *Arachnocampa luminosa* reveals bioluminescence-related genes. *BMC Genomics, 16*(1), 825.

Simon, H. R. (1964). Zum Abwehrverhalten von *Lithobius forficatus* L. (Myriapoda, Chilopoda). *Entomologische Zeitschrift, 74*, 114–118.

Sivinski, J. M. (1998). Phototrophism, bioluminescence, and the Diptera. *Florida Entomologist, 81*(3), 282–292.

Smith, A. M. (2016). *Biological adhesives*. Cham: Springer.

Spitzer, R.H. and Koch, E.A. (1998). Hagfish skin and slime glands. In: *The Biology of hagfishes,* ed. by Jørgensen, J.M., Lomholt, J.P., Weber, R.E. And Malte, H. London: Chapman & Hall, 109–132.

Spitzer, R. H., Downing, S. W., Koch, E. A., Salo, W. L., & Saidel, L. J. (1984). Hagfish slime gland thread cells. II. Isolation and characterization of intermediate filament components associated with the thread. *The Journal of Cell Biology, 98*(2), 670–677.

Spitzer, R. H., Koch, E. A., & Downing, S. W. (1988). Maturation of hagfish gland thread cells: Composition and characterization of intermediate filament polypeptides. *Cell Motility and the Cytoskeleton, 11*(1), 31–45.

Stellwagen, S. D., Opell, B. D., & Short, K. G. (2014). Temperature mediates the effect of humidity on the viscoelasticity of glycoprotein glue within the droplets of an orb-weaving spider's prey capture threads. *The Journal of Experimental Biology, 217*(Pt 9), 1563–1569.

Storch, V., & Lehnert-Moritz, K. (1974). Zur Entwicklung der Kolloblasten von *Pleurobrachia pileus* (Ctenophora). *Marine Biology, 28*, 215–219.

Storch, V. and Ruhberg, H. (1993). Onychophora. In: *Microscopic anatomy of invertebrates,* ed. by Harrison, F.W. and Rice, M.E. New York: Wiley-Liss, 11–56.

Storch, V., Alberti, G., & Ruhberg, H. (1979). Light and electron microscopical investigations on the salivary glands of *Opisthopatus cinctipes* and *Peripatopsis moseleyi* (Onychophora: Peripatopsidae). *Zoologischer Anzeiger, 203*, 35–47.

Stringer, I. A. N. (1967). The larval behaviour of the New Zealand glow-worm *Arachnocampa luminosa*. *Tane, 13*, 107–117.

Stringer, I. A. N., & Meyer-Rochow, V. B. (1993). Fishing in the dark: Unusual habits of a Jamaican fly. *Jamaica Naturalist, 3*, 17–18.

Stringer, I. A. N., & Meyer-Rochow, V. B. (1996). Distribution of flying insects in relation to predacoius web-spinning larvae of *Neoditomyia farri* (Diptera:Mycetophilidae) in a Jamaican cave. *Annals of the Entomological Society of America, 89*(6), 849–857.

Sturm, H. (1973). Fanggespinste und Verhalten der Larven von *Neoditomyia andina* und *N. colombiana* Lane (Diptera, Mycetophilidae). *Zoologischer Anzeiger, 191*(1/2), 61–86.

Subramanian, S., Ross, N. W., & MacKinnon, S. L. (2008). Comparison of the biochemical composition of normal epidermal mucus and extruded slime of hagfish (*Myxine glutinosa* L.) *Fish & Shellfish Immunology, 25*(5), 625–632.

Suter, R. B., & Stratton, G. E. (2005). *Scytodes* vs. *Schizocosa*: Predatory techniques and their morphological correlates. *Journal of Arachnology, 33*, 7–15.

Suter, R. B., & Stratton, G. E. (2010). Spitting performance parameters, and their biomechanical implications in the spitting spider, *Scytodes thoracica*. *Journal of Insect Science, 9*(62), 1–15.

Terakado, K., Ogawa, M., Hashimoto, Y., & Matsuzaki, H. (1975). Ultrastructure of the thread cells in the slime gland of Japanese hagfishes, *Paramyxine atami* and *Eptatretus burgeri*. *Cell and Tissue Research, 159*(3), 311–323.

Turcato, A. and Minelli, A., (1990). Fine structure of the ventral glands of *Pleurogeophilus mediterraneus* (Meinert) (Chilopoda Geophilomorpha). In *Proceedings of the 7th international congress of myriapodology*, ed. by Minelli, A. Leiden: E.J. Brill, 165–173.

Turcato, A., Fusco, G., & Minelli, A. (1995). The sternal pore of centipedes (Chilopoda: Geophilomorpha). *Zoological Journal of the Linnean Society, 115*, 185–209.

Tyler, M.J. (2010). Adhesive dermal secretions of the Amphibia, with particular reference to the Australian limnodynastid genus *Notaden*. In: *Biological adhesive systems: From nature to technical and medical application,* ed. by von Byern, J. And Grunwald, I. Wien/NewYork: Springer, 181–186.

Undheim, E. A., Fry, B. G., & King, G. F. (2015). Centipede venom: Recent discoveries and current state of knowledge. *Toxins, 7*(3), 679–704.

Valerio, C. E. (1981). Spitting spiders (Araneae, Scytodidae, *Scytodes*) from Central America. *Bulletin of the American Museum of Natural History, 170*, 80–89.

van Walraven, L., Daan, R., Langenberg, V. T., & van der Veer, H. W. (2017). Species composition and predation pressure of the gelatinous zooplankton community in the western Dutch Wadden Sea before and after the invasion of the ctenophore *Mnemiopsis leidyi* A. Agassiz, 1865. *Aquatic Invasions, 12*(1), 5–21.

Vences, M. (1988). Zum Beutefangverhalten der europäischen Amphibien. *Herpetofauna, 10*(57), 6–10.

Verhoeff, K. W. (1905). Über die Entwicklungsstadien der Steinläufer, Lithobiiden, und Beiträge zur Kenntnis der Chilopoden. *Zoologische Jahrbücher Supplement, 8*, 195–298.

Vollrath, F. (1999). Biology of spider silk. *International Journal of Biological Macromolecules, 24*(2–3), 81–88.

Vollrath, F., & Knight, D. P. (2001). Liquid crystalline spinning of spider silk. *Nature, 410*(6828), 541–548.

von Byern, J., Mills, C.E. and Flammang, P. (2010). Bonding tactics in ctenophores – Morphology and function of the colloblast system. In: *Biological adhesive systems: From nature to technical and medical application,* ed. by von Byern, J. And Grunwald, I. Wien/NewYork: Springer, 29–40.

von Byern, J., Dicke, U., Heiss, E., Grunwald, I., Gorb, S., Staedler, Y., & Cyran, N. (2015). Morphological characterization of the glue-producing system in the salamander *Plethodon shermani* (Caudata, Plethodontidae). *Zoology (Jena, Germany), 118*(5), 334–347.

von Byern, J., Dorrer, V., Merritt, D. J., Chandler, P., Stringer, I. A. N., Marchetti-Deschmann, M., McNaughton, A., Cyran, N., Thiel, K., Noeske, M., & Grunwald, I. (2016). Characterization of the fishing lines in Titiwai (=*Arachnocampa luminosa* Skuse, 1890) from New Zealand and Australia. *Public Library of Science One, 11*(12), e0162687_1–e0162687_30.

von Byern, J., Grunwald, I., Kosok, M., Saporito, R. A., Dicke, U., Wetjen, O., Thiel, K., Kowalik, T., & Marchetti-Deschmann, M. (2017a). Chemical characterization of the adhesive secretions of the salamander *Plethodon shermani* (Caudata, Plethodontidae). *Scientific Reports, 7*(1), 6647.

von Byern, J., Mebs, D., Heiss, E., Dicke, U., Wetjen, O., Bakkegard, K. A., Grunwald, I., Wolbank, S., Mühleder, S., Gugerell, A., et al. (2017b). Salamanders on the bench – A biocompatibility study of salamander skin secretions in cell cultures. *Toxicon, 135*, 24–32.

Vujisic, L. V., Vuckovic, I. M., Makarov, S. E., Ilic, B. S., Antic, D. Z., Jadranin, M. B., Todorovic, N. M., Mrkic, I. V., Vajs, V. E., Lucic, L. R., et al. (2013). Chemistry of the sternal gland secretion of the Mediterranean centipede *Himantarium gabrielis* (Linnaeus, 1767) (Chilopoda: Geophilomorpha: Himantariidae). *Naturwissenschaften, 100*(9), 861–870.

Walker, A. A., Weisman, S., Church, J. S., Merritt, D. J., Mudie, S. T., & Sutherland, T. D. (2012). Silk from crickets: A new twist on spinning. *PLoS One, 7*(2), e30408.

Walker, A. A., Weisman, S., Trueman, H. E., Merritt, D. J., & Sutherland, T. D. (2015). The other prey-capture silk: Fibres made by glow-worms (Diptera: Keroplatidae) comprise cross-beta-sheet crystallites in an abundant amorphous fraction. *Comparative Biochemistry and Physiology. B, 187*, 78–84.

Weill, M. R. (1935). Structure, origine et interpretation cytologique des colloblastes de *Lampetia pancerina* Chun (Ctenophores). *Comptes Rendus. Academy of Sciences, 17*, 1628–1630.

Weinrauch, A.M., Edwards, S.L. and Goss, G.G. (2017). Anatomy of the Pacific hagfish (*Eptatretus stoutii*). In: *Hagfish biology,* ed. by Edwards, S.L. and Goss, G.G. Boca Raton: CRC Press, 2–39.

Whitear, M. (1986). The skin of fishes including cyclostomes - epidermis. In: *Biology of the integument, Vol. 2 Vertebrates,* ed. by Bereiter-Hahn, J., Matoltsy, A.G., Richards, K.S. Berlin: Springer, 8–38.

Williams, T. A., & Anthony, C. D. (1994). Technique to isolate salamander granular gland products with a comment on the evolution of adhesiveness. *Copeia, 2*(540), 540–541.

Williams, T. A., & Larsen, J. H. (1986). New function for the granular skin glands of the eastern long-toed salamander, *Ambystoma macrodactylum columbianum*. *The Journal of Experimental Zoology, 239*, 329–333.

Willis, R. E., White, C. R., & Merritt, D. J. (2010). Using light as a lure is an efficient predatory strategy in *Arachnocampa flava*, an Australian glowworm. *Journal of Comparative Physiology B, 181*(4), 477–486.

Winegard, T. M. (2012). *Thesis: Slime gland cytology and mechanisms of slime thread production in the Atlantic hagfish* (Myxine glutinosa). Guelph: The University of Guelph.

Winegard, T. M., & Fudge, D. S. (2010). Deployment of hagfish slime thread skeins requires the transmission of mixing forces via mucin strands. *The Journal of Experimental Biology, 213*(Pt 8), 1235–1240.

Winegard, T., Herr, J., Mena, C., Lee, B., Dinov, I., Bird, D., Bernards, M., Hobel, S., van Valkenburgh, B., Toga, A., & Fudge, D. S. (2014). Coiling and maturation of a high-performamce fibre in hagfish slime gland thread cells. *Nature Communications, 5*(3534), 1–5.

Wolff, J. O., Rezac, M., Krejci, T., & Gorb, S. N. (2017). Hunting with sticky tape: Functional shift in silk glands of araneophagous ground spiders (Gnaphosidae). *The Journal of Experimental Biology, 220*(Pt 12), 2250–2259.

Yeargan, K. V. (1994). Biology of bolas spiders. *Annual Review of Entomology, 39*, 81–99.

Zheden, V., Klepal, W., von Byern, J., Adolf, F. R., Thiel, K., Kowalik, T., & Grunwald, I. (2014). Biochemical analyses of the cement float of the goose barnacle *Dosima fascicularis*. *Biofouling, 30*(8), 949–963.

Zheden, V., Kovalev, A. E., Gorb, S. N., & Klepal, W. (2015). Characterization of cement float buoyancy in the stalked barnacle *Dosima fascicularis* (Crustacea, Cirripedia). *Interface Focus, 5*(1), 20140060.

Zintzen, V., Roberts, C. D., Anderson, M. J., Stewart, A. L., Struthers, C. D., & Harvey, E. S. (2011). Hagfish predatory behaviour and slime defence mechanism. *Scientific Reports, 1*(131), 1–6.

Zobel-Thropp, P. A., Correa, S. M., Garb, J. E., & Binford, G. J. (2014). Spit and venom from scytodes spiders: A diverse and distinct cocktail. *Journal of Proteome Research, 13*(2), 817–835.

Chapter 8
Visualization of the Number of Tarsal Adhesive Setae Used During Normal and Ceiling Walk in a Ladybird Beetle: A Case Study

Lars Heepe, Constanze Grohmann, and Stanislav N. Gorb

Abstract The hairy attachment devices of climbing animals consist of hundreds to billions of micro- to nanoscopic adhesive setae which can form an intimate contact with the substrate and thus allow for sufficient adhesion to walk on vertical walls or even on the ceiling. In previous studies, the combination of microscopic visualization of the pad morphology and adhesive force measurements at the level of individual setae aided in the estimation of the maximum adhesive capability of different animals by assuming all setae being in contact with the substrate. These estimates, however, did not necessarily coincide with adhesion measurements performed at the level of the whole animal. We hypothesize that this discrepancy may arise due the fact that not all setae are simultaneously applied during locomotion. To test this hypothesis, we visualized the number of adhesive setae used during normal and ceiling walk in a ladybird beetle. We found that ladybird beetles had significantly more setae in contact with a smooth substrate during ceiling walk than during normal walk. Moreover, during ceiling walk mainly spatula-shaped setae were used during locomotion, which are expected to provide high adhesive forces.

8.1 Introduction

Reliable and repeatable attachment to diverse and unpredictable substrates for resting and locomotion plays an important role in the niche occupation of climbing animals. Independently in some animal groups, such as insects (e.g., Gorb 2001), arachnids (e.g., Wolff and Gorb 2016), and reptiles (e.g., Hiller 1968; Autumn et al. 2000) hairy attachment devices with similar structure have been evolved. In order to

L. Heepe (✉) · C. Grohmann · S. N. Gorb
Department of Functional Morphology and Biomechanics, Zoological Institute,
Kiel University, Kiel, Germany
e-mail: lheepe@zoologie.uni-kiel.de

understand the physical principles underlying the performance of such biological attachment systems, microscopic and biomechanical investigations at the various hierarchical levels (from individual setal tips, adhesive pads to the whole animal) of attachment organs were performed.

However, some discrepancies were observed when extrapolating adhesion force measurements of individual setae to measurements on the level of adhesive pads or whole animal adhesion. For geckos, for example, force measurements on individual spatula-shaped setal tips of *Gekko gecko* revealed pull-off forces (perpendicular to the surface) of about 10 nN (Huber et al. 2005a). Considering about 10^9 spatulae covering a gecko foot, the authors estimated a theoretical adhesion force of about 10 N per foot. Pull-off force measurements at the level of the whole animal with the same species revealed, however, only a value of order 1–2 N per foot (Pugno et al. 2011). Shear force measurements at the level of an isolated seta which has about 100–1000 individual spatulae and at the level of the whole animal led to a similar observed discrepancy (Irschick et al. 1996; Autumn et al. 2000). All extrapolations mentioned above assumed the simultaneous application of all setal tips into the contact with substrate.

Such discrepancies may arise from various factors which can influence the obtained results. For example, it has been shown that different levels of relative humidity lead to both different material properties of the keratinous setae and thus to different adhesion properties on the one side and different relative contributions from intermolecular van der Waals forces and capillarity (Huber et al. 2005b; Puthoff et al. 2010) on the other side. This is of particular importance for nano- and microscopic measurements with ablated, single setae/spatulae (Autumn et al. 2000; Huber et al. 2005a). Moreover, it is known that the overall attachment ability of whole animals strongly depends on the antagonistic work of opposing legs, an effect explained by the multiple peeling theory (Pugno 2011; Wohlfart et al. 2014; Heepe et al. 2017).

Besides these factors, we assume that these deviations can also be addressed to the question of how many individual setae are actually used in contact for locomotion. This question, however, remains elusive so far. The reason for this may be attributed to the following technical challenge. In order to visualize the number of contacting hairs during locomotion, one would need a large field of view to monitor the motion of the whole animal (or at least one foot), but at the same time a sufficient optical and temporal resolution to observe individual setal tips in contact. In case of geckos and spiders with tip dimensions of order 100–400 nm this seems to be impossible with conventional optical methods. Insects, however, are usually much smaller, but have setal tip dimensions in the range of several micrometers, which may allow answering this question.

To address this question, we performed a case study using high-speed video recordings and reflection contract microscopy with seven-spotted ladybird beetles (*Coccinella septempunctata*) which were allowed to walk freely on a glass slide. The total number of adhesive setae used during normal and ceiling walk was then analyzed and correlated to the overall equipment by tarsal setae of the beetle.

8.2 Materials and Methods

8.2.1 Insects

For this study, females of the seven-spotted ladybird beetle *Coccinella septempunctata* LINNAEUS 1758 (Coleoptera, Coccinellidae) were used as a model species (Fig. 8.1a). Adult beetles were collected in the New Botanical Garden at Kiel University, Schleswig-Holstein, Germany. They were kept in ventilated boxes at 10 °C and fed with honey. Figure 8.1b–g shows scanning electron micrographs of the hairy attachment devices of female *C. septempunctata*. For detailed description see e.g. Gorb et al. (2010). The tarsi of forelegs, midlegs, and hindlegs are composed of three tarsomeres and two ventrally curved claws (Fig. 8.1b–d). Only the first two tarsomeres, referred to as the proximal and distal adhesive pads, are ventrally covered by tenent setae. Both pads are covered with different types of adhesive setae. The distal pad (second tarsomere) has spatula-shaped setae (Fig. 8.1e) located distal, transitional type of setae with lanceolate tips (Fig. 8.1f) located in the middle, and
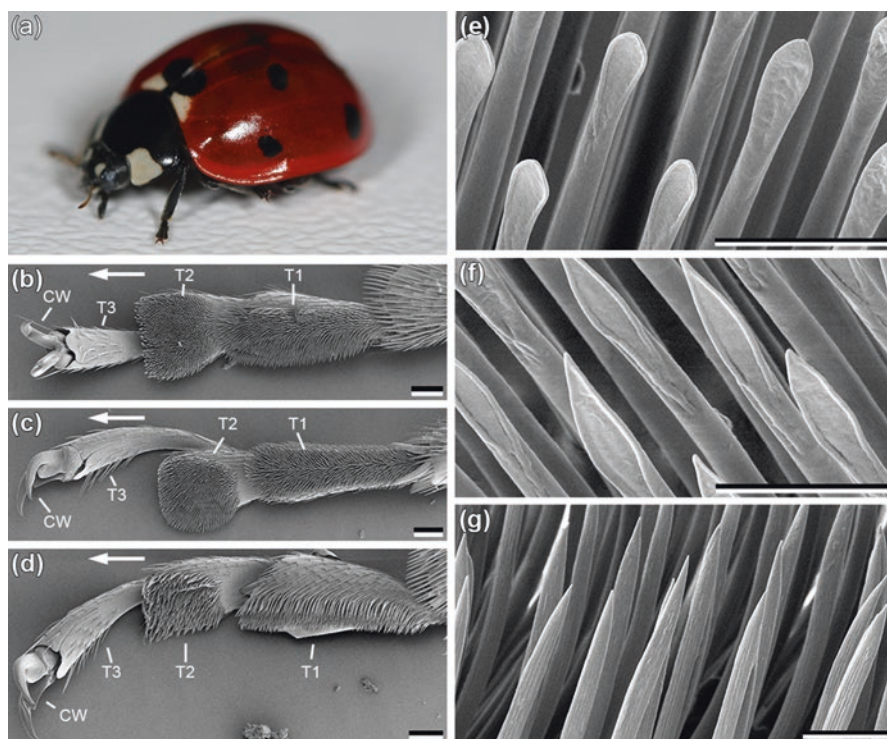
Fig. 8.1 Attachment devices of female *Coccinella septempunctata* (**a**). Tarsi of forelegs (**b**), midlegs (**c**), and hindlegs (**d**) in females are ventrally covered by tenent setae (**e–g**). White arrows in (**b–d**) indicate distal direction. CW, claws; T1, first tarsomere; T2, second tarsomere; T3, third tarsomere. Scale bars in (**b–d**), 100 μm. Scale bars in (**e–g**), 10 μm (Adapted from Heepe et al. 2016)

setae with pointed tips (Fig. 8.1g) located proximal and lateral. The proximal pad (first tarsomere) has transitional setae and setae with pointed tips. Based on scanning electron micrographs of forelegs, midlegs, and hindlegs of various individual beetles, the total number of setae per leg and pad was estimated. For all leg pairs and adhesive pads, a total number of setae was found to be of order 1000.

8.2.2 Visualization of Applied Tarsal Setae During Normal and Ceiling Walk

In order to visualize the number of tarsal setae in contact with a surface during normal ground walk and ceiling walk, a microscopic technique based on the reflection contrast was applied (Ploem 1975; Federle et al. 2002; Heepe et al. 2014). Beetles were allowed to walk freely on a glass slide (Fig. 8.2a, GS), confined in an acrylic housing (Fig. 8.2a, H) with dimensions in width, length, and height of 32 mm × 24 mm × 5 mm. The height was chosen to ensure that beetles could not climb up the housing, but at the same time not to abut against the housing with their elytra during locomotion. For the normal walk (Fig. 8.2a), this setup was installed on an inverse microscope Observer.A1 (Carl Zeiss MicroImaging GmbH, Göttingen, Germany) equipped with a 10× objective lens (Carl Zeiss MicroImaging GmbH). The interaction of beetle tarsi with the glass slide was recorded with an attached high-speed camera Photron Fastcam SA1.1 (VKT Video Kommunikation GmbH, Pfullingen, Germany) operated at a frame rate of 500 frames per second. For the ceiling walk (Fig. 8.2b), the setup was installed on an upright microscope Axio Imager.M1m (Carl Zeiss MicroImaging GmbH) equipped with the same objective lens and same high-speed video camera. The tenfold magnification was a compromise between being able to visualize a complete leg during the contact with the
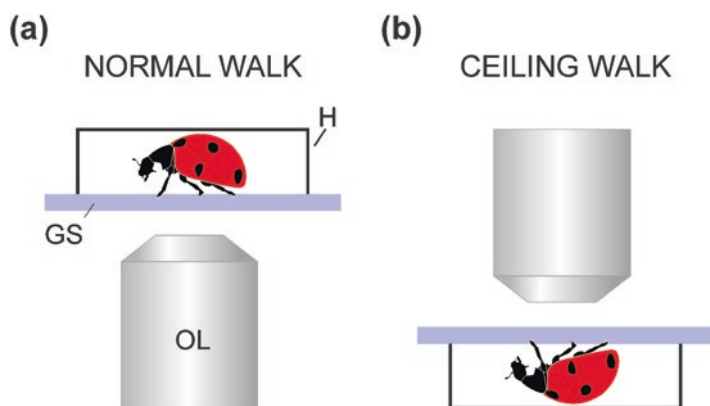
Fig. 8.2 Schematic of the experimental setup: (**a**) normal ground walk and (**b**) ceiling walk. *OL* objective lens, *GS* glass slide, *H* housing

glass slide and a sufficient resolution to visualize individual setae in contact. Prior experiments, beetles were allowed to acclimate in the lab for 15 min. Then the beetles were placed inside the housing and only sequences of leg attachment and detachment were recorded with both adhesive pads within the field of view of the focal plane. After each second or third sequence, the glass slide was renewed to reduce contamination effects on the visualization of contacting setae with the glass slide. Only sequences, where it was possible to determine, if a fore-, mid- or hindleg was recorded, were considered in further analysis.

8.2.3   Estimation of the Number of Setae Used During Normal and Ceiling Walk

In still images, the silhouette of the ventral side of the leg is clearly visible and setae in direct contact with the glass appear as dark spots (Fig. 8.3). Due to the large number of setae in contact, the large number of frames, and the high number
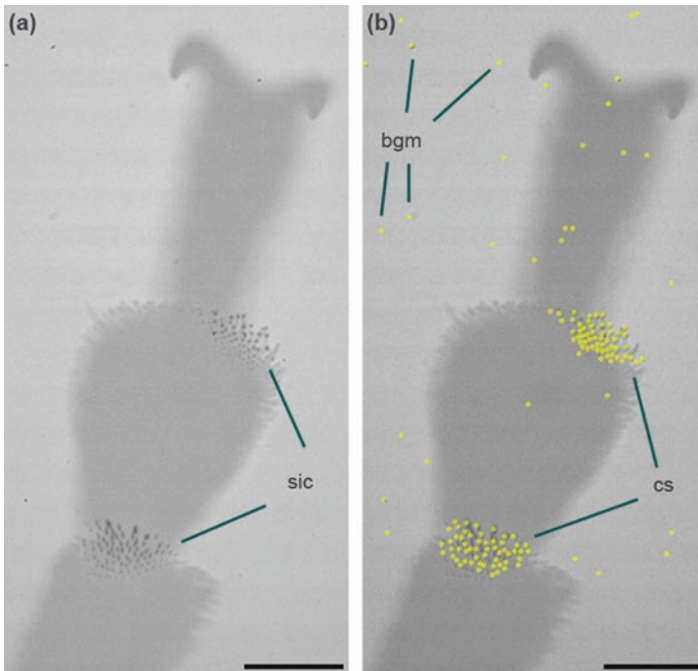
Fig. 8.3 (**a**) Representative still image obtained from a video sequence of a beetle leg in partial contact with transparent glass. Dark spots correspond to setae in contact (sic) with the surface. (**b**) Local minima of gray scale values seen in the image (**a**) are highlighted by yellow points. This allowed us to estimate and count the real number of setae in real contact (cs) by subtraction of detected background minima (bgm), which were caused by image noise and/or contaminations on the transparent surface (Images have been cropped for better visibility. Scale bar, 200 μm)

of recorded sequences, counting of setae in contact was done with an automated image processing procedure. Local minima in gray scale values (dark spots) were detected with ImageJ (Rasband, W.S., ImageJ, U. S. National Institutes of Health, Bethesda, Maryland, USA) using the plugin "Find maxima". The sensitivity to detect local minima could be adjusted and was manually set for each sequence depending on the noise level of the videos. Contaminations due to particles on the glass slide or on the sensor led to falsely detected minima (Fig. 8.3b). That is why we accounted for this systematic error by analyzing the local minima in a frame of the same sequence without the leg in the field of view and subtracted this constant number from the results of all analyzed frames. This provided an estimate for the real number of counted setae (Fig. 8.3b). Fluctuations in the illumination and noise within each frame were another possible source of false counts. However, we compared, for a couple of frames, the results from the automated procedure with results from manually counting the setae in contact. We estimated a relative error of order 10%.

For the comparison of the number of setae used during normal and ceiling walk we have chosen the maximum number of setae in contact during one step (Fig. 8.4).
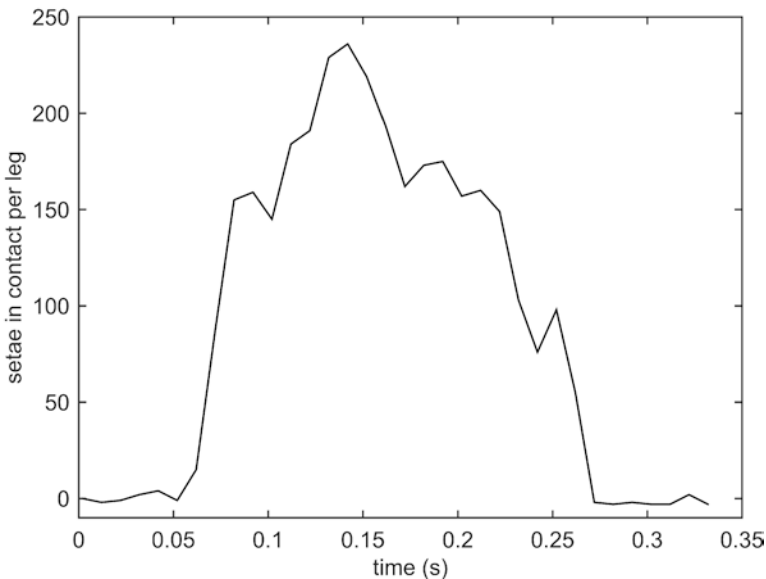
Fig. 8.4 Temporal course of the number of setae in contact during the attachment and detachment of a single leg

8.3   Results and Discussion

Figure 8.5 shows the maximum number of setae in contact for normal and ceiling walk for one individuum. For both scenarios, 33 sequences were analyzed and the data for the different leg pairs were pooled (normal walk: forelegs, $N = 14$, midlegs, $N = 12$, hindlegs $N = 7$; ceiling walk: forelegs, $N = 14$, midlegs, $N = 11$, hindlegs $N = 8$). A statistically significant difference between the median values of maximum setae in contact with the surface for normal and ceiling walk was observed (Mann–Whitney rank sum test, $U = 293$, $T = 854$, $n_{1,2} = 33$, $P = 0.001$). During normal walk, in average 208 (interquartile range: 164–284) setae were in contact per leg, which corresponds to approximately 10% of the setal coverage per leg. During ceiling walk, the beetle attached in average 353 (interquartile range: 254–446) setae per leg to the surface which correspond to approximately 18% of the total number of setae per leg.

For beetles in both scenarios, a tripod gait pattern during locomotion was observed, i.e. three legs were simultaneously in contact with the surface, showing that three legs in contact are sufficient for the beetle locomotion on the ceiling in contrast to some other groups of insects (Gorb and Heepe 2018). Taking into account a typical weight of *C. septempunctata* of 30 mg (i.e. a weight force of about ~0.3 mN) and equal load sharing (see Bullock and Federle (2011)), the average

Fig. 8.5 Maximum number of setae in contact for normal and ceiling walk. The data for fore-, mid-, and hindlegs were pooled (normal walk $n = 33$, ceiling walk $n = 33$). Lines within the boxes show the median values, ends of boxes indicate 25th and 75th percentiles, error bars indicate 10th and 90th percentiles, and outliers are indicated by plus signs. Bar with asterisk indicates a statistical difference, see text for statistical evaluation
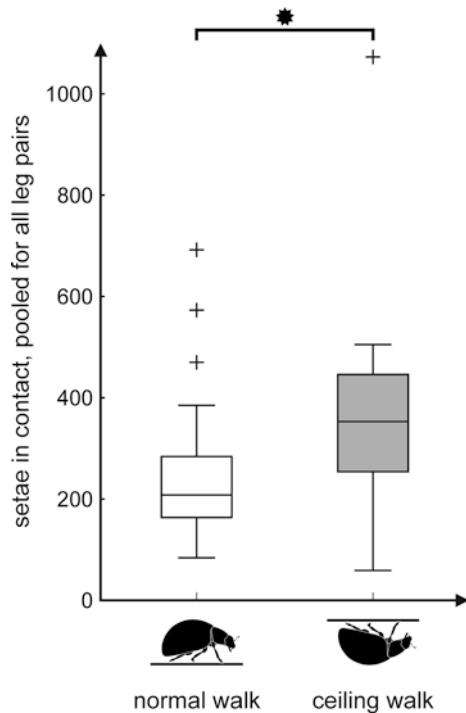
force suspended per setae (3 × 353) is estimated to ~0.3 μN during ceiling walk. This result is of the same order of magnitude compared to *in vivo* adhesion measurements on individual setae in the beetle *Gastrophysa viridula* (Bullock and Federle 2011). Here an average pull-off force of ~0.6 μN for spatula-shaped setae and ~0.1 μN for pointed setae were obtained (Bullock and Federle 2011).

Since we obtained a complete data set for one beetle only, we refrain from analyzing differences between different leg pairs and moreover differences between both proximal and distal adhesive pads. However, we observed, especially for the ceiling walk, that setae in the distal region of both pads came primarily in contact for all leg pairs. Figure 8.6 illustrates the areal distribution of setae in contact during ceiling walk for a foreleg (a–c), a midleg (d–f), and a hindleg (g–i) at the initial phase of contact formation of the legs with the surface (a, d, g), at the phase where approximately the maximum number of setae were in contact (b, e, h), and right before the very moment of detachment (c, f, i). Correlating this observation with the distribution of setal types on tarsomeres (see Sect. 8.2.1) reveals that in the distal pad spatula-shaped and transitional setae were mainly in contact. Those types of setae with flattened tips are assumed to provide intimate contact with surfaces, thus generating high adhesion (see for example Gorb 1998, 2001; Autumn et al. 2000, 2006; Kesel et al. 2003; Varenberg et al. 2010).

The role of different types of setae in the locomotion of *G. viridula* on vertical and horizontal surfaces has been recently discussed (Bullock and Federle 2009, 2011). In agreement with our observations, it was hypothesized that spatula-shaped setae are primarily used to generate high adhesion in ceiling situations (Bullock and Federle 2011). Whereas setae with pointed tips were hypothesized to generate considerable friction forces when pressed against the surface and making side contact, thus increasing the real area of contact (Bullock and Federle 2009, 2011), which is important for scaling vertical surfaces either heads upward or downward.

Such "division of labour" of differently structured parts of attachment devices was also shown for nubby and smooth parts of attachment devices in some stick insects and crickets. Nubby pads were shown to be mainly applied in situations, where the animals are climbing vertically, i.e. shear forces are primarily acting on the pads surfaces (Labonte and Federle 2013; Grohmann et al. 2015). Force measurements confirmed that nubby pads generate high friction forces, especially on rough surfaces, rather than adhesion (Bußhardt et al. 2012; Labonte and Federle 2013). In contrast, smooth parts of attachment devices were mainly applied in ceiling situations where strong adhesion is necessary to securely support the animals' weight.

8.4   Summary and Outlook

The present study demonstrates, for the first time, the number of tarsal adhesive setae used during normal and ceiling walk in a ladybird beetle. It was shown that the beetle had significantly more setae in contact to the substrate while walking on the
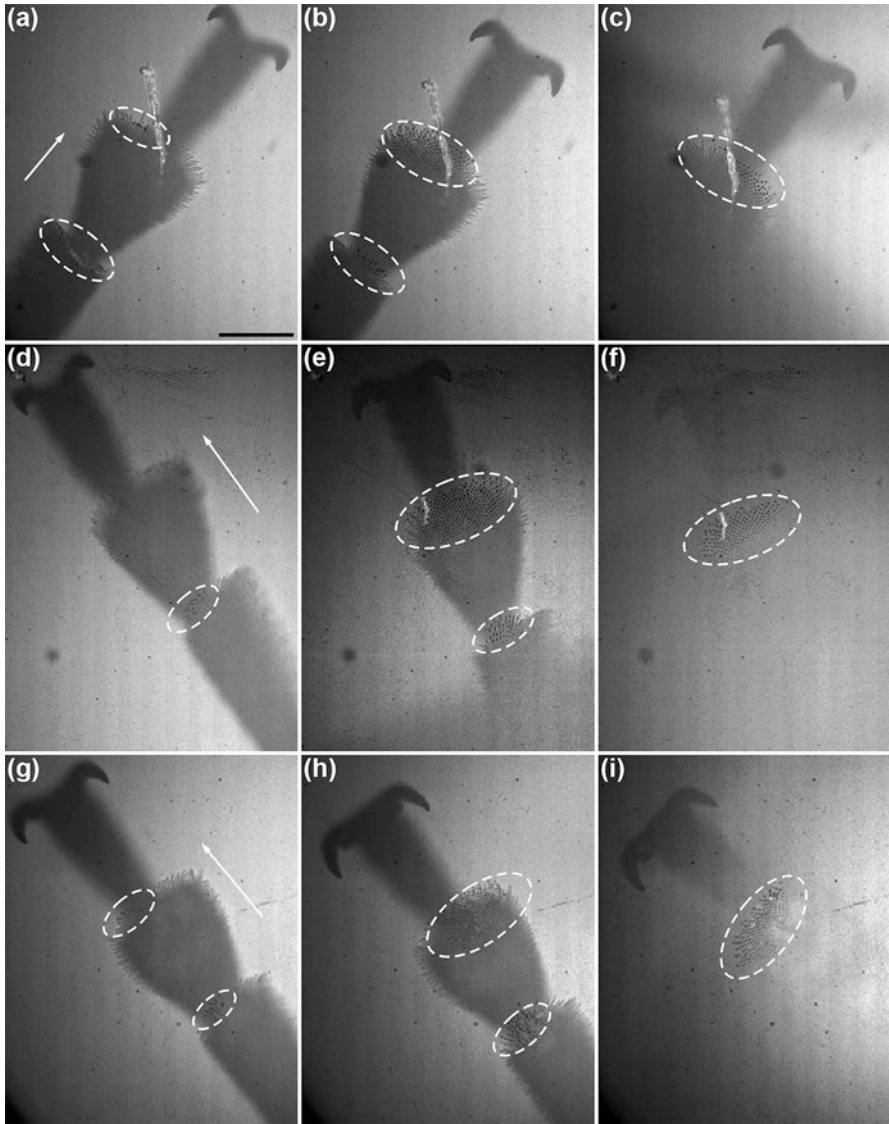
Fig. 8.6 Representative still images of a foreleg (**a–c**), a midleg (**d–f**), and a hind leg (**g–i**) in contact with the transparent surface during ceiling walk. Dark spots correspond to setae in contact (see area within white dashed ellipses). Images (**a, d, g**) indicate the situation close to the moment of the leg attachment. Images (**b, e, h**) roughly correspond to the moment of the maximum number of setae in contact. Images (**c, f, i**) indicate the moment of leg detachment. White arrows indicate distal direction. Scale bar in (**a**) applies for all images, 200 μm

ceiling than while walking upright. Moreover, during ceiling walk, mainly spatula-shaped setae were in contact rather than setae with pointed tips. This result seems to support that different setal types serve different functional roles in the locomotion of climbing animals.

So far, biomimetic fibrillar adhesive surfaces are only composed of pillar-like structures with one particular contact shape. However, based on current methodology, visualization of the actual application of hairy attachment systems among different species walking normally, on the ceiling, and on the vertical wall could help to design novel hybrid adhesive surfaces. These could have differently shaped microstructures that reflect the functional needs during different walking situations. Such hybrid adhesive surfaces could be employed in walking robots to extent the possible range of maneuverability.

References

Autumn, K., Liang, Y. A., Hsieh, S. T., Zesch, W., Chan, W. P., Kenny, T. W., Fearing, R., & Full, R. J. (2000). Adhesive force of a single gecko foot-hair. *Nature, 405*, 681–685.

Autumn, K., Dittmore, A., Santos, D., Spenko, M., & Cutkosky, M. (2006). Frictional adhesion: A new angle on gecko attachment. *The Journal of Experimental Biology, 209*, 3569–3579.

Bullock, J. M., & Federle, W. (2009). Division of labour and sex differences between fibrillar, tarsal adhesive pads in beetles: Effective elastic modulus and attachment performance. *The Journal of Experimental Biology, 212*, 1876–1888.

Bullock, J. M., & Federle, W. (2011). Beetle adhesive hairs differ in stiffness and stickiness: In vivo adhesion measurements on individual setae. *Naturwissenschaften, 98*, 381–387.

Bußhardt, P., Wolf, H., & Gorb, S. N. (2012). Adhesive and frictional properties of tarsal attachment pads in two species of stick insects (Phasmatodea) with smooth and nubby euplantulae. *Zoology, 115*, 135–141.

Federle, W., Riehle, M., Curtis, A. S., & Full, R. J. (2002). An integrative study of insect adhesion: Mechanics and wet adhesion of pretarsal pads in ants. *Integrative and Comparative Biology, 42*, 1100–1106.

Gorb, S. N. (1998). The design of the fly adhesive pad: Distal tenent setae are adapted to the delivery of an adhesive secretion. *Proceedings of the Royal Society B, 265*, 747–752.

Gorb, S. N. (2001). *Attachment devices of insect cuticle*. Dordrecht/Boston/London: Kluwer Academic Publishers.

Gorb, S. N., & Heepe, L. (2018). Biological fibrillar adhesives: Functional principles and biomimetic applications. In L. F. M. da Silva, A. Oechner, & R. Adams (Eds.), *Handbook of adhesion technology* (Vol. 2). Berlin: Springer.

Gorb, E. V., Hosoda, N., Miksch, C., & Gorb, S. N. (2010). Slippery pores: Anti-adhesive effect of nanoporous substrates on the beetle attachment system. *Journal of the Royal Society Interface, 7*, 1571–1579.

Grohmann, C., Henze, M. J., Nørgaard, T., & Gorb, S. N. (2015). Two functional types of attachment pads on a single foot in the Namibia bush cricket *Acanthoproctus diadematus* (Orthoptera: Tettigoniidae). *Proceedings of the Royal Society B, 282*, 20142976.

Heepe, L., Kovalev, A. E., & Gorb, S. N. (2014). Direct observation of microcavitation in underwater adhesion of mushroom-shaped adhesive microstructure. *Beilstein Journal of Nanotechnology, 5*, 903–909.

Heepe, L., Wolff, J. O., & Gorb, S. N. (2016). Influence of ambient humidity on the attachment ability of ladybird beetles (*Coccinella septempunctata*). *Beilstein Journal of Nanotechnology, 7*, 1332–1329.

Heepe, L., Raguseo, S., & Gorb, S. N. (2017). An experimental study of double-peeling mechanism inspired by biological adhesive systems. *Applied Physics A: Materials Science & Processing, 123*, 124.

Hiller, U. (1968). Untersuchungen zum Feinbau und zur Funktion der Haftborsten von Reptilien. *Zoomorphology, 62*, 307–362.

Huber, G., Gorb, S. N., Spolenak, R., & Arzt, E. (2005a). Resolving the nanoscale adhesion of individual gecko spatulae by atomic force microscopy. *Biology Letters, 1*, 2–4.

Huber, G., Mantz, H., Spolenak, R., Mecke, K., Jacobs, K., Gorb, S. N., & Arzt, E. (2005b). Evidence for capillarity contributions to gecko adhesion from single spatula nanomechanical measurements. *Proceedings of the National Academy of Sciences of the United States of America, 102*, 16293–16296.

Irschick, D. J., Austin, C. C., Petren, K., Fisher, R. N., Losos, J. B., & Ellers, O. (1996). A comparative analysis of clinging ability among pad-bearing lizards. *Biological Journal of the Linnean Society, 59*, 21–35.

Kesel, A. B., Martin, A., & Seidl, T. (2003). Adhesion measurements on the attachment devices of the jumping spider *Evarcha arcuata*. *The Journal of Experimental Biology, 206*, 2733–2738.

Labonte, D., & Federle, W. (2013). Functionally different pads on the same foot allow control of attachment: Stick insects have load-sensitive "heel" pads for friction and shear-sensitive "toe" pads for adhesion. *PLoS One, 8*, e81943.

Ploem, J. S. (1975). Reflection-contrast microscopy as a tool for investigation of the attachment of living cells to a glass surface. In R. van Furth (Ed.), *Mononuclear phagocytes in immunity, infection and pathology* (pp. 405–421). Oxford: Blackwell.

Pugno, N. M. (2011). The theory of multiple peeling. *International Journal of Fracture, 171*, 185–193.

Pugno, N., Lepore, E., Toscano, S., & Pugno, F. (2011). Normal adhesive force-displacement curves of living geckos. *The Journal of Adhesion, 87*, 1059–1072.

Puthoff, J. B., Prowse, M. S., Wilkinson, M., & Autumn, K. (2010). Changes in materials properties explain the effects of humidity on gecko adhesion. *The Journal of Experimental Biology, 213*, 3699–3704.

Varenberg, M., Pugno, N. M., & Gorb, S. N. (2010). Spatulate structures in biological fibrillar adhesion. *Soft Matter, 6*, 3269–3272.

Wohlfart, E., Wolff, J. O., Arzt, E., & Gorb, S. N. (2014). The whole is more than the sum of all its parts: collective effect of spider attachment organs. *The Journal of Experimental Biology, 217*, 222–224.

Wolff, J. O., & Gorb, S. N. (2016). *Attachment structures and adhesive secretions in arachnids*. New York: Springer.

Chapter 9
Comparative Study of Tongue Surface Microstructure and Its Possible Functional Significance in Frogs

Thomas Kleinteich and Stanislav N. Gorb

Abstract Frogs (Lissamphibia: Anura) use adhesive tongues to capture fast moving, elusive prey. For this, the tongues are moved quickly and adhere instantaneously to various prey surfaces. Recently, the functional morphology of frog tongues was discussed in context of their adhesive performance. It was suggested that the interaction between the tongue surface and the mucus coating is important for generating strong pull-off forces. However, despite the general notions about its importance for a successful contact with the prey, little is known about the surface structure of frog tongues. Previous studies focused almost exclusively on species within the Ranidae and Bufonidae, neglecting the wide diversity of frogs. Here we examined the tongue surface in nine different frog species, comprising eight different taxa, i.e., the Alytidae, Bombinatoridae, Megophryidae, Hylidae, Ceratophryidae, Ranidae, Bufonidae, and Dendrobatidae. In all species examined herein, we found fungiform and filiform papillae on the tongue surface. Further, we observed a high degree of variation among tongues in different frogs. These differences can be seen in the size and shape of the papillae, in the fine-structures on the papillae, as well as in the three-dimensional organization of subsurface tissues. Notably, the fine-structures on the filiform papillae in frogs comprise hair-like protrusions (Megophryidae and Ranidae), microridges (Bufonidae and Dendrobatidae), or can be irregularly shaped or absent as observed in the remaining taxa examined herein. Some of this variation might be related to different degrees of adhesive performance and may point to differences in the spectra of prey items between frog taxa.

T. Kleinteich · S. N. Gorb (✉)
Department of Functional Morphology and Biomechanics, Zoological Institute,
Kiel University, Kiel, Germany
e-mail: sgorb@zoologie.uni-kiel.de

9.1   Introduction

Frogs (Lissamphibia: Anura) are famous for their adhesive tongues, which allow them to catch elusive prey. While the movements of the tongue during feeding in different groups of frogs have received considerable attention in the past (Emerson 1977; Gans and Gorniak 1982a, b; Ritter and Nishikawa 1995; Nishikawa and Gans 1996; Nishikawa 2000), little is known about the functional mechanisms for the adhesiveness of frog tongues. Obviously, adhesion is critical to secure the prey item and to move it into the mouth. In a previous study we demonstrated for South American horned frogs (genus *Ceratophrys*) that the adhesive forces that frog tongues can produce and withstand are even higher than the body weight of the animals, at least if measured against a glass surface (Kleinteich and Gorb 2014). Further, we found that adhesive forces are higher if less mucus remained on our test surface and that the amount of the mucus coverage increases with increasing contact duration. These results suggested (1) that during the initial contact formation, only small amounts of mucus are present on the tongue and (2) that besides chemical and physical properties of the mucus, other mechanisms at the interface between a frog tongue and a target will have an important impact on tongue adhesiveness (Kleinteich and Gorb 2014).

Frog tongues are known to have two types of papillae on their surface. So-called fungiform papillae (type 1) are surrounded by numerous, smaller filiform papillae (type 2) (Iwasaki 2002). The fungiform papillae are suggested to act as chemoreceptors, while the filiform papillae are the places for mucus production (Jaeger and Hillman 1976; Osculati and Sbarbati 1995; Iwasaki et al. 1997, 1998). Owing to the fact that the filiform papillae cover wide parts of the adhesive tongue surface in frogs, the interaction between the filiform papillae, the mucus layer, and the target surface of a prey item will be critical for a successful feeding event. Thus, besides mucus production, the filiform papillae as surface microstructures might actually mediate adhesive performance. More recently we discussed the contribution of the filiform papillae to the adhesive mechanism of the tongue in the frog *Ceratophrys ornata* (Kleinteich and Gorb 2015). We suggested that the papillae increase the adaptability of the tongue to uneven surfaces and may help to form and anchor fibrils of mucus that emerge before a frog tongue is about to loose the contact with a target surface.

While it has been shown before that the anatomy of frog tongues can be very diverse in different anuran taxa (Regal and Gans 1976), little is known about the diversity of tongue surface structures in frogs. Besides a study on the ornamentation of the tongue in the dicroglossid frog *Fejervarya cancrivora* (Iwasaki and Wanichanon 1993) (the frog is referred to as *Rana cancrivora* in that study), only the tongue surfaces in a few species of the genera *Rana* (Helff and Mellicker 1941a, b; Iwasaki and Wanichanon 1991, 1993; Ojima et al. 1997; Eşrefoğlu et al. 2000; Guiraldelli et al. 2011) and *Bufo* (Iwasaki and Kobayashi 1988; Iwasaki et al. 1989; Elsheikh et al. 2013) have been described in the literature. Further accounts on tongues in *Hyla arborea* (Jaeger and Hillman 1976) and *Calyptocephalella gayi*

(Stensaas 1971) focus on the fungiform papillae but neglect the filiform papillae despite their presumably important role in tongue adhesion. Iwasaki (2002) highlights notable differences in the filiform papillae between *Rana* spp. and *Bufo japonicus*. In *Rana* spp., the filiform papillae appear as hair-like structures, while in *B. japonicus*, the filiform papillae rather take the form of ridges. In a more recent study, however, Elsheikh et al. (2013) described hair-like filiform papillae for another species within the Bufonidae, i.e., *Sclerophrys regularis* (in Elsheikh et al. (2013) as *Bufo regularis*).

Besides the surface profile and mechanical properties of the tongue surface, the tissues underlying the surface represent another important factor for the adhesive performance of the tongue. The configuration of subsurface tissues will determine how well a tongue can adapt to a target surface and how well the tongue withstands the forces that act during protraction and retraction. Besides our recent description of the inner anatomy of the tongue in *Ceratophrys ornata* (Kleinteich and Gorb 2015), nothing is known about the three-dimensional architecture of the tissues underneath the tongue surface in frogs. This kind of data might shed light on the presence of potential gradients of the material stiffness that were previously described for attachment structures in beetles (Peisker et al. 2013; Gorb and Filippov 2014), grasshopers (Perez Goodwyn et al. 2006), and geckos (Gilman et al. 2015).

Here we combine scanning electron microscopy and high-resolution microcomputed tomography (micro-CT) to provide comparative accounts on the surface profiles and subsurface structures of the tongues in nine different frog species. The aims of this study are: (1) to evaluate patterns of the diversity of tongue surfaces in frogs, (2) to provide descriptions on the three-dimensional organization of the tissues underneath the frog tongue surface, and (3) to understand patterns of tongue variation in frogs within both evolutionary and biomechanical contexts.

9.2   Experimental

We studied the tongue anatomy of nine different species comprising eight of the currently 55 recognized taxa (families) within the Anura (AmphibiaWeb). A list of specimens is provided in Table 9.1. The specimens were either made available by the Zoological Museum Hamburg (ZMH) or were derived from the uncatalogued stock of the Zoological Institute and Museum at Kiel University. In the latter case, we used our own specimen IDs (TK) herein. All specimens were stored in 70% ethanol. Two specimens actually belonged to the same genus but comprised two different species: *Litoria infrafrenata* and *L. caerulea*. As these two species appeared to be very similar in their tongue anatomy, they are referred to as *Litoria* spp. herein. The two specimens of *Ceratophrys ornata* have been examined in prior studies on feeding and tongue adhesion in frogs of the genus *Ceratophrys* (Kleinteich 2015; Kleinteich and Gorb 2015). The *Litoria caerulea* specimen studied herein was previously used for a study on toe-pad anatomy in tree frogs (Barnes et al. 2013).

Table 9.1 Specimens examined herein

Taxon (family)	Species	Collection ID	SVL (mm)	Method	Voxel size µCT (µm)
Alytidae	*Discoglossus pictus*	ZMH A11869	48	SEM	–
Alytidae	*Discoglossus pictus*	ZMH A11885	48	µCT	0.67
Bombinatoridae	*Bombina variegata*	ZMH A11872	38	SEM	–
Bombinatoridae	*Bombina variegata*	ZMH A11873	37	µCT	0.67
Bufonidae	*Bufo bufo*	TK Bufo01	N/A	µCT & SEM	0.73
Ceratophryidae	*Ceratophrys ornata*	ZMH A11916	59	SEM	–
Ceratophryidae	*Ceratophrys ornata*	ZMH A119176	70	µCT & SEM	0.87
Dendrobatidae	*Oophaga histrionica*	ZMH A11874	29	µCT	0.87
Dendrobatidae	*Oophaga histrionica*	ZMH A11875	32	SEM	–
Hylidae	*Litoria caerulea*	TK Litoria01	68	µCT& SEM	0.53
Hylidae	*Litoria infrafrenata*	ZMH A11870	75	µCT & SEM	0.87
Megophryidae	*Megophrys nasuta*	ZMH A11865	71	SEM	–
Megophryidae	*Megophrys nasuta*	ZMH A11866	103	µCT	0.87
Megophryidae	*Megophrys nasuta*	ZMH A11868	68	µCT	0.67
Ranidae	*Rana* (*Lithobates*) *pipiens*	TK Rana01	N/A	µCT	1.13
Ranidae	*Rana* (*Lithobates*) *pipiens*	TK Rana01	N/A	SEM	–

We examined the surface structures of frog tongues by using scanning electron microscopy (SEM). For SEM we prepared pieces from the central regions of the tongues. These pieces were first dehydrated in an ascending series of ethanol (70%, 90%, 100%; each step was maintained for 24 h). For specimens that were also used for micro-computed tomography prior to SEM (see Table 9.1), two additional dehydration steps (30% and 50%) were necessary, as the micro-CT imaging was performed in distilled water. After dehydration, the tongue specimens were critical point dried with a Quorum E3000 critical point drying system (Lewes, UK). Then the tongue specimens were mounted with the dorsal side facing upwards onto aluminum stubs using carbon-containing double-sided adhesive tape. The specimens were then coated with a 10 nm gold–palladium layer by using a Leica SCD05 Sputter Coater (Leica Microsystems GmbH, Wetzlar, Germany). For scanning electron microscopy, we used a Hitachi S-4800 scanning electron microscope at an accelerating voltage of 3 kV (Hitachi High-Technologies Europe GmbH, Krefeld, Germany).

We used micro-computed tomography (micro-CT or µCT) to study the three-dimensional arrangement of tissues underneath the tongue surface. To visualize soft tissue structures, such as the epithelium and muscle fibers, we stained the frogs with 4% Lugol's iodine potassium iodide solution before we dissected the tongues. For this purpose, we followed the protocol by Metscher (2009) but adjusted the staining duration to 2 weeks to allow the staining solution to diffuse deep into entire frog specimens. After staining, we dissected the tongues and cut out pieces that were approximately 1.5 mm × 1.5 mm × 2 mm (length × width × height) from the dorsal surface in central regions of the tongue. These pieces were then placed into the tips

of pipettes that we filled with distilled water. To prevent leakage during the scan, we wrapped the pipette tips with laboratory film (Parafilm M®, Bemis Company Inc., Oshkosh, WI, USA). We then mounted the pipette tips with the tongue specimens into a Skyscan 1172 desktop micro-CT scanner (Bruker microCT, Kontich, Belgium). We operated the micro-CT scanner with a source voltage of 40 kV and a current of 250 μA. The small size of the specimens allowed us to fit the pieces of tongue tissue into a very narrow field of view (<2 mm) during the scan, which corresponds to the maximal magnification of the Skyscan 1172 and resulted in voxel sizes of less than 1 μm (Table 9.1). From the X-ray images, captured during micro-CT scanning, we reconstructed image stacks of virtual cross-sections through the entire specimen with the software NRecon (Bruker microCT, Kontich, Belgium). These image stacks were then exported as 16 bit TIFF files, which we analyzed and visualized with the 3D visualization software package Amira 6.0 (FEI SAS, Mérignac Cedex, France). The micro-CT data of the *Ceratophrys ornata* specimen was already used in a previous study (Kleinteich and Gorb 2015) and is accessible at http://dx.doi.org/10.5061/dryad.066mr.

9.3   Results

9.3.1   Tongue Surface Structures

Two types of papillae cover the dorsal surface of frog tongues: numerous filiform papillae build a matrix in that the larger fungiform papillae are embedded (Fig. 9.1). We observed notable interspecific differences in the size and shape of these papillae. The fungiform papillae have roughly the same diameter of 70–90 μm in the *Bombina variegata, Discoglossus pictus, Ceratophrys ornata, Litoria* spp. (Fig. 9.1A–D), and *Bufo bufo* (Fig. 9.1G) specimens examined (Table 9.2). However, in *Megophrys nasuta* (Fig. 9.1E) and *Rana (Lithobates) pipiens* (Fig. 9.1F), the fungiform papillae appear larger than in the remainder species. In *Oophaga histrionica*, the fungiform papillae are smaller (Fig. 9.1H; Table 9.2).

The filiform papillae appear as rod-like protrusions with a diameter of approximately 7 μm in *Bombina variegata, Discoglossus pictus,* and *Oophaga histrionica*. In *Ceratophrys ornata*, the filiform papillae also appear rod-like, but with a thicker diameter of 20 μm and a lower aspect ratio (Fig. 9.1C). In *Megophrys nasuta, Rana (Lithobates) pipiens,* and *Bufo bufo,* the filiform papillae are thicker than in the remainder species, and clutches of filiform papillae form ridge-like structures (Fig. 9.1E–G). In *Litoria* spp., unlike any other species studied herein, the filiform papillae were found to be elongated and hair-like (Fig. 9.1D). The terminal parts of the filiform papillae in frog tongues have a rounded shape except for *M. nasuta,* in which the filiform papillae have flat tips (Fig. 9.1E).

Further we found interspecific variation in the surface patterns of the filiform papillae (Fig. 9.2). In *Megophrys nasuta*, the tips of the filiform papillae are covered by hair-like protrusions, which were approximately 80 nm in diameter (Fig. 9.2E).
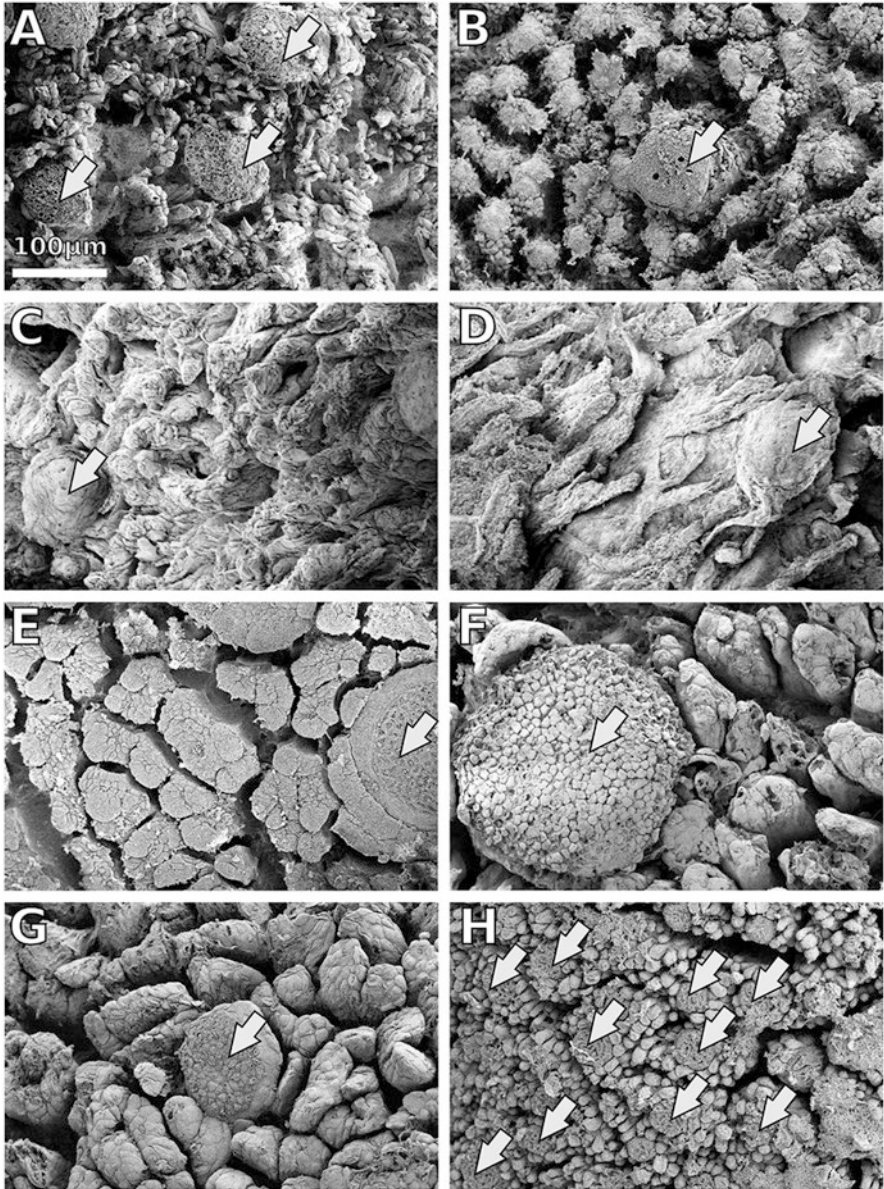
Fig. 9.1 Scanning electron microscopy of frog tongue surfaces. All images are at the same scale. (**A**) *Bombina variegata*, (**B**) *Discoglossus pictus*, (**C**) *Ceratophrys ornata*, (**D**) *Litoria infrafrenata*, (**E**) *Megophrys nasuta*, (**F**) *Rana (Lithobates) pipiens*, (**G**) *Bufo bufo*, (**H**) *Oophaga histrionica*. Frog tongue surfaces are covered by fungiform papillae (arrows), which are embedded in a matrix of smaller filiform papillae. The examined species differ notably in the size and the shape of the papillary surface structures

Table 9.2 Measurements of tongue papillae in micrometers based on Fig. 9.1

	Bombina variegata	Disco-glossus pictus	Cerato-phrys ornata	Litoria infra-frenata	Mego-phrys nasuta	Rana (Lithobates) pipiens	Bufo bufo	Oophaga histrio-nica
Fungiform papillae	62.87	79.72	78.24	85.27	125.00	216.15	87.69	30.29
	69.98	–	78.19	81.73	–	–	–	29.34
	67.73	–	–	–	–	–	–	27.55
Average	66.86	79.72	78.22	83.50	125.00	216.15	87.69	29.06
Filiform papillae	8.46	5.47	21.39	16.47	19.86	52.19	32.56	8.99
	6.02	6.02	19.19	17.46	21.08	51.77	34.04	9.64
	7.00	8.77	23.93	19.28	25.41	51.47	34.88	8.19
	7.09	7.14	19.88	13.58	18.27	43.50	35.03	8.25
	6.60	6.34	14,89	12.71	20.91	53.93	32.00	8.01
	5.94	7.21	22.33	11.38	20.86	38.35	21.07	7.96
Average	6.85	6.38	20.19	15.15	21.07	48.54	33.26	8.51

In *Rana (Lithobates) pipiens*, hair-like protrusions are also present on the filiform papillae. However, these structures in *R. pipiens* are much larger compared to *M. nasuta* and appear only in patches (Fig. 9.2F). The filiform papillae in *Bufo bufo* and *Oophaga histrionic*a differ from the remainding species examined by being covered with nanoscale surface ridges (Fig. 9.2G, H). In *Bombina variegata, Discoglossus pictus, Ceratophrys ornata,* and *Litoria* spp., no notable surface structures could be observed. The surfaces of the filiform papillae in these species appear irregularly shaped (Fig. 9.2A–D).

9.3.2   Three-Dimensional Organization of the Tongue Tissue

Contrast enhanced high-resolution micro-CT imaging allowed us to visualize the three-dimensional organization of subsurface soft tissue structures in frog tongues (Figs. 9.3 and 9.4). The resulting voxel sizes for the micro-CT datasets ranged from 0.53 μm to 1.13 μm (Table 9.1). With this spatial resolution, we were able to identify structures in the micrometer scale, such as the filiform and fungiform papillae (Fig. 9.3). In *Oophaga histrionica*, however, the spatial resolution of the micro-CT dataset was not sufficient to discriminate between the two types of surface papillae (Fig. 9.3H).

Underneath the surface papillae, we found a layer of lacunar structures that in the micro-CT data appear to be almost hollow inside (Fig. 9.4). In *Bombina variegata, Discoglossus pictus, Litoria* spp., and *Rana (Lithobates) pipiens*, these lacunae are elongated and of cylindrical shape. Muscle fibers of the tongue musculature emerge between these cylinders towards the tongue surface (Fig. 9.4). In *Megophrys nasuta*
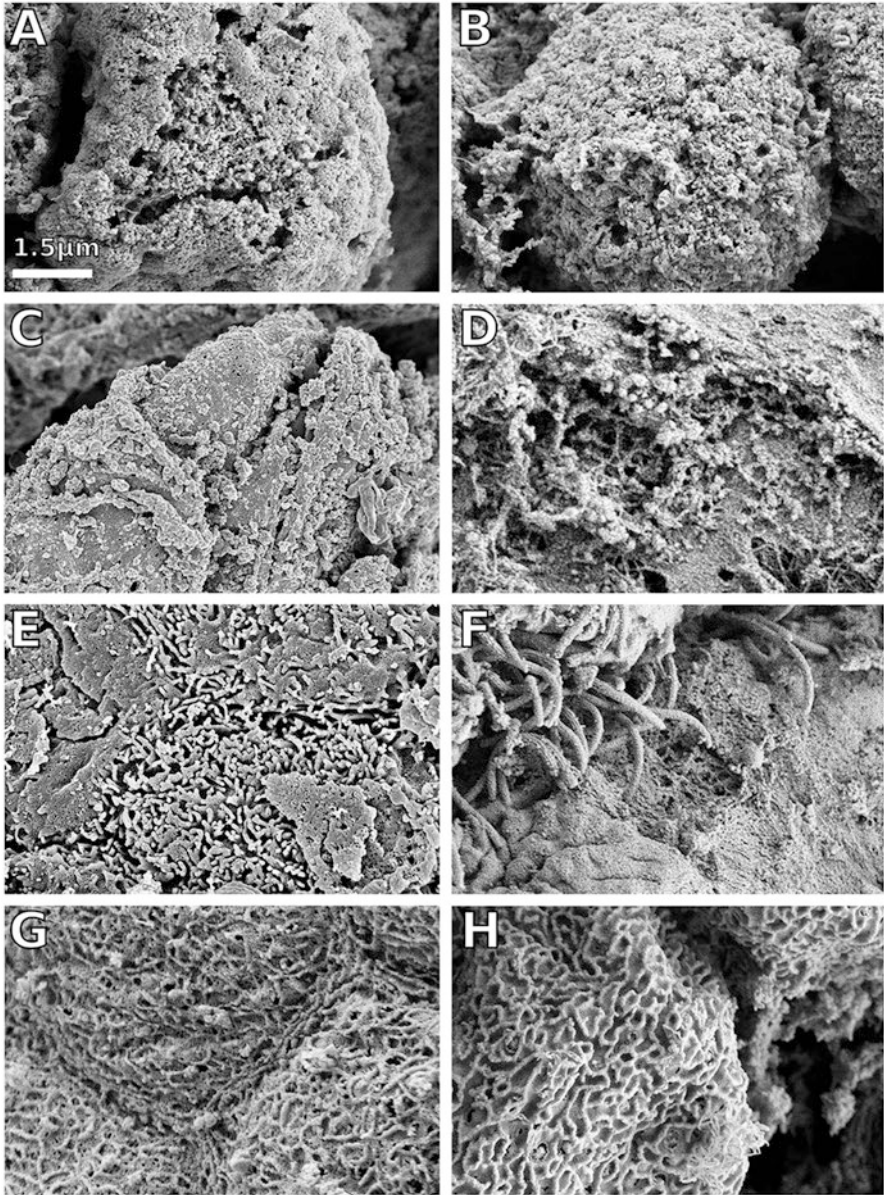
Fig. 9.2 Scanning electron microscopy of the filiform papillae on frog tongues. All images are at the same scale. (**A**) *Bombina variegata*, (**B**) *Discoglossus pictus*, (**C**) *Ceratophrys ornata*, (**D**) *Litoria infrafrenata*, (**E**) *Megophrys nasuta*, (**F**) *Rana (Lithobates) pipiens*, (**G**) *Bufo bufo*, (**H**) *Oophaga histrionica*. The filiform papillae show a remarkable degree of interspecific variation. In *M. nasuta* (**E**) and *R. pipiens* (**F**), we found hair-like outgrowths on the filiform papillae; in *B. bufo* (**G**) and *O. histrionica* (**F**), the filiform papillae are covered by micro-ridges
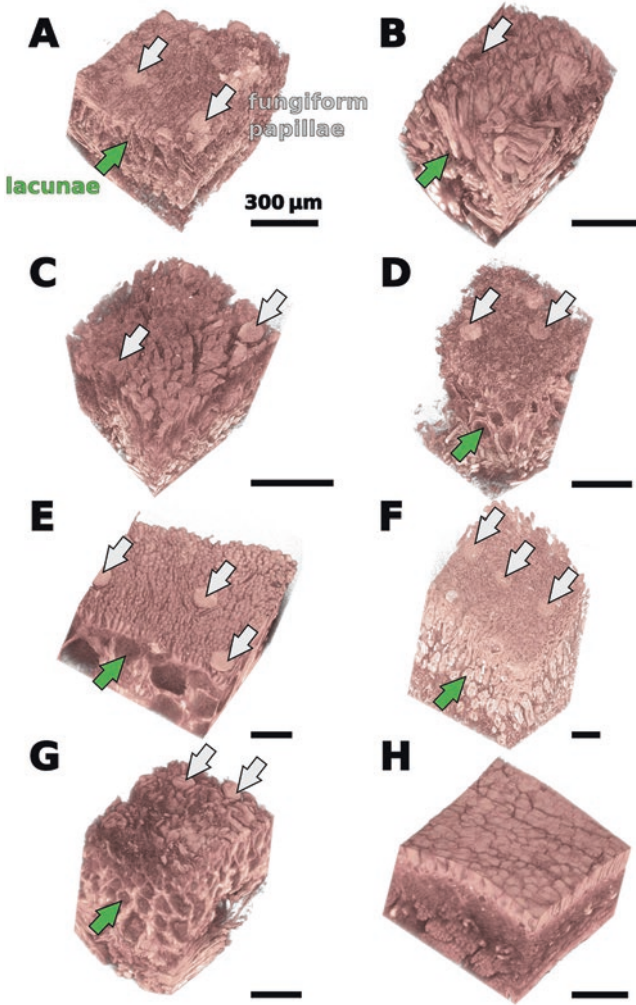
Fig. 9.3 Micro-CT images of tissue fragments that were derived from the surfaces of frog tongues. (**A**) *Bombina variegata*, (**B**) *Discoglossus pictus*, (**C**) *Ceratophrys ornata*, (**D**) *Litoria infrafrenata*, (**E**) *Megophrys nasuta*, (**F**) *Rana (Lithobates) pipiens*, (**G**) *Bufo bufo*, (**H**) *Oophaga histrionica*. Except for *C. ornata* (**C**) and *O. histrionica* (**H**), the fungiform papillae (grey arrows) can easily be identified in the micro-CT data. Underneath the papillary surface structures lies a layer with lacunar structures that appear hollow in the micro-CT scan (green arrows). Both size and shape of these lacunae strongly vary among different species

and *Bufo bufo*, the lacunar structures appear to be more spherical than in *B. variegata, D. pictus, Litoria* spp., and *R. pipiens*. Further, in *M. nasuta*, the lacunae are stacked in two, in *B. bufo* even in up to four layers. In the *Ceratophrys ornata* specimen, the layer underneath the surface papillae was only poorly stained in the micro-CT scan and lacunae are not visible. However, in a deeper layer, spherical structures

Fig. 9.4 Virtual section through the micro-CT data of tongue tissue fragments at the level of the lacunar layer. (**A**) *Bombina variegata*, (**B**) *Discoglossus pictus*, (**C**) *Ceratophrys ornata*, (**D**) *Litoria infrafrenata*, (**E**) *Megophrys nasuta*, (**F**) *Rana (Lithobates) pipiens*, (**G**) *Bufo bufo*, (**H**) *Oophaga histrionica*. In *B. variegata* (**A**), *D. pictus* (**B**), and *L. infrafrenata* (**D**), the lacunae seem to be more similar than in the remainder species. In *C. ornata* (**C**) and *O. histrionica* (**H**), we were not able to find lacunae by using micro-CT imaging. Muscle fibers (red arrows) emerge between the lacunae and face towards the tongue surface
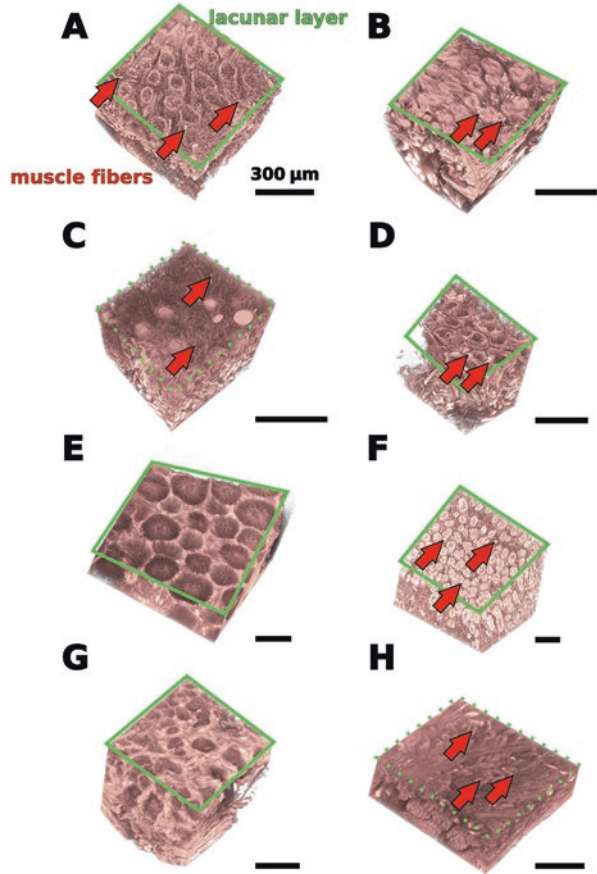
can be seen that differ from the hollow lacunae in the remainder species and show a strong X-ray absorption contrast (Fig. 9.4C). Muscle fibers run in-between these spherical structures towards the dorsal surface of the tongue in *C. ornata*. In *Oophaga histrionica*, we were not able to identify lacunae underneath the surface papillae by using micro-CT imaging. Underneath the layer consisting of lacunar, respectively spherical structures in the case of *Ceratophrys ornata*, bundles of tongue muscle fibers are arranged parallel and perpendicular to the tongue surface. In *Oophaga histrionica*, the fibers of the tongue musculature appear to run directly underneath the surface papillae of the tongue (Fig. 9.4H).

9.4   Discussion

Here we demonstrate a high degree of interspecific variation in the surface anatomy of frog tongues. Differences can be seen in the arrangement of tissue layers close to the tongue surface and in the density, shape, and surface profiles of the filiform

papillae. Although we lack experimental data on tongue performance for most of the species discussed herein, we hypothesize that these differences are likely to have effects on the adhesive and frictional properties of the tongues in frogs.

Especially the numerous filiform papillae may play a key-role in tongue adhesion besides their function in mucus production. The papillae themselves deform under compression and thus help to make the tongue adaptable to surface asperities of the prey item. In *Megophrys nasuta* and *Rana (Lithobates) pipiens*, where we found hair-like structures on top of the filiform papillae, this second level of hierarchical organization is hypothesized to increase the adaptability of the tongue under load. The micro-ridges on the filiform papillae in *Bufo bufo* and *Oophaga histrionica* and the irregular surface structures in *Bombina variegata, Discoglossus pictus, Ceratophrys ornata,* and *Litoria* spp. probably will not deform as much under compression as the hair-like structures in *M. nasuta* and *R. pipiens*. Thus, in *B. variegata, D. pictus, C. ornata,* and *Litoria* spp., the adaptability of the tongue to surface asperities of the prey will only depend on the filiform papillae themselves.

It seems reasonable to assume that species that form and maintain a better contact with the prey surface are more likely to generate high adhesive forces during tongue feeding. Other than for *Ceratophrys* sp. (Kleinteich and Gorb 2014), we have no force data on tongue adhesion available at this time. However, another measure for tongue adhesive performance might be the sizes of typical prey items as these are captured with the tongues. *Bufo bufo* and *Oophaga histrionica* are known to feed on relatively small prey, such as ants (Emerson 1985; Santana and Juncá 2007; Wells 2010; Crnobrnja-Isailović et al. 2012), while *M. nasuta* and *R. pipiens* are considered to be generalist feeders capturing a wide variety of prey items of different sizes and even preying upon small vertebrates (Wells 2010). This picture, however, becomes much more complicated if one also considers the other species examined herein. Especially frogs within the genus *Ceratophrys* are known to be voracious generalist feeders (Parsons 1932; Duellman and Lizana 1994; Silva et al. 2014; Kleinteich 2015) and their tongues can produce notable adhesive forces (Kleinteich and Gorb 2014). However, the *C. ornata* examined in the work described herein lacks hair-like outgrowths on its filiform papillae and, therefore, its tongue might be less adaptable to the prey surface than those of *M. nasuta* or *R. pipiens*.

We previously argued that the filiform papillae also interact with the mucus covering the tongues in live frogs (Kleinteich and Gorb 2015) (see also Sperry and Wassersug (1976)). Frog tongues might thus be considered as composite structures of mucus plus papillae. The size, aspect ratio, and distribution of the papillae will have an impact on how this composite is stabilized. Denser arrays of surface papillae are likely to improve the cohesion within the mucus-papillae composite, and thus prevent failure of the mucus layer during tongue retraction. It is plausible to assume that different species have different physical (rheological) properties of the mucus, and that these properties are correlated with a particular microstructure of the tongue or vice versa. The viscosity of the mucus is critical for attachment especially given the short time frames between tongue impact and retraction, which happens within milliseconds (Deban and Nishikawa 1992; Nishikawa and Gans 1996; Nishikawa 2000; Kleinteich and Gorb 2014). The rapidness with which mucus can wet a target surface will decrease with increasing viscosity. Denser

arrays of filiform papillae might allow for less viscose mucus that is still stable enough to withstand the tongue pulling forces. Based on the size of the filiform papillae (Fig. 9.1), we would therefore expect for our specimen sample that *Oophaga histrionica* has the least viscous mucus, while *Bufo bufo, Rana (Lithobates) pipiens,* and *Megophrys nasuta* are predicted to have the most viscous mucus. This hypothesis, however, remains to be tested in future studies.

Besides the profile of the surface, also the composition of the underlying tissues will have an impact on the adhesive performance of the tongue. Such a role of deeper tissue layers, which influence the compliance of the adhesive structure, has recently been shown for the feet of grasshoppers (Perez Goodwyn et al. 2006) and geckos (Gilman et al. 2015). Although we did not measure the material attributes herein, the architecture of the subsurface layers might suggest the presence of a material gradient in frog tongues as well. It seems reasonable to assume that the mucus coverage on the tongue surface is more compliant than the filiform papillae themselves, which are in turn more flexible than the lacunar subsurface layer. The muscle fibers underneath the lacunar layer supposedly have even higher stiffness than the lacunar layer. Such material gradients can be beneficial for adhesion as they will allow for a high adaptability to a target surface profile, while maintaining mechanical stability (Peisker et al. 2013; Gorb and Filippov 2014) and integrity of layered tissues.

The lacunar subsurface layer that we describe herein for frog tongues is very similar in the three species that use mechanical pulling for feeding (as defined by Nishikawa (2000)), i.e., *Bombina variegata, Discoglossus pictus,* and *Litoria* spp. but very diverse in the remainder species that use tongue projection. During mechanical pulling, the tongue deforms by action of the tongue musculature and is slightly protracted over the tip of the lower jaw (Deban and Nishikawa 1992; Nishikawa 2000). However, other than during tongue projection, the tongue is not passively elongated by inertia. A more complete taxon sampling and evaluation of the physical properties of the lacunar layer in different frog tongues are needed to test if there is a mechanical benefit of cylindrical lacunae for mechanical pulling.

Further, it is important to keep in mind the limitations of micro-CT imaging here. The voxel sizes of the tongue surface scans were less than one micrometer. However, to visualize structures, several connected voxels are needed. Thus the spatial resolution of our approach is more likely in the range of three to four micrometers. Structures that are in the sub-micrometer range, such as the hair-like extrusions on top of the filiform papillae in *Megophrys nasuta*, therefore cannot be detected with the micro-CT. The absence of lacunae in *Ceratophrys ornate* and *Oophaga histrionica*, might be an artifact that is caused by a limited spatial resolution of our micro-CT setup. Further, although the lacunae generally appear hollow in the micro-CT scans, they might be filled with structures that could either be too thin to be detected with the micro-CT that are X-ray transparent, or that cannot be stained by LUGOL's solution. For *Pelophylax porosus*, a close relative to *Rana (Lithobates) pipiens,* Iwasaki et al. (1998) prepared histological sections of the tongue and according to Fig. 9.1 in their publication, the small lacunar structures in *L. pipiens* we describe herein relate to alveolar salivary glands. For *C. ornata*, we prepared fractured pieces of a critical point dried tongue and examined them with the SEM and also did not

find lacunar spaces (Kleinteich and Gorb 2015). Future studies on the comparative histology of frog tongues will shed more light into this variation of the tongue at the microscopic level. The benefit of micro-CT imaging, however, is the immediate availability of the three-dimensional architecture of the investigated structures, which cannot be provided with other methods.

Despite the adhesive and frictional properties, also evolutionary relationships between the species examined might provide explanations for the interspecific variation we found herein. The tongues in *Discoglossus pictus* and *Bombina variegata* are rather similar, if compared to the remainder species examined herein. The two taxa, to which *D. pictus* and *B. variegata* belong to, i.e., the Alytidae and Bombinatoridae are widely considered as sister groups within anuran phylogeny (Frost et al. 2006; Roelants et al. 2007; Pyron and Wiens 2011). Furthermore, *Bufo bufo* (Bufonidae) and *Oophaga histrionica* (Dendrobatidae) are closely related as the Bufonidae were either found to be the sister taxon to the Dendrobatidae (Roelants et al. 2007; Pyron and Wiens 2011) or to the Dendrobatidae plus species within the genus *Thoropa* (Frost et al. 2006). The micro-ridges on the surface of the filiform papillae in *B. bufo* and *O. histrionica* are thus likely to be homologous and might represent a synapomorphy of the Bufonidae and Dendrobatidae. Similar ridges were previously described for a second species within the Bufonidae, i.e., *Bufo japonicus* (Iwasaki and Kobayashi 1988).

However, besides the presence of micro-ridges on the surface of the filiform papillae, the tongues in *Bufo bufo* and *Oophaga histrionica* differ notably in their arrangement of the surface papillae and their three-dimensional organization. While the presence of micro-ridges in these two species might be explained by a close phylogenetic relationship of the Bufonidae and Dendrobatidae, the variation found in the shape and arrangement of the surface papillae and tongue tissue layers in these two species seems to be manifested at a smaller taxonomic scale. Further, the tongues of *Megophrys nasuta, Rana (Lithobates) pipiens, Litoria* spp., and *Ceratophrys ornata* all have unique characters, such as the hair-like protrusions on the flat tips of the filiform papillae in *M. nasuta*, the patches of hairs on the filiform papillae in *R. pipiens*, the shape of the filiform papillae in *Litoria* spp. and the presence of X-ray dense spherical subsurface structures in *C. ornata*. Our taxon sampling herein proves insufficient to trace these unique tongue characteristics through anuran phylogeny. Many questions regarding the evolutionary and functional implications of this structural diversity remain and certainly inspire future research endeavors.

References

AmphibiaWeb. http://www.amphibiaweb.org. Accessed 2 Mar 2016.

Barnes, W. J. P., Baum, M., Peisker, H., & Gorb, S. N. (2013). Comparative Cryo-SEM and AFM studies of hylid and rhacophorid tree frog toe pads. *Journal of Morphology, 274*, 1384–1396.

Crnobrnja-Isailović, J., Ćurčić, S., Stojadinović, D., Tomašević-Kolarov, N., Aleksić, I., & Tomanović, Ž. (2012). Diet composition and food preferences in adult common toads (*Bufo bufo*) (Amphibia: Anura: Bufonidae). *Journal of Herpetology, 46*, 562–567.

Deban, S. M., & Nishikawa, K. C. (1992). The kinematics of prey capture and the mechanism of tongue protraction in the Green Tree Frog *Hyla cinerea*. *The Journal of Experimental Biology, 170*, 235–256.

Duellman, W. E., & Lizana, M. (1994). Biology of a sit-and-wait predator, the leptodactylid frog *Ceratophrys cornuta*. *Herpetologica, 50*, 51–64.

Elsheikh, E. H., Atta, K. E., & Al-Zahaby, S. A. (2013). Comparative study on the tongue of *Bufo regularis* and *Chalcides ocellatus* in relation to their habitats. *The Journal of Basic & Applied Zoology, 66*, 131–138.

Emerson, S. B. (1977). Movement of the hyoid in frogs during feeding. *The American Journal of Anatomy, 149*, 115–120.

Emerson, S. B. (1985). Skull shape in frogs: Correlations with diet. *Herpetologica, 41*, 177–188.

Eşrefoğlu, M., Temelli, A., & Eşrefoğlu, M. (2000). Fine structure of the dorsal lingual epithelium of the frog, *Rana ridibunda*. *Journal of Inonu University Medical Faculty, 7*, 67–72.

Frost, D. R., Grant, T., Faivovich, J., Bain, R. H., Haas, A., Haddad, C. F. B., de Sá, R. O., Channing, A., Wilkinson, M., Donnellan, S. C., Raxworthy, C. J., Campbell, J. A., Blotto, B. L., Moler, P., Drewes, R. C., Nussbaum, R. A., Lynch, J. D., Green, D. M., & Wheeler, W. C. (2006). The amphibian tree of life. *Bulletin of the American Museum of Natural History, 297*, 1–370.

Gans, C., & Gorniak, G. C. (1982a). Functional morphology of lingual protrusion in marine toads (*Bufo marinus*). *The American Journal of Anatomy, 163*, 195–222.

Gans, C., & Gorniak, G. C. (1982b). How does the toad flip its tongue? Test of two hypotheses. *Science, 216*, 1335–1337.

Gilman, C. A., Imburgia, M. J., Bartlett, M. D., King, D. R., Crosby, A. J., & Irschick, D. J. (2015). Geckos as springs: Mechanics explains across-species scaling of adhesion. *PLoS One, 10*, e0134604.

Gorb, S. N., & Filippov, A. E. (2014). Fibrillar adhesion with no clusterisation: Functional significance of material gradient along adhesive setae of insects. *Beilstein Journal of Nanotechnology, 5*, 837–845.

Guiraldelli, M. F., Lopes, R. A., Sala, M. A., & Lopes, T. R. V. P. (2011). Morphological, morphometrical and histochemical study of the lining and glandular epithelia of the tongue of the bullfrog *Rana catesbeiana*. *International Journal of Morphology, 29*, 226–233.

Helff, O., & Mellicker, M. (1941a). Studies on amphibian metamorphosis. XIX. Development of the tongue in *Rana sylvatica*, including the histogenesis of "premetamorphic" and filiform papillae and the mucous glands. *The American Journal of Anatomy, 68*, 339–369.

Helff, O. M., & Mellicker, M. C. (1941b). Studies on amphibian metamorphosis. XX. Development of the fungiform papillae of the tongue in *Rana sylvatica*. *The American Journal of Anatomy, 68*, 371–395.

Iwasaki, S. (2002). Evolution of the structure and function of the vertebrate tongue. *Journal of Anatomy, 201*, 1–13.

Iwasaki, S., & Kobayashi, K. (1988). Fine structure of the dorsal tongue surface in the japanese toad, *Bufo japonicus* (Anura, Bufonidae). *Zoological Science, 5*, 331–336.

Iwasaki, S., & Wanichanon, C. (1991). Fine structure of the dorsal lingual epithelium of the frog, *Rana rugosa*. *Tissue and Cell, 23*, 385–391.

Iwasaki, S., & Wanichanon, C. (1993). An ultrastructural study of the dorsal lingual epithelium of the crab-eating frog, *Rana cancrivora*. *Journal of Morphology, 215*, 89–100.

Iwasaki, S., Miyata, K., & Kobayashi, K. (1989). Fine structure of the lingual dorsal epithelium of the japanese toad, *Bufo japonicus* (Anura: Bufonidae). *Zoological Science, 6*, 681–689.

Iwasaki, S., Iwabuchi, Y., & Asami, T. (1997). Histological and ultrastructural study of the effects of cholinergic and adrenergic agonists on salivary secretion from the lingual epithelium and the lingual gland of the Tokyo Daruma pond frog. *Tissue and Cell, 29*, 323–338.

Iwasaki, S., Iwabuchi, Y., & Okumura, Y. (1998). Histological and ultrastructural studies of the effects of tachykinins on protein secretion from the lingual epithelium and the lingual gland of the Tokyo daruma pond frog (*Rana porosa poros*a). *Archives of Oral Biology, 43*, 463–471.

Jaeger, C. B., & Hillman, D. E. (1976). Morphology of gustatory organs. In R. Llinás & W. Precht (Eds.), *Frog neurobiology* (pp. 588–606). Heidelberg: Springer.

Kleinteich, T. (2015). To have a frog in the throat: Micro-CT imaging of anuran prey in *Ceratophrys ornata* (Anura: Ceratophryidae). *Salamandra, 51*, 209–211.

Kleinteich, T., & Gorb, S. N. (2014). Tongue adhesion in the horned frog *Ceratophrys* sp. *Scientific Reports, 4*, 5225.

Kleinteich, T., & Gorb, S. N. (2015). Frog tongue acts as muscle-powered adhesive tape. *Royal Society Open Science, 2*, 150333.

Kleinteich, T., & Gorb, S. N. (2016). Frog tongue surface microstructures: Functional and evolutionary patterns. *Beilstein Journal of Nanotechnology, 7*, 893–903.

Metscher, B. D. (2009). MicroCT for comparative morphology: Simple staining methods allow high-contrast 3D imaging of diverse non-mineralized animal tissues. *BMC Physiology, 9*, 11.

Nishikawa, K. C. (2000). Feeding in frogs. In K. Schwenk (Ed.), *Feeding: Form, function, and evolution in tetrapod vertebrates* (pp. 117–147). London: Academic Press.

Nishikawa, K. C., & Gans, C. (1996). Mechanisms of tongue protraction and narial closure in the marine toad *Bufo marinus*. *The Journal of Experimental Biology, 199*, 2511–2529.

Ojima, K., Takeda, M., Saiki, C., Takahashi, T., & Matsumoto, S. (1997). Angioarchitectural classification of the fungiform papillae on the dorsal surface of the bullfrog tongue. *Annals of Anatomy – Anatomischer Anzeiger, 179*, 393–397.

Osculati, F., & Sbarbati, A. (1995). The frog taste disc: A prototype of the vertebrate gustatory organ. *Progress in Neurobiology, 46*, 351–399.

Parsons, C. W. (1932). Habits of the toad, *Ceratophrys*. *Nature, 130*, 279–279.

Peisker, H., Michels, J., & Gorb, S. N. (2013). Evidence for a material gradient in the adhesive tarsal setae of the ladybird beetle *Coccinella septempunctata*. *Nature Communications, 4*, 1661.

Perez Goodwyn, P., Peressadko, A., Schwarz, H., Kastner, V., & Gorb, S. (2006). Material structure, stiffness, and adhesion: Why attachment pads of the grasshopper (*Tettigonia viridissima*) adhere more strongly than those of the locust (*Locusta migratoria*) (Insecta: Orthoptera). *Journal of Comparative Physiology. A, 192*, 1233–1243.

Pyron, R. A., & Wiens, J. J. (2011). A large-scale phylogeny of Amphibia including over 2800 species, and a revised classification of extant frogs, salamanders, and caecilians. *Molecular Phylogenetics and Evolution, 61*, 543–583.

Regal, P. J., & Gans, C. (1976). Functional aspects of the evolution of frog tongues. *Evolution, 30*, 718–734.

Ritter, D., & Nishikawa, K. C. (1995). The kinematics and mechanism of prey capture in the African pig-nosed frog (*Hemisus marmoratum*): Description of a radically divergent anuran tongue. *The Journal of Experimental Biology, 198*, 2025–2040.

Roelants, K., Gower, D. J., Wilkinson, M., Loader, S. P., Biju, S. D., Guillaume, K., Moriau, L., & Bossuyt, F. (2007). Global patterns of diversification in the history of modern amphibians. *Proceedings of the National Academy of Sciences of the United States of America, 104*, 887–892.

Santana, A. S., & Juncá, F. A. (2007). Diet of *Physalaemus cf. cicada* (Leptodactylidae) and *Bufo granulosus* (Bufonidae) in a semideciduous forest. *Brazilian Journal of Biology, 67*, 125–131.

Silva, N. R., Souza, P. R., Gonçalves, M. F., Demétrio, M. F., & Prado, C. P. A. (2014). A voracious female during the courtship of *Ceratophrys cranwelli* (Anura: Ceratophryidae) in the Brazilian Chaco. *Herpetology Notes, 7*, 93–95.

Sperry, D. G., & Wassersug, R. J. (1976). A proposed function for microridges on epithelial cells. *The Anatomical Record, 185*, 253–257.

Stensaas, L. J. (1971). The fine structure of fungiform papillae and epithelium of the tongue of a South American toad, *Calyptocephalella gayi*. *The American Journal of Anatomy, 131*, 443–461.

Wells, K. D. (2010). *The ecology and behavior of amphibians* (1400 p). Chicago: University of Chicago Press.

Part V
Friction

Chapter 10
Mucus Matters: The Slippery and Complex Surfaces of Fish

Dylan K. Wainwright and George V. Lauder

Abstract Teleost scales are extremely diverse in morphology, with different categories (cycloid, crenate, spinoid, ctenoid) once used to define major groups of fish. We describe these different classical categories of scales and discuss the structure and potential function of small features of scale morphology such as spines, ctenii, radii, and circuli. Modern techniques now make analysis of scale morphology using three-dimensional quantitative data possible. This ability is crucial because many of the hydrodynamic and protective hypotheses concerning the function of scales are dependent on three-dimensional structure. We discuss different techniques to investigate and image the structure of fish scales and skin, and we highlight gel-based surface profilometry as a new valuable tool for studying fish skin. In addition to bony scales, fish skin is also covered by an epidermis that secretes mucus that can coat the exterior of scales. Fish scales are often studied in isolation with the epidermis removed; here we present topographic, three-dimensional, analyses of fish skin surfaces from seven species with the mucus, epidermis, and relative positions of scales intact. We compare these images qualitatively and quantitatively to the same individuals with the epidermis and mucus removed to show a previously unexplored axis of diversity in fish: how mucus and epidermis interact with scale morphology to create surface texture. The three-dimensional structure of fish skin has important implications for hydrodynamic function during locomotion, but this remains a largely unexplored area.

10.1 Introduction – Fish Surfaces

Fish skin is generally similar to the skin of other vertebrates, with a few important distinctions. Like other vertebrates, fish have an epidermis as their outermost dermal layer and a dermis beneath that, but fish skin is distinguished by the presence of two

D. K. Wainwright (✉) · G. V. Lauder
Department of Organismic and Evolutionary Biology, Harvard University,
Cambridge, MA, USA
e-mail: dylanwainwright@fas.harvard.edu

important features – goblet cells full of mucus in the epidermis, and bony scales embedded in the dermis and epidermis (Hawkes 1974; Fast et al. 2002; Zaccone et al. 2001). Other vertebrates may have one of these features, such as bony scales in crocodiles and goblet cells in human mucus membranes, but never both together as in fishes. In teleosts, bony scales appear as overlapping, layered-bone plates embedded in the skin. In this chapter, we will focus on fish surfaces composed of elasmoid scales, thereby excluding both the ganoid scales of basal fish groups (gars and polypterids) and the placoid scales of sharks and rays (Meyer and Seegers 2012; Motta et al. 2012).

Scales likely serve a number of functions in fishes, including physical protection from predators and parasites, prevention of surface fouling, and modification of flow during swimming. However, scales are only a part of a fish's surface, and in fact, scales are not even the outermost part of the skin – instead, an epidermis covers scales and secretes a layer of mucus that covers fish (Fig. 10.1) (Whitear 1970). This layer of epidermis and mucus covers scales and is necessary for scale growth, regeneration, and maintenance (Bereiter-Hahn and Zylberberg 1993; Shephard 1994). The mucus layer is also known to be important for immune function in fishes (Shephard 1994; Rakers et al. 2010; Esteban 2012; Xu et al. 2013), and some authors have also suggested that mucus plays a role in modifying flow conditions around fish to increase swimming efficiency (Rosen and Cornford 1971; Daniel 1981; Bernadsky et al. 1993).

Fig. 10.1 Histological transverse cross-section of skin from a brook trout (*Salvelinus fontinalis*) showing epidermis with goblet cells, scales in scale pockets, and the underlying dermis and muscle. Stained with hematoxylin and eosin. Anterior is coming out of the page, posterior is going into the page. *d* dermis, *e* epidermis, *g* goblet cell, *ll* lateral line canal, *m* muscle, *s* scale. Scale bar: 100 μm

Together, the mucus layer, epidermis, and scales of a fish create the outermost barrier between a fish's body and the external fluid (Fig. 10.1). These tissues also combine to create the topographic texture of a fish's skin. For example, scales overlap in a pattern where the posterior of each scale is inclined towards the outside of the fish, with epidermis and mucus covering the surface of the scales. Scales, epidermis, and mucus interact to create surface topography on the outside of the fish, but the degree to which each of these tissues contributes to topography is unclear. Additionally, structures such as spines, ctenii, and circuli occur on fish scales and create texture on fish (these structures are further discussed below). Fish skin texture in various species has been hypothesized to create favorable flow conditions for swimming by reducing drag, increasing thrust, or increasing efficiency (Bone 1972; Burdak 1986; Liyan et al. 2017); however, these ideas have yet to be tested in a rigorous way. Many ideas about hydrodynamic functions of scales concern how structures on scales, such as spines, can influence the flow around the body of a fish in a favorable way (Burdak 1986; Sagong et al. 2008; Wainwright and Lauder 2016), but these ideas tend to neglect how the epidermis and mucus could also change the topography that the water encounters during swimming.

In this chapter, we will discuss both the diversity of fish scales and how different scale morphologies interact with epidermis and mucus. We will show how mucus changes the topography of fish scale surfaces in a variety of species and elaborate on what that might mean for hypotheses of fish scale function.

10.2   Fish Scales – Complex Surfaces

10.2.1   Scale Types: A Classification

Elasmoid scales of bony fish have three layers (external to internal: limiting layer, external layer, and elasmodine), but the bulk of their structure is elasmodine, a plywood-like structure of collagen fibers that mineralizes into acellular bone with development (Huysseune and Sire 1998; Sire and Huysseune 2003; Meunier 2011). Elasmoid scales are embedded in the epidermis of fishes and are often arranged in an overlapping pattern over the body and sometimes fins. Scales are sheathed in scale pockets, which are connective tissue wrappings that either completely or partially surround the scale (Fig. 10.1) (Bereiter-Hahn and Zylberberg 1993; Sire and Akimenko 2004). Scales grow with the fish – bony fish will replace scales if they fall off or are damaged, but fish do not typically increase the number of scales with growth (Taylor 1916; Thomson 1956; Casselman 1990). Although there is tremendous size diversity in fish scales, scales are routinely 2–15 mm in length, 0.1–2 mm in thickness, and features such as spines and ridges may be tens to hundreds of microns (many exceptions exist to these estimates) (Taylor 1916; Roberts 1993; Wainwright and Lauder 2016; Bergman et al. 2017; Wainwright et al. 2017).

Elasmoid scales of most teleosts have been categorized into different types according to their morphology, with the four main types being cycloid, crenate,
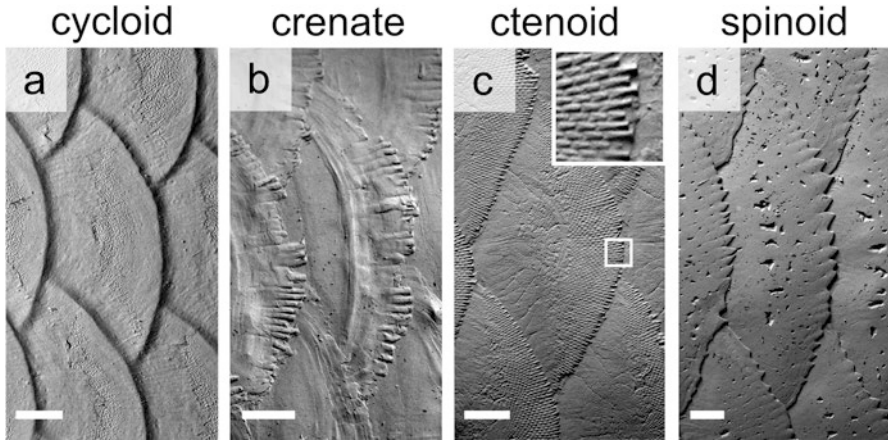
Fig. 10.2 Scale types of teleost fishes illustrated using gel-based profilometry. (**a**) Cycloid scales of bonefish (*Albula vulpes*) with smooth edges. (**b**) Crenate scales of Chacunda gizzard shad (*Anodontostoma chacunda*) with flat, finger-like projections at the posterior edge. (**c**) Ctenoid scales of blackspot sergeant (*Abudefduf sordidus*) with small interlocking spines, enlarged in inset. (**d**) Spinoid scales of sabre squirrelfish (*Sargocentron spiniferum*) with large, flattened, continuous spines. Scale bars: 1 mm
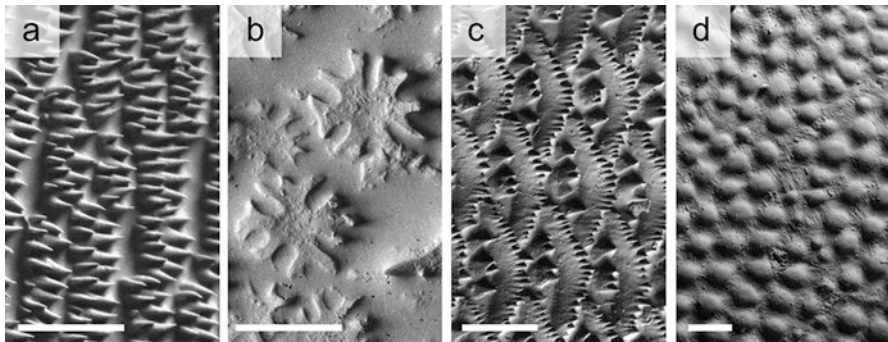
Fig. 10.3 Diversity of fish scales illustrated with gel-based profilometry. (**a**) Complex spiny scales of Moorish idol (*Zanclus cornutus*). (**b**) Oak-leaf-shaped scales of louvar (*Luvarus imperialis*). (**c**) Spiny scales of deepbody boarfish (*Antigonia capros*). (**d**) Interlocking plate-like bumpy scales of scrawled cowfish (*Acanthostracion quadricornis*). Scale bars: 1 mm

ctenoid, and spinoid (Roberts 1993). Figure 10.2 illustrates these four different categories of scales with typical examples of each category. Cycloid scales have smooth posterior edges, crenate scales have edges with flat, blunt projections, ctenoid scales have posterior edges made of separate ossified interlocking spines called ctenii (plural; Fig. 10.2c inset), and spinoid scales have spines that are continuous with the ossification of the scale itself (Roberts 1993).

As is often the case in biology, these classifications hold for large portions of diversity, but there are many exceptions. In Fig. 10.3, we show images of four dif-

ferent fish skin surfaces that illustrate some of the challenges to scale classification. In Fig. 10.3a, we show scales of the Moorish idol (*Zanclus cornuta*) that have many densely-packed spines. We would classify these scales as spinoid because they have spines that are continuous with the ossification of the scale plate themselves, but these look markedly different from the spinoid scales in Fig. 10.2d. Similarly, Fig. 10.3c shows spinoid scales from the boarfish (*Antigonia capros*), which have both spines on the posterior margin of the scale and on the body of the scale. Figure 10.3a, c illustrate how diverse spinoid scales are – so diverse that the classification of spinoid seems to be too broad to have much meaning. C. Roberts (Roberts 1993) remedied this by further classifying scales into subtypes within the different categories, especially in the case of spinoid and ctenoid scales. However, this author also acknowledged how little we know about the evolution and development of different scale types – both of which are relevant to making meaningful categorizations. We also know little about how scale morphology correlates with function, which would inform categorization based not only on morphology, but also on the relationship between morphology and function.

Figure 10.3b shows the bizarre, leaf-shaped scales of a juvenile louvar (*Luvaris imperialis*). These louvar scales are so modified that they do not fit in any current category of scale classification – they are vaguely oak leaf-shaped and sit atop pedestals connected to the rest of the body of the scale. In Fig. 10.3d, the thickened and sutured scales in the scrawled cowfish (*Acanthostracion quadricornis*) are also modified to the point that they defy classification into normal categories and as such, they are often referred to as scutes or dermal plates instead of scales (Besseau and Bouligand 1998). The four species in Fig. 10.3 illustrate a small part of the vast diversity of scales found in different species of fish. It is important that we continue to explore scale diversity in both qualitative and quantitative studies to gain a better understanding of the morphological disparity of scales, the evolutionary patterns of scale morphology, and scale structure-function relationships.

10.2.2 Hypotheses for Functional Diversity in Scales

Although scale morphology is diverse, there are some structural features that are common to most scaled species. We have briefly mentioned some of the microstructures on fish scales above, such as the interlocking ctenii of ctenoid scales and the spines of spinoid scales, but there are other relevant structures like circuli and radii that also occur on many scales. Below we discuss these structural features and potential functions for them.

Circuli are concentric circles usually starting from the scale's center (called the focus), and that represent periods of growth of a scale (similar to tree rings) (Fig. 10.4). They are raised above the surface of the scale and are present on the external surface of scales, facing the water. In many studies, circuli are used to estimate the age of fish, although not by a direct count (Batts 1964; Beardsley 1967; Hill et al. 1989); instead some circuli (called annuli) are closer together and represent
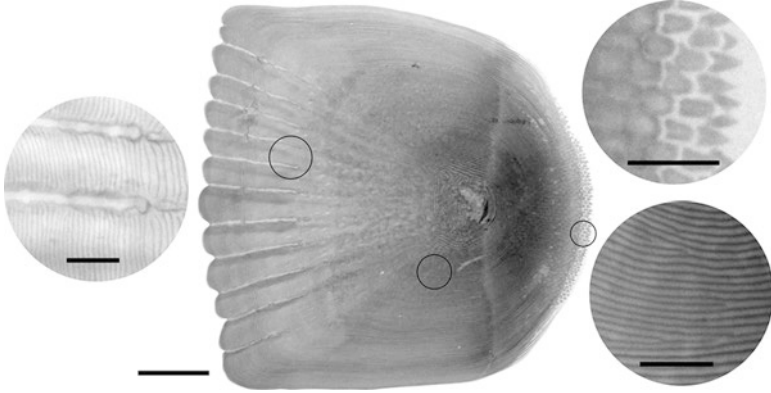
Fig. 10.4 Common features of fish scales. A single cleared and stained scale from a bluegill is shown, anterior to the left and dorsal above. Left inset shows radii, which appear as gaps in the mineralized layers of the scale. Top right inset shows ctenii, which are separate ossified spines that occur at the edge of ctenoid scales. In this scale, the outermost two rows of ctenii are separate mineralizations from the body of the scale, while the other inner (and older) rows of ctenii become mineralized together. Bottom right inset shows circuli, which are concentric ridges on the surface of scales. Scale bar for center image: 1 mm. Scale bars for insets: 200 μm
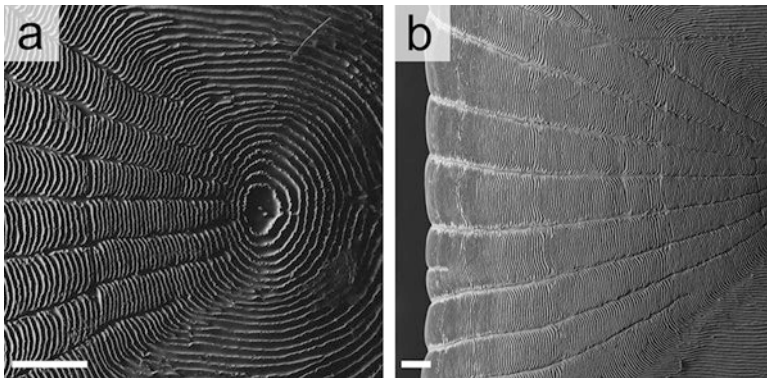
Fig. 10.5 Images of bluegill (*Lepomis macrochirus*) scales taken with scanning electron micros-copy (SEM). Anterior is to the left. (**a**) The concentric raised ridges called circuli are clearly visible starting from the focus. Radii are also evident on the anterior part of the scale (left) as breaks in the circuli that radiate from the center to the edge of the scale. (**b**) The anterior margin of the scale with the radii is shown. Scale bars 200 μm (Images credited to James Weaver)

a yearly mark. Circuli can be seen clearly in Figs. 10.4 and 10.5a as they grow around the center of a bluegill scale.

Radii are radial breaks in the mineralization of the scale (but not the unmineralized tissues; Schönbörner et al. 1979) that look like physical gaps in CT scans and cleared and stained scales (Fig. 10.4) or cracks in SEM (Fig. 10.5). Radii are visible in most fish only when the scale is removed from the body because they occur on the anterior

portion of the scale, which is normally covered and layered below more anterior scales (Roberts 1993; Esmaeili et al. 2012). However, some species have radii on the dorsal and ventral regions of the scale (the lateral fields) (e.g. Daniels 1996).

Ctenii are spines that come in a variety of sizes and shapes, and it is often the case that most of the visible portion of the scale (called the posterior field) is made of interlocking ctenii. In these cases, usually only the posterior-most one or two rows of ctenii are whole spines, while the other older ctenii are reduced to shortened interlocking stubs, as shown in Fig. 10.4 (Roberts 1993). The further towards the outer scale margin ctenii are, the younger they are – similar to circuli which grow around the scale center as the scale grows at the edge (Sire 1986; Sire and Arnulf 1990). Because ctenii are separate ossifications from the body of the scale (Fig. 10.4), they may be flexible and can potentially bend relative to the body of the scale to either point externally or internally.

Circuli, radii, ctenii, spines, and other scale features such as overall shape suggest a host of different hypotheses concerning scale function. We have discussed multiple hypotheses for scale structure-function relationships previously (Wainwright and Lauder 2016) and we will summarize several here. Ctenii, spines, circuli, radii, scale shape, and scale curvature may all result in changes in scale stiffness compared to scales without these features. For example, flexibility may be added by fields of separate spiny ctenii, as well as by radii. Increased scale flexibility could benefit undulatory swimmers by decreasing the force needed to bend the scales and skin. Stiffness may be increased using circuli that increase the second moment of area of a scale or by adding curvature to scales, which creates anisotropic stiffness by increasing the second moment of area with respect to different bending axes. Increasing the stiffness of scales could be beneficial for functions like physical protection – creating a scale resistant to bending with little material allows for economical armor.

Fish scales and their features have also been proposed to function hydrodynamically in swimming, with flow being directed in a beneficial way by scale surface structures (Burdak 1986; Wainwright and Lauder 2016; Lauder et al. 2016). Circuli, ctenii, spines of spinoid scales, and scale pattern may either generate turbulence or control turbulence in ways that decrease the overall drag on a fish's body (Anderson et al. 2001; Wainwright and Lauder 2016; Liyan et al. 2017). These fluid mechanisms are dependent on many factors including flow speed, fish size and shape, swimming kinematics, and scale morphology, making it very difficult to investigate the hydrodynamic roles of scale surface structures in these dynamic, small-scale, and species-specific systems. There have been some attempts to assign hydrodynamic functions to fish scales (Aleyev 1977; Burdak 1986; Sagong et al. 2008; Liyan et al. 2017), but these studies either do not present quantitative results or do not test real fish skin. We still know little about how fish surfaces impact the flow around them, and in fact we know little in general about the boundary layer flows around swimming fish (although see Anderson et al. 2001, Yanase and Saarenrinne 2015).

In addition to a potential hydrodynamic role, the microroughness of fish scales created by circuli and ctenii may also function to hold the epidermis and mucus on scales. Covering circuli and ctenii with mucus would make the fish's surface

smoother, which could act to either maintain laminar flow close to the body or prevent boundary layer separation, thereby reducing surface friction (Daniel 1981; Bernadsky et al. 1993). In this case, perhaps fish skin satisfies immune and hydrodynamic functions through the epidermis and mucus, and creates physical protection with bony scales. The functional hypotheses we have outlined above are in no way an exhaustive list of fish scale function and certainly different species may utilize scales and skin in different ways. Furthermore, scales, epidermis, and mucus are undoubtedly a system with multiple biological functions and many of the potential functions of fish skin mentioned above could occur together.

Because of our lack of knowledge tying particular scale morphologies to function, it is important to continue to investigate scale morphology so that we can better understand the diversity of scales and begin to understand how different scales may influence interactions between a fish and its environment. To do this, we first need to understand scale structure in both two and three dimensions to build a strong foundation for testing hypotheses of scale function. Hydrodynamic interactions happen in three dimensions, making it necessary for us to understand the surface topography of scaled surfaces before theorizing about mechanisms fish scales may employ to alter flow during locomotion. This includes the need for additional study of mucus on fish skin and *in vivo* fish surfaces, as seen below in Sect. 10.3.

10.2.3   *Investigating Scales – SEM, μCT, Histology, and Profilometry*

Studying fish scales and fish skin requires techniques that are able to image sizes in the micron to centimeter range and detect tissues from mucus to bone, which exhibit a range of material and optical properties, and different degrees of hydration. Not many techniques can accomplish all of these at once, but researchers have used optical microscopy, scanning electron microscopy (SEM), micro x-ray computed tomography (μCT), histology, and profilometry to study fish scales and skin. We will briefly discuss some of the benefits of SEM, μCT, histology, and profilometry below. To our knowledge, few studies to date have used μCT and profilometry on fish skin and scales to generate three-dimensional data (Sudo et al. 2002; Wainwright and Lauder 2016; Lauder et al. 2016; Wainwright et al. 2017) – historically, SEM and histology have been the most common approaches to the study of fish skin.

SEM has been a popular way to image and measure scale features for decades and has produced many valuable scale descriptions that reveal patterns of scale evolution and detailed two-dimensional scale morphology of particular species (e.g. Roberts 1993; Johal et al. 2006; Jawad and Al-Jufaili 2007; Sankar et al. 2008; Esmaeili et al. 2012). SEM is an effective technique for investigating scale microstructures such as ctenii, radii, and circuli (Sire and Arnulf 2000; Sire and Huysseune 2003; Meunier and Brito 2004), especially when epidermis and mucus coatings have been removed using dehydration and sample preparation. SEM has also been used to investigate the plywood-like arrangement of fibers in the elasmodine layer

of scales (Meunier 1981; Zylberberg et al. 1988). SEM benefits from fields of view anywhere from a few square micrometers to a few square millimeters and reveals surface details within this range to great effect. However, SEM usually requires specimen preparation (drying, sputter coating) and traditionally only offers two-dimensional information (although environmental SEM requires less specimen preparation). Thus, SEM is not a good technique for understanding the topography of scales or mucus-covered surfaces, but it is a good technique for observing fine details on scale surfaces. Figure 10.5 shows some examples of SEM images of blue-gill (*Lepomis macrochirus*) scales, which clearly demonstrate the radii and circuli.

μCT has become an increasingly widespread technique used in research to obtain three-dimensional information about morphology. Because μCT uses x-ray projections to reconstruct morphology, it works best on mineralized biological tissues like bone and shell, although there are now several effective techniques for staining soft tissues with metal ions to enhance CT scan contrast of neural tissue, connective tissues, and muscle (e.g. Descamps et al. 2014; Gignac et al. 2016). Scales are mineralized and thus make good specimens for μCT analysis and the average laboratory μCT resolution of 5–50 microns is within the appropriate range for imaging most fish scales. μCT scans are excellent for reconstructing the full three-dimensionality of scale shape and larger scale features, and they provide a good mechanism for developing computer and physical models of fish scales that could be tested in various experimental and simulation approaches in the future. One downside of laboratory μCT is that this technique is not particularly good at reconstructing the smallest surface features of scales such as individual ctenii or circuli (Wainwright and Lauder 2016). Reconstructing surface renderings of x-ray slices at typical resolutions of 5–50 micron voxel size tends to smooth out small features such as circuli and small ctenii, and the degree of surface roughness is greatly affected by the quality of the render and the values used for thresholding gray values to create the surface.

However, for investigating the volume, structure, and shape of scales in three dimensions, μCT is a good technique to use. We show an example of μCT scans of scales from two different species in Fig. 10.6, illustrating the three-dimensional nature of the data generated with this approach, which can produce three-dimensional surfaces and two-dimensional cross sections through different anatomical planes. Such cross-sectional views are useful for visualizing the relative placement of groups of scales *in situ*, the degree of scale overlap, and the nature of inter-scale connections and contact (Fig. 10.6).

Histology is a tool for investigating scale internal structure and it has the benefit of imaging both soft and hard tissues. Although histological sections can be used as image stacks to reconstruct morphology in three dimensions, it is traditionally a two-dimensional technique. Histology allows us to gain an understanding of relative position of scales and associated soft tissues, and it provides a wealth of information about the structure and composition of different tissues. Compared to SEM and μCT, histology is excellent at displaying soft tissues like the epidermis of fish and goblet cells filled with mucus (Fig. 10.7). Furthermore, histology also provides a method to measure the relative thickness of different skin elements in different species and to generally inspect the structure of the dermis, scales, epidermis, and
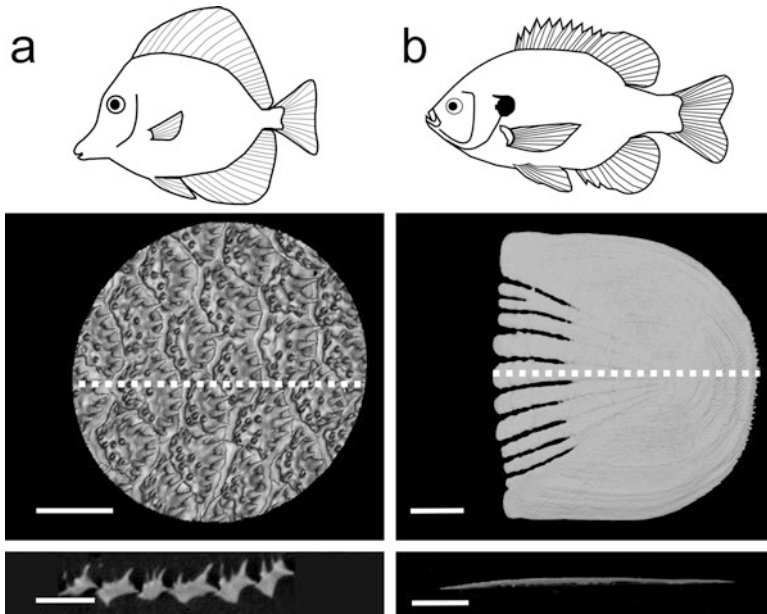
Fig. 10.6 Surface renderings and cross-sections of scales from two species illustrated with models generated from μCT. (**a**) Scales from the yellow tang (*Zebrasoma flavescens*) are shown in a surface rendering containing over 20 scales. A cross-section also shows the three-dimensional nature of these scales and the complex surface texture. (**b**) A scale from a bluegill (*Lepomis macrochirus*) with typical teleost scale morphology. Gaps on the anterior edge are radii, and ctenii are visible on the posterior edge. Cross sectional view below shows that the scale is a single bony plate; note also substantial differences in scale size between these two species. Scale bars: 1 mm
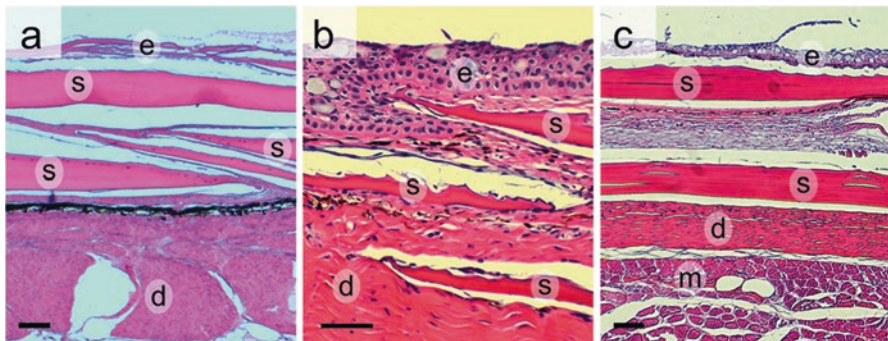
Fig. 10.7 Histological sections of skin and scales for three different fish species. Each sample is stained with hematoxylin and eosin. (**a**) Bigeye tuna (*Thunnus obesus*) has 200 μm thick scales but only a very thin epidermal layer. A dark layer of pigmented tissue is visible above the connective tissue of the dermis. (**b**) Brook trout (*Salvelinus fontinalis*) has a thick epidermis with many goblet cells and thin scales embedded in scale pockets. (**c**) Bluegill (*Lepomis macrochirus*) shows a clear epidermis above and between scales. The dermis lies external to deeper muscle fibers. d: dermis, e: epidermis, m: muscle fibers, s: bony scales. Scale bars: 100 μm

underlying muscle. Disadvantages of histology include difficulty in reconstructing accurate 3D information from slice data and challenges in sectioning fish skin, due to the proximity and location of soft, delicate tissue (epidermis) that is external to hard mineralized tissue (scales). We show histological sections through the skin from three species in Fig. 10.7 to highlight selected structural differences among these species. The relative thickness of the epidermis, scales, and dermis is different in each species, even when the general pattern of bony scales embedded in the dermis remains similar.

For research on fish surface topography, we have found that gel-based surface profilometry (described below) is an excellent method for capturing details of fish surfaces in three dimensions, regardless of skin optical or material properties and without the need for specimen preparation (Wainwright et al. 2017). We use a gel-based profilometry system manufactured by GelSight Inc. (Waltham, MA) that takes images through clear flexible gels pressed onto a surface of interest (Johnson and Adelson 2009; Johnson et al. 2011; Li and Adelson 2013). The contact surface of these clear gels has an opaque coating that standardizes the optical properties of the surface. Six photographs are taken of each surface using a different lighting angle for each image. These photographs are then reconstructed into a three-dimensional topographic map of the surface, which can be quantified using surface metrology metrics such as root-mean-square roughness (Table 10.1). This method

Table 10.1 Root mean square roughness (Sq) values for the nine species in Figs. 10.2, 10.3 and 10.7. Common manufactured surfaces are included for reference

Surface	Roughness Sq (μm)	
Extruded aluminum	0.06	
1000 grit sandpaper	6.3	
Back of hand (*Homo sapiens*)	14.3	
Moorish Idol (*Zanclus cornuta*)	14.9	
500 grit sandpaper	16.2	
Bonefish (*Albula vulpes*)	17.9	
Shad (*Anodontosoma chacunda*)	20	
Sergeant (*Abudefduf sordidus*)	25.2	
Smelt (*Osmerus mordax*)	26.1	
Squirrelfish (*Sargocentron spiniferum*)	30.1	
Boarfish (*Antigonia capros*)	32.7	
Cowfish (*Acanthostracion quadricornis*)	38.6	
80 grit sandpaper	53.6	
Louvar (*Luvaris imperialis*)	76.5	

allows for the study of skin on living (anesthetized) fishes, providing a means of understanding the effect of the mucus coating over the surface of scales.

Gel-based profilometry provides significant advantages for studying fish surfaces involved in interactions with the environment because it can reconstruct surfaces in three dimensions, and because this technique can image large fields of view (square centimeters to square millimeters) at high spatial resolutions (each topographic image represents over 18 million three-dimensional points in *x, y,* and *z*). The high-throughput and non-invasive nature of this technique also allows for the study of living animals with the mucus coating intact. Three-dimensional surface data are crucial to furthering the study of hypotheses regarding hydrodynamic function, and techniques like gel-based profilometry allow us to quickly gather this topographic data without damaging or destroying specimens.

We show a reconstruction of the surface of a rainbow smelt (*Osmerus mordax*) from gel-based profilometry and analysis using MountainsMap 7 (Digital Surf Inc., Besançon, France). In Figs. 10.8 and 10.9 displaying this technique, warmer colors correspond to higher elevations on the surface. Using surface profilometry data, elevation profiles can be easily created for analyzing specific surface features, and the surface itself can be used to calculate a large number of canonical surface metrology parameters. We have calculated root-mean-square roughness (Sq) of
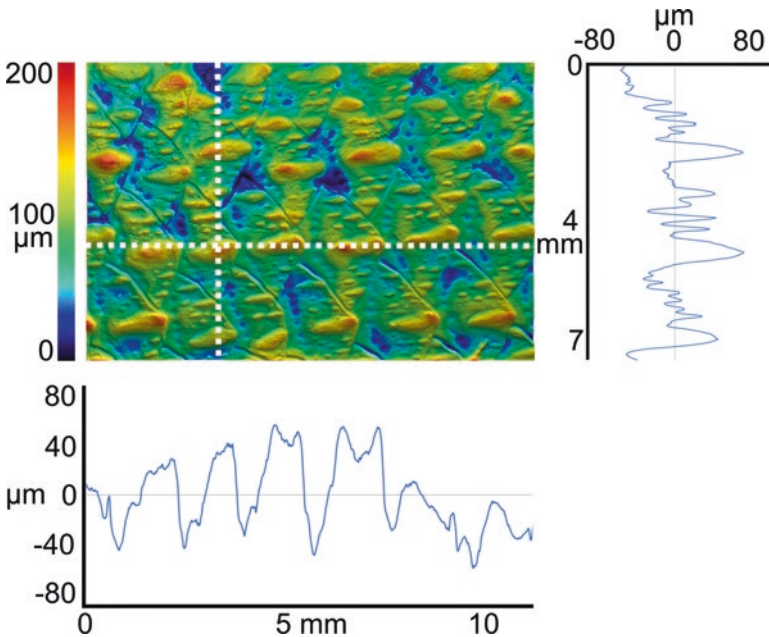
Fig. 10.8 Topographic surface of scales from a rainbow smelt (*Osmerus mordax*) reconstructed using gel-based profilometry. Color refers to elevation, with red colors being highest above the surface. Two orthogonal profile lines are shown to illustrate the three-dimensional nature of these surface data

Fig. 10.9 The effect of mucus on fish surface topography. (**a**) Yellow tang (*Zebrasoma flavescens*). (**b**) Niger triggerfish (*Odonus niger*). (**c**) Spotbanded scat (*Selenotoca multifasciatus*). (**d**) Bluegill (*Lepomis macrochirus*). (**e**) Singular bannerfish (*Heniochus singularis*). (**f**) African moony (*Monodactylus sebae*). (**g**) Brook trout (*Salvelinus fontinalis*)
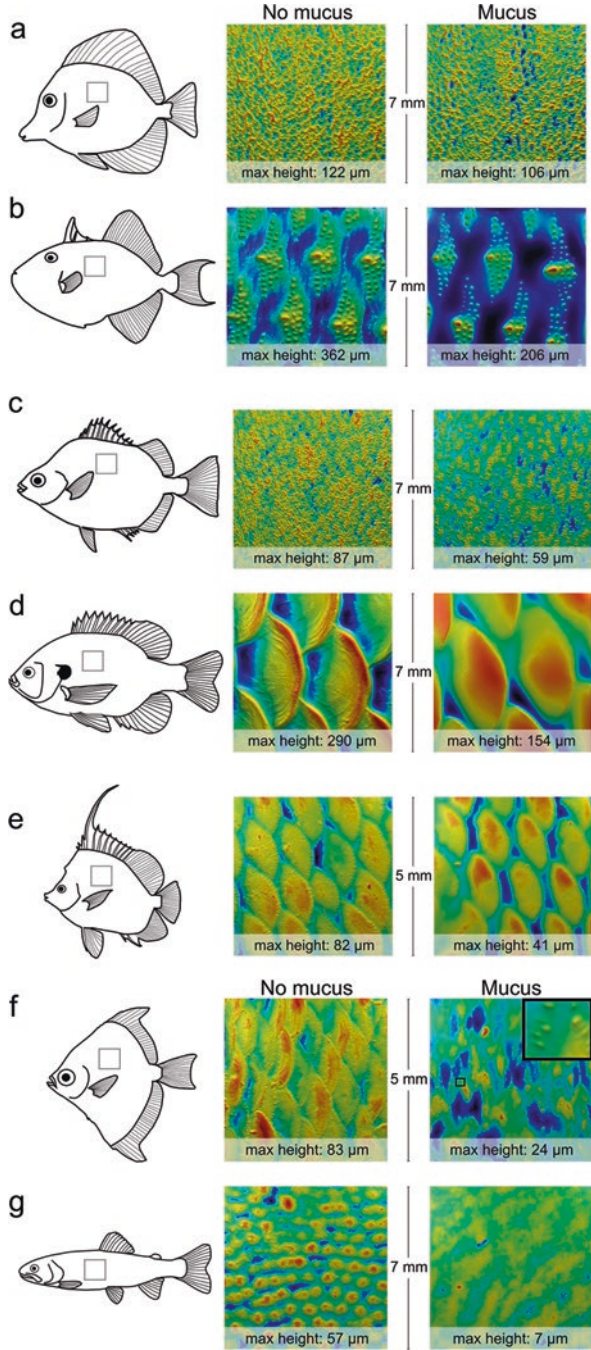
many fish surfaces as well as some manufactured surfaces (extruded aluminum and various sandpapers). Sq represents an average distance a point is from the mean height of the surface. The Sq parameter is calculated by taking a mean height of the surface and then for each point on the surface, subtracting its value from the mean height. These differences between the point and the mean are then squared, integrated across all of the points on the surface, and averaged. Finally, this integrated average value is square-rooted to account for squaring the differences in height. Table 10.1 shows Sq roughness values for several different species of fish discussed in this chapter compared to some manufactured materials. Many other surface metrology parameters exist that describe other topographic qualities. We have previously used skew and kurtosis (which describe the distribution of heights over a surface), max height (another measure of roughness), and texture direction (which evaluates the direction of dominant topographic patterns) (Wainwright and Lauder 2016; Wainwright et al. 2017), but there are an additional 20–30 common surface metrology parameters used in a variety of applications (Whitehouse 1994). We can use these numerous parameters to search for functional traits of fish scales by studying how parameters such as Sq roughness change with different fish that exhibit different behaviors or levels of swimming performance.

10.3   Slippery Surfaces – How Mucus Changes Fish Skin Texture

10.3.1   Fish Surfaces with Mucus

We have previously demonstrated how gel-based profilometry can be used to image the mucus and epidermis that covers scales on anesthetized fishes (Wainwright et al. 2017) and here we present data including *in vivo* surface images from seven different species: yellow tang (*Zebrasoma flavescens*), niger triggerfish (*Odonus niger*), spotbanded scat (*Selenotoca multifasciatus*), bluegill sunfish (*Lepomis macrochirus*), singular bannerfish (*Heniochus singularis*), African moonys (*Monodactylus sebae*), and brook trout (*Salvelinus fontinalis*). We used gel-based profilometry to image the lateral midbody and the peduncle region on each living fish after anesthetizing them with tricaine methanesulfonate (MS-222). We then preserved each individual in a 3.4% formalin solution and imaged the surface again after brushing the surface to remove preserved mucus and epidermis. We imaged one individual of each species in this manner.

We present images of the surfaces both with and without mucus of each species imaged in Fig. 10.9. Note that each image has a different elevation range and we give the maximum height (the elevation value that corresponds to the darkest red) for each image. We have ordered the presentation of these seven species to illustrate how mucus can change the apparent features created by fish scales. The yellow tang in Fig. 10.9a has a surface that changes very little with the presence of mucus and

epidermis. Yellow tangs have scales made of many small laterally projecting spines that protrude clearly above the mucus layer so removing mucus has little effect on the overall topography of their surfaces (Fig. 10.6a also shows yellow tang scales). The niger triggerfish (Fig. 10.9b) and spotband scat (Fig. 10.9c) show similar trends but at different sizes. Both species have raised portions of their scales that clearly protrude past the mucus layer when it is present. However, the boundaries of individual scales are only clear when mucus is removed (i.e. mucus fills the surface and obscures the scale boundaries).

In Fig. 10.9d and e, we show surfaces from a bluegill and a bannerfish, which have similar patterns with and without mucus. Without mucus, the scales of both species are obvious, as are small features on the scale surfaces such as ctenii at the margin and circuli on the body of the scale. However, mucus and the epidermis obscure these small features when present, and instead only the general shape of the scale is obvious in our images with mucus present. Next, we show the surfaces of the moony, which has small scales with ctenii at the posterior margin (Fig. 10.9f). These scales become almost completely obscured in the presence of mucus and epidermis, and instead the only visible features are the small ctenii at the posterior margin of each scale (inset in Fig. 10.9f). Finally, we show how the brook trout's surface changes with and without mucus: trout have small smooth-edged cycloid scales that become completely covered when the epidermis and mucus layers are intact in anesthetized specimens, and maximum surface height is only 7 μm (Fig. 10.9g).

From tang to trout, we see a clear gradient of increasing changes to surface topography with the presence of mucus; yellow tang have surfaces that are very similar with or without mucus, and in contrast, trout scales are completely concealed by mucus. Fish in the middle of this gradient either have scale microstructures obscured (bluegill, bannerfish), scale boundaries obscured (trigger, scat), or most of the scales obscured, and only a few features visible (moony) when mucus and epidermis are present. We also measured the roughness of these seven species with and without mucus and compare values in Table 10.2. We show both quantitatively (Table 10.2) and qualitatively (Fig. 10.9) that surfaces without mucus are rougher than those with mucus, yet there is considerable diversity in this effect. The yellow tang has the smallest decrease in roughness with a 0% change (although the peduncle region of the yellow tang actually shows a curious increase in roughness with mucus) while the trout has the largest percentage decrease in roughness, with a 93% loss. A nominal range from a 0% to a 93% drop in roughness illustrates a challenge of studying fish surfaces – sometimes mucus matters a great deal, but other times it has little effect on surface roughness. We are puzzled by the increase in roughness measured on the yellow tang peduncle scales with mucus compared to without mucus, but we believe this could result from having flexible scales before preservation, that when pressed, will rotate to have spines elevated in line with the z-axis of our measurements, creating higher roughness (whereas in preserved specimens, the scales are fixed and no longer flexible in the skin).

Table 10.2 Roughness of fish surfaces with and without mucus at mid-lateral body (shown in Fig. 10.9) and peduncle positions

Species	Location	No mucus roughness Sq (µm)	Mucus roughness Sq (µm)
Tang	Body	15.2	15.2
	Peduncle	26.0	36.9
Triggerfish	Body	38.7	21.8
	Peduncle	43.5	43.5
Scat	Body	10.9	6.2
	Peduncle	13.9	7.4
Bluegill	Body	55.7	33.5
	Peduncle	61.5	40.8
Bannerfish	Body	10.8	6.9
	Peduncle	9.5	4.4
Moony	Body	11.0	2.7
	Peduncle	11.5	6.1
Trout	Body	8.6	0.6
	Peduncle	10.3	3.9

10.3.2   What Mucus Means for Hypotheses of Function

Mucus has long been considered an important part of fish swimming (Daniel 1981; Bernadsky et al. 1993), and our topographic data have important implications for how fish surfaces may function hydrodynamically, as mucus clearly alters surface roughness and the effect of mucus in obscuring surface roughness changes along the body (Table 10.2). Furthermore, there is not necessarily a correlation between the appearance of scales and what those scales look like when covered by epidermis and mucus. For example, both the moony (Fig. 10.9f) and the bannerfish (Fig. 10.9e) have similar size and elevated features on their scales, but anesthetized specimens with mucus intact appear different in these two species. This indicates that not only does scale morphology differ between species, but so too does the morphology of the epidermis and mucus layers, showing us that the topography of live fish is determined by interactions between scale, epidermis, and mucus morphology.

The interaction between the complex structure of scales and the slippery nature of epidermis and mucus changes many of the hypotheses concerning the function of fish scale morphology. Many of the species we imaged have part or all of their ctenii and circuli completely obscured by epidermal tissues or mucus and thus, it seems that in these species and others like them, ctenii and circuli will not play a role in locomotor hydrodynamics except perhaps an indirect one by holding mucus and epidermis on the surface. However, we do not know if patterns of body bending during swimming might expose ctenii to water flow as scales bend and slide past each other as the body undulates. The effect of body bending patterns on scale relative position and surface feature exposure remains entirely unknown.

One additional complexity is that fish scale morphology changes across a fish's body (e.g. Jawad 2005; Wainwright and Lauder 2016), and we have noted rougher and more rugose scales in the peduncle and other posterior regions in many species that we have investigated (Wainwright and Lauder 2016; Wainwright et al. 2017). Because of this, it is possible that anterior scales or scale features could be covered by mucus and epidermis, but more extreme-featured posterior scales may be less changed by the epidermis and mucus layers. Fluid flow along the body of a fish will change as flow moves from head to tail because of the natural development of boundary layer flow coupled with changes in movement and body shape. It is possible that scales are hidden under mucus on anterior parts of a fish where there is a laminar boundary layer and then protrude into the boundary layer towards the tail to create turbulence and maintain flow attachment.

Functional measurements of how fish scales change boundary layer flow do not exist. There are some measurements of fish boundary layers (Anderson et al. 2001; Yanase and Saarenrinne 2015) and they indicate that swimming fish likely experience both laminar and turbulent boundary layers depending on Reynolds number, fish kinematics, and the region of the fish being investigated. These measurements come from just two species of bony fish, however, and thus cannot provide much information on the effect of scales. In order for us to begin to answer how scales interact with boundary layer flows, we need careful experimental measurements of the boundary layer of fish skin, starting with static conditions and eventually moving towards dynamic testing with flapping skin pieces with and without mucus, and finally to free-swimming fish. To investigate different skin topographies, we need careful choice of fish species to compare not just one species to another, but to compare general scale morphologies against one another. These experiments could also be accomplished with physical models if models are validated as having similar flow properties to fish scales, as has been done in placoid shark scales (Wen et al. 2014; Wen et al. 2015).

Until experiments on boundary layer flow over different fish scale morphologies are completed, we can focus the discussion on scale topography and boundary layer interactions in another way. The engineering parameter k+, also known as roughness Reynolds number (Jimenez 2004), provides an estimate of whether surface roughness will change boundary layer characteristics. k+ values do not estimate whether an effect on the boundary layer will be beneficial or not – they simply estimate if a surface has features that are large enough to change flow in the boundary layer relative to a smooth surface. The k+ parameter is calculated by multiplying friction velocity of the fluid by the height of surface features and dividing by the viscosity of the fluid of interest (Jimenez 2004; Schultz and Flack 2007). Viscosity of salt or freshwater is known, the size of surface features can be measured with gel-based profilometry, and friction velocity can be estimated using power law equations involving the Reynolds number (Smits 2000). Because calculating friction velocity uses the Reynolds number, a known or estimated swimming speed is needed, along with the distance from the anterior tip of the body to the region under investigation. This also means that each k+ value is relevant only for a particular swimming speed and location on the body. k+ values of less than three indicate that

surface features are too small to disturb the boundary layer; values over three indicate that surface features are likely to change the boundary layer flow.

Although the height of surface features is incorporated into k+ estimation, surface geometry and patterning are also important to boundary layer effects and are not taken into account with k+. For example, if two surfaces have the same feature size, but one surface is covered in smooth-sloping ridges while the other is covered in sharp-peaked ridges, the sharp ridges will be more likely to change boundary layer flow because sharp features provide natural separation points on the surface. Aside from ignoring surface geometry, simple calculations of k+ also assume that objects are not moving across the flow, a condition that is violated during undulatory fish swimming, especially on posterior regions of the body. Nonetheless, a cutoff value of three for k+ is sufficiently conservative and our k+ values will give us a guide for future data collection. Questions relating to boundary layer flows on a deforming flexible object with a surface coating are complex, and k+ can provide a useful initial piece of a broader multivariate approach.

We can use k+ as a way of narrowing the field of potential scale functions – if a particular fish's surface has a k+ below three, then its surface features are simply too small to have a substantial effect on the boundary layer. In Fig. 10.10 we present k+ values for the different species in Fig. 10.8 using surface profilometry data and estimates of swimming speed. We include values for surfaces with mucus and for swimming both at one body-length per second and three body lengths per second. We also include values calculated from scale height data at the midbody of each fish (Fig. 10.8) as well as from the peduncle of the fish. Note that these values are for the specific specimens we used in this study and the specific regions we imaged on their body surfaces. Caution should be used before extrapolating these results to larger individuals of the same species or different regions on the same species. Additionally, we are not accounting for either surface geometry (sharpness of corners of edges, spacing between peaks) or body undulation, so our k+ values should be viewed as hypotheses instead of corroborated results.
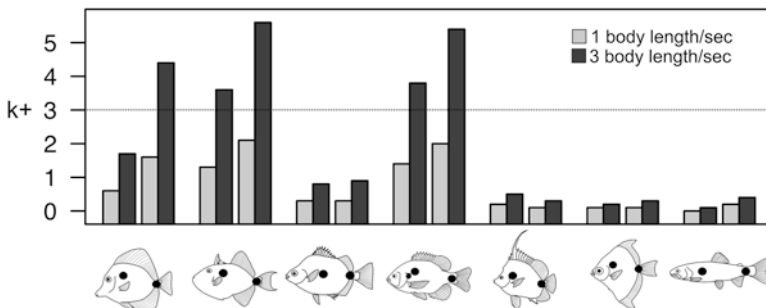
Fig. 10.10 Calculated k+ values of fish with mucus at body and peduncle regions at two different swimming speeds, one and three body lengths per second (see legend). From left to right species, with body region always followed by the peduncle region: yellow tang, niger triggerfish, scat, bluegill, bannerfish, moony, trout. k+ cutoff value of three is marked with a line – values above three indicate surfaces where flow may be altered in the boundary layer

We find that the only fish with k+ values above three are yellow tang, niger triggerfish, and bluegill (Fig. 10.10). These fish have the roughest surfaces among the seven species we investigated (Table 10.2), so it is unsurprising that these are the fish that are most likely to have scales that change the boundary layer flow in some way, even with the presence of mucus and epidermis. Yellow tang has skin with many small distal-pointing spines on their scale surfaces and these spines increase in size at the peduncle, just anterior to the scalpel-like spine also located there. It is these larger spines that are likely the reason the yellow tang shows a k+ over three only on the peduncle at the higher swimming speed of three body lengths per second. The triggerfish has k+ values above three on body and peduncle regions, but only at swimming speeds of three body lengths per second, indicating surface geometry may only affect the boundary layer at high swimming speeds. Bluegill also shows high k+ values on both body and peduncle regions only at the faster swimming speed of three body lengths per second. Calculating k+ provides a way of identifying potential candidates for future experimental studies of boundary layers around swimming fish.

10.4   Concluding Remarks

Fish scales display a vast diversity of morphology – scale size, shape, and internal structure vary among species, different populations of the same species, and on different regions of the same fish (Margraf and Riley 1993; Roberts 1993; Dapar et al. 2012; Wainwright and Lauder 2016). While we have a basic understanding about how scales vary and develop (Suzuki 1971; Roberts 1993; Sire and Akimenko 2004) and we have been able to quantify scales in two dimensions (Ibañez et al. 2007; Ibañez et al. 2009), we have only just begun to understand the surface of scales and fish skin in three dimensions, and we still have no understanding of how scale morphology and deployment changes with fish activity. Gel-based profilometry provides a method of reconstructing the surface topography of scales in different species of fish with the hopes of eventually using this information to elucidate the function of different scale morphologies (Wainwright and Lauder 2016; Lauder et al. 2016; Wainwright et al. 2017). Understanding scale topography in three dimensions is both necessary and important for studying fish scale hydrodynamic function because of the role surface features have in changing boundary layer flows. Furthermore, understanding the three-dimensional morphology of fish scales in a quantitative manner allows for more rigorous exploration of fish surfaces in the contexts of morphology, evolutionary patterns, and the form-function relationship of scales.

We also demonstrated how fish scale topography changes on fish where mucus and skin are still intact atop the scales. Using gel-based profilometry, we have discovered that mucus and epidermis can often obscure and cover small structures present on fish scales, which changes the roughness and structure of a mucus-coated surface compared to a preserved fish without mucus or epidermis. By imaging a diverse sample of seven species, we show that scale morphology alone is a poor predictor of *in vivo* skin topography, and that mucus, epidermis, and scales interact

to form complicated 3D surfaces. Some fish have rough surfaces that are barely changed with the presence of live skin tissues (yellow tang, triggerfish), while others have scales that are completely changed by mucus and epidermis to create a very smooth external surface (trout). It is likely that most fish fall in the middle of this spectrum, with most scale microstructure obscured by mucus but with general scale shape still visible, perhaps also with some spines or ctenii. The imaging and quantitative comparison of mucus-covered fish surfaces is a new area of research and reveals what surfaces are like on living fish, which is vital information for understanding what type of surface the water interacts with during swimming.

Despite promising new techniques to image and quantify fish scale topography, we still know little about fish scale function. Other authors have studied the armorlike aspects of fish scales (Vernerey and Barthelat 2010; Song et al. 2011; Browning et al. 2013; Chintapalli et al. 2014; Vernerey and Barthelat 2014; Duro-Royo et al. 2015), and the roles fish skin have in body and skin bending (Long et al. 1996; Ghosh et al. 2014; Szewciw et al. 2017), yet work on the hydrodynamic effect of fish scales remains hypothetical (Walters 1963; Burdak 1986; Sudo et al. 2002; Liyan et al. 2017). In part, it is challenging to experimentally study fine-scale flows on swimming fish, which is compounded by the fact that we also know little about boundary layer flow around freely-swimming fishes. In order to investigate how and if fish scales change boundary layer flow for better or worse, we can use metrics like k+ to search for surfaces of potential interest, and then investigate function experimentally. Using micro-scale particle image velocimetry with real fish skin pieces, using physical models of scales or fish surfaces, or using phylogenetic comparative methods to link different scale morphologies with ecology or swimming performance are all key areas for future study. The functional implications of the complex and slippery surfaces of fish remains an intriguing and understudied area of fish biology, and with research on scale morphology, surface topography, fluid mechanics, and evolutionary patterns, we can move toward a comprehensive understanding of the form and function of fish surfaces.

References

Aleyev, Y. G. (1977). *Nekton*. Hague: Dr. W. Junk b.v. Publishers.

Anderson, E. J., McGillis, W. R., & Grosenbaugh, M. A. (2001). The boundary layer of swimming fish. *The Journal of Experimental Biology, 204*, 81–102.

Batts, B. S. (1964). Lepidology of the adult pleuronectiform fishes of Puget Sound, Washington. *Copeia, 4*, 666–673.

Beardsley, G. L. (1967). Age, growth, and reproduction of the Dolphin, *Coryphaena hippurus*, in the Straits of Florida. *Copeia, 1967*, 441.

Bereiter-Hahn, J., & Zylberberg, L. (1993). Regeneration of teleost fish scale. *Comparative Biochemistry and Physiology, 105A*, 625–641.

Bergman, J. N., Lajeunesse, M. J., & Motta, P. J. (2017). Teeth penetration force of the tiger shark *Galeocerdo cuvier* and sandbar shark *Carcharhinus plumbeus*. *Journal of Fish Biology, 91*, 460–472.

Bernadsky, G., Sar, N., & Rosenberg, E. (1993). Drag reduction of fish skin mucus: Relationship to mode of swimming and size. *Journal of Fish Biology, 42*, 797–800.

Besseau, L., & Bouligand, Y. (1998). The twisted collagen network of the box-fish scutes. *Tissue & Cell, 30*, 251–260.

Bone, Q. (1972). Buoyancy and hydrodynamic functions of integument in the Castor oil fish, *Ruvettus pretiosus* (Pisces: Gempylidae). *Copeia, 1972*, 78–87.

Browning, A., Ortiz, C., & Boyce, M. C. (2013). Mechanics of composite elasmoid fish scale assemblies and their bioinspired analogues. *Journal of the Mechanical Behavior of Biomedical Materials, 19*, 75–86.

Burdak, V. D. (1986). Morphologie fonctionnelle du tegument ecailleux des poissons. *Cybium, 10*, 1–128.

Casselman, J. M. (1990). Growth and relative size of calcified structures of fish growth and relative size of calcified structures of fish. *Transactions of the American Fisheries Society, 119*, 673–688.

Chintapalli, R. K., Mirkhalaf, M., Dastjerdi, A. K., & Barthelat, F. (2014). Fabrication, testing and modeling of a new flexible armor inspired from natural fish scales and osteoderms. *Bioinspiration & Biomimetics, 9*, 36005.

Daniel, T. L. (1981). Fish mucus: In situ measurements of polymer drag reduction. *The Biological Bulletin, 160*, 376–382.

Daniels, R. A. (1996). Guide to the identification of scales of inland fishes of northeastern North America. *New York State Museum Bulletin, 488*, 1–93.

Dapar, M. L. G., Torres, M. A. J., Fabricante, P. K., & Demayo, C. G. (2012). Scale morphology of the Indian goatfish, *Parapeneus indicus* (Shaw, 1803) (Perciformes: Mullidae). *Advance Envirronmental Biologico, 6*, 1426–1432.

Descamps, E., Sochacka, A., de Kegel, B., Van Loo, D., Hoorebeke, L., & Adriaens, D. (2014). Soft tissue discrimination with contrast agents using micro-ct scanning. *Belgian Journal of Zoology, 144*, 20–40.

Duro-Royo, J., Zolotovsky, K., Mogas-Soldevila, L., Varshney, S., Oxman, N., Boyce, M. C., & Ortiz, C. (2015). MetaMesh: A hierarchical computational model for design and fabrication of biomimetic armored surfaces. *Computer-Aided Design, 60*, 14–27.

Esmaeili, H. R., Gholamifard, A., Zarei, N., & Arshadi, A. (2012). Scale structure of a cyprinid fish, *Garra rossica* (Nikol'skii, 1900) using scanning electron microscope (SEM). *International Journal of Science, Technology and Society, 4*, 487–492.

Esteban, M. Á. (2012). An overview of the immunological defenses in fish skin. *ISRN Immunology, 2012*, 1–29.

Fast, M. D., Sims, D. E., Burka, J. F., Mustafa, A., & Ross, N. W. (2002). Skin morphology and humoral non-specific defence parameters of mucus and plasma in rainbow trout, coho and Atlantic salmon. *Comparative Biochemistry and Physiology A, 132*, 645–657.

Ghosh, R., Ebrahimi, H., & Vaziri, A. (2014). Contact kinematics of biomimetic scales. Applied Physics Letters. *105*, 233701-1-233701-5.

Gignac, P. M., Kley, N. J., Clarke, J. A., Colbert, M. W., Morhardt, A. C., Cerio, D., Cost, I. N., Cox, P. G., Daza, J. D., Early, C. M., et al. (2016). Diffusible iodine-based contrast-enhanced computed tomography (diceCT): An emerging tool for rapid, high-resolution, 3-D imaging of metazoan soft tissues. *Journal of Anatomy, 228*, 889–909.

Hawkes, J. W. (1974). The structure of fish skin I. General organization. *Cell and Tissue Research, 149*, 147–158.

Hill, K. T., Cailliet, G. M., & Radtke, R. L. (1989). A comparative analysis of growth zones in four calcified structures of Pacific Blue Marlin, *Makaira nigricans*. *Fishery Bulletin, 87*, 829–843.

Huysseune, A., & Sire, J.-Y. (1998). Evolution of patterns and processes in teeth and tooth-related tissues in non-mammalian vertebrates. *European Journal of Oral Sciences, 106*, 437–481.

Ibañez, A. L., Cowx, I. G., & O'Higgins, P. (2007). Geometric morphometric analysis of fish scales for identifying genera, species, and local populations within the Mugilidae. *Canadian Journal of Fisheries and Aquatic Sciences, 1100*, 1091–1100.

Ibañez, A. L., Cowx, I. G., & O'Higgins, P. (2009). Variation in elasmoid fish scale patterns is informative with regard to taxon and swimming mode. *Zoological Journal of the Linnean Society, 155*, 834–844.

Jawad, L. A. (2005). Comparative scale morphology and squamation patterns in triplefins (Pisces: Teleostei: Perciformes: Tripterygiidae). *Tuhinga, 16*, 137–167.

Jawad, L. A., & Al-Jufaili, S. M. (2007). Scale morphology of greater lizardfish *Saurida tumbil* (Bloch, 1795) (Pisces: Synodontidae). *Journal of Fish Biology, 70*, 1185–1212.

Jimenez, J. (2004). Turbulent flows over rough walls. *Annual Review of Fluid Mechanics, 36*, 173–196.

Johal, M. S., Esmaeili, H. R., & Sharma, M. L. (2006). Scale structure of a cobitid fish, *Cobitis linea* (Heckel, 1849) using different modes of SEM. *Current Science, 91*, 1464–1466.

Johnson, M.K. and Adelson, E.H. (2009). Retrographic sensing for the measurement of surface texture and shape. In: *2009 IEEE Conference on Computer Vision and Pattern Recognition*, 1070–1077.

Johnson, M. K., Cole, F., Raj, A., & Adelson, E. H. (2011). Microgeometry capture using an elastomeric sensor. *ACM Transactions on Graphics, 30*, 46.

Lauder, G. V., Wainwright, D. K., Domel, A. G., Weaver, J., Wen, L., & Bertoldi, K. (2016). Structure, biomimetics, and fluid dynamics of fish skin surfaces. *Physical Review Fluids, 1*, 060502.

Li, R., & Adelson, E. H. (2013). Sensing and recognizing surface textures using a GelSight sensor. In: *2013 IEEE Conference on Computer Vision and Pattern Recognition*, pp. 1241–1247.

Liyan, W. U., Zhibin, J., Yuqiu, S., Wentao, R., Shichao, N., & Zhiwu, H. (2017). Water-trapping and drag-reduction effects of fish *Ctenopharyngodon idellus* scales and their simulations. *Science China Technological Sciences, 60*, 1111–1117.

Long, J. H., Hale, M. E., McHenry, M. J., & Westneat, M. W. (1996). Functions of fish skin: Flexural stiffness and steady swimming of longnose gar *Lepisosteus osseus*. *The Journal of Experimental Biology, 199*, 2139–2151.

Margraf, F. J., & Riley, L. M. (1993). Evaluation of scale shape for identifying spawning stocks of coastal Atlantic striped bass (*Morone saxatilis*). *Fisheries Research, 18*, 163–172.

Meunier, F. J. (1981). "Twisted plywood" structure and mineralization in the scales of a primitive living fish *Amia calva*. *Tissue & Cell, 13*, 165–171.

Meunier, F. J. (2011). The Osteichtyes, from the Paleozoic to the extant time, through histology and palaeohistology of bony tissues. *Comptes Rendus Palevol, 10*, 347–355.

Meunier, F. J., & Brito, P. M. (2004). Histology and morphology of the scales in some extinct and extant teleosts. *Cybium, 28*, 225–235.

Meyer, W., & Seegers, U. (2012). Basics of skin structure and function in elasmobranchs: A review. *Journal of Fish Biology, 80*, 1940–1967.

Motta, P., Habegger, M. L., Lang, A., Hueter, R., & Davis, J. (2012). Scale morphology and flexibility in the shortfin mako *Isurus oxyrinchus* and the blacktip shark *Carcharhinus limbatus*. *Journal of Morphology, 273*, 1096–1110.

Rakers, S., Gebert, M., Uppalapati, S., Meyer, W., Maderson, P., Sell, A. F., Kruse, C., & Paus, R. (2010). "Fish matters": The relevance of fish skin biology to investigative dermatology. *Experimental Dermatology, 19*, 313–324.

Roberts, C. D. (1993). Comparative morphology of spined scales and their phylogenetic significance in the Teleostei. *Bulletin of Marine Science, 52*, 60–113.

Rosen, M. W., & Cornford, N. E. (1971). Fluid friction of fish slimes. *Nature, 234*, 49–51.

Sagong, W., Kim, C., Choi, S., Jeon, W.-P. and Choi, H. (2008). Does the sailfish skin reduce the skin friction like the shark skin? *Physics of Fluids*, *20*, 101510-1-101510-10.

Sankar, S., Sekar, S., Mohan, R., Rani, S., Sundaraseelan, J., & Sastry, T. P. (2008). Preparation and partial characterization of collagen sheet from fish (*Lates calcarifer*) scales. *International Journal of BIological Macromolecules, 42*, 6–9.

Schönbörner, A. A., Boivin, G., & Baud, C. A. (1979). The mineralization processes in teleost fish scales. *Cell and Tissue Research, 202*, 203–212.

Schultz, M. P., & Flack, K. A. (2007). The rough-wall turbulent boundary layer from the hydraulically smooth to the fully rough regime. *Journal of Fluid Mechanics, 580*, 381.

Shephard, K. L. (1994). Functions for fish mucus. *Reviews in Fish Biology and Fisheries, 4*, 401–429.

Sire, J.-Y. (1986). Ontogenic development scales in a cichlid *Hemichromis bimaculatus* (Cichlidae). *Journal of Fish Biology, 28*, 713–724.

Sire, J.-Y., & Akimenko, M.-A. (2004). Scale development in fish: A review, with description of sonic hedgehog (shh) expression in the zebrafish (*Danio rerio*). *The International Journal of Developmental Biology, 48*, 233–247.

Sire, J.-Y., & Arnulf, I. (1990). The development of squamation in four Teleostean fishes with a survey of the literature. *Jpn. Journal of Ichthyology, 37*, 133–143.

Sire, J., & Arnulf, I. (2000). Structure and development of the ctenial spines on the scales of a teleost fish, the cichlid *Cichlasoma nigrofasciatum*. *Acta Zoologica, 81*, 139–158.

Sire, J.-Y., & Huysseune, A. (2003). Formation of dermal skeletal and dental tissues in fish: A comparative and evolutionary approach. *Biological Reviews of the Cambridge Philosophical Society, 78*, 219–249.

Smits, A. J. (2000). *A physical introduction to fluid mechanics*. New York: John Wiley and Sons.

Song, J., Ortiz, C., & Boyce, M. C. (2011). Threat-protection mechanics of an armored fish. *Journal of the Mechanical Behavior of Biomedical Materials, 4*, 699–712.

Sudo, S., Tsuyuki, K., Ito, Y., & Ikohagi, T. (2002). A study on the surface shape of fish scales. *Trans. Jpn. Soc. Mechanical Engineering, 45*, 1100–1105.

Suzuki, T. (1971). Some scale patterns of the scad, Decapterus maruadsi (Temminck et Schlegel), and their variations with body parts. *Bulletin of the Japan Sea Regional Fisheries Research Laboratory 23*, 1–19.

Szewciw, L., Zhu, D., & Barthelat, F. (2017). The nonlinear flexural response of a whole teleost fish: Contribution of scales and skin. *Journal of the Mechanical Behavior of Biomedical Materials, 17*, 30252–30257.

Taylor, H. F. (1916). The structure and growth of the scales of the squeteague and the pigfish as indicative of life history. *Fishery Bulletin, 34*, 285–330.

Thomson, J. M. (1956). Interpretation of the scales of the yellow-eye mullet, *Aldrichetta forsteri* (Cuvier & Valenciennes) (Mugilidae). *Australian Journal of Marine and Freshwater Research, 8*, 14–30.

Vernerey, F. J., & Barthelat, F. (2010). On the mechanics of fishscale structures. *International Journal of Solids and Structures, 47*, 2268–2275.

Vernerey, F. J., & Barthelat, F. (2014). Skin and scales of teleost fish: Simple structure but high performance and multiple functions. *Journal of the Mechanics and Physics of Solids, 68*, 66–76.

Wainwright, D. K., & Lauder, G. V. (2016). Three-dimensional analysis of scale morphology in bluegill sunfish, *Lepomis macrochirus*. *Zoology, 119*, 182–195.

Wainwright, D. K., Lauder, G. V., & Weaver, J. C. (2017). Imaging biological surface topography *in situ* and *in vivo*. *Methods in Ecology and Evolution*. in press.

Walters, V. (1963). The Trachipterid integument and an hypothesis on its hydrodynamic function. *Copeia, 1963*, 260–270.

Wen, L., Weaver, J. C., & Lauder, G. V. (2014). Biomimetic shark skin: Design, fabrication and hydrodynamic function. *The Journal of Experimental Biology, 217*, 1656–1666.

Wen, L., Weaver, J. C., Thornycroft, P. J. M., & Lauder, G. V. (2015). Hydrodynamic function of biomimetic shark skin: Effect of denticle pattern and spacing. *Bioinspiration & Biomimetics, 10*, 066010.

Whitear, M. (1970). The skin surface of bony fishes. *Journal of Zoology, 4*, 437–454.

Whitehouse, D. J. (1994). *Handbook of surface metrology*. Philadelphia: Institute of Physics Publishing.

Xu, Z., Parra, D., Gomez, D., Salinas, I., Zhang, Y.-A., von Gersdorff Jørgensen, L., Heinecke, R. D., Buchmann, K., LaPatra, S., & Sunyer, J. O. (2013). Teleost skin, an ancient mucosal surface that elicits gut-like immune responses. *Proceedings of the National Academy of Sciences of the United States of America, 110*, 13097–13102.

Yanase, K., & Saarenrinne, P. (2015). Unsteady turbulent boundary layers in swimming rainbow trout. *The Journal of Experimental Biology, 218*, 1373–1385.

Zaccone, G., Kapoor, B. G., Fasulo, S., & Ainis, L. (2001). Structural, histochemical and functional aspects of the epidermis of fishes. *Advnces in Marine Biology, 40*, 253–348.

Zylberberg, L., Bereiter-Hahn, J., & Sire, J. Y. (1988). Cytoskeletal organization and collagen orientation in the fish scales. *Cell and Tissue Research, 253*, 597–607.

Chapter 11
Surface-Contacts During Mating in Beetles: Stiffness Gradient of the Beetle Penis Facilitates Propulsion in the Spiraled Female Spermathecal Duct

Yoko Matsumura, Alexander E. Kovalev, Alexander E. Filippov, and Stanislav N. Gorb

Abstract Substantial diversity of genitalia found in animals is regarded as a result of sexual selection. This means that surface interactions of the male and female genitalia during copulation play a key role in its evolution. However morpho/physical diversity and biomechanics of the structures in sexual intercourse are not well linked. Here we estimated relative stiffness of hyper-elongated male and female genitalia in cassidine beetles based on material composition gradient analyses and numerically modeled this system to gain insights about how genital features affect penile propulsion. The material composition analyses suggested that only the hyper-elongated penis has stiffness gradient, the tip of the penis could be softer than the rest of it, and the highly spiraled female spermathecal duct is constantly stiffer than the penis. The numerical stimulation with different conditions of the penile stiffness showed effects of stiffness gradients of the penises on its propulsion into the female duct. This simulation demonstrated that the realistic type of the stiffness gradients aids in faster propulsion than other types and a constantly rigid penis causes largest local deviation of the female duct. It seems that the soft end of the penis is flexible enough to quickly adjust small curvature in the spermathecal duct, and at the same time, it may be strongly pushed by the rigid basal part. This study indicates that previously ignored physical properties of genital materials are of crucial importance in understanding physical interactions of sexes.

Y. Matsumura (✉)
Department of Functional Morphology and Biomechanics, Zoological Institute,
Kiel University, Kiel, Germany

Department of Biology, Keio University, Yokohama, Japan
e-mail: yoko.matsumura.hamupeni@gmail.com

A. E. Kovalev · S. N. Gorb
Department of Functional Morphology and Biomechanics, Zoological Institute,
Kiel University, Kiel, Germany

A. E. Filippov
Department of Functional Morphology and Biomechanics, Zoological Institute,
Kiel University, Kiel, Germany

Department N5, Donetsk Institute for Physics and Engineering, Donetsk, Ukraine

11.1 Introduction

Biological surfaces interact with the environment including organisms. Surface contacts can occur also between sexes within a species during copulation, although it is not usually mentioned in the context of surface contacts. In vertebrate research community, biomechanics of biological surfaces between sexes is one of highlighted topics worked from the evolutionary point of view (Kelly 2016) and the medical point of view including human beings (Udelson 2007). On the contrary to this situation, biomechanical studies of invertebrate animals have just started due to challenges of small size of them. Currently technical difficulties have been overcome by innovative techniques to visualize interactions of a tiny penetration processes of genitalia in bushcrickets (Wulff et al. 2017) and an ovipositor in a parasitic wasp (Cerkvenika et al. 2017). In this chapter we introduce our numerical approach to understand the surface interaction between sexes.

Male and female genitalia evolved more quickly and yielded remarkable diversity in comparison with other characters (Eberhard 1985, Hosken and Stockley 2004, Macagno et al. 2011, Rowe and Arnqvist 2012, Simmons 2014). This phenomenon has previously attracted attention of evolutionary biologists, and its mechanisms have been intensively investigated by sophisticated experiments (e.g. Arnqvist and Rowe 1995, Rodriguez 1995, Arnqvist and Danielsson 1999, House and Simmons 2003, Cordoba-Aguilar 2005, Holwell et al. 2009, Simmons et al. 2009, van Lieshout and Elgar 2010, Rowe and Arnqvist 2012, Sakurai et al. 2012, Dougherty et al. 2015). It is widely accepted that the immense diversity of genital structures is driven by sexual selection in general (Eberhard 1985, Arnqvist 1998, Hosken and Stockley 2004, Simmons 2014). Moreover most researches in this field were focused on the male genitalia (Ah-King et al. 2014), however, it has been recently uncovered that females play an active role in sexual selection by active choice of males (Villavaso 1975, Rodriguez 1994) and that interactions between sexes are very important factors for genital evolution of both sexes (Miller and Pitnck 2002, Tanabe and Sota 2013).

Knowledge of how male and female genital properties affect physical interaction during sexual intercourse is essential in the evolutionary studies of genital structures. Since natural selection does not act directly on shapes, but rather influences shapes indirectly through functions, links between genital morpho-physical features and their functional significance are critically important to understand evolutionary mechanisms of diversity. Nevertheless biomechanics which challenges comprehensive understanding of kinematics and dynamics of movements in relation to the structural features have been largely ignored in this field, but recently this topic started to contribute more to our knowledge due to modern experimental techniques, elaborate modeling tools, and by increasing number of interdisciplinary studies (Matushkina and Gorb 2007, Matsumura et al. 2014, Dougherty et al. 2015, Filippov et al. 2015, Michels et al. 2015, Sentenská et al. 2015, Willkommen et al. 2015) in addition to a direct observation technique developed by Wulff et al. (2017).

Hereby we numerically modeled hyper-elongated male and female genitalia especially focusing on physical properties observed in cassidine beetles, to gain

insights about how genital features affect penile propulsion that is an initial and vital process of male and female physical interactions during copulation. In these beetles, the male penises represent an elongated cuticular flagellum, transferring sperm, and female genitalia where the flagellum is inserted represent a partly cuticular and helical spermathecal duct including some reversal turns called knots (Rodriguez et al. 2004) (Figs. 11.1 and 11.2). Recently impacts of the shapes of the female spermathecal duct on male penile propulsion were numerically evaluated in this system (Filippov et al. 2015). Moreover for insect cuticular and fibrous structures, tenent
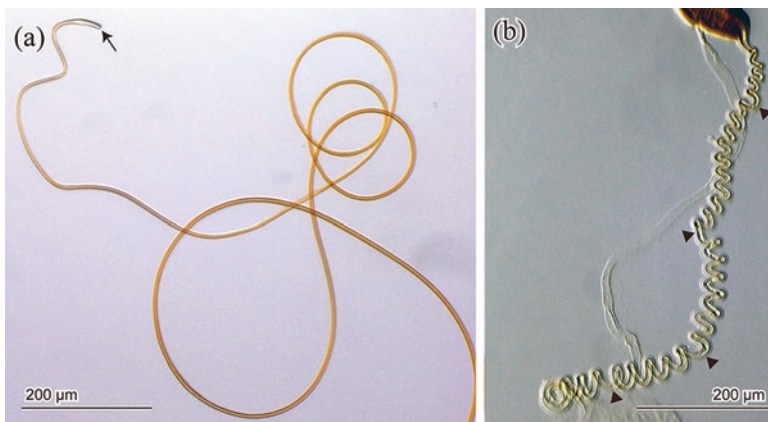
Fig. 11.1 Light microscopic images of a male flagellum (**a**) and a female spermathecal duct (**b**). The arrow indicates the tip of the flagellum, the arrowheads represent knots (reversal turns) (After Matsumura et al. 2017)
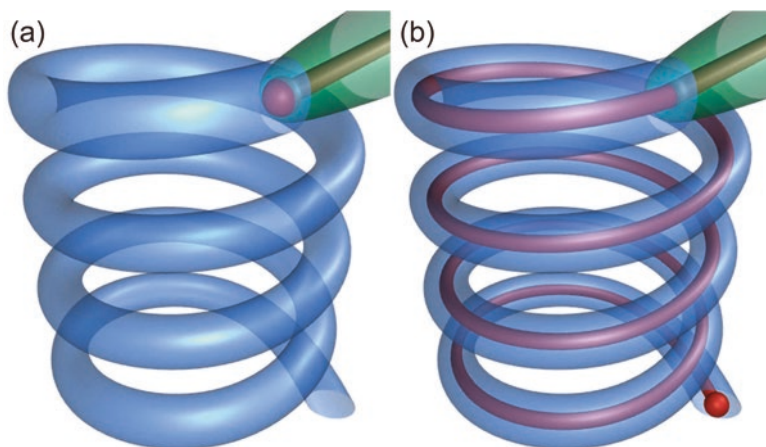
Fig. 11.2 Schematics of female ducts (blue), male flagella (red) and male flagella guiding structures (green). Spheres on the male flagella show the tips of the male flagella. For simplicity, reversal turns (knots) are not depicted. (**a**) Mating is just stated; the tip of male flagella guiding structure is inserted to the female duct. (**b**) The male flagellum is fully inserted into the female duct

setae of beetle tarsi were demonstrated to have longitudinal material and stiffness gradients (Peisker et al. 2013), which result in specific mechanical behavior of the entire attachment system (Gorb and Filippov 2014). Therefore, material components and stiffness properties of the male flagellum and female spermathecal duct were hypothesized to be an important parameter, which might influence flagellum motion within the female spermathecal duct.

In order to test this hypothesis, we analyzed the autofluorescence composition of the genitalia based on the differences of different biopolymers using confocal laser scanning microscopy (Michels and Gorb 2012). This method provides indications for the material composition of arthropod cuticle structures (Michels et al. 2012, 2016). The effect of the estimated properties on the genitalia propulsion was then evaluated using the numerical model previously established by Filippov et al. (2015) with certain modifications. Our study challenges to the question how the male-female interactions during copulation are affected by the material properties of the genitalia. In this chapter we report on material component gradient of the male flagellum along the duct, whereas no gradient was observed in the internal wall of the female spermathecal duct. This type of material distributions in the male and female genitalia showed the highest velocity in the numerical simulation, if compared to other variants of distributions of material properties.

11.2 Results

11.2.1 Autofluorescence Composition Along the Flagellums

The confocal laser scanning microscopy analysis revealed a gradient in the autofluorescence composition along the flagellum (Fig. 11.3). Except for the apical regions, the flagellum exhibited strong green and red autofluorescences. The tips (nearly 1% of the total length: ca. 82 μm, 97 μm, 127 μm) of the flagellum showed mainly blue autofluorescence inside the curve and green autofluorescence on another side (Fig. 11.3d, f). In the material of the spermathecal ducts of the females no longitudinal gradient in the autofluorescence composition was found (Fig. 11.3g), but we revealed a transversal gradient in the autofluorescence composition (Fig. 11.3h). The internal wall showed mainly orange to green autofluorescence and the external layer shows the dominance of the blue autofluorescence. The duct showed blue autofluorescence in the outer part of the duct wall and mainly green and partially red autofluorescence in the inner part of the wall (Fig. 11.3g, h). Same tendency was observed, when we analyzed male and female structures simultaneously, but the females showed stronger intensity of green and red autofluorescence in comparison to that of the male (Fig. 11.4).
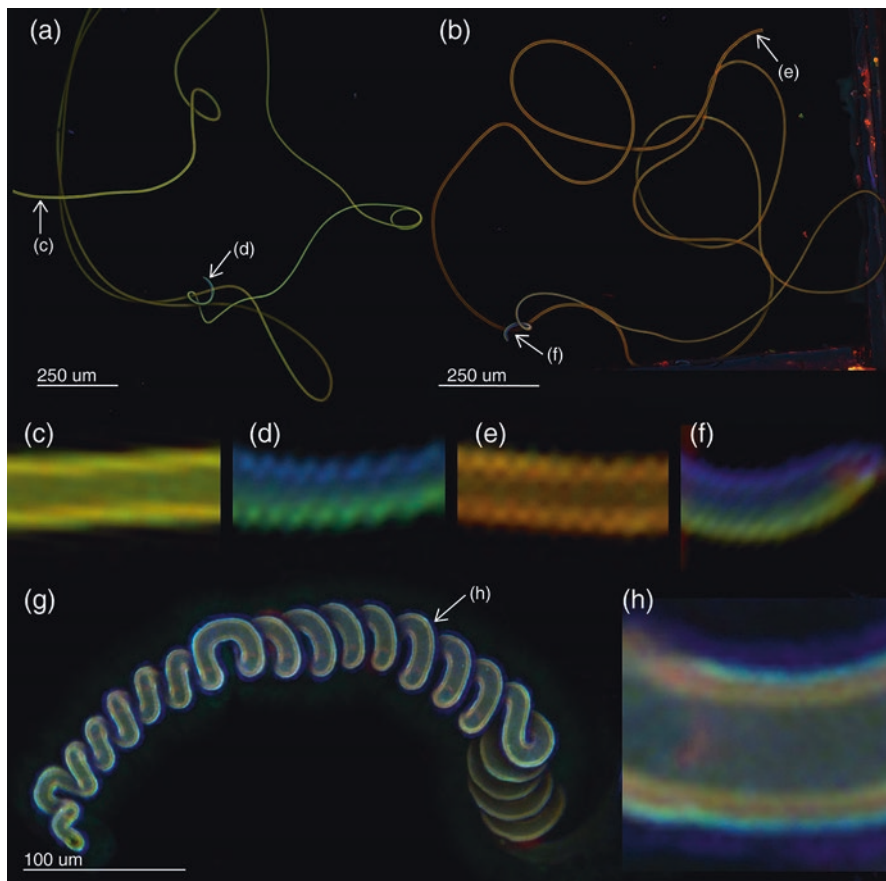
Fig. 11.3 Confocal laser scanning micrographs of flagella ((**a**) and (**b**) for two individuals, respectively) and spermathecal duct (**g**) of *Cassida rubiginosa*. (**c–f**) The details of the base (**c, e**) and the tips (**d, f**) of the flagella are digitally enlarged from the original images (**a**) and (**b**), respectively. The stripes are artifacts of image processing. (**g**) The spermathecal duct, the left end corresponds to the beginning of the spermatheca and the right end corresponds to the beginning of the vagina. (**h**) The details of the duct. We visualized the emitted wavelengths 420–480, ≥490, ≥560, and ≥640 with blue, green, red and red, respectively

11.2.2 Numerical Simulation

We hereby applied the previous numerical model (Filippov et al. 2015) in which we numerically created the fibrous male flagellum as an elastic uncompressible fiber and the highly helical spermathecal duct as an elastic channel (Figs. 11.5 and 11.6; females: blue lines, males: red lines). Although the female spermathecal duct is not only helical but also the whole helical duct is convoluted in reality, not straightened (Filippov et al. 2015, Matsumura et al. 2017), we created the female model excluding the convoluted shape of the whole helical duct as shown in Figs. 11.5 and 11.6. For

Fig. 11.4 Confocal laser scanning micrographs of the flagella and spermathecal duct of *Cassida rubiginosa*. (**a**) All four autofluorescences which we used are shown. (**b**) Only red colored autofluorescences are shown
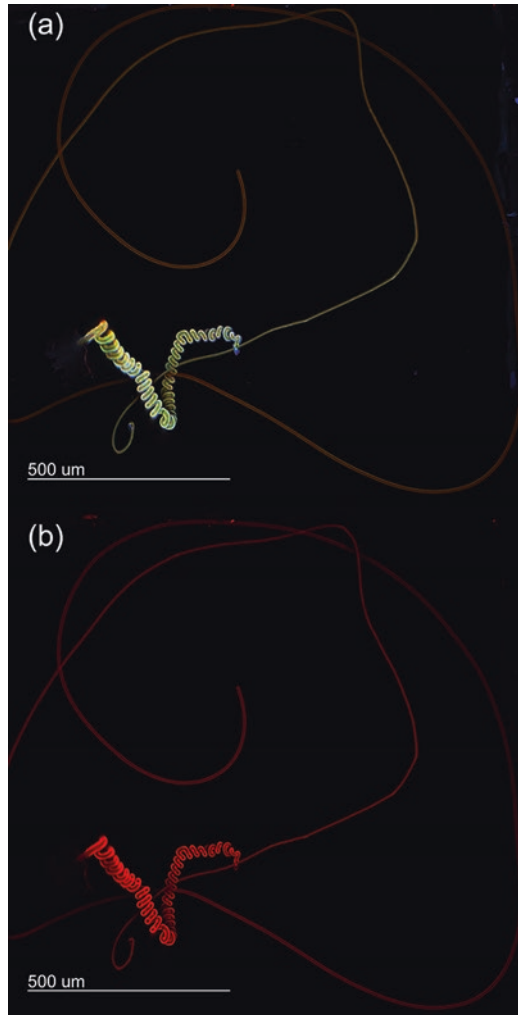
females, we included the knots on the duct, which were demonstrated to increase the male energy expenditure for penile propulsion in the previous study (Filippov et al. 2015) (Figs. 11.5 and 11.6). The end of the male flagellum was just pushed to propel it into the female spermathecal duct to imitate the genital motion during penile penetration. This propulsion mechanism had been confirmed based on detailed functional morphological study on the *Cassida* species (Matsumura et al. 2017).

Results of the simulations for the flagellum with uniform and gradient of rigidity (Figs. 11.5 and 11.6) are summarized in Figs. 11.7 and 11.8. Because the longitudinal material gradient was found only in the male flagellum and the inner wall of the female spermathecal duct showed constantly green to red autofluorescence, we
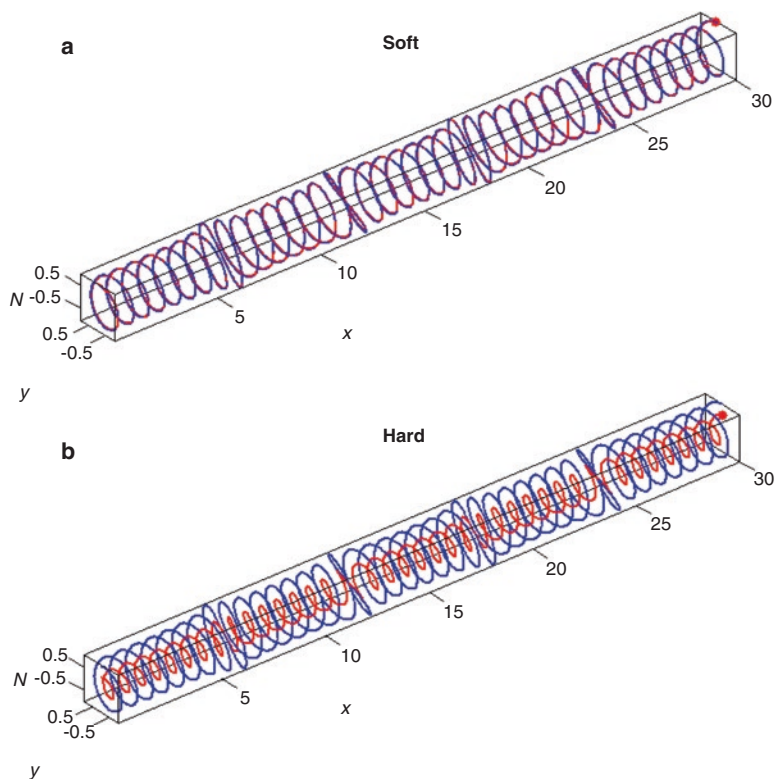
Fig. 11.5 3D scheme of numerical experiments. Two extreme cases of the male flagellum stiffness are presented. (**a**) Continuously soft. (**b**) Continuously hard. The central axis of the female duct is shown by the blue line, the male flagellum is shown by the red line. The entire flagellum is inserted in the female spermathecal duct

focused on the analysis of the material gradient of the male flagellum below. First of all we analyzed the local deviation of the flagellum from the intact female duct axis along the x-coordinate of the duct for four cases: constantly soft, constantly hard, almost constantly soft with the hard end, and almost constantly hard with the soft end (Fig. 11.7). Each curve in Fig. 11.7 corresponds to the flagella rigidity distribution depicted in the Figs. 11.5 and 11.6. There is a clear difference between the curves obtained for the female systems without and with the knots. This difference between them is mainly due to the various degrees of oscillations caused by the phase shift of the knots between segments of the flagellum and female duct having the same index j, which is produced by the phase shift around every knot j.

A correlation between maxima of the absolute tip velocity along the female duct and positions of the knots is presented in Fig. 11.8. Using Eq. 11.2 in the materials and methods, instant velocity of the flagellum tip was calculated for each case as a
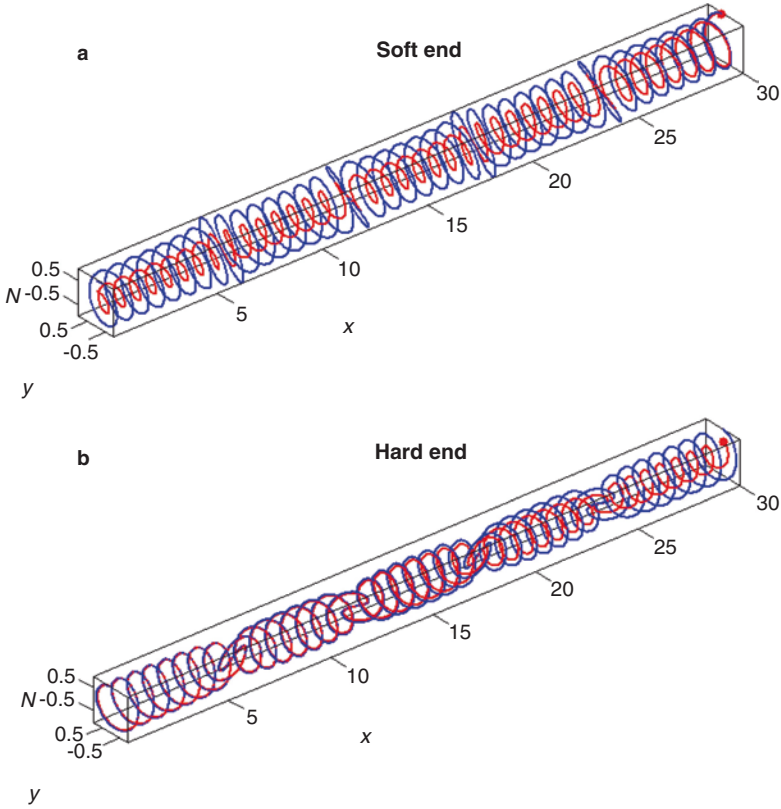
Fig. 11.6 3D scheme of numerical experiments. Other two cases of the male flagellum stiffness are presented as in the Fig. 11.5. (**a**) The flagellum gradually softening from its basis (left side) to its end ("Soft end"). (**b**) The flagellum gradually hardening from its basis to its end. The central axis of the female duct is shown by the blue line, the male flagellum is shown by the red line. The entire flagellum is inserted in the female spermathecal duct

function of time. However, for the comparison, this velocity is plotted here as a function of the tip coordinate x(1). Every curve here presents the velocity averaged over moving time window with the width comparable to the time interval between neighboring minima. The averaging makes the maxima in velocity more pronounced. Thick lines in the figure show the velocities calculated for the same systems without knots. The propulsion velocity strongly depends on the stiffness of the flagellum. The velocity for the rigid flagellum with soft end is much higher than the same value for all other cases. Accelerated flagellum propulsion was observed at the knot sites.
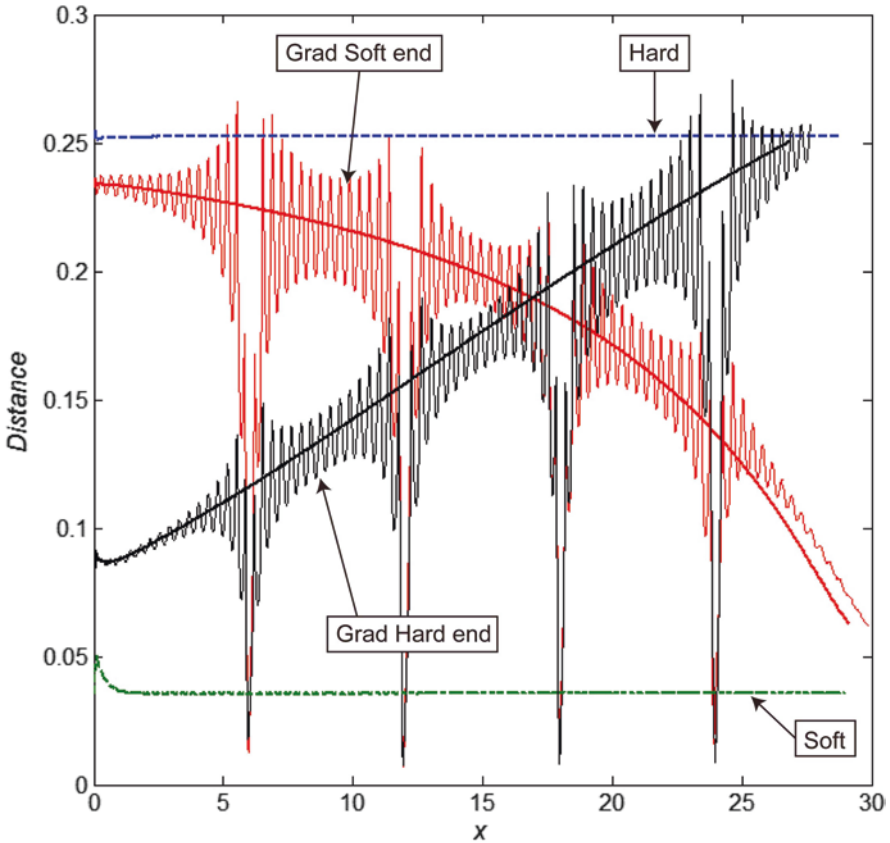
Fig. 11.7 Local deviation distances of a male flagellum from a female duct axis along the x-coordinate of the channel for four cases presented in Figs. 11.5 and 11.6. Corresponding cases are marked by arrows. Smooth curves represent cases for the channels without knots. Oscillating curves show the distances for the cases when male flagella had gradient and female channels had four knots

11.3 Discussion

The CLSM results of the present study indicate longitudinal gradient in the material composition of the flagellum and the absence of such a longitudinal gradient in the female spermathecal duct. According to Michels and Gorb (2012) and Michels et al. (2016), orange (which is a mixture of the green and red) to green autofluorescence and no autofluorescence gradient along the female spermathecal duct, observed in the inner wall, suggest that the inner wall is almost homogeneously composed of sclerotized cuticle. On the contrary, the observed autofluorescence compositions of the flagellum suggest that larger parts of the flagellum are mainly composed of sclerotized cuticle, while the flagellum tip contains mainly non-sclerotized cuticle
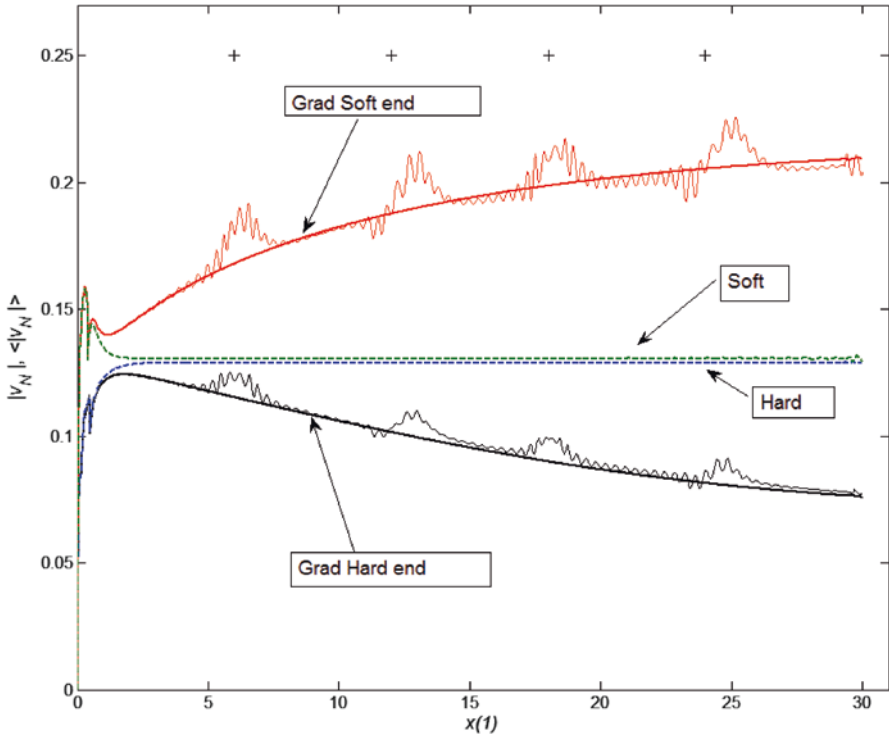
Fig. 11.8 Correlation between maxima in the velocity of the male flagellum tip along the female channel coordinate x(1) and the locations of the knots (shown with cross symbols "+"). The curves corresponding to male flagella with stiffness gradient and female channels with four knots are oscillating lines. The curves corresponding to flagella with stiffness gradient and channels without knots are shown as thick lines. Finally, the curves corresponding to flagella without stiffness gradient and female channels without knots are shown as dashed lines. The tip velocity curves are averaged over moving time window with the width corresponding to the time interval between neighboring minima

and relatively high proportions of the rubber-like protein resilin, whose concentration increases towards distal end. For other cuticular outgrowths, such as hairy attachment pads reported for many insects (Gorb and Beutel 2001, Gorb et al. 2002), correlations between material and stiffness gradients were demonstrated recently (Peisker et al. 2013, Michels et al. 2015). The preceding simulation showed that such a stiffness gradient, found in the hairy attachment system, affects the mechanical behavior of the hairs during contact formation/breakage (Filippov et al. 2015). In addition to it, the female structures, which we have analyzed simultaneously in the same CLSM scan with the male structures, had generally stronger intensity of green to red autofluorescence, which suggests larger thickness of the cuticular wall in females. These results inspired us to hypothesize that the beetle flagellum also may have a stiffness gradient and the inner wall of the spermathecal duct is constantly stiffer than the flagellum. Our model implemented those male and

female genital properties clearly demonstrated that the stiffness gradient along the flagellum impacts flagellum penetration in the relatively stiff helical-like counterpart of the female.

The flagellum that is equally stiff along its length results in a greater deformation between the original and penetrated positions of the female duct (Fig. 11.7). It means the flagellum simply "ignores" the duct's shape and its resultant mechanical disturbance which was demonstrated in Filippov et al. (2015). Nevertheless, the absolute velocity of the flagellum is the slowest in this condition (Fig. 11.8). Contrary to these results, the hard flagellum with the soft tip, possibly reflecting the real beetle system, shows quite different results (Figs. 11.7 and 11.8), especially the velocity. It seems that the soft end of the flagellum is flexible enough to quickly adjust small curvature in the duct, and at the same time, it is strongly pushed by the rigid basal part. In reality, not only the longitudinal stiffness gradient, but also a transverse stiffness gradient observed in the apical region of the flagellum, i.e. the relatively soft inner curve and the rigid outer curve, would aid the flagellum tip to adjust to the small curvature of the female duct. Interestingly, the uniform soft flagellum and almost uniform soft flagellum with the stiff tip show worse performances in comparison with the rigid flagellum with the soft end, i.e. very big deformation of the female duct and/or much slower velocity of the male flagellum (Figs. 11.7 and 11.8). It is conceivable that a flagellum with lower transversal stiffness strongly absorbs propulsion forces that in turn decrease the degree of further propulsion. Thus, the results obtained from our simulations, strongly support the hypothesis that the stiffness gradient in the beetle flagellum facilitates penile propulsion.

In our previous study (Filippov et al. 2015), the effects of variable shapes of female ducts on the penile propulsion were analyzed. It was found that certain parameters of the female duct, such as the presence of knots and the small curvature of the duct, affect the velocity decrease of the penile propulsion or the increase of the energy expenditure for propulsion. Because sexual intercourses in the field can be disrupted by other males or by natural enemies, it is highly likely that males inserting a penis and ejaculating quickly can be preferred in the course of sexual selection. Therefore, the stiffness gradient of the flagellum capable of quick penetration of the female duct can be selected as a favorable structure for both males and females, even if it could increase the energy expenditure for male penile propulsion (Filippov et al. 2015).

There are several sophisticated experimental studies investigating driving and stabilizing mechanisms of hyper-elongation (Rodriguez 1995, Tadler 1999, Rodriguez et al. 2004, van Lieshout and Elgar 2010, Kamimura 2013, Dougherty et al. 2015). However, neither of the authors took into account the material properties of genitalia. It has been recently shown that the males with the cut off tip of the flagellum in bugs acquired lower paternity (Dougherty et al. 2015). This result might be partly explained by the results of our simulation. It is likely that the absence of the softer tip causes troubles for sexual behavior, because of less effective propulsion, although the question why the slower insertion causes lower paternity in the lab condition must be considered in further details. As Dougherty et al. (2015)

pointed out, the functional morphology has been largely ignored in the studies of genital evolution. The hyper-elongated genitalia are ubiquitous in animals, not only in insects but also in vertebrates like ducks (Brennan et al. 2007), and it is very interesting to broaden studying taxa for comparing the mechanical properties among animals. Our approach shed light on the importance of studying materials' properties with the combination of experimental and numerical approaches for better understanding biological surface interactions during mating.

11.4 Methods

11.4.1 Autofluorescence Composition of the Male Flagellum and Female Spermathecal Duct

The autofluorescence composition of the flagellum was investigated with the confocal laser scanning microscope Zeiss LSM 700 (Zeiss, Germany). For this purpose, beetles *Cassida rubiginosa* (Chrysomelidae, Cassidinae) were collected in Jena (Germany) in May 2014 and in June 2015, kept in plastic jars with fresh leaves of thistles *Cirsium* spp. (Asteraceae) and grew to the next generation of adults. The shape and measurements of the male flagellum and female spermathecal duct of this species had reported in Filippov et al. (2015). Four males and three females were analysed. Of the treated samples, one male and female were analysed simultaneously to compare the intensity of autofluorescences. The flagella and spermathecal ducts were freshly dissected in the 1x phosphate butter solution (pH 7.4) (Carl Roth, Germany), and embedded in glycerine overnight. Subsequently, they were mounted on glass slides, and their autofluorescences were visualized, as described by Michels and Gorb (2012). The wave lengths of lasers 405, 488, 555, and 639 nm laser lines were used, and we applied a band-pass emission filter 420–480 and long pass emission filters transmitting light with wavelengths of ≥490, ≥560, and ≥640, respectively. Then we visualized the emitted wavelengths 420–480, ≥490, ≥560, and ≥640 with blue, green, red and red, respectively. All samples were observed using tenfold objective lens with different digital zoom.

11.4.2 Numerical Model

Here we have developed further a numerical model previously proposed in Filippov et al. (2015). The model basically consists of two conceptual components: an elastic uncompressible fiber (flagellum), which can move inside an elastic channel. The transversal rigidity of the fiber and elasticity of the channel are adjustable. The flagellum motion is generated by pushing on its base by an external force. In the previous model, it was supposed that the female duct is generally stiffer than the flagellum, as it is suggested by our analysis of autofluorescence composition.

The flagellum was numerically constructed from a big number N (up to $N = 10^5$) of elastically connected discrete segments. In the present study, we needed more accurate calculation than before and created more segments in comparison with the previous model (Filippov et al. 2015). Each segment has a length of $dr \leq 1$ μm defined by a total length of the system $L = 10$ mm measured from the microscopic images for our model beetle, *Cassida rubiginosa* (Filippov et al. 2015).

The flagellum model is provided with strong longitudinal stiffness $k^{\parallel}$ which prevents extension and compression of the practically rigid segments and two components of elastic forces $\vec{f}^{elastic} = \left\{ f^{\parallel} f^{\perp} \right\}$: $\vec{f}^{\parallel}_{jj\pm1} = k^{\parallel} \left(\vec{r}_j - \vec{r}_{\pm1} \right) \left[1 - \left(\left(\vec{r}_j - \vec{r}_{\pm1} \right) / dr \right)^2 \right]$, and $\vec{f}^{\perp}_j = k^{\perp} \left(2\vec{r}_j - \vec{r}_{j+1} - \vec{r}_{j-1} \right)$, acting between the neighboring nodes $\vec{r}_j$.

Longitudinal force $\vec{f}^{\parallel}_{jj\pm1}$, tends to conserve a distance between the nodes $\vec{r}_j$ and $\vec{r}_{j\pm1}$ close to the equilibrium dr.

Like in the previous model (Filippov et al. 2015), we supposed that the transverse stiffness $k^{\perp} = const$ is much weaker $k^{\parallel} \gg k^{\perp}$ than the longitudinal one. In the real system, the flagellum seems to have different stiffness along its length (see below), which was taken into account in the current analysis. It means that $k^{\perp}$ varies from segment to segment. From preliminary experiments we expect that $k^{\perp}$ should be a nonlinear function, which is almost constant at the beginning and quickly falls down near the end. For definiteness we apply:

$$k^{\perp} = k_0^{\perp} \left[1 - g \left(\frac{r_j - r_1}{r_N - r_1} \right)^{\alpha} \right] \tag{11.1}$$

Here parameters $k_0^{\perp}$ and g determine general rigidity and a rigidity gradient along the flagellum. In particular, at $g = 0$, large/small constant $k_0^{\perp}$ corresponds to the uniform hard/soft flagellum, respectively. If $g = 0.99$, then the tip of the flagellum is 100 times softer than its base. Using different combinations of the parameters, we analyzed four different variants of the system: constantly soft, constantly hard, almost constantly soft with the hard end, and almost constantly hard with the soft end. To reproduce the two last cases, we had used exponent $\alpha = 5$.

Female duct along the coordinate $X \in [0, L_x]$ was defined by its spiral core:

$$\begin{aligned} Y &= A_0 \sin\left(2\pi X / \lambda_0 \right) + R \sin\left(2\pi X / \lambda \right); \\ Z &= Z_0 \left(X \right) + R \cos\left(2\pi X / \lambda + \varphi\left(X \right) \right) \end{aligned} \tag{11.2}$$

with the parameters $R = L_x/30$; $\lambda = L_x/40$, $0.1L_x < A_0 < 0.5L_x$ and $0.2L_x < \lambda_0 < 0.4L_x$. It has secondary structure with some number N_{knots} of knot points at positions X_n, where direction of spiral rotation changes to a reverse one. The phase rotations were caused by the phase function $\varphi(X)$ defined as a sum of step-like functions $\varphi\left(X \right) = \sum_{n=1}^{N_{knots}} \left(-1 \right)^n \left[\pi / 2 + \tan^{-1} \left(\left(X - X_n \right) / 2\tau \right) \right]$ with factors $(-1)^n = \pm 1$ for mutually opposite phase rotations around even and odd nods, respectively.

The female spermathecal duct is not only helical but also convoluted (Filippov et al. 2015). However following the former paper (Filippov et al. 2015), we concentrated on the role of spiral and knot geometries and neglected all the variations of the spiral core $Y_0 = A_0 \cos(2\pi X/\lambda_0) = 0$ and limited ourselves by the straight spiraled-duct only. Such spirals having four knots $N_{knots} = 4$ and different combinations of the flagellum rigidities are shown in Figs. 11.5 and 11.6. In each figure, the spiral axis of the female elastic channel is shown by a blue line. The position of the flagellum inside the female channel is shown by red curves and the flagellum tip is marked by a red circle. Numerically, the female duct was defined as an elastic confinement acting on every segment $\{z_j(x_j),\ y_j(x_j)\}$ of the male flagellum by the returning forces: $f_y^{confinement}\left(X = x_j\right) = K\left(Y(X) - y_j\right);\quad f_z^{confinement}\left(X = x_j\right) = K\left(Z(X) - z_j\right),$ which are regulated by the elastic constant K.

For reflecting a probable uniform stiffness which is suggested by CLSM images, we fixed everywhere below, i.e. a general flagellum rigidity $k_0^\perp = K$ for the rigid and $k_0^\perp = 0.01K$ for the soft uniform flagellum (g = 0), respectively. Parameters g = 0.99 and $k_0^\perp = K$ are chosen for the rigid gradient flagellum with the soft end and g = −99 and for $k_0^\perp = 0.01K$ the soft flagellum with the hard end.

The presence of liquid inside the channel was taken into account by introducing a proportional to the velocity $\vec{v}_j$ damping force: $f_j^{damping} = \gamma \vec{v}_j$. This force was also added to the equations of motion of all the segments, which are the same as in previous study (Filippov et al. 2015):

$$\frac{\sigma \vec{v}_j}{\sigma \tau} = f_j^{elastic} + f_j^{confinement} + f_j^{damping} \tag{11.3}$$

References

Ah-King, M., Barron, A. B., & Herberstein, M. E. (2014). Genital evolution: Why are females still understudied? *PLoS Biology, 12*, e1001851.

Arnqvist, G. (1998). Comparative evidence for the evolution of genitalia by sexual selection. *Nature, 393*, 784–786.

Arnqvist, G., & Danielsson, I. (1999). Copulatory behavior, genital morphology and male fertilization success in water striders. *Evolution, 5*, 147–156.

Arnqvist, G., & Rowe, L. (1995). Sexual conflict and arms races between the sexes: A morphoogical adaptation for contral of mating in a female insect. *Proceedings of the Royal Society B: Biological Sciences, 261*, 123–127.

Brennan, P. L. R., Prum, R. O., McCracken, K. G., Sorenson, M. D., Wilson, R. E., & Birkhead, T. R. (2007). Coevolution of male and female genital morphology in waterfowl. *PLoS One, 5*, e418.

Cerkvenika, U., van de Straata, B., Gussekloa, S. W. S., & van Leeuwena, J. L. (2017). Mechanisms of ovipositor insertion and steering of a parasitic wasp. *Proceedings of the National Academy of Sciences of the United States of America*. https://doi.org/10.1073/pnas.1706162114.

Cordoba-Aguilar, A. (2005). Possible coevolution of male and female genital form and function in a calopterygid damselfly. *Journal of Evolutionary Biology, 18*, 132–137.

Dougherty, L. R., Rahman, I. A., Burdfield-Steel, E. R., Greenway, E. V., & Shuker, D. M. (2015). Experimental reduction of intromittent organ length reduces male reproductive success in a bug. *Proceedings of the Royal Society B: Biological Sciences, 282*, 20150724.

Eberhard, W. G. (1985). *Sexual selection and animal genitalia*. Cambridge, MA: Harvard University Press.

Filippov, A. E., Kovalev, A. E., Matsumura, Y., & Gorb, S. N. (2015). Male penile propulsion into spiraled spermathecal ducts of female chrysomelid beetles: A numerical simulation approach. *Journal of Theoretical Biology, 384*, 140–146.

Gorb, S. N., & Beutel, R. G. (2001). Evolution of locomotory attachment pads of hexapods. *Naturwissenschaften, 88*, 530–534.

Gorb, S. N., Beutel, R. G., Gorb, E. V., Jiao, Y., Kastner, V., Niederegger, S., Popov, V. L., Scherge, M., Schwarz, U., & Vötsch, W. (2002). Structural design and biomechanics of friction-based releasable attachment devices in insects. *Integrative and Comparative Biology, 42*, 1127–1139.

Gorb, S. N., & Filippov, A. E. (2014). Fibrillar adhesion with no clusterisation: Functional significance of material gradient along adhesive setae of insects. *Beilstein Journal of Nanotechnology, 5*, 837–845.

Holwell, G. I., Winnick, C., Tregenza, T., & Herberstein, M. E. (2009). Genital shape correlates with sperm transfer success in the praying mantis *Ciulfina klassi* (Insecta: Mantodea). *Behavioral Ecology and Sociobiology, 64*, 617–625.

Hosken, D. J., & Stockley, P. (2004). Sexual selection and genital evolution. *Trends in Ecology & Evolution, 19*, 87–93.

House, C. M., & Simmons, L. W. (2003). Genital morphology and fertilization success in the dung beetle *Onthophagus taurus*: An example of sexually selected male genitalia. *Proceedings of the Royal Society B: Biological Sciences, 270*, 447–455.

Kamimura, Y. (2013). Promiscuity and elongated sperm storage organs work cooperatively as a cryptic female choice mechanism in an earwig. *Animal Behaviour, 85*, 377–383.

Kelly, D. A. (2016). Intromittent organ morphology and biomechanics: Defining the physical challenges of copulation. *Integrative and Comparative Biology, 56*, 630–634.

van Lieshout, E., & Elgar, M. A. (2010). Longer exaggerated male genitalia confer defensive sperm-competitive benefits in an earwig. *Evolutionary Ecology, 25*, 351–362.

Macagno, A. L. M., Pizzo, A., Parzer, H. F., Palestrini, C., Rolando, A., & Moczek, A. P. (2011). Shape - but not size - codivergence between male and female copulatory structures in *Onthophagus* beetles. *PLoS One, 6*, e28893.

Matsumura, Y., Michels, J., Appel, E., & Gorb, S. N. (2017). Functional morphology and evolution of the hyper-elongated intromittent organ in *Cassida* leaf beetles (Coleoptera: Chrysomelidae: Cassidinae). *Zoology, 120*, 1–14.

Matsumura, Y., Yoshizawa, K., Machida, R., Mashimo, Y., Dallai, R., Gottardo, M., Kleinteich, T., Michels, J., Gorb, S. N., & Beutel, R. G. (2014). Two intromittent organs in *Zorotypus caudelli* (Insecta, Zoraptera): The paradoxical coexistence of an extremely long tube and a large spermatophore. *Biological Journal of the Linnean Society, 112*, 40–54.

Matushkina, N., & Gorb, S. N. (2007). Mechanical properties of the endophytic ovipositor in damselflies (Zygoptera, Odonata) and their oviposition substrates. *Zoology, 110*, 167–175.

Michels, J., Appel, E., & Gorb, S. N. (2016). Functional diversity of resilin in Arthropoda. *Beilstein Journal of Nanotechnology, 7*, 1241–1259.

Michels, J., & Gorb, S. N. (2012). Detailed three-dimensional visualization of resilin in the exo-skeleton of arthropods using confocal laser scanning microscopy. *Journal of Microscopy, 245*, 1–16.

Michels, J., Gorb, S. N., & Reinhardt, K. (2015). Reduction of female copulatory damage by resilin represents evidence for tolerance in sexual conflict. *Journal of the Royal Society Interface, 12*, 20141107.

Michels, J., Vogt, J., & Gorb, S. N. (2012). Tools for crushing diatoms-opal teeth in copepods feature a rubber-like bearing composed of resilin. *Scientific Reports, 2*, 465.

Miller, G. T., & Pitnck, S. (2002). Sperm-female coevolution in *Drosophila*. *Science, 298*, 1230–1233.

Peisker, H., Michels, J., & Gorb, S. N. (2013). Evidence for a material gradient in the adhesive tarsal setae of the ladybird beetle *Coccinella septempunctata*. *Nature Communications, 4*, 1661.

Rodriguez, V. (1994). Function of the spermathecal muscle in *Chelymorpha alternans* Boheman (Coleoptera: Chrysomelidae: Cassidinae). *Physiological Entomology, 19*, 198–202.

Rodriguez, V. (1995). Relation of flagellum length to reproductive success in male *Chelymorpha alternans* Boheman (Coleoptera: Chrysomelidae: Cassidinae). *The Coleopterists Bulletin, 49*, 201–205.

Rodriguez, V., Windsor, D. M., & Eberhard, W. G. (2004). Tortoise beetle genitalia and demonstrations of a sexually selected advantage for flagellum length in *Chelymorpha alternans* (Chrysomelidae, Cassidini, Stolaini). In P. Jolivet, J. A. Santiago-Blay, & M. Schmitt (Eds.), *New developments in the biology of Chrysomelidae* (pp. 739–748). The Hague: Academic Publisher.

Rowe, L., & Arnqvist, G. (2012). Sexual selection and the evolution of genital shape and complexity in water striders. *Evolution, 66*, 40–54.

Sakurai, G., Himuro, C., & Kasuya, E. (2012). Intra-specific variation in the morphology and the benefit of large genital sclerites of males in the adzuki bean beetle (*Callosobruchus chinensis*). *Journal of Evolutionary Biology, 25*, 1291–1297.

Sentenská, L., Pekár, S., Lipke, E., Michalik, P., & Uhl, G. (2015). Female control of mate plugging in a female-cannibalistic spider (*Micaria sociabilis*). *BMC Evolutionary Biology, 15*, 18.

Simmons, L. W. (2014). Sexual selection and genital evolution. *Austral Entomology, 53*, 1–17.

Simmons, L. W., House, C. M., Hunt, J., & Garcia-Gonzalez, F. (2009). Evolutionary response to sexual selection in male genital morphology. *Current Biology, 19*, 1442–1446.

Tadler, A. (1999). Selection of a conspicuous male genitalic trait in the seedbug *Lygaeus simulans*. *Proceedings of the Royal Society B: Biological Sciences, 266*, 1773–1777.

Tanabe, T., & Sota, T. (2013). Both male and female novel traits promote the correlated evolution of genitalia between the sexes in an arthropod. *Evolution, 68*, 441–452.

Udelson, D. (2007). Biomechanics of male erectile function. *Journal of the Royal Society Interface, 4*, 1031–1047.

Villavaso, E. J. (1975). Functions of the spermathecal muscle of the boll weevil, *Anthonomus grandis*. *Journal of Insect Physiology, 21*, 1275–1278.

Willkommen, J., Michels, J., & Gorb, S. N. (2015). Functional morphology of the male caudal appendages of the damselfly *Ischnura elegans* (Zygoptera: Coenagrionidae). *Arthropod Structure & Development, 44*, 289–300.

Wulff, N. C., van de Kamp, T., dos Santos Rolo, T., Baumbach, T., & Lehmann, G. U. C. (2017). Copulatory courtship by internal genitalia in bushcrickets. *Scientific Reports, 7*, 42345.

Index